# BROMINE AND CHLORINE CHEMISTRY IN THE ARCTIC BOUNDARY LAYER

A Dissertation
Presented to
The Academic Faculty

by

Jin Liao

In Partial Fulfillment
of the Requirements for the Degree
Doctor of Philosophy in the
School of Earth and Atmospheric Sciences

Georgia Institute of Technology
December 2011

# BROMINE AND CHLORINE CHEMISTRY IN THE ARCTIC BOUNDARY LAYER

Approved by:


Dr. L. Gregory Huey, Advisor
School of Earth and Atmospheric Sciences
*Georgia Institute of Technology*

Dr. Rodney J. Weber
School of Earth and Atmospheric Sciences
*Georgia Institute of Technology*

Dr. Yuhang Wang
School of Earth and Atmospheric Sciences
*Georgia Institute of Technology*

Dr. J. Andrew Neuman
Earth System Research Laboratory
*NOAA*

Dr. Paul H. Wine
School of Earth and Atmospheric Sciences and chemistry and Biochemistry
*Georgia Institute of Technology*


Date Approved: October 27, 2011

*To my family*

# ACKNOWLEDGEMENTS

I am deeply indebted to my advisor, Professor Greg Huey, for his insightful guidance and continuous support throughout my Ph.D studies. None of my graduate research work would be done without him. He is not only my advisor, but also my mentor and teacher. He always made himself available to me when I had research ideas or questions to discuss, although he was always very busy. He always provided me friendly research environment, and directed me with good timing. I also really appreciate the great opportunities he provided for me to present my research results in top scientific conferences and workshops.

I would like to express my gratitude to the CIMS research group members: DaveTanner, Bob Stickel, Saewung Kim, Steven Sjodtedt, Dexian Chen, Eric Parker, Arsineh Hecobian, Bonnie Reichardt, and Tony Cummings, for their help during my stay at Georgia Tech. Dave and Bob taught me the first hand experience of how to setup, maintain, and trouble shoot the instrument during three field campaigns. Dave was always there when I got stuck with the CIMS and need help.

I am thankful for the science team and organizers in the OASIS and GSHOX campaigns especially the NCAR folks. Many of them are also coauthors of my research papers. Their help in the field and their measurements dataset make this study possible. I am also grateful to lab collaborators Jack Dibb and Eric Scheuer. Their support facilitates the study of soluble bromide measurements characterization. I appreciate the input from Zhen Liu in Dr. Wang's group at Georgia Tech in Flexpart footprint residence time calculation.

I would like to thank my committee members Andy Neuman, Yuhang Wang, Paul Wine and Rodney Weber for their support and comments in my thesis study.

Finally, I would like to thank my parents, my brother, and my husband for their continuous encouragement and love.

# TABLE OF CONTENTS

# LIST OF TABLES

# LIST OF FIGURES

# SUMMARY

Halogen chemistry plays an important role in spring time ozone and mercury depletion events (ODEs and MDEs) and may efficiently oxidize hydrocarbons such as the important greenhouse gas methane ($CH_4$) in the polar marine boundary layer. However, measurements of bromine and chlorine species other than bromine oxide (BrO) are still very limited. This thesis presents a detailed study of bromine and chlorine chemistry in the Arctic boundary layer based upon measurements of bromine and chlorine containing species using chemical ionization mass spectrometry (CIMS).

A series of bromine species (BrO, hypobromous acid (HOBr), and molecular bromine ($Br_2$)) were measured by CIMS at Barrow, AK (71°19′ N, 156° 39′ W) in spring 2009 during the Ocean-Atmospheric-Sea ice-Snowpack (OASIS) campaign. The *in situ* CIMS BrO measurements were in excellent agreement ($R^2 = 0.85$) with observations by long path-differential optical absorption spectroscopy (LP-DOAS). This demonstrated the ability of CIMS to selectively and accurately detect BrO. The first direct HOBr observations were achieved and found to be in agreement with the predictions from a steady-state photochemical model constrained to BrO observations except for periods of high wind speeds (> 6 m $s^{-1}$). Blowing snow associated with high wind speeds in the polar environment may provide surface that can convert HOBr to BrO via $Br_2$ production. BrO were also found to increase at high wind speeds. Ozone levels were strongly anti-correlated with nighttime $Br_2$. Finally, we demonstrated that average diurnal profiles of BrO, HOBr and $Br_2$ can be reasonably well predicted with a time-dependent model that

allows for efficient heterogeneous recycling of HOBr, hydrogen bromide (HBr), and bromine nitrate ($BrONO_2$) back to more reactive forms of bromine.

Unexpectedly high levels of molecular chlorine ($Cl_2$) (up to ~400 pptv) were also observed at Barrow, AK during OASIS. Diurnal profiles of $Cl_2$ were frequently observed with maximum levels in the early morning and late afternoon and no significant concentrations at night. $Cl_2$ levels were well correlated ($R^2 = 0.71$) with $O_3$. Predicted chlorine monoxide (ClO) and hypochlorous acid (HOCl) from a simple time dependent box model were 4-5 times lower than $Cl_2$. Back trajectories from a Lagrangian particle dispersion model (Flexpart) showed that the air masses with high levels of $Cl_2$ observed had more residence time in the boundary layer near Barrow supporting the hypothesis that surfaces covered by snow can be the source of active chlorine emissions and recycling. Chlorine radicals produced from photolysis of $Cl_2$ dominate $CH_4$ oxidation and play a significant role in the ODEs and MDEs. This phenomenon may be ubiquitous in polar marine regions and is in need of further study.

BrO, the hydroxyl radical (OH), the sum of peroxy radicals ($HO_2 + RO_2$), and other species were measured at Summit, Greenland during the Greenland Summit Halogen-$HO_x$ (GSHOX) Campaign in spring 2007 and summer 2008 to investigate the impact of BrO on $HO_x$ ($OH + HO_2$) cycling above the Greenland Ice Sheet. A photochemical 0-D box modeled reasonably predicted $HO_2$+$RO_2$ but under predicted OH. We found that including bromine chemistry in the model constrained by observations of BrO brought the average hourly OH and $HO_2 + RO_2$ predictions closer to the observations. This indicates that BrO impacted the OH levels at Summit. Although, significant discrepancies between observed and predicted OH could not be explained by

the measured BrO. Observations of enhanced RGM were found to be coincident with under prediction of OH.

Airborne measurements of BrO, active bromine (HOBr + $Br_2$) and soluble bromide were performed on the NASA DC-8 research aircraft during the Arctic Research of the Composition of the Troposphere from Aircraft and Satellites (ARCTAS) mission to examine bromine photochemistry in the spring time. We determined the mist chamber (MC) detection efficiency to $Br_2$, HOBr, BrO, and HBr as soluble bromide ($Br^-$) in the laboratory. The detection efficiencies combined with steady-state model calculations constrained to *in situ* BrO measurements by CIMS are used to estimate soluble bromide levels along the DC-8 flight track of 17 April 2008, where the highest levels BrO and $Br^-$ were detected. The excellent agreement ($R^2$ = 0.76; slope = 0.98; intercept = –3.5 pptv) between modeled and observed soluble bromide, when BrO was above detection limit (> 2 pptv) under unpolluted conditions (NO < 100 pptv), indicates that the CIMS BrO measurements were consistent with the MC soluble bromide measurements.

# CHAPTER 1

# INTRODUCTION

Bromine and chlorine radicals are strong atmospheric oxidants and can significiantly affect the fates and lifetime of important atmospheric constituents. It is well known that chlorine radicals play a key role in stratospheric ozone ($O_3$) hole formation [e.g. Crutzen and Arnold, 1986; Anderson et al., 1991; Solomon, 1999]. Bromine and chlorine radicals can catalyze surface ozone [e.g. Barrie et al., 1988; Hausmann and Platt, 1994; Oltmans, 1981; Bottenheim et al., 2002; Simpson et al., 2007a; Tuckermann et al., 1997] and mercury [e.g. Schroeder et al., 1998; Lindberg et al., 2002; Berg et al., 2003; Donohoue et al., 2005] depletions in polar marine boundary layer. During ozone and mercury depletion events (ODEs and MDEs), relatively benign elemental mercury is oxidized to more soluble and toxic forms of mercury, which can be accumulated in the ecosystem and have potential impacts on human health [e.g. Steffen et al., 2008]. Chlorine radicals can also impact hydrocarbon (e.g. the greenhouse gas methane) oxidation in the troposphere [Jobson et al., 1994; Platt et al., 2004; Boudries and Bottenheim, 2000; Sander et al., 2006] and may therefore influence climate change and air quality.

Barrie et al [1988] first observed that filterable bromide was strongly anti-correlated with $O_3$ and proposed bromine catalyzed mechanisms to account for ozone depletion events (ODEs) in the arctic marine boundary layer. The first measurements of bromine oxide (BrO) [Hausmann and Platt, 1994] confirmed the importance of a bromine radicals in ODEs. BrO, the key species thought to determine $O_3$ loss rates, has been

measured in the Arctic (up to 30-40 pptv) [e.g. Pöhler et al., 2010], Antarctic (up to 20 pptv) [e.g. Saiz-Lopez et al., 2007] and Atlantic (up to 4 pptv) [e.g. Read et al., 2008] marine boundary layer. Airborne measurements [Ridley et al., 2003] found that ODEs can extend over several hundreds kilometers horizontally and from the surface to altitude as high as several hundreds meters to ~1 km vertically in the Arctic. High levels of soluble bromide were detected by mist chamber during low $O_3$ flight legs [Ridley et al., 2003]. Currently, long path-differential optical absorption spectroscopy (LP-DOAS), which observes average BrO over several kilometers, is the best developed and most commonly used technique to measure BrO. Satellite sensors that examine the same spectral features as LP-DOAS can be used to map global BrO column densities [Wagner and Platt, 1998; Chance, 1998; Richter et al., 1998]. BrO observations from satellites are often used to constrain the models that are used to simulate global ozone and mercury concentrations [e.g. Zeng et al., 2003; Holmes et al., 2010]. Model simulation, based on the proposed bromine chemical mechanisms, has been developed to predict the concentrations of speciated bromine and chlorine compounds [e.g. Fan and Jacob, 1992; Evans et al., 2003].

Efforts have also been made to investigate chlorine chemistry but the understanding of chlorine chemistry is more restricted in the polar marine boundary layer. Chlorine atoms levels, indirectly derived from the oxidation of VOCs by chlorine atoms, have been estimated to be in the range of $10^3$–$10^4$ atoms $cm^{-3}$ in the Arctic [Jobson et al., 1994; Boudries and Bottenheim, 2000]. Up to 21 pptv of chlorine monoxide (ClO), much higher than that derived from VOCs oxidation, was measured at Ny-Ålesund, Svalbard [Tuckermann et al., 1997] by a LP-DOAS with a detection limit of ~10 pptv. Models

[Vogt et al., 1996; Evans et al., 2003] have been used to predict chlorine species concentrations in the polar marine boundary layer according to current reaction mechanisms [e.g. Sander et al., 2006]. Under high $NO_x$ conditions high levels of nitryl chloride ($ClNO_2$) of up to ~1 ppbv and ~450 pptv coincident with dinitrogen pentoxide ($N_2O_5$) were detected at Houston, Texas [Osthoff et al., 2008] and Boulder, Colorado [Thornton et al., 2010] at night, respectively. This demonstrates that condensed phase chlorine ($Cl^-$) can be activated to gas phase chlorine species (i.e by uptake of $N_2O_5$). However, no measurements of chlorine radical precursors have been made in the polar marine boundary layer.

Current bromine and chlorine chemical mechanisms for the troposphere are summarized in a recent review paper [Simpson et al., 2007a] and are illustrated in Figure 1.1. Molecular bromine ($Br_2$) photolyzes to produce bromine atoms (Br) at sun rise. Br atom reacts with $O_3$ to form BrO. $O_3$ is then; destroyed by reactions initiated by $O_3$ reacting with Br followed by self-reaction of BrO and reactions of BrO with hydroperoxy radicals ($HO_2$) and ClO. Hypobromous acid (HOBr), formed from reaction of BrO with $HO_2$, can either photolyze to produce Br atoms and hydroxyl radicals (OH) or react on surfaces. Br atom also reacts with formaldehyde ($CH_2O$) and hydroperoxy radials ($HO_2$) to form HBr especially under low $O_3$ condition. The $HO_x$ (OH and $HO_2$) cycling is then impacted by bromine chemistry. Under high $NO_x$ conditions, BrO reacts with nitrigen dioxide ($NO_2$) to produce bromine nitrate ($BrONO_2$) [Sander et al., 2006]. HOBr and $BrONO_2$ likely undergo heterogeneous reactions to regenerate $Br_2$ [Fan and Jacob, 1992]. Br atoms can also react with gaseous elemental mercury (GEM) to form reactive gaseous

mercury efficiently [Donohoue et al., 2006], which is more soluble and can deposit to surfaces and accumulate in ecosystems.

Chlorine radical precursors (molecular chlorine ($Cl_2$) or $ClNO_2$) can efficiently photolyze to produce Cl during the day. Cl atoms efficiently react with many hydrocarbons (RH) to produce hydrogen chloride (HCl). Cl atoms can also react with $O_3$ to produce ClO. The reaction of ClO with BrO can contribute to tropospheric ODEs significiantly [Friedl and Sander, 1989; Turnipseed et al., 1991; Sander et al., 2006]. Hypochlorous acid (HOCl), which is formed from the reaction of ClO and $HO_2$, can either photolyze to reproduce Cl atoms or deposit to heterogeneous surfaces and probably react with chloride to reform $Cl_2$. Recently, uptake of $N_2O_5$ on chloride ($Cl^-$) containing surface was found to convert $Cl^-$ to gas phase $ClNO_2$ in high $NO_x$ regions [Osthoff et al., 2008; Thornoton et al., 2010]. The formation mechanisms of $Cl_2$ and bromine monochloride (BrCl) in the atmosphere are not well established [Vogt et al., 1996; Finley and Saltzman, 2008; Neuman et al., 2010; Lawler et al., 2011].

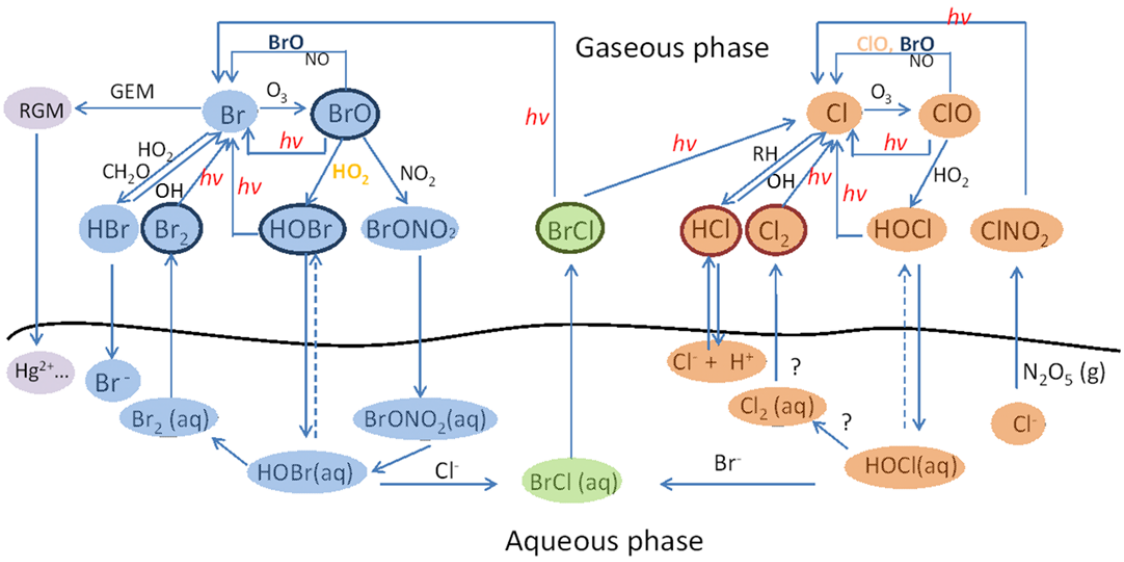


Figure 1.1 Bromine and chlorine chemical mechanisms in gaseous and aqueous phase.

Although the role of active bromine in catalyzing surface ozone and mercury depletions is established and our understanding of halogen chemistry in the troposphere has been greatly improved in recent years, many questions regarding the sources, vertical and horizontal distributions, speciation, and the impact of bromine and chlorine compounds remain. This thesis seeks to advance our understanding of halogen chemistry by addressing the following issues.

1. What is the distribution of bromine species horizontally and vertically in the troposphere? Can BrO be measured with an *in situ* method? Can this method perform airborne BrO measurements accurately? Are airborne BrO measurements consistent with the soluble bromide measurements [Ridley et al., 2003]? Are the *in situ* BrO measurements consistent with the satellite observations? Can tropospheric BrO columns be accurately retrieved from satellite observations?
2. The measurements of speciated bromine compounds other than BrO are very limited. There are a few observations of $Br_2$ [e.g. Foster et al., 2001; Finley and Saltzman, 2008; Neuman et al., 2010]; however, significant $Br_2$ observed in the daytime is likely due to conversion of HOBr on the inlet [Neuman et al., 2010]. Can we directly measure speciated bromine compounds (BrO, HOBr, $Br_2$, HBr, and $BrONO_2$) simultaneously? Can the observed levels be explained by known chemistry? What is the role of heterogeneous reactions in sustaining the bromine concentrations? What conditions favor bromine activation?

3. What are the concentrations of chlorine radicals (Cl and ClO) or chlorine radical precursors (e.g. $Cl_2$ and $ClNO_2$) in the Arctic? Are Cl concentrations consistent with those derived indirectly from hydrocarbon oxidation? Can the observed chlorine species be explained by the known mechanisms? What are the potential sources and impact?
4. No BrO measurements in non-marine Arctic regions have been reported. Are significant levels of BrO (> 1 pptv) present in non-marine Arctic regions? Can snow chemistry be a source of BrO? Does BrO impact other chemistry (e.g. $HO_x$ cycling)? Is there any bromine associated ozone loss or mercury oxidation present?

This thesis aims to investigate the detailed bromine and chlorine chemistry in the Arctic troposphere by using chemical ionization mass spectrometry (CIMS) to attempt to answer the above questions. A main focus of this thesis is a study of bromine and chlorine chemistry at Barrow, AK in the Arctic marine boundary layer (chapter 2, 3 and 4). Moreover, the impact of BrO levels on OH and $HO_2$ cycling at Summit, located in the middle of Greenland ice sheet about 400 km away from the ocean, is also investigated (chapter 5). In addition, the consistency between airborne *in situ* BrO and soluble bromide measurements and between the *in situ* and satellite BrO measurements is discussed (chapter 6).

In chapter 2 [Liao et al., 2011a], the CIMS detailed instrument configuration, inlet setup, reagent ion, background determination, and calibration methods in measuring halogen species are described. The detection limit of BrO obtained for CIMS is 2.6 pptv

(3σ) for a 4 s integration period and the estimated detection uncertainty is ±30%. The capability of CIMS to accurately and selectively measure BrO is demonstrated by the excellent agreement ($R^2$ = 0.85) of the BrO measurements by CIMS and long path differential optical absorption spectroscopy (LP-DOAS) at moderate wind speeds (> 3 $ms^{-1}$ or < 8 $ms^{-1}$) and low NO conditions (< 100 pptv). These conditions likely favor homogeneous distribution of BrO over spatial scales of up to at least 4 km.

In chapter 3 [Liao et al., 2011c], the simultaneous measurements of bromine species (HOBr, $Br_2$ and BrO) by CIMS at Barrow, AK in spring 2009 are reported. The first measurements of the important bromine species HOBr were achieved. The HOBr measurements reasonably well agreed with the predictions from a steady-state photochemical model constrained to BrO observations except for the periods of high wind speeds (> 6 m $s^{-1}$). High wind and blowing snow likely provide more surfaces for loss of HOBr. The study also provides direct evidence for high wind speed and blowing snow in activating bromine including potentially producing higher total inorganic gas phase bromine species. There is no clear relationship between BrO and $O_3$. Nighttime $Br_2$ were found to be clearly anti-correlated with $O_3$, which indicates that air masses with depleted ozone were likely transported from the regions rich in $Br_2$. Finally, the observed diurnal bromine speciation can be reasonably simulated by a time dependent box model which allowed efficient heterogeneous recycling of HOBr, HBr and $BrONO_2$ to more active forms of bromine.

In chapter 4 [Liao et al., 2011e], high levels of $Cl_2$ of up to ~400 pptv observed at Barrow, AK in spring 2009 are reported. The diurnal profiles of $Cl_2$ frequently observed had maximum concentrations in the early morning or later afternoon with no significiant

concentrations at night. A time dependent model was constructed to estimate the impact of observed $Cl_2$ on chlorine chemistry. A Lagrangian particle dispersion model (Flexpart) was used to track the potential sources of high levels of $Cl_2$ and air masses with high levels of $Cl_2$ were found to have more residence time in the boundary layer around Barrow. High levels of $Cl_2$ have a large impact on methane oxidation and significantly contribute to ODEs and MDEs.

Chapter 5 [Liao et al., 2011b] investigates the impact of BrO on $HO_x$ cycling above Greenland Ice Sheet during the Greenland Summit Halogen-$HO_x$ (GSHOX) Campaign in spring 2007 and summer 2008. The BrO levels observed by CIMS were less than 2 pptv on average. The median midday values of $HO_2 + RO_2$ and OH concentrations observed by CIMS were $2.7\times10^8$ molec $cm^{-3}$ and $3.0\times10^6$ molec $cm^{-3}$ in spring 2007, and $4.2\times10^8$ molec $cm^{-3}$ and $4.1\times10^6$ molec $cm^{-3}$ in summer 2008. A basic photochemical 0-D box model highly constrained by observations of $H_2O$, $O_3$, CO, $CH_4$, NO, and J values predicted $HO_2 + RO_2$ (R = 0.90, slope = 0.87 in 2007; R = 0.79, slope = 0.96 in 2008) reasonably well and under predicted OH (R = 0.83, slope = 0.72 in 2007; R = 0.76, slope = 0.54 in 2008). Including bromine chemistry in the model constrained by observations of BrO improved the correlation between observed and predicted $HO_2 + RO_2$ and OH, and brought the average hourly OH and $HO_2 + RO_2$ predictions closer to the observations. These model comparisons confirmed our understanding of the dominant $HO_x$ sources and sinks in this environment and indicated that BrO impacted the OH levels at Summit. Although, significant discrepancies between observed and predicted OH could not be explained by the measured BrO. Finally, observations of enhanced RGM were found to be coincident with under prediction of OH.

In chapter 6 [Liao et al., 2011d], a CIMS instrument measuring speciated bromine compounds and a mist chamber measuring soluble bromide were used to characterize the measurements of soluble bromide in the laboratory. The MC detection efficiency to molecular bromine ($Br_2$), hypobromous acid (HOBr), bromine oxide (BrO), and hydrogen bromide (HBr) as soluble bromide ($Br^-$) was 0.9 ± 0.1, 1.06 ± 0.30, 0.4 ± 0.1, and 0.95 ± 0.1, respectively. These efficiency factors were used to estimate soluble bromide levels along the DC-8 flight track of 17 April 2008 based on photochemical model calculation constrained to *in situ* BrO measured by CIMS. During this flight, the highest levels of soluble bromide and BrO were observed and atmospheric conditions were ideal for the space-borne observation of BrO. The good agreement ($R^2 = 0.76$; slope = 0.98; intercept = –3.5 pptv) between modeled and observed soluble bromide, when BrO was above detection limit (> 2 pptv) under unpolluted conditions (NO < 100 pptv), indicates that the CIMS BrO measurements were consistent with the MC soluble bromide as well as our current understanding of inorganic photochemistry. Tropospheric BrO vertical column densities ($BRO_{TROP}^{VCD}$) derived from CIMS BrO observations compare reasonably well with $BRO_{TROP}^{VCD}$ from OMI on 17 April 2008.

Finally, chapter 7 summarizes the findings in the previous five chapters and points out some of the unresolved issues in bromine and chlorine chemistry in the Arctic.

# CHAPTER 2

# A COMPARISON OF ARCTIC BRO MEASUREMENTS BY CHEMICAL IONIZATION MASS SPECTROMETRY AND LONG PATH DIFFERENTIAL OPTICAL ABSORPTION SPECTROSCOPY

## 2.1 Introduction

Bromine plays an important role in tropospheric ozone depletion events (ODEs). Barrie et al. [1988] first observed that filterable bromine (f-Br) strongly anticorrelates with ozone ($O_3$). Hausmann and Platt [1994] reported the first measurements of BrO during ODEs in the Arctic at Alert, Canada. Frequent surface ODEs have been observed in the springtime polar marine boundary layer in a variety of locations such as Barrow, Alaska [Oltmans, 1981; Oltmans and Komhyr, 1986; Oltmans and Levy, 1994], Alert, Canada [Bottenheim et al., 1986, 2002], Ny-Ålesund, Svalbard [Lorenzen-Schmidt et al., 1998; Tuckermann et al., 1997] and Halley Bay, Antarctica [Jones et al., 2006]. A bromine radical catalyzed cycle, including Br and BrO, was proposed to destroy $O_3$ in the troposphere [Barrie et al., 1988; Hausmann and Platt, 1994; Fan and Jacob, 1992; McConnell et al., 1992]. The relevant mechanisms are reviewed by Simpson et al. [2007a] and summarized in the chapter 1. The self-reaction of BrO is often considered the rate limiting step for $O_3$ destruction as it destroys odd oxygen and regenerates active bromine [Sander et al., 2006; Fan and Jacob, 1992]. Consequently, accurate measurements of BrO

at low pptv levels are needed to quantify the active bromine concentrations and the $O_3$ destruction rate catalyzed by bromine chemistry.

Although evidence of bromine chemistry inducing surface $O_3$ depletion events is strong, the sources of bromine and the bromine activation mechanisms remain unclear [Simpson et al., 2007a]. In addition, the horizontal and vertical distribution of BrO in the troposphere is uncertain, especially where BrO levels are expected to be low even though the impact of a few pptv of BrO can be significant. Satellite data suggest that the average global daytime tropospheric BrO mixing ratio is of the order 0.5–2 pptv [Sinnhuber et al., 2005; Richter et al., 2002]. A series of DOAS data [Fitzenberger et al., 2000; Friess et al., 1999; Hendrick et al., 2007; Schofield et al., 2004] also indicate that a background level (~1 pptv) of BrO exists in the free troposphere. Moreover, recent studies indicate that the derivation of tropospheric BrO column densities from satellite data may need to be reassessed [Salawitch et al., 2010; Theys et al., 2009]. Consequently, *in situ* measurements of BrO with high sensitivity and time resolution will be useful to address these issues.

Understanding the mercury cycle in the polar boundary layer and potentially other locations requires knowledge of BrO mixing ratios. Schroeder et al. [1998] observed that gaseous elemental mercury (GEM) undergoes rapid decreases in concentration during an ODE in the Arctic springtime. GEM was generally thought to be very stable (lifetime = ~6–24 months) in the atmosphere [Schroeder and Munthe, 1998]. However, these results indicated that relatively benign GEM could be oxidized by halogen species to more reactive and soluble mercury compounds which can deposit to the surface or on aerosol [Steffen et al., 2008].

The connections between the observed GEM depletion and simultaneous $O_3$ loss in the Arctic have been studied in field campaigns in Barrow, Ny-Ålesund and other Arctic sites [e.g., Lindberg et al., 2002; Berg et al., 2003], where reactive gaseous mercury (RGM) anticorrelated with GEM during GEM depletion events. At this time the role of $O_3$ and hydroxyl radical (OH) as oxidants of mercury (Hg) is not well established as the rate constants for these species may be too small to be important [Hall, 1995; Sommar et al., 2001]. However, Br atoms have been demonstrated to effectively oxidize Hg (e.g., convert GEM into RGM) [Ariya et al., 2002; Donohoue et al., 2006]. Br atom levels are usually estimated from BrO measurements and the ratio calculated assuming photochemical steady state (Br/BrO ratio ranges from 0.07 to 1 when $O_3$ ranges from 40 ppbv to 3 ppbv) [Zeng, 2005]. Thus, accurate measurements of BrO concentrations are needed to estimate the oxidation rate of elemental mercury by bromine atoms and further understanding of the atmospheric chemistry of mercury.

As BrO is a short-lived radical species with low atmospheric abundance, accurate and reliable detection of BrO is quite challenging. The most developed and commonly used technique for ground based BrO measurement is long path-differential optical absorption spectroscopy (LP-DOAS). Column abundances of trace gases integrated along a path of several kilometers [Platt, 1994] are determined using specific narrow-band absorption structures in the ultraviolet and visible spectral regions. This technique has been used to measure BrO at: Alert, Canada [Hausmann and Platt, 1994]; Ny-Ålesund, Spitsbergen [Tuckermann et al., 1997]; Halley Station, Antarctica [Saiz- Lopez et al., 2007]; aboard the research ice-breaker in the Amundsen Gulf, Arctic Ocean [Pöhler et al., 2010], and in many other locations. LP-DOAS can provide measurements of $O_3$, IO, ClO,

$NO_2$, OClO, OIO, $I_2$, and other species as well as BrO [Tuckermann et al., 1997; Saiz-Lopez et al., 2007; Stutz et al., 2002]. In recent years, cavity enhanced absorption techniques have been developed to provide DOAS measurements with much higher spatial resolution [e.g., Ball et al., 2004; Langridge et al., 2006]. A review of principles and applications of LPDOAS is given by Platt and Stutz [2008].

Satellite sensors that examine the same spectral features as LP-DOAS can be used to map the global BrO column density [Wagner and Platt, 1998; Chance, 1998; Richter et al., 1998]. However, there are challenges associated with deriving the tropospheric distribution of BrO from satellite data, especially in the vertical dimension. One difficulty in satellite measurements of BrO is that the tropospheric column must be obtained by subtracting the stratospheric column from the total column [Theys et al., 2009; Richter et al., 1998]. This can lead to significant errors where the stratospheric column is not accurately known [Salawitch et al., 2010; Theys et al., 2009].

The first *in situ* measurement of tropospheric BrO was by chemical conversion/resonance fluorescence (CC/RF) [Avallone et al., 2003]. This technique was originally developed for measurement of BrO in the stratosphere [Brune et al., 1989; Avallone et al., 1995]. Due to the quenching of the fluorescence signal and the absorption of the fluorescence signal by oxygen and water, the detection sensitivity of this instrument decreases as altitude decreases [Toohey et al., 1990]. The uncertainty of BrO measurements by the CC/RF technique during ARCTOC'96 in the troposphere was typically about 5 pptv [Avallone et al., 2003]. The overall accuracy of BrO measurements was estimated to be about −30%/+50% (2s) for ARCTOC'96 and ±35% (2s) at Alert 2000 [Avallone et al., 2003].

In recent years, methods to measure halogens such as BrO, $Br_2$, $Cl_2$, and $ClNO_2$ by chemical ionization mass spectrometry (CIMS) have been developed [e.g., Finley and Saltzman, 2008; Kercher et al., 2009; Neuman et al., 2010]. The CIMS methods to measure bromine species from the NASA DC-8 and NOAA P3 during the research flights in the Arctic [Neuman et al., 2010] are very similar to those used in this work. However, the BrO levels measured during these flight campaigns were always below 10 pptv [Neuman et al., 2010], which was lower than expected from satellite data [Salawitch et al., 2010]. Therefore, comparison of the CIMS with the well established LPDOAS method is important to validate the ability of the CIMS to measure BrO. In this work, the comparison of BrO measurements by CIMS and LP-DOAS in Barrow, Alaska during the OASIS 2009 campaign is presented. Both techniques are described, and ancillary measurements are examined to analyze the instrument comparison.

## 2.2 Methods

### 2.2.1 Measurement Site

The CIMS and LP-DOAS measurements of BrO were carried out from 3 March to 14 April 2009 at Barrow, Alaska (71°19′ N, 156° 39′ W), during the Ocean-Atmosphere-Sea-Ice-Snowpack (OASIS) campaign. A major focus of the OASIS campaign was to study halogen chemistry and its impact on the Arctic environment. The main research site included two trailers and the Barrow Arctic Research Center (BARC) which was located ~800 m from the Chukchi Sea to the northwest, ~15 km from the Beaufort Sea to the northeast and ~5 km to the northeast of Barrow. The prevailing wind direction was from the northeast (e.g., from the Arctic Ocean) during the measurement

period which minimized, but did not eliminate, the impacts of local emissions. The layout of the CIMS and LP-DOAS instruments is shown in Figure 2.1. The CIMS was installed in the northwest corner of trailer 2 with an inlet approximately 1.5 m above the snow surface. The LP-DOAS telescope was located at the northeast side of the BARC building. Two retro-reflectors (summer-camp and hangar) were installed at a distance of 3623 and 1074 m from the telescope and provided a light path of 7246 and 2148 m, respectively (black arrows in Figure 2.1). The height above the surface of both LP-DOAS light paths was ~2 m and varied little with horizontal position. The CIMS instrument was located about 200 m to the southeast of the LP-DOAS telescope. Most of the other chemical measurements were located in one of the two trailers including a 4 channel chemiluminescence instrument used to measure $O_3$, NO, $NO_2$, and $NO_y$ [Weinheimer et al., 1998]. The NO observations from this instrument were used as the primary indicator of local pollution.

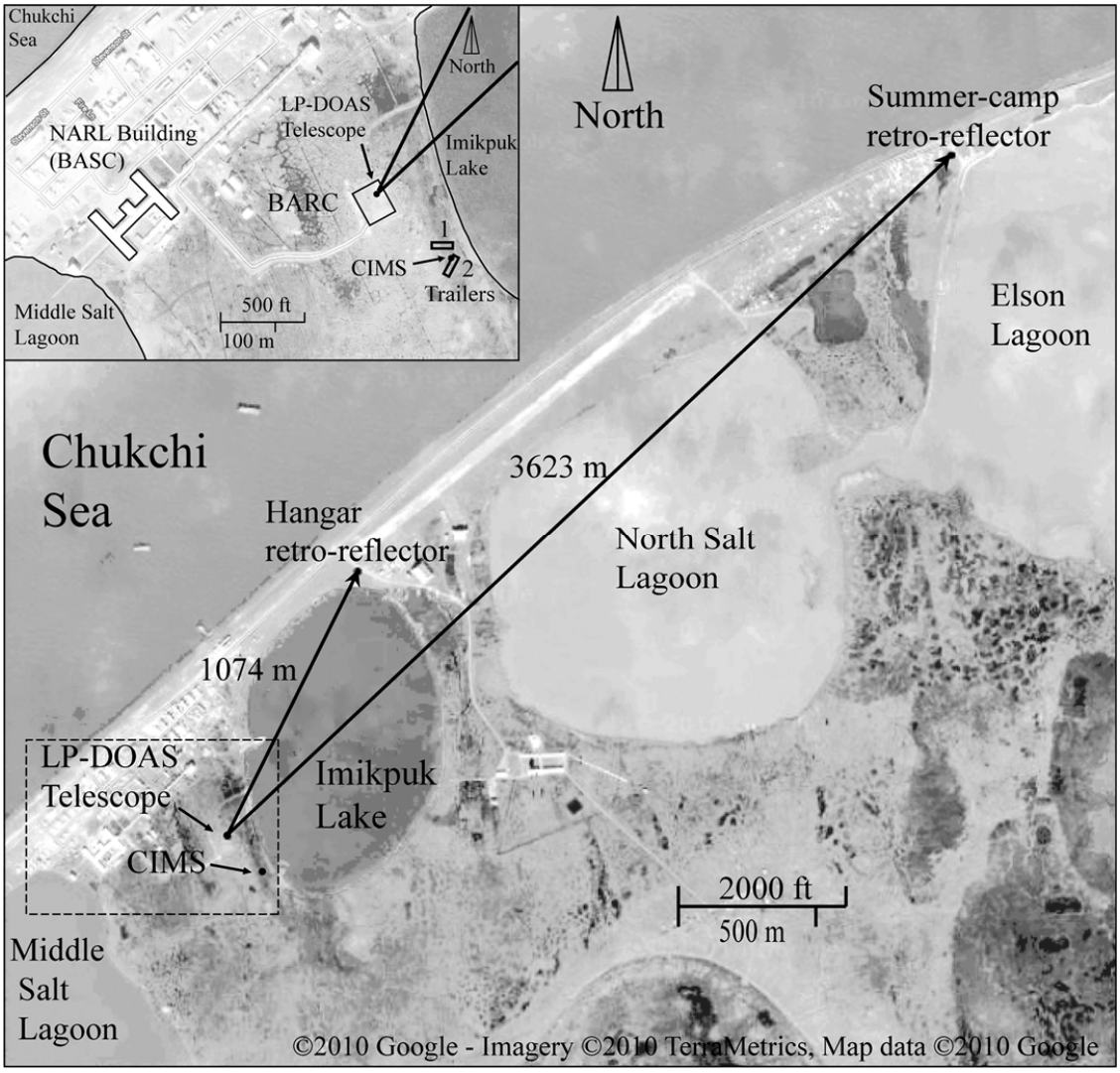


Figure 2.1 The layout of the CIMS and LP-DOAS instruments during the OASIS campaign. The CIMS instrument and LP-DOAS telescope were located ~800 m from the Chukchi Sea to the northwest and ~5 km to the northeast of Barrow. Two retro-reflectors (summer-camp and hangar) were installed at distances of 3623 and 1074 m from the telescope and provided light paths of 7246 and 2148 m, respectively (black arrows). The CIMS instrument was about 200 m to the southeast of LP-DOAS telescope. The geometries of the CIMS instrument and LP-DOAS telescope (dashed rectangle area) are displayed in the inset. The CIMS instrument was installed in the northwest corner of Trailer 2 (black dot). The NO and $O_3$ instrument was installed in Trailer 1. The telescope of the LP-DOAS instrument was located in northeast side of the BARC building (black dot).

### 2.2.2 CIMS

2.2.2.1 Instrument

The CIMS used to detect halogen species at Barrow is very similar to that used to measure PANs and other species [Slusher et al., 2004; Kim et al., 2007; Nowak et al., 2006; Huey, 2007]. The inlet configuration is essentially identical to that used previously to measure $HNO_3$ and $NH_3$ [Huey et al., 2004; Nowak et al., 2006]. The design of the inlet is similar to that used to sample highly reactive gases such as OH [Eisele et al., 1997]. Consequently, only details relevant to the BrO measurements are described. The instrument and inlet configuration are shown in Figure 2.2.

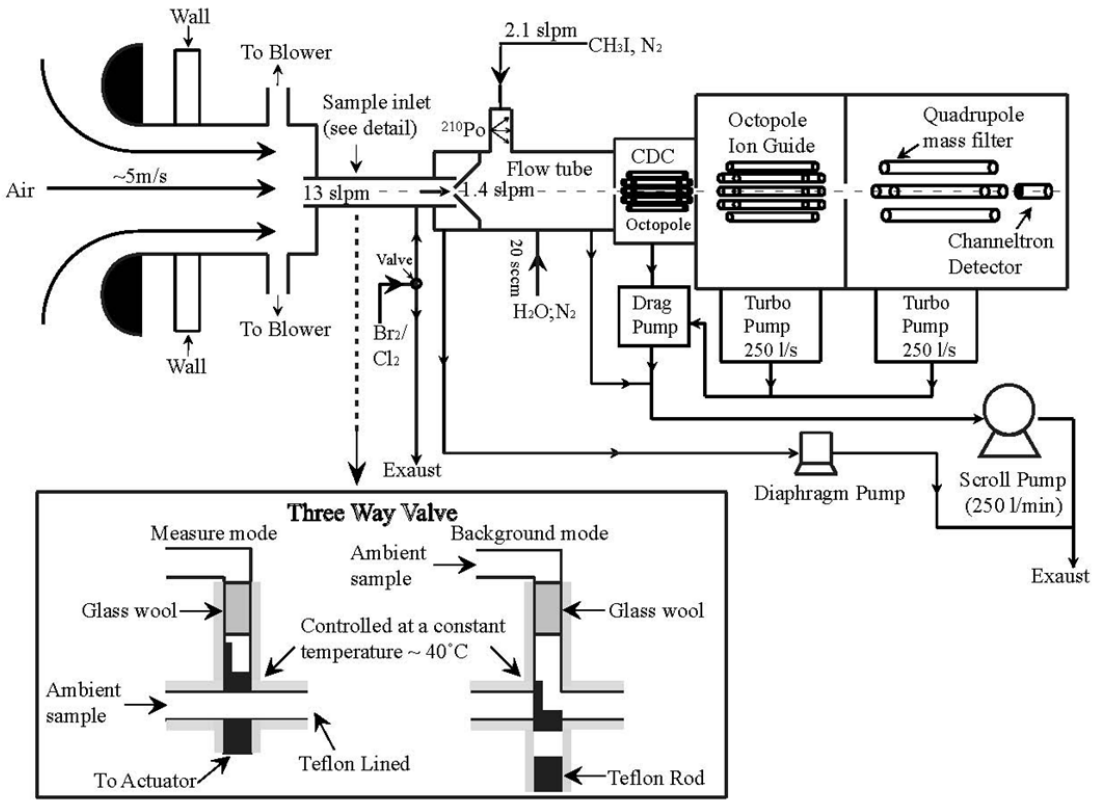


Figure 2.2 The instrument and inlet configuration of the CIMS system.

The outer portion of the inlet was a 7.6 cm ID aluminum pipe that extended about 20 cm beyond the wall of the sampling trailer. A total flow of approximately 900 standard liters per minute (slpm, standard temperature = 273 K, standard pressure = 1.01 $\times 10^5$ Pa) was maintained in the pipe with a blower (AMETEK Windjammer 116637–03). A portion of this flow (13.0 slpm) was sampled into a custom three way valve, constructed of perfluoroalkoxy (PFA) Teflon, which connected the center of the pipe to the CIMS sampling orifice. Most of this flow (11.6 slpm) was exhausted through a mass flow controller in series with a small diaphragm pump, with the rest (1.4 slpm) entering the CIMS flow reactor through a 0.51mm dia. orifice. The valve was maintained at a constant temperature of 40°C and could be automatically switched between two flow paths. The first path was equivalent to a 25 cm long, 0.65 cm ID, Teflon tube. The second configuration delivered ambient air through a glass wool scrubber to the CIMS to determine background levels. Finally, the output of either a $Br_2$ (118 ng $min^{-1}$) or $Cl_2$ (183 ng $min^{-1}$) permeation tube was periodically delivered to the upstream end of the Teflon valve to monitor the CIMS sensitivity toward halogens.

The CIMS flow reactor was operated at 20 hPa with a total flow of 3.5 slpm maintained by a scroll pump. The total flow consisted of 1.4 slpm of ambient air and 2.1 slpm of ion source flow that consisted of $N_2$ containing approximately 5 ppmv methyl iodide. The methyl iodide was delivered to the ion source by adding 10 standard cubic centimeters per minute (sccm) of a 0.1% mixture in nitrogen to the ion source flow. A flow of 20 sccm $N_2$ was passed through a room temperature bubbler (~20°C) containing deionized water and introduced directly to the flow reactor. Water vapor was added to the flow tube to increase the sensitivity to BrO and other halogens [Neuman et al., 2010].

The primary reagent ion produced by this configuration is hydrated $I^-$ which was used to detect a series of halogens using reactions R2.1–R2.5. Due to collisional dissociation of the hydrated ions in the sampling process, described below, only the detected core ions are listed in the reactions. The collisional rate constants for the ion molecule reactions R2.2a and R2.3a are estimated by standard methods assuming that on average $I^-$ is clustered with four water molecules [Su and Chesnavich,1982; Chesnavich et al.,1980; Johnson et al., 2010]. The rate constants for R2.1 and R2.4a are estimated relative to R2.2a from the sensitivity ratio of BrO and HOBr to $Br_2$. The reaction rate constant of R2.5a is estimated relative to R2.3a from the sensitivity ratio of $ClNO_2$ to $Cl_2$.

$$I^- + BrO \rightarrow IBrO^- \qquad (k_{2.1} = \sim 1.4 \times 10^{-10}\ cm^3\ molec^{-1}\ s^{-1}) \qquad \text{R2.1}$$

$$I^- + Br_2 \rightarrow IBr_2^- \qquad (k_{2.2a} = \sim 2.8 \times 10^{-10}\ cm^3\ molec^{-1}\ s^{-1}) \qquad \text{R2.2a}$$

$$\rightarrow Br^- + IBr \qquad \text{R2.2b}$$

$$I^- + Cl_2 \rightarrow ICl_2^- \qquad (k_{2.3a} = \sim 3.0 \times 10^{-10}\ cm^3\ molec^{-1}\ s^{-1}) \qquad \text{R2.3a}$$

$$\rightarrow Cl^- + ICl \qquad \text{R2.3b}$$

$$I^- + HOBr \rightarrow IHOBr^- \qquad (k_{2.4a} = \sim 1.4 \times 10^{-10}\ cm^3 molec^{-1} s^{-1}) \qquad \text{R2.4a}$$

$$\rightarrow Br^- + IOH \qquad \text{R2.4b}$$

$$\rightarrow IBr^- + OH \qquad \text{R2.4c}$$

$$I^- + ClNO_2 \rightarrow IClNO_2^- \qquad (k_{2.5a} = \sim 2.0 \times 10^{-10}\ cm^3\ molec^{-1} s^{1}) \qquad \text{R2.5a}$$

$$\rightarrow Cl^- + INO_2 \qquad \text{R2.5b}$$

A small portion (~100 sccm) of the ion reactor flow was sampled through a 0.81 mm dia. orifice into a collisional dissociation chamber (CDC) maintained at 0.67 hPa with a molecular drag pump. An electric field of approximately 4 V $cm^{-1}$ is applied in the CDC to produce energetic collisions to dissociate weakly bound water clusters. Ions at the exit of the CDC are guided by an octopole and sampled into a differentially pumped quadrupole mass spectrometer. The ions are filtered and detected with an electron multiplier detector (K+M) and counted as individual pulses. The signals are reported in Hz, which represents the number of ion counts per second. Each cluster ion resides at a unique mass, and the measurement of different bromine (and chlorine) isotopes provided a critical test of the measurement technique. A typical measurement cycle (15.5 s) monitored the masses listed in Table 2.1 for the indicated integration times. As a consequence, BrO was measured with a 6% duty cycle which gives a ~4 s integration period for the CIMS data used to derive the 1 min average used in this work. On the other hand, the LP-DOAS has a duty cycle of ~40% for BrO. The remaining time was used for background spectra and other wavelengths. The smaller duty cycle for the CIMS is partially responsible for the larger variability in the CIMS data.

Table 2.1 Summary of monitored masses, ionized products, neutral reactants and integration time for CIMS measurements during OASIS campaign.

| Mass (amu) | Ion | Neutral | Integration Time (ms) | Comments |
|---|---|---|---|---|
| 147 | $IH_2{}^{18}O^-$ | NA | 1000 | Hydrated reagent ion isotope; the signal of $IH_2{}^{16}O^-$ at 145 amu was saturated |
| 79 | $^{79}Br^-$ | Multiple | 1000 | Significant channel for $Br_2$ that is more important at lower $H_2O$ levels |
| 222 | $I^{79}BrO^-$ | BrO | 1000 | Channel enhanced at higher $H_2O$ levels |
| 224 | $I^{81}BrO^-$ | BrO | 1000 | |
| 287 | $I\ ^{79}Br^{81}Br^-$ | $Br_2$ | 1000 | |
| 289 | $I\ ^{81}Br^{81}Br^-$ | $Br_2$ | 1000 | |
| 285 | $I\ ^{79}Br^{79}Br^-$ | $Br_2$ | 1000 | |
| 197 | $I^{35}Cl^{35}Cl^-$ | $Cl_2$ | 1000 | |
| 199 | $I^{35}Cl^{37}Cl^-$ | $Cl_2$ | 1000 | |
| 223 | $IHO^{79}Br^-$ | HOBr | 1000 | |
| 225 | $IHO^{81}Br^-$ | HOBr | 1000 | |
| 208 | $I^{35}ClNO_2^-$ | $ClNO_2$ | 1000 | Species other than $ClNO_2$ also present at 208 amu; HOBr detected as $IBr^-$ at 208amu |
| 210 | $I^{37}ClNO_2^-$ | $ClNO_2$ | 1000 | Background not well determined |
| 241 | $I^{79}Br^{35}Cl^-$ | BrCl | 1000 | |
| 243 | $I^{81}Br^{35}Cl^-$ | BrCl | 1000 | |
| 62 | $NO_3^-$ | $NO_3$, $N_2O_5$, $ClNO_3$ | 500 | |

2.2.2.2 Background Determination

Instrumental background signals were measured regularly, and subtracted from the total signals to determine BrO mixing ratios. The background signal at the mass used

for BrO detection as well as other halogen species was determined periodically (approximately every 40 min) by scrubbing ambient air with glass wool. The custom made Teflon valve was used to switch between the two flow paths. Laboratory tests [Neuman et al., 2010] have shown that many inorganic halogens ($Br_2$, HOBr, BrO, $Cl_2$, and HCl) can be efficiently removed from a gas stream via contact with glass wool. The effectiveness of halogen removal by the glass wool was confirmed every few days by adding either $Cl_2$ or $Br_2$ upstream of the scrubber. However, we found that $ClNO_2$ is essentially unreactive toward glass wool and a background measurement for this species could not be provided by this method. The ion reactor pressure decreased slightly (~26.7 Pa or 1.3%) during background measurements. In order to diminish this effect, after 29 March the ion reactor was actively pressure controlled by modulating the ion source flow to maintain constant pressure. The water vapor concentration in the flow tube was not found to change significantly during these background measurements, as the signal due to $I^-(H_2O)$ was found to be essentially constant. Thus, the modulation of the ion source flow to maintain constant pressure did not alter halogen sensitivity but slightly increased the stability of the background measurement. The median absolute difference between successive background measurements was 0.89 pptv before pressure control and 0.77 pptv after pressure control. A typical example of the raw BrO signal (224 amu) with a series of background measurements is shown in Figure 2.3.

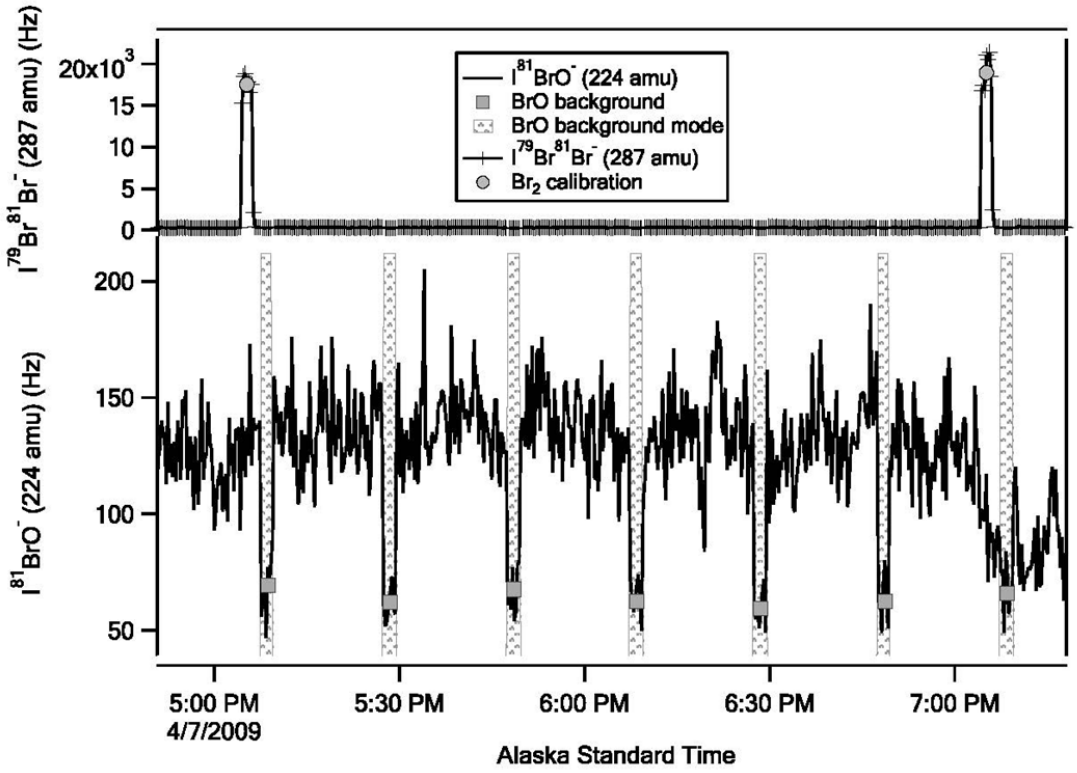


Figure 2.3 Typical raw signal of $I^{81}BrO^-$ (224 amu) (black line) and $I^{79}Br^{81}Br^-$ (287 amu) (black line with cross markers) from the OASIS campaign. (top) The gray dots show the average $I^{79}Br^{81}Br^-$ (287 amu) signal during an addition of the $Br_2$ standard. (bottom) The gray squares illustrate the average $I^{81}BrO^-$ (224 amu) signal during background measurements (shaded areas).

2.2.2.3 Calibration

Because a portable, constant calibration source for BrO has not been developed, $Br_2$ and $Cl_2$ permeation tubes (Kin-tek) were used as the primary calibration standards for the OASIS campaign. $Br_2$ and $Cl_2$ were detected by the association reactions (R2.2a and R2.3a). A known amount of $Br_2$ (1.47 ppbv) or $Cl_2$ (5.18 ppbv) was added to the inlet every 2 h to track the sensitivity of the observed halogen species including BrO. A typical example of the raw signal from a $Br_2$ calibration is shown in Figure 2.3.

The emission rates of the permeation tubes were measured every few days by conversion to $I_3^-$ in aqueous solution. This was accomplished by passing the output of the permeation tube in a 10 sccm flow of nitrogen through an aqueous solution of KI (2%w/w KI, 1mM phosphate buffer, pH = 7). $Br_2$ or $Cl_2$ quantitatively oxidizes $I_{(aq)}^-$ to form $I_{3(aq)}^-$ via the following net reactions [Wu et al., 1963; Kazantseva et al., 2002].

$$Br_2 + 3I^- \Leftrightarrow I_3^- + 2Br^- \qquad \text{R2.6}$$

$$Cl_2 + 3I^- \Leftrightarrow I_3^- + 2Cl^- \qquad \text{R2.7}$$

The resulting $I_3^-$ was quantified by optical absorption at 352 nm [Finley and Saltzman, 2008]. The quantitative conversion of $Br_2$ to $I_3^-$ was also confirmed in the laboratory by ion chromatographic measurements of $Br^-$. The average emission rate of the $Br_2$ permeation tube for the OASIS campaign was 118 ng $min^{-1}$ with a standard deviation of 5%. The average emission rate of the $Cl_2$ permeation tube for the OASIS campaign was 183 ng $min^{-1}$ with a standard deviation of 7%. The sensitivity for the detection of $Cl_2$ relative to $Br_2$ at the most abundant isotopes (mass 197 and mass 287) was determined to be 1.6 ± 0.1. The measurement of this ratio allowed the use of either permeation tube as the primary standard during OASIS. The $Br_2$ permeation tube was used as the primary standard for most of the campaign. The $Cl_2$ permeation tube was used from 28 March to 4 April 2009.

The relative rates of reactions R2.1 and R2.2a were measured before the campaign. BrO was generated from $Br_2$ by the reaction of $O(^3P)$ with $Br_2$ in excess $O_3$. $O_3$ and $Br_2$ were flowed through an oven upstream of the inlet to the CIMS. When the oven was heated to ~350°C, BrO was produced by the following series of reactions.

$$O_3 + M \rightarrow O_2 + O(^3P) + M \quad \text{R2.8}$$

$$Br_2 + O(^3P) \rightarrow BrO + Br \quad \text{R2.9}$$

$$Br + O_3 \rightarrow BrO + O_2 \quad \text{R2.10}$$

By using a large excess of $O_3$, each $Br_2$ molecule was quantitatively converted to two BrO molecules. The sensitivity of BrO relative to $Br_2$ is measured to be 0.47 ± 25% which is very similar to that determined by Neuman et al. [2010] using a microwave discharge to make Br atoms from $Br_2$ [Orlando et al., 1991]. We have found that for a given set of conditions the relative sensitivity of the CIMS to different compounds is generally stable within 10% [Kim et al., 2007]. The uncertainty in the measurement over a range of experimental conditions is estimated to be 25%. Combining this with the estimated uncertainties in the $Br_2$ and $Cl_2$ permeation rate of 5% and 7%, and an estimated uncertainty in the $Cl_2$ to $Br_2$ sensitivity ratio of 6%, the total uncertainty of the BrO measurement is estimated to be 29% using $Br_2$ as the calibration gas and 34% using $Cl_2$ as the calibration gas.

2.2.2.4. CIMS Performance

The CIMS instrument performance is assessed by examining the detection sensitivity and the background signal levels to estimate a limit of detection for BrO. The sensitivity was determined from the response to a standard addition of $Br_2$. The typical sensitivity of the CIMS for $Br_2$ (R2.2a) during OASIS was 12 Hz per pptv. This corresponds to a typical sensitivity for BrO of 6 Hz per pptv. The median background signal at the BrO mass was 69 Hz which is equivalent to ~12 pptv of BrO. Because BrO

was monitored for 4 s out of every minute by CIMS, the standard deviation of the background measurement due to counting statistics is calculated to be 0.70 pptv for a 1 min integration period. The absolute difference between successive 1 min average background measurements was essentially normally distributed with a median of 0.86 pptv for the whole data set and with a median of 0.78 pptv after pressure control was instituted. This indicates that variance of the background due to factors other than counting statistics such as electrical noise, flow turbulence, etc., is small and that the CIMS detection limit will improve with averaging. We estimate the 3s limit of detection as 2.6 pptv for a 4 s integration period which is calculated by multiplying the variance of individual determinations of the background signal by a factor of three. As most of the background variance is due to counting statistics, the detection limit may decrease to 1 pptv for a 1 min integration period when the BrO measurement time is increased to 60% of the duty cycle.

The natural isotopic abundances of $^{79}Br$ and $^{81}Br$ are 50.69% and 49.31%, respectively. The total raw signal in ambient mode at $I^{79}BrO^-$ (222 amu) is plotted against the signal at $I^{81}BrO^-$ (224 amu) from 18 March to 14 April 2009 in Figure 2.4. The correlation is excellent, $R^2 = 0.85$, but if only random error due to counting statistics was present, the correlation would be higher for this data set (maximum $R^2 = 0.96$). This indicates that 10% of the observed variation is due to other sources such as a small interference in mass 222 (see below). An equally weighted, bivariate regression analysis gives a slope of 1.11 and an intercept of −0.84 Hz (−0.14 pptv). These results strongly indicate that a species containing one bromine atom is detected at these masses and there are no large interferences present. Observations during the campaign indicate that mass

222 did have a small interference during pollution events and for that reason mass 224 was used to derive BrO levels.

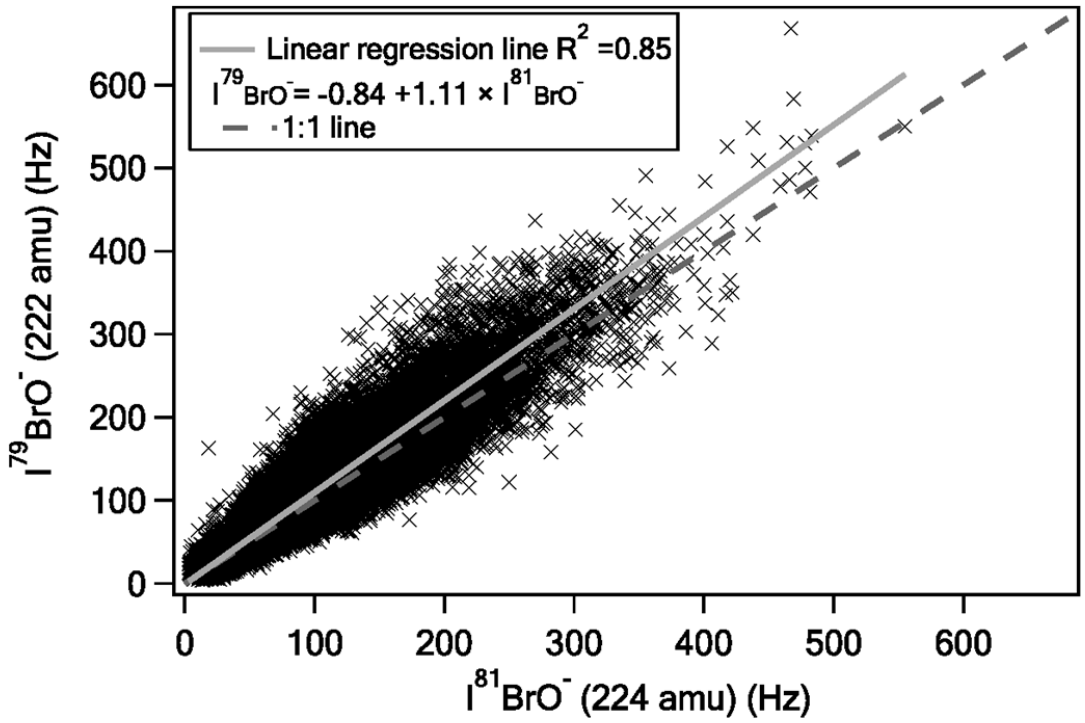


Figure 2.4 The raw ambient signal at $I^{79}BrO^-$ (222 amu) versus $I^{81}BrO^-$ (224 amu). The correlation coefficient is 0.85 ($R^2$) with a slope of 1.11 and an intercept of −0.84 Hz or −0.14 pptv.

### 2.2.3 LP-DOAS

2.2.3.1 Instrument

Long path-differential optical absorption spectroscopy quantifies the average concentration of trace gases along a well-defined light path using their individual absorption cross sections [e.g., Platt and Stutz, 2008]. The LP-DOAS instrument used in this study was previously deployed aboard the Amundsen RV in Spring 2008 and

described by Pöhler et al. [2010]. See section 2.2.1 and Figure 2.1 for details about the setup of the light paths at Barrow.

The active part of the LP-DOAS instrument consisted of the following components: Radiation from a broadband light source (Xenon arc lamp, usually Osram XBO 75, Osram XBO500 between 19 and 30 March) was coupled into a single 600 mm mode-mixing quartz fiber using a fused silica lens. The exit end of the single fiber was connected to six transmitting 200 mm fibers at one arm of a Y bundle (total length 10 m). At the bottom of the Y, which was placed close to the focal point of a telescope mirror (30 cm diameter, 1.5 m focal length), these six fibers surrounded a single 200 mm receiving fiber. The pointing of the telescope could be adjusted by stepper motors. The receiving fiber, the other arm of the Y, led to an Acton 300i spectrometer equipped with a CCD camera. For stray-light reduction, a BG24A filter or a UG5 filter (both manufactured by Schott, 2 mm thickness) was placed behind the entrance slit of the spectrometer.

The light path through the atmosphere could be blocked using an aluminum diffuser plate placed at about 1 mm distance in front of the single end of the Y bundle. This “shortcut” configuration was applied after each measurement and was used to record the light source reference spectrum $I_0$. In addition, a “background spectrum” for each spectrum was obtained with the artificial light source blocked. This was necessary to eliminate a possible signal offset due to scattered sunlight entering the telescope. The offset, as well as the dark-current signal of the CCD electronics, was also accounted for in the evaluation procedure.

2.2.3.2. Measurement Regime

Varying spectral structures originated from fluctuations of the light source and of ambient illumination (scattered sunlight), which was an issue during the day due to high surface albedo close to the retro-reflector arrays. In order to minimize these effects, atmospheric absorption (I) spectra and reference ($I^0$) spectra, as well as their respective background signal, were recorded in quick succession. The light path had to be manually adjusted depending on meteorological conditions. During periods of poor visibility due to fog, clouds, mirages, or blowing snow, the short light path was chosen instead of the long light path.

2.2.3.3. Evaluation and Error Analysis

In order to obtain the concentrations of BrO by LP-DOAS at a similar time resolution as for CIMS, individual measurements (integration time 1 to 50 s depending on signal strength) were used for the spectral analysis. The dispersion of the spectrometer was calibrated using the position of mercury emission lines.

The spectral analysis was performed in the wavelength interval between 315.5 nm and 348.0 nm and included the cross sections of the trace gases listed in Table 2.2. Usually, the trace gas column densities are determined by fitting a linear combination of the narrow-band trace gas absorption structures to the measured optical density spectra $t = -\ln(I/I_0)$ using a nonlinear Levenberg-Marquardt algorithm [Kraus, 2004]. In this study, however, the standard evaluation scheme needed to be altered in order to overcome a still relatively large residual background signal. The disadvantageous influence of the high intensity of scattered sunlight on the background signal was amplified by a malfunction of the camera software, which slightly altered the exposure time between measurements

depending on the illumination of the CCD. Thus, in addition to a set of trace-gas absorption spectra and the initial intensity $\ln(I_0)$, three further correction spectra were used to fit the measurement spectrum ln(I). The additional correction spectra consisted of the logarithm of the actual atmospheric background spectrum ln(BG) as well as the squared spectra $\ln(BG^2)$ and $\ln(I_0^2)$, which represent the second term of the Taylor expansion of the exponential Beer-Lambert Law. This approach improves the modeling of nonlinear artifacts within the otherwise linear DOAS algorithm and was first published by Puķīte et al. [2009]. The calculated optical density as well as the absorption cross sections adapted from the literature were filtered using a binomial high-pass filter with 1000 iterations prior to the analysis. A third-order polynomial accounted for residual broadband structures. Finally, the amplitude of the residual spectrum was used as a quality criterion in order to filter unsuccessful fit results due to poor signal quality.

The spectral analysis yields the column density of each fitted absorber. The path-averaged concentration of a particular trace gas is then calculated by dividing its column density by the optical path length. To account for remaining systematic structures in the residual, the measurement error (s) of the Levenberg-Marquardt analysis error is multiplied by a factor of 1.8 according to Stutz and Platt [1996]. In accordance to the evaluation of the CIMS, the detection limit is estimated to $3\sigma$. This leads to an optimum nighttime detection limit of $2 \times 10^7$ molecules $cm^{-3}$ (0.7 pptv) for the long light path and $6 \times 10^7$ molecules $cm^{-3}$ (2 pptv) for the short light path. During the day, however, due to larger interferences with sunlight scattered into the light path, the detection limits were usually higher depending on the viewing conditions and light source used. Mean daytime

detection limits are estimated to be $5 \times 10^7$ molecules $cm^{-3}$ (2 pptv) and $1.5 \times 10^8$ molecules $cm^{-3}$ (5 pptv) for long and short light paths, respectively.

Table 2.2 Literature cross-sections included in the presented spectral evaluation.

| Species | Reference | Temperature |
|---|---|---|
| $O_3$ | [*Burrows et al.*,1999] | 241K |
| BrO | [*Wilmouth et al.*, 1999] | 228K |
| $O_4$ | [*Greenblatt et al.*, 1990] | |
| HONO | [*Stutz et al.*, 2000] | 298K |
| $NO_2$ | [*Burrows et al.*, 1998] | 241K |
| HCHO | [*Meller and Moortgat*, 2000] | 298K |
| OClO | [*Bogumil et al.*, 2003] | 293K |
| $SO_2$ | [*Bogumil et al.*, 2003] | 243K |

2.2.3.4. Systematic Errors

It is important to consider systematic errors, in particular when comparing two different instruments measuring the same parameter. While the DOAS retrieval is a selfcalibrating procedure, the largest contributions to systematic error come from the absolute calibration of cross sections reported in the literature. During the measurements of laboratory cross sections it is crucial to determine the exact concentration of the target trace gas [Wilmouth et al., 1999; Fleischmann et al., 2004]. The differential cross sections of BrO differ significantly within the literature. Therefore a systematic error of 10% for the retrieved BrO concentration is a realistic assumption [Dorf, 2005].

## 2.3 Results and Discussion

The CIMS and the LP-DOAS instruments were operated independently to detect BrO from early March to mid-April during the OASIS campaign. BrO measurements

from both instruments and $O_3$ observations from a chemiluminescence instrument from the National Center for Atmospheric Research (NCAR) are shown in the time series plot in Figure 2.5. All data are averaged to a 1 min time basis from 18 March to 14 April 2009. The gaps in the CIMS data are either due to power outages or instrument malfunction. Due to the low BrO duty cycle for the CIMS, the background variance mostly due to counting statistics is 2.6 pptv for the 1 min data average. This largely statistical variance can explain many of the cases when the BrO observed by CIMS is more variable than the LP-DOAS. Both instruments show clear diurnal profiles of BrO with maxima in the daytime and no evidence for significant nighttime levels. The highest BrO concentrations measured by the CIMS and the LP-DOAS are 41 and 42 pptv, respectively. These levels are comparable to the maximum BrO detected in the Amundsen Gulf (41 pptv) by Pöhler et al. [2010]; in Ny-Ålesund, Spitsbergen (~30 pptv) by Tuckermann et al. [1997]; in Alert, Canada (~ 30 pptv) by Hönninger and Platt [2002] and in Halley station, Antarctica (~20 pptv) by Saiz-Lopez et al. [2007].

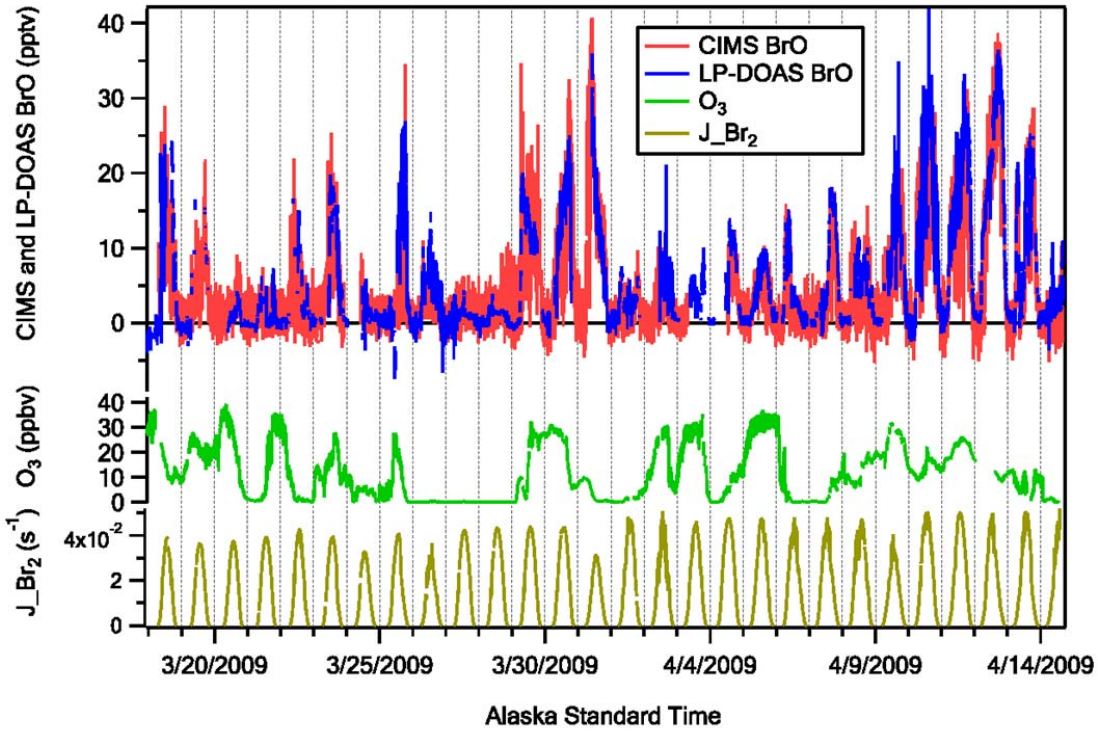


Figure 2.5 Time series of CIMS (red) and LP-DOAS (blue) BrO observations, $O_3$ measurements (green), and j values of $Br_2$ (gold) from 18 March to 14 April 2009.

Similar diurnal BrO profiles were also detected by LP-DOAS in coastal Antarctica [Saiz-Lopez et al., 2007], at the Dead Sea [Hebestreit et al., 1999] and in the Amundsen Gulf [Pöhler et al., 2010]. The OASIS data are consistent with BrO behaving as a short-lived photochemically produced species. It is interesting to note that some model studies have predicted comparable diurnal profiles of BrO with maxima of ~30 pptv by assuming an initial bromide concentration of ~50 pptv [Fan and Jacob, 1992; Evans et al., 2003]. These studies predict the highest BrO concentrations near sunrise and sunset with a local minimum at near noon. This behavior is apparent in the diurnal profiles observed by Pöhler et al. [2010] in the Amundsen straits. However, the

BrO measurements at Barrow did not show the same diurnal pattern. Consequently, this data set will provide an interesting opportunity to further test models of halogen chemistry.

BrO levels do not have a simple relationship with $O_3$. Midday (0900 LST to 1800 LST) BrO concentrations are listed in Table 2.3 as a function of $O_3$. The lowest average BrO mixing ratios were observed at low $O_3$ which is consistent with decreasing the formation rate of BrO via reaction R2.10. The highest BrO levels were observed between 5 and 30 ppbv of $O_3$ and were associated with the "edges" of ozone depletion events (e.g., 25, 30, and 31 March 2009) or regions of partial ozone depletion (10−13 April 2009). Lower BrO concentrations at high $O_3$ levels (>30 ppbv) were also observed, consistent with little halogen chemistry having impacted the air mass. Mixing can also influence the relationship between BrO and $O_3$: during midday there is some increased turbulent mixing that may increase $O_3$ by mixing down from aloft, and dilution of the surface-mediated bromine chemistry that may result in lower BrO concentrations.

Table 2.3 Daytime (9 am – 6 pm) BrO concentrations observed by CIMS as a function of $O_3$.

| $O_3$ (ppbv) | $BrO_{mean}$ (pptv) | $BrO_{median}$ (pptv) | $BrO_{std}$ (pptv) | Data points |
|---|---|---|---|---|
| 0 – 5 | 4.3 | 2.3 | 6.3 | 3128 |
| 5 – 10 | 7.4 | 4.2 | 8.1 | 956 |
| 10 – 15 | 13.6 | 13.1 | 9.4 | 871 |
| 15 – 20 | 9.7 | 8.5 | 6.9 | 1035 |
| 20 – 25 | 9.5 | 9.3 | 6.4 | 1163 |
| 25 – 30 | 8.4 | 8.4 | 5.4 | 1262 |
| 30 – 35 | 4.3 | 3.1 | 4.0 | 361 |
| 35 – 40 | 4.9 | 5.2 | 2.3 | 106 |

The unfiltered BrO data from the CIMS and LPDOAS are well correlated ($R^2$ = 0.74) (Figure 2.6, top). A weighted, bivariate regression analysis was performed on the data, where the weighting of CIMS and DOAS data was based on the estimated errors described above. The regression analysis yielded a slope of 1.10 and an intercept of −0.15 pptv with a linear correlation coefficient ($R^2$) of 0.74. The median ratio of LP-DOAS data to CIMS data (when [BrO] > 10 pptv) is 1.09 with a standard deviation of 0.34. BrO measured by the LP-DOAS was larger than CIMS observations by approximately 10% with no significant offset. With over 15000 data points and dissimilar spatial scales and duty cycles, such a strong correlation indicates that the atmosphere is reasonably homogeneous over the spatial scale of the experiment (~4 km) and constant on the measurement time scales (1 min) and that both instruments accurately determine BrO mixing ratios.

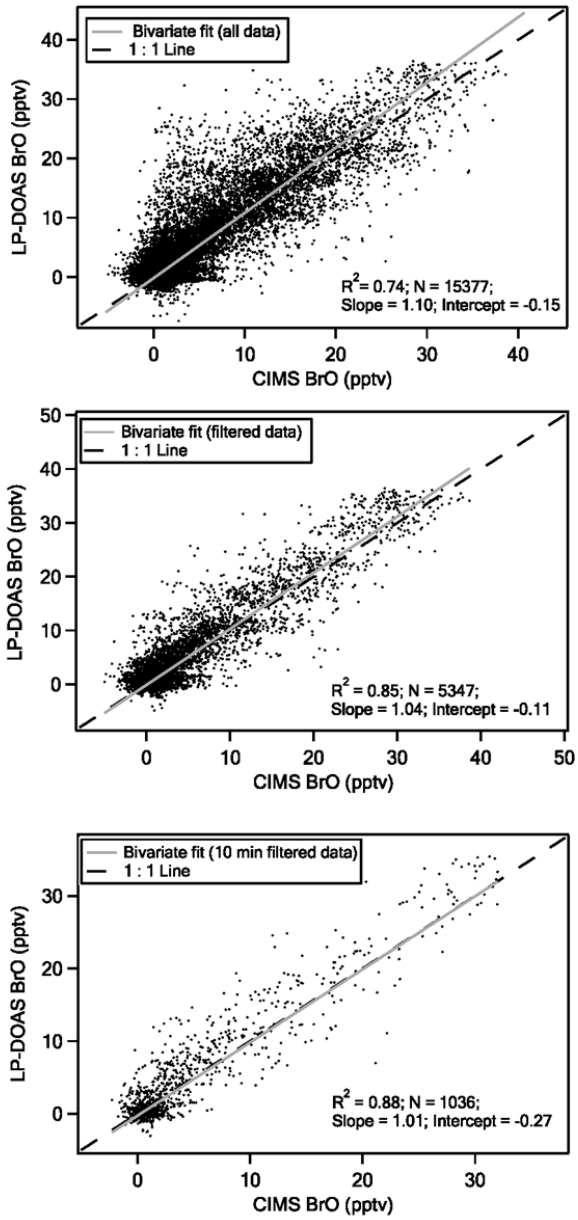


Figure 2.6 The 1 min LP-DOAS observations plotted against CIMS observations with (top) all data and (middle) filtered data. (bottom) The 10 min LP-DOAS observations plotted against CIMS observations with filtered data. The filtered data exclude points when NO is larger than 100 pptv and wind speeds are less than 3 m $s^{-1}$ or more than 8 m $s^{-1}$. The correlation coefficients ($R^2$) for the 1 min unfiltered and filtered data are 0.74 and 0.85, respectively. A bivariate fit of all 1 min data gives a slope of 1.10 and an intercept of −0.15 pptv. A bivariate fit of 1 min filtered data gives a slope of 1.04 and an intercept of −0.11 pptv. The correlation coefficient ($R^2$) for the 10 min filtered data is 0.88. A bivariate regression analysis of the 10 min data yields a slope of 1.01 and an intercept of −0.27 pptv.

The correlation of the BrO measurements is even better, $R^2 = 0.85$ (number of points N = 5347) (Figure 2.6, middle), if the data are filtered to exclude points when NO is larger than 100 pptv and wind speeds are less than 3 m $s^{-1}$ or more than 8 m $s^{-1}$. Note that, due to the lack of NO data after 12 April 2009, the BrO data are not filtered to exclude points at high NO mixing ratio after 12 April 2009. We did not find a clear relationship between the CIMS and LPDOAS agreement and other variables such as solar radiation or humidity. Using a bivariate regression analysis as above, the slope of the correlation is 1.04 with an intercept of −0.11 pptv. The median ratio of the LP-DOAS to the CIMS data (when [BrO] > 10 pptv) is 1.08 with a standard deviation of 0.29. This analysis probably provides the best comparison of the instruments and indicates that both instruments are measuring BrO within their stated uncertainties.

The correlation of BrO measurements is further improved ($R^2 = 0.88$) when the measurements are averaged to a 10 min time base and filtered to exclude points when NO is larger than 100 pptv and wind speeds are less than 3 m $s^{-1}$ or more than 8 m $s^{-1}$ (Figure 2.6, bottom). This is consistent with some of the variability in the CIMS data being due to counting statistics. The same bivariate regression analysis is applied weighted by the estimated errors. The slope of the correlation is 1.01 with an intercept of −0.27 pptv. The median ratio of the LP-DOAS to the CIMS data (when [BrO] > 10 pptv) is 1.08 with a standard deviation of 0.27 for the 10 min data.

To illustrate the difference between the two measurements as a function of mixing ratio, the normalized difference (ND) of the CIMS and LP-DOAS data is plotted versus

the CIMS observations in Figure 2.7 (filtered 1 min data). The normalized difference is defined by the following equation.

$ND = ([BrO]_{CIMS} - [BrO]_{LP\text{-}DOAS})/([BrO]_{CIMS} \times [BrO]_{LP\text{-}DOAS})^{0.5}$.

The average ND for each interval and the standard deviation are shown as black dots and bars, respectively. There is no evident bias above 5 pptv of BrO. Below this level the plot becomes scattered as expected given the detection limits of both instruments.

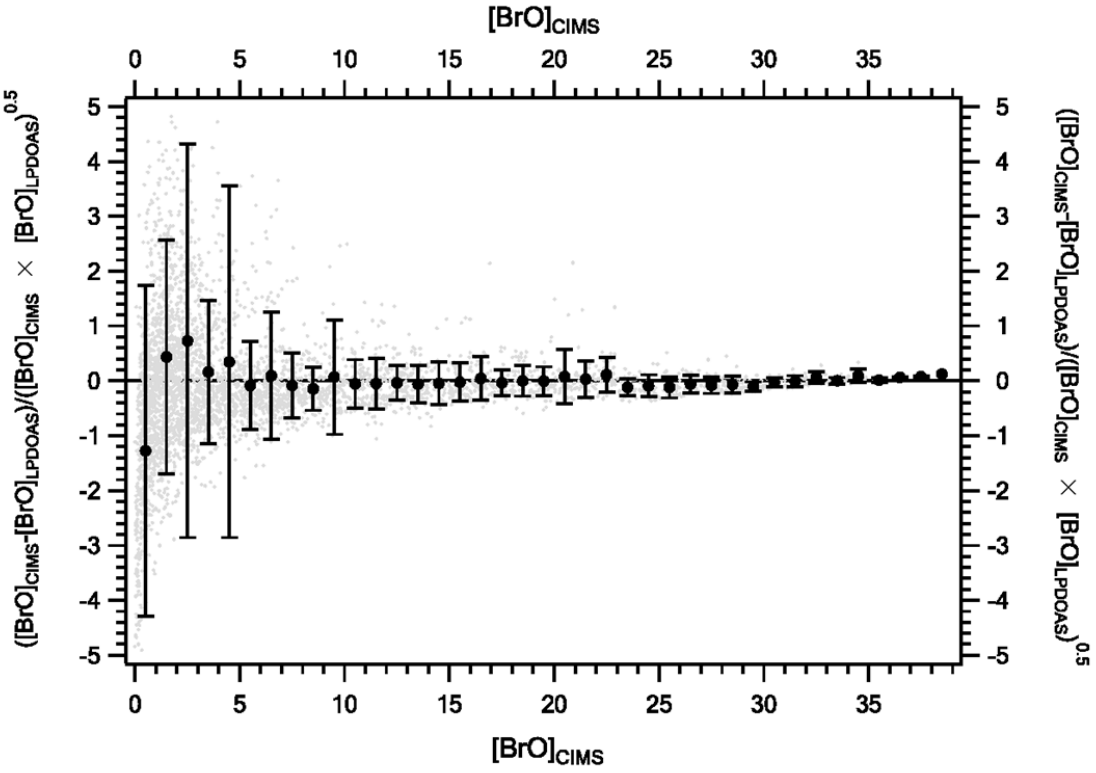


Figure 2.7 The normalized difference (ND) of CIMS and LP-DOAS measurements versus CIMS measurements(filtered 1 min data). ND is defined as: $ND = ([BrO]_{CIMS} - [BrO]_{LP\text{-}DOAS})/([BrO]_{CIMS} \times [BrO]_{LP\text{-}DOAS})^{0.5}$. Individual ND values are shown as gray dots. The average ND for each interval and the standard deviation are shown as black dots and error bars. The horizontal axis has units of pptv.

The decreased correlation between the CIMS and LP-DOAS data at high NO levels likely results from an inhomogeneous spatial distribution of BrO, caused at least in part by the spatial inhomogeneity of NO. Local variations of BrO due to high NO (such as due to generator plumes, etc.) can affect the *in situ* CIMS measurement more than the LP-DOAS which averages over a few kilometers. This effect is illustrated in Figure 2.8 (top), where the CIMS observations are much more variable than the LP-DOAS.

The rapid decreases in the CIMS observations correspond to elevated NO which impacts BrO levels through the reaction of BrO and NO. In addition, other species such as $NO_2$ that are likely to be present with the NO can also impact BrO. For example at 1006 LST in Figure 2.8, the NO level is approximately 430 pptv which corresponds to a lifetime of BrO due to reaction with NO of 3 s. The typical lifetime of BrO in this environment under clean conditions is of the order of a minute in the daytime, primarily due to photolysis. Conversely, the LP-DOAS BrO observations were much less variable during the same time period (Figure 2.8). Most of the high-NO episodes occurred when the wind speed was lower than 2 m $s^{-1}$ from the west. This suggests that the high NO might be from local sources such as power generators. These results indicate that the local pollution plumes could impact BrO levels on spatial scales smaller than the DOAS path length.

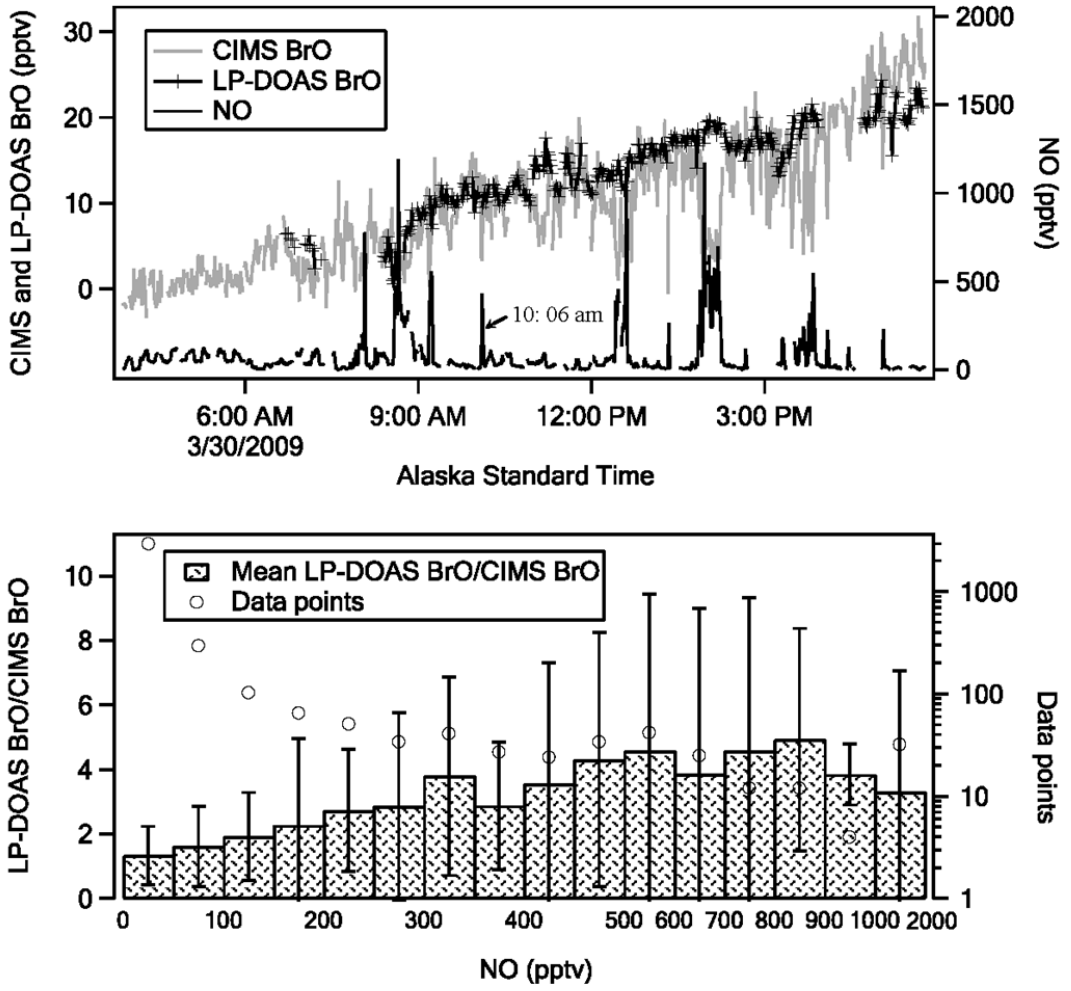


Figure 2.8 (top) An example of a time period with CIMS observations (gray line) and elevated NO levels (black line). The LP-DOAS observations are less variable (black line with cross markers). (bottom) The $[BrO]_{LP\text{-}DOAS}/[BrO]_{CIMS}$ values are binned according to NO level. The average $[BrO]_{LP\text{-}DOAS}/[BrO]_{CIMS}$ ratio in each bin is shown as the height of the shaded boxes. The standard deviation is shown as the error bar and the number of points in each bin is plotted on the right-hand axis as an open circle.

The effect of high NO on BrO ratios observed by the CIMS and LP-DOAS is further illustrated in Figure 2.8 (bottom). The LP-DOAS to CIMS ratios (when [BrO] > 1 pptv) are binned according to NO mixing ratios. The average value of $[BrO]_{LP\text{-}}$

$_{DOAS}$/[BrO]$_{CIMS}$ in each bin is shown as the height of the shaded boxes. The average [BrO]$_{LP\text{-}DOAS}$/[BrO]$_{CIMS}$ ratios increase from 1.3 to almost 5 as NO mixing ratios increase from <100 pptv to 2 ppbv. This is consistent with localized pollution plumes decreasing the BrO levels observed by the CIMS. However, most (85%) of the BrO data were observed when NO < 100 pptv, with a median LP-DOAS to CIMS ratio of 1.12.

Low wind speeds (<3 m $s^{-1}$) and high wind speeds (>8 m $s^{-1}$) also contributed to the discrepancy between the CIMS and LP-DOAS measurements. These results are consistent with low wind speeds decreasing the homogeneity of the vertical and horizontal spatial distribution of BrO and high wind speeds inducing blowing snow and lower visibility. Moreover, potential bromine heterogeneous reactions on blowing snow surface may also impact the spatial distribution of BrO [Sjostedt et al., 2007; Jones et al., 2009].

## 2.4 Conclusion

The observations of BrO by CIMS and LP-DOAS during the OASIS campaign were highly correlated and agreed within their uncertainties ($R^2$ = 0.74, N > 15,000, slope = 1.10, intercept = −0.15 pptv). The agreement between CIMS and LP-DOAS measurements is best ($R^2$ = 0.85, N = 5347, slope = 1.04 and intercept = −0.11 pptv) at low NO concentrations and moderate wind speeds (>3 m $s^{-1}$ and <8 m $s^{-1}$). These conditions favor a more homogeneous spatial distribution of BrO which allows the best comparison between the *in situ* CIMS and the spatially averaged LP-DOAS. The excellent agreement between the CIMS and LP-DOAS measurements demonstrates the capability of both instruments to accurately measure BrO and is extremely important to

link future findings by CIMS to previous observations of bromine species using the DOAS technique. The comparison of BrO measured by *in situ* and long-path instruments indicates that BrO is often distributed homogeneously on spatial scales of up to at least ~4 km, although local NOx emissions can cause large variability in BrO over small spatial scales. We believe that concerted applications of long-path observations and *in situ* methods such as CIMS will provide a more complete picture of halogen chemistry.

# CHAPTER 3

# OBSERVED AND MODELED INORGANIC BROMINE (HOBR, BRO, AND BR2) SPECIATION AT BARROW, AK IN SPRING 2009

## 3.1 Introduction

Surface ozone depletion events (ODEs), where ozone drops from 30-40 ppbv to below 10 ppbv, have been frequently observed in spring in polar regions [e.g. Oltmans, 1981; Bottenheim et al., 2009; Jones et al., 2010]. The importance of bromine chemistry in catalyzing ozone depletion has been established by field observations of filterable bromide and bromine oxide (BrO) during ODEs [e.g. Barrie et al., 1988; Hausmann and Platt, 1994].

BrO is a key species that impacts ozone loss rates during ODEs. Ozone is destroyed by the rapid recycling between Br atoms reacting with $O_3$ (R3.1) and the reaction of BrO and $HO_2$ (R3.2) or self-reaction of BrO (R3.3a and R3.3b). These reactions effectively convert $O_3$ to $O_2$.

$$Br + O_3 \rightarrow BrO + O_2 \qquad \text{R3.1}$$

$$BrO + HO_2 \rightarrow HOBr + O_2 \qquad \text{R3.2}$$

$$BrO + BrO \rightarrow 2Br + O_2 \qquad \text{R3.3a}$$

$$\rightarrow Br_2 + O_2 \qquad \text{R3.3b}$$

$$BrO + h\nu \rightarrow Br + O \qquad \text{R3.4}$$

$$BrO + NO \rightarrow Br + NO_2 \qquad \text{R3.5}$$

BrO has been detected in numerous ground based campaigns at levels of up to 30–40 pptv [e.g, Tuckermann et al., 1997; Pöhler et al., 2010] in the Arctic marine boundary layer (MBL) and up to 20 pptv in the Antarctic MBL [e.g. Saiz-Lopez et al., 2007], primarily by differential optical absorption spectroscopy (DOAS). Airborne observations of up to ~7 pptv [Liao et al., 2011b; Neuman et al., 2010] in the Arctic MBL by chemical ionization mass spectrometry (CIMS) have been reported. In chapter 3, a comparison of CIMS and long path DOAS (LP DOAS) demonstrated that both instruments could sensitively and accurately measure BrO [Liao et al., 2011a]. Diurnal patterns of BrO with maxima in the daytime have been observed [e.g. Liao et al., 2011a; Saiz-Lopez et al., 2007], which confirmed that BrO is a photochemically generated species with a short lifetime [e.g. Evans et al., 2003; Fan and Jacob, 1992]. BrO is the dominant bromine radical when $O_3$ is not severely depleted ($O_3$ > 1 ppbv), and observations of this species are crucial for understanding the chemical processing that leads to ODEs [e.g. Yang et al., 2010].

Br and BrO are rapidly converted into the non-radical bromine reservoirs hypobromous acid (HOBr), bromine nitrate ($BrONO_2$) and hydrogen bromide (HBr) via reactions R3.2, R3.8, R3.11 and R3.12. HOBr is a short lived reservoir (photolysis lifetime ~10 minutes) of active bromine (R3.2), as it can both photolyze to reform Br atoms (R3.6) and react on surfaces with $Br^-$ to generate reactive gas phase bromine (e.g. $Br_2$) (R3.7) [Fan and Jacob, 1992]. $BrONO_2$ is also a short lived active bromine reservoir as it photolyzes to form active bromine (photolysis lifetime = ~20 minutes) and undergoes heterogeneous reactions that eventually form molecular bromine ($Br_2$) (R3.10 and R3.7) [Fan and Jacob, 1992]. HBr is mainly lost by uptake on surfaces and can react

with HOBr in the condensed phase to generate $Br_2$ (R3.7). Small amounts of HBr can be converted back to Br atoms via R3.13.

$$HOBr + h\nu \rightarrow Br + OH \qquad R3.6$$

$$HOBr + Br^- + H^+ \rightarrow Br_2 + H_2O \qquad R3.7$$

$$BrO + NO_2 \rightarrow BrONO_2 \qquad R3.8$$

$$BrONO_2 + h\nu \rightarrow BrO + NO_2 \qquad R3.9a$$

$$\rightarrow Br + NO_3 \qquad R3.9b$$

$$BrONO_2 + H_2O\ (s/aq) \rightarrow HOBr\ (aq) + HNO_3 \qquad R3.10$$

$$Br + HO_2 \rightarrow HBr + O_2 \qquad R3.11$$

$$Br + CH_2O \rightarrow HBr + HCO \qquad R3.12$$

$$HBr + OH \rightarrow H_2O + Br \qquad R3.13$$

The recycling efficiencies of non-radical bromine to radical bromine through heterogeneous reactions largely determine the active bromine concentrations and ozone depletion intensity. However, the efficiencies of the heterogeneous processes are not well known. Observations of the concentrations and diurnal behaviors of HOBr, $BrONO_2$ and HBr allow the examination of current bromine mechanisms. Impey et al. [1999] reported HOBr up to ~260 pptv inferred from the measurements of total photolyzable bromine ($Br_2$ and HOBr) in the springtime Arctic boundary layer. However, to our knowledge there are no *in situ* measurements of HOBr, $BrONO_2$, or HBr.

$Br_2$ is photolyzed rapidly by sun light to form Br atoms (R3.14) (lifetime = ~30 seconds) which can initiate the bromine catalyzed ozone depletion cycles. $Br_2$ is likely a precursor of bromine radicals at sunrise and a reservoir of reactive gas phase bromine at night [e.g. Fan and Jacob, 1992].

$$Br_2 + h\nu \rightarrow 2Br \qquad \text{R3.14}$$

Accurately measuring $Br_2$ is challenging because HOBr easily converts to $Br_2$ on inlet surfaces [Neuman et al., 2010]. $Br_2$ concentrations of up to 27 pptv in the daytime and up to 15 pptv at night were measured in the Arctic boundary layer by Foster et al. [2001]. $Br_2$ levels of up to 4 pptv in the daytime and up to 9 pptv at night were observed in Pacific MBL by Finley and Saltzman [2008]. The sum of $Br_2$ and HOBr was measured as high as 20 pptv in the daytime by Neuman et al. [2010] onboard the NOAA P-3 over the Arctic Ocean in spring 2008. However, all these measurements of high levels of $Br_2$ in the daytime are likely susceptible to interference from conversion of HOBr on inlet surfaces [Neuman et al., 2010]. Efficient conversion of HOBr to $Br_2$ on the walls of sampling inlets demands a sampling system with limited wall interaction and the consideration of the potential role of HOBr as an interference to achieve accurate measurement of $Br_2$.

An intensive field study took place at Barrow, Alaska in spring 2009 during the Ocean – Atmosphere – Sea Ice – Snowpack (OASIS) campaign (http://www.oasishome.net/barrow2009.php) to investigate air-surface interactions in the Arctic and their evolution in future climates. This provided a unique opportunity to further study halogen chemistry in the Arctic. In this chapter, the first simultaneous measurements of BrO, HOBr and $Br_2$ are reported. Molecular chlorine ($Cl_2$) and bromine monochloride (BrCl) were also observed during the same campaign and are reported in Liao et al. [2011e]. HOBr observations are compared to a photochemical model and the diurnal speciation of inorganic bromine species is investigated by comparison with a time dependent box model.

## 3.2 Methods

### 3.2.1 Measurement overview

BrO, HOBr, and $Br_2$ were measured by a CIMS in March and April 2009 at Barrow, AK. Measurements of other trace gases (NO, $NO_2$, $NO_y$, $O_3$, CO and $CH_2O$) and actinic flux were also obtained at the same site. The measurement of aerosol size distributions was carried out at a site ~700 m northwest. The observations of wind speed and wind direction were made 28 m south-east of the chemical measurements. The layout of the instruments is provided in chapter 2 and Liao et al. [2011a]. The measurements used in this study are summarized in Table 3.1.

Table 3.1 Summary of the measurements used in this study.

| Species and parameters | Instrument | Uncertainty | Reference |
|---|---|---|---|
| BrO | CIMS | ±34% | *Liao et al.* [2011a] |
| HOBr | CIMS | +44%/-30% | this paper |
| $Br_2$ | CIMS | +7%/-26% | this paper |
| $HO_2$ | CIMS | ±30% | *Edwards et al.* [2003] |
| $O_3$ | chemiluminescence | ±5% | *Weinheimer et al.* |
| $NO/NO_2/NO_y$ | chemiluminescence | ±10-15% | *Weinheimer et al.* |
| CO | CO instrument | ±5% | |
| $CH_2O$ | Tunable Diode Laser Spectroscopy | ±15% | *Fried et al.* [2003] |
| Aerosol Number den. | Scanning Mobility Particle Sizer | ±10% | *Woo et al.* [2001] |
| Aerosol total Surface areas | Scanning Mobility Particle Sizer | ±15% | *Woo et al.* [2001] |
| j values | CAFS | ~±12% | *Shetter and Muller*[1999] |
| Wind speeds | Sonic | ±6% | |

The measurement frequency is higher than every 10 minutes for all the species and parameters listed in table3.1.

### 3.2.2 CIMS measurements

The details of the CIMS instrument and inlet configuration to measure halogen species are described in detail by Liao et al. [2011a]. The sampling inlet was equivalent to a 25 cm long, 0.65 cm ID, Teflon tube. The short Teflon inlet minimized (but did not completely eliminate) the conversion of HOBr to $Br_2$ on the walls of tubing. Hydrated $I^-$ was used to selectively ionize the halogen species including BrO, HOBr, and $Br_2$.

$$BrO + I^- \rightarrow IBrO^- \qquad \text{R3.15}$$

$$HOBr + I^- \rightarrow IHOBr^- \qquad \text{R3.16}$$

$$Br_2 + I^- \rightarrow IBr_2^- \qquad \text{R3.17}$$

The mass resolution of the CIMS was better than 1 amu, which allowed HOBr (at 223 and 225 amu) to be distinguished from BrO (at 222 and 224 amu).

#### 3.2.2.1 Measurements of background signals

Instrument background signals were measured and subtracted from the total signals to determine the contributions from halogen species in the ambient atmosphere. The instrumental background levels for the halogen measurements were determined periodically (every 20 minutes) by scrubbing ambient air with glass wool [Liao et al., 2011a]. Lab experiments showed that glass wool effectively removes many halogen species (e.g. BrO, HOBr and $Br_2$) from a gas stream [Neuman et al., 2010]. An example of typical raw signals of $Br_2$ (287amu) and HOBr (223 amu) with a series of background measurements are shown in Figure 3.1. The background for the $Br_2$ measurement was unstable for a few days in the later period of the campaign. These measurements with reduced accuracy were removed from the dataset. The unstable background may be

because $Br_2$ was not only scrubbed by the glass wool but was also produced from conversion of HOBr in the scrubber. Flowing $N_2$ through the glass wool scrubber continuously when the instrument is not measuring background signals may improve the stability of $Br_2$ background signals. The raw signal obtained for BrO (224 amu) has been previously shown in chapter 2 and Liao et al. [2011a].

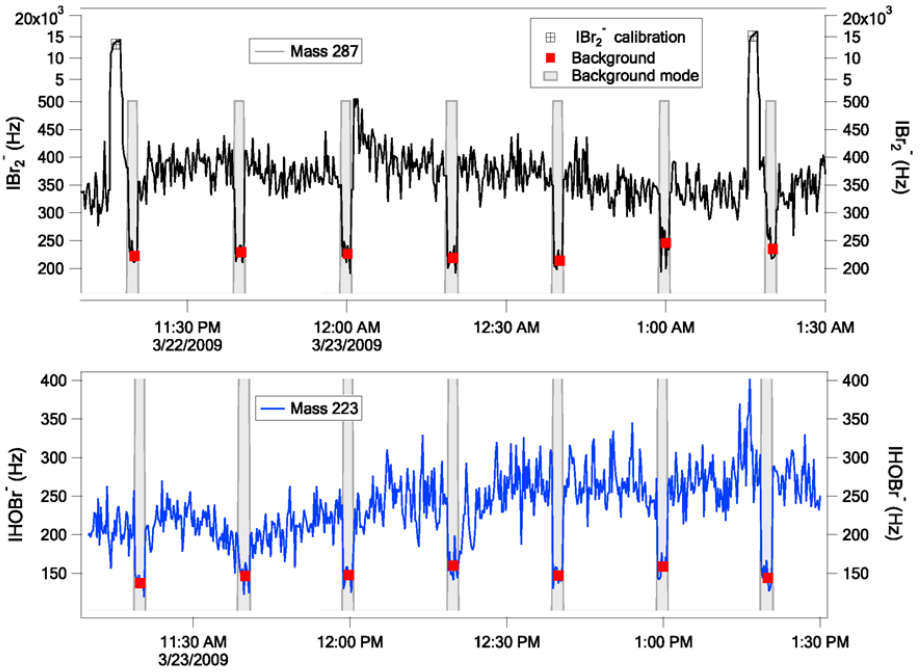


Figure 3.1 Raw signals (Hz) of $IBr_2^-$ (black) and $IHOBr^-$ (blue) at mass 287 amu and 223 amu. Open squares with a cross in the middle represent the average calibration signal when 1.47 ppbv of $Br_2$ was added. Note the time scales of the x axes are different. Red squares denote the average background signals (shaded areas) when sampled air went through glass wool scrubber.

### 3.2.2.2 Calibration

$Br_2$ and $Cl_2$ permeation tubes (Kin-tek) were used as the primary calibration standards for the OASIS campaign. Known amounts of the standard gases were

periodically added to the CIMS inlet. The details of the calibration procedures and the verification of the output rates of the permeation tubes are provided in chapter 2 and Liao et al. [2011a]. An example of the raw signals for the $Br_2$ standard addition is displayed in the top panel of Figure 3.1. The typical sensitivity of $Br_2$ during OASIS was 12 ± 4 Hz per pptv. The concentrations of other halogens were determined from the sensitivity of these specific halogens relative to that of $Br_2$ or $Cl_2$. The sensitivity of BrO relative to $Br_2$ was determined to be 0.47 ± 25% [Liao et al., 2011a]. The sensitivity of HOBr relative to $Br_2$ was determined to be 0.5 ± 25% [Liao et al., 2011b]. The typical sensitivity for BrO and HOBr was about 6 Hz/pptv.

3.2.2.3 Limits of Detection

Measurement precision and background stability affected the limit of detection for each compound. The absolute difference between successive one minute average background measurements of HOBr was essentially normally distributed with a median of 1.3 pptv. The detection limit (3σ) of HOBr is then estimated to be 3.9 pptv for 1 minute data. This variance is very close to that due to the counting statistics of the background level which was 121 Hz (~20 pptv). For this reason, we expect the detection limit due to counting statistics to decrease as approximately the square root of the averaging time. However, as it is difficult to determine the non statistical component of the background variance we estimate the detection limit (3σ) of HOBr to be 2.0 pptv for 10 minute data. Similarly, the detection limit (3σ) for $Br_2$ is estimated to be ~2.0 pptv for 10 minute data before April 8 2009 and ~4.0 pptv for 10 minute data after April 8 2009.

The estimated detection limit for BrO is 1.1 pptv (3σ) for 10 minute data according to chapter 2 and Liao et al. [2011a].

3.2.2.4 Accuracy

The accuracy of the $Br_2$ measurements, when operating well above detection limits, is estimated to be 7% due to the uncertainty in the permeation rate of the calibration source [Liao et al., 2011a]. However, daytime levels of observed $Br_2$ higher than 1 pptv were almost certainly due to the conversion of HOBr on the wall of the sampling inlet. We estimate that on average less than 20% of HOBr was converted to $Br_2$ on the 25 cm long Teflon inlet. Combining the uncertainties in the sensitivity ratio of HOBr to $Br_2$ (25%), the output of permeation tubes (7%) and the interferences of the conversion of HOBr to $Br_2$ on the sampling inlet (20%), the uncertainties in HOBr measurements are estimated to be –30% /+44%. The accuracy of the BrO measurements is estimated to be 30% [Liao et al. 2011a]. The concentrations of $Br_2$ and HOBr that have not been corrected for conversion of HOBr to $Br_2$ are shown in Figure 3.3. The concentrations of $Br_2$ and HOBr corrected for conversion of HOBr to $Br_2$ assuming 20% conversion in the inlet are shown in Figure 3.4. The daytime $Br_2$ measurements during April 9 – April 13 2009 were assumed to be zero in Figure 3.4.

3.2.2.5 Isotope Comparison

Bromine has two naturally occurring isotopes of almost equal abundance which enables the detection of a bromine species at two (or more) different masses by the CIMS. In many cases this provides a valuable test of the quality of the bromine measurements.

The raw ambient signals for mass 223 amu ($IHO^{79}Br^-$) are plotted against the signals at mass 225 amu ($IHO^{81}Br^-$) in Figure 3.2. The correlation is very good ($R^2 = 0.85$) except for a few polluted periods (gray crosses) when $NO_x$ levels were higher than 10 ppbv. An equally weighted bivariate regression applied to the filtered data yielded a slope of 1.05 and an intercept of 1.68 Hz (0.28 pptv). This is a strong indication that HOBr is being detected at these masses. However, there is a small unknown interference at mass 225 during polluted periods. For this reason, mass 223 was used to derive the HOBr concentrations. The signal of $Br_2$ at mass 287 ($I^{79}Br^{81}Br^-$) was correlated well with that at mass 285 ($I^{79}Br^{79}Br^-$) ($R^2 = 0.84$) or 289 ($I^{81}Br^{81}Br^-$) ($R^2 = 0.91$) as well. The most abundant isotope at mass 287 did not have significant interferences and was used to derive the concentrations of $Br_2$. The correlation between mass 222 ($I^{79}BrO^-$) and 224 ($I^{81}BrO^-$) amu was illustrated by Liao et al. [2011a].

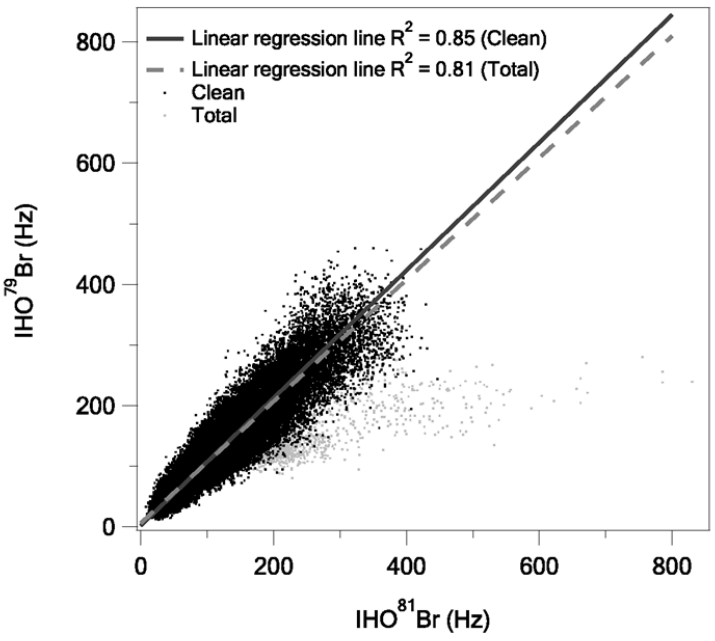


Figure 3.2 The raw ambient signal of HOBr at mass 223 amu (Hz) vs 225 amu (Hz). The correlation coefficient is 0.85 ($R^2$) with a slope of 1.05 and an intercept of 1.68 Hz or 0.28 pptv when small periods of interference in mass 225 amu (gray) are excluded. Due to the small periods of interferences in mass 225 amu, mass 223 amu was used to obtain the concentrations of HOBr.

### 3.2.3 Models

The observations are compared to two models. A steady state photochemical model run with and without HOBr loss on aerosol surfaces is used to analyze the HOBr observations. A time-dependent model operated with four different halogen recycling mechanisms and compared to the average temporal evolution of the observed halogen species.

#### 3.2.3.1 Steady-state calculation of HOBr

HOBr concentrations were predicted using the steady-state assumption as its lifetime due to photolysis is relatively short (~10 minutes in the daytime). The predictions

considered two cases: a. no heterogeneous loss of HOBr on surfaces; b. inclusion of loss of HOBr on aerosol surfaces.

a. $[HOBr]_{pred\_noaeroloss}=\frac{k_2[HO_2][BrO]}{J_{HOBr}}$ eqn. 3.1

b. $[HOBr]_{pred}=\frac{k_2[HO_2][BrO]}{J_{HOBr}+k_a}$. eqn. 3.2

$k_a$ is the loss rate of HOBr on aerosol surfaces, assuming that the heterogeneous loss rate of HOBr is limited by the diffusion rate of gas phase HOBr to aerosol surfaces [Seinfeld and Pandis, 1998]. $k_a$is calculated as: $k_a= 4\pi R_p D_g f$.

Where

$R_p$: Particle radius;

$D_g$: Diffusivity of gas species in the air;

f: Transition regime formula $\frac{0.75\alpha(1+Kn)}{Kn^2+Kn+0.283Kn.\alpha+0.75\alpha}$ [*Fuchs and Sutugin*, 1971];

$\alpha$: Mass accommodation coefficient; Kn = $\lambda/D_p$; $\lambda=3D_g/c$; $c=\sqrt{\frac{8kT}{\pi m}}$.

$D_g$ is assumed to be 0.1 $cm^2 s^{-1}$.

The mass accommodation coefficient of HOBr on aerosol particles in the calculation of $k_a$ is estimated to be 0.6 [Wachsmuth et al., 2002]. The rate coefficient for R3.2, $k_2$, is taken from a kinetics database [Sander et al., 2006]. The photolysis rate, $J_{HOBr}$, was derived from actinic flux measurements. BrO levels were obtained from CIMS observations. $HO_2$ concentrations were predicted from a 0-D steady-state $HO_x$ model [Sjostedt et al., 2007] constrained to the measurements of $CH_2O$, $H_2O$, $O_3$, $CH_4$, CO, NO and j values. $HO_2$ was also predicted from a modified $HO_x$ model ($HO_x$_halogen) by

adding bromine and chlorine chemistry (R3.2, R3.6, heterogeneous loss of HOBr, R3.11, R3.12, R3.18 and R3.19) to test the impact of halogens on $HO_2$ levels.

$$Cl + CH_2O + O_2 \rightarrow HCl + HO_2 + CO \qquad R3.18$$

$$Cl + CH_4 + O_2 \rightarrow HCl + CH_3O_2 \qquad R3.19$$

As the CIMS BrO measurements used in the calculation are in agreement with BrO measurements by LP-DOAS [Liao et al., 2011a], the uncertainty of the HOBr calculation are likely dominated by the uncertainty in $HO_2$ concentrations. However, we found the agreement with observed HOBr was similar whether observed $HO_2$ or predicted $HO_2$ from either the base or halogen model was used to derive HOBr predictions. It is interesting to note that the predicted $HO_2$ levels from the halogen model would have been 35% lower than the basic $HO_x$ model if only bromine chemistry were added. However, the inclusion of chlorine chemistry significantly elevates $HO_2$ levels via oxidation of methane. The correlation coefficients and slopes between the measured and predicted HOBr using measured $HO_2$ and predicted $HO_2$ from the basic $HO_x$ model or from the $HO_x$_halogen model are provided in section 3.3.1.2. As the predicted $HO_2$ from the basic model has a better time coverage, it was used to predict the HOBr shown in Figure 3.5.

3.2.3.2 Time dependent box model

A time dependent box model is used to simulate the average diurnal speciation of bromine during the OASIS campaign. The model incorporates gas phase and heterogeneous phase reactions R3.1–R3.14 and loss of gas phase non-radical bromine (HOBr, HBr and $BrONO_2$) on aerosols. The diurnal evolution of the boundary layer height or the bromine recycling on blowing snow surfaces is not included in the model.

The model is run with 4 cases to investigate the chemical processes that sustain the observed bromine species.

Bromine species including $Br_2$, BrO, HOBr, $BrONO_2$, HBr and Br are predicted in the model. The inputs are 10 minutes average diurnal data (e.g. j values, NO, etc.). The typical concentrations of the diurnal data used as model inputs are given in Table 3.2. Because high levels of NO and $NO_2$ detected at Barrow were likely due to local pollution, NO and $NO_2$ concentrations larger than 20 pptv are excluded. The average NO and $NO_2$ concentrations are ~5 pptv and 7 pptv. The initial concentration of $Br_2$ is specified to be 15 pptv, based on the average $Br_2$ concentrations observed at night. The initial concentrations of aqueous phase $Br^-$ in case C is assumed to be equal to 2 pptv in the gas phase or 0.04 M in aqueous phase. The initial concentrations of other bromine species are assumed to be zero. The gas phase reaction rate constants, photolysis rates, and HOBr mass accommodation coefficients are from the same sources as in section 3.2.3.1. The mass accommodation coefficient of HBr on aerosol particles is estimated to be 0.3 from the data measured for HOBr relative to HBr in Fluckiger and Rossi [2003]. The mass accommodation coefficient of $BrONO_2$ is estimated to be 0.8 [Sander et al., 2006; Deiber et al., 2004; Hanson et al., 1996].

Table 3.2. Typical concentrations of the input species for the time dependent model.

| Input species | Concentration | Sources |
|---|---|---|
| $O_3$ | 12 ppbv | Observations |
| $CH_2O$ | 293 pptv | Observations |
| NO | 5 pptv | Estimated from the observations (exclude NO > 20 pptv) |
| $NO_2$ | 7 pptv | Estimated from the observations (exclude $NO_2$ > 20 pptv) |
| $HO_2$/OH | $5.6 \times 10^7$ molec.cm$^{-3}$ /$6.1 \times 10^5$ molec.cm$^{-3}$ (daytime) | $HO_x$ model [*Sjostedt et al.*, 2007] |
| Aerosol surfaces | 56 $\mu m^2$ cm$^{-3}$ | Observations |

In case A only gas phase bromine reactions are considered. The average daytime lifetimes of HOBr, $BrONO_2$ and HBr are 11 minutes, 19 minutes, and 39 hours, respectively.

In cases B-D the loss of HOBr, $BrONO_2$ and HBr to the condensed phase is included. The diffusive loss of these species to aerosol surfaces is taken into account in each of the cases. The loss of these species to the snowpack is not considered. The production of $Br_2$ and HOBr (R3.7 and R3.10) from the condensed phase is included.

In case B the loss of HOBr, $BrONO_2$, and HBr from the gas phase is only limited by diffusion to the aerosol (lifetime due to heterogeneous loss: ~10 minutes, ~ 10 minutes, and ~20 minutes). The average total lifetime of HOBr, $BrONO_2$, and HBr is ~7 minutes, ~7 minutes and ~20 minutes, respectively. The production rate of $Br_2$ is assumed to be equal to the sum of the heterogeneous loss rates of HOBr and $BrONO_2$. This case is used to simulate the maximum heterogeneous regeneration rate of $Br_2$ with no limitation on $Br^-$.

In case C the heterogeneous loss rate of HOBr is assumed to also be limited by the rate of its reaction with $Br^-$ in the condensed phase. The heterogeneous loss rate of HBr is assumed to be equal to the production rate of $Br^-$. The production rates for $Br_2$ and $Br^-$ are given by the following equations:

$$\frac{d[Br_2]}{dt} \left(\text{or} -\frac{d[HOBr]}{dt}\right) = \frac{k_{3.7}[H^+]\,[HOBr]_{(g)} H\,[Br^-]}{M} \qquad \text{eqn. 3.3}$$

$$\frac{d[Br^-]}{dt} = k_{HBr}\,[HBr] \qquad \text{eqn. 3.4}$$

where $k_{3.7}$ is the reaction rate constant ($M^{-2}s^{-1}$) of R3.7; H is the Henry's law equilibrium at 250K as $3 \times 10^4$ M/atm [Waschewsky and Abbatt, 1999]; M is the concentration

(molec.cm$^{-3}$) of air at 1 atm; pH = 3 – 6; $k_{HBr}$ is the diffusion rate of HBr to aerosols. The lifetime of HBr and $BrONO_2$ is the same as case B. However, the lifetime of HOBr is 7 minutes on average in the daytime and increases to ~20 hours after sunset. This simulates the case of active bromine production being limited by $Br^-$ supplied from HBr.

In case D, as the concentrations of $Br^-$ available for reaction R3.7 are not well known, the following assumptions are made. The heterogeneous loss of HOBr and $BrONO_2$ are efficiently (100%) recycled back to produce $Br_2$ when $Br^-$ supplied from the heterogeneous loss of HBr is abundant. When the heterogeneous loss of HOBr and $BrONO_2$ are higher than the $Br^-$ supplied from the heterogeneous loss of HBr, the production rate of $Br_2$ is assumed to be equal to the heterogeneous loss rate of HBr plus 50% of the difference between the sum of the heterogeneous loss rate of HOBr and $BrONO_2$ and HBr.

Heterogeneous $Br_2$ production rate =

$$\begin{cases} k_{HBr}[HBr] + 0.5\,(k_{HOBr}[HOBr] + k_{BrONO2}[BrONO_2] - k_{HBr}[HBr]), & (k_{HOBr}[HOBr] + k_{BrONO2}[BrONO_2] > k_{HBr}[HBr]) \\ k_{HOBr}[HOBr] + k_{BrONO2}[BrONO_2], & (k_{HOBr}[HOBr] + k_{BrONO2}[BrONO_2] < k_{HBr}[HBr]) \end{cases}$$

eqn. 3.5

This case assumes that HOBr and $BrONO_2$ still react to form $Br_2$ to the gaseous phase with 50% efficiency when $Br^-$ from HBr is depleted.

## 3.3 Results and discussion

### 3.3.1 BrO, HOBr, and $Br_2$ measurements by CIMS

10 minute averages of the BrO, HOBr, $Br_2$, and $O_3$ observations from March 18 to April 14, 2009 during the OASIS campaign are shown in a time series plot in Figure 3.3. The gaps in BrO and HOBr measurements are due to the malfunction of the instrument

and power outages. The extra gaps in the $Br_2$ measurements are due to unstable $Br_2$ background measurements leading to observations that are below detection limits.

3.3.1.1 BrO measurements

The hourly average diurnal profile of BrO from March 18th to April 14th is shown in Figure 3.4. BrO concentrations increase at sunrise and decrease at sunset as expected. The daytime (9 am – 6 pm) BrO concentrations on days with significant BrO (maximum BrO > = 10 pptv) observed and low NO (< 100 pptv) have an average value of 11.9 pptv and ranged up to 37 pptv. The BrO concentrations observed by CIMS were correlated well with that measured by a nearly co-located LP DOAS during the OASIS campaign [Liao et al., 2011a]. No simple relationship between BrO and ozone was observed (Figure 3.7 middle panel).

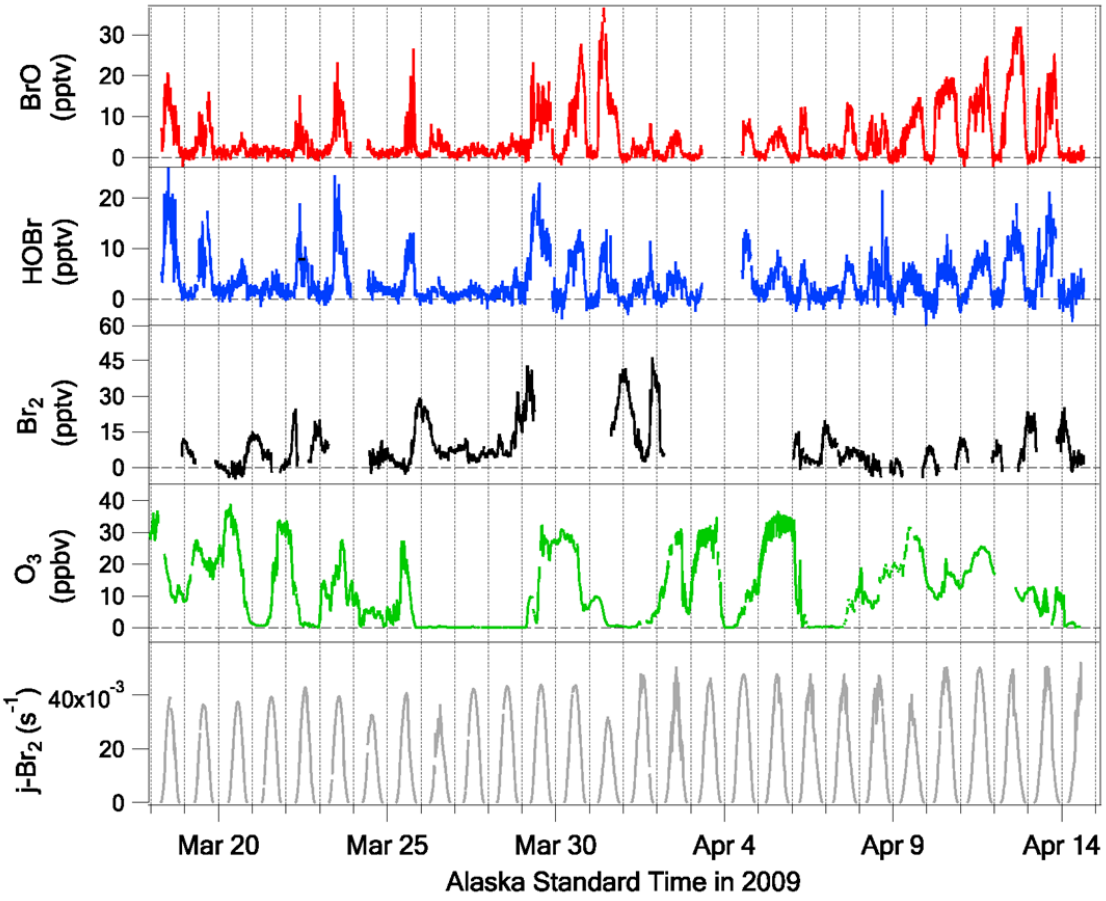


Figure 3.3 A time series of measurements of BrO (red), HOBr (blue), $Br_2$ (black), $O_3$ (green) and j values of $Br_2$ (gray) averaged to 10 minutes from March 18$^{th}$ to April 14$^{th}$ 2009 during the OASIS campaign.

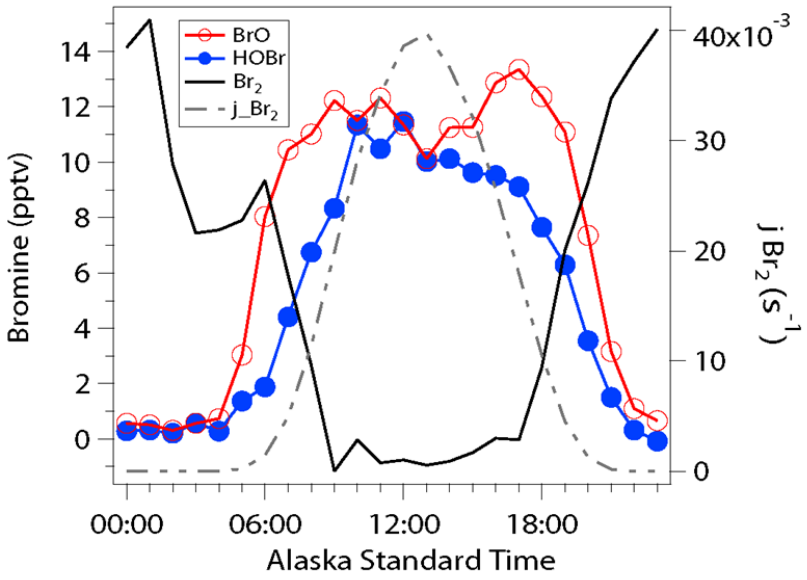


Figure 3.4 Hourly average diurnal profiles of observed BrO (red), HOBr (blue) and $Br_2$ (black). The $Br_2$ and HOBr concentrations were corrected for the conversion of HOBr to $Br_2$ on instrument sampling lines.

3.3.1.2 HOBr measurements and predictions

The hourly average diurnal profile of HOBr from March 18th to April 14th is also shown in Figure 3.4. Approximately 9.8 pptv of HOBr were observed in the daytime (9 am – 6 pm) on average during the campaign. Up to ~26 pptv of HOBr were detected for the 10 minute average data (Figure 3.3). HOBr has similar diurnal patterns to BrO with maximum in the daytime and no evidence of significant nighttime concentrations. This is consistent with the production of HOBr by the reaction of photochemically short lived species BrO and $HO_2$ (R3.2), and the rapid loss of HOBr from the gas phase. The concentrations of HOBr increased slightly later than BrO at sunrise and decreased slightly earlier than BrO at sunset. This is consistent with the mechanism that HOBr is

formed by reaction BrO and $HO_2$, which increased later than BrO at sunrise and decreased earlier than BrO at sunset.

The steady-state box model predictions of HOBr in case (a) and case (b) (see 3.2.3.1) plotted against the HOBr measurements are shown in Figures 3.5(a) and 3.5(b), respectively. HOBr data taken under polluted conditions (NO > 100 pptv) are excluded from the comparison. HOBr predictions are well correlated ($R^2$ = 0.70 in case a; $R^2$ = 0.63 in case b) with HOBr measurements at low wind speeds (< 6 m $s^{-1}$) with a slope of 2.42 for case (a) and 1.38 for case (b) from equally weighted bivariate linear regressions through zero. The average ratio of $HOBr_{pred}$ to $HOBr_{obs}$ (when $[HOBr]_{obs}$> 2 pptv) is 2.02 with a standard deviation of 1.26 for case (a) at wind speeds < 6 m $s^{-1}$. The average ratio of $HOBr_{pred}$ to $HOBr_{obs}$ (when $[HOBr]_{obs}$ > 2 pptv) is 0.91 with a standard deviation of 0.76 for case (b) at wind speeds < 6 m $s^{-1}$.The predicted HOBr (in case b) using $HO_2$ prediction from the $HO_x$_halogen model has a correlation coefficient of 0.63 at wind speeds < 6 m $s^{-1}$ ($R^2$ = 0.40 for all data) with HOBr measurements and a slope of 0.98 (wind speeds < 6 m $s^{-1}$, slope = 1.29 for all data). The average ratio of $HOBr_{pred}$ to $HOBr_{obs}$ (when $[HOBr]_{obs}$ > 2 pptv) is 0.82 with a standard deviation of 0.63 for case (b) at wind speeds < 6 m $s^{-1}$. Similarly, the predicted HOBr (in case b) using $HO_2$ measurements has a correlation coefficient of 0.57 at wind speeds < 6 m $s^{-1}$ ($R^2$ = 0.44 for all data) with HOBr measurements and a slope of 1.67 (wind speeds < 6 m $s^{-1}$, slope = 2.07 for all data). The average ratio of $HOBr_{pred}$ to $HOBr_{obs}$ (when $[HOBr]_{obs}$ > 2 pptv) is 1.49 with a standard deviation of 1.18 for case (b) at wind speeds < 6 m $s^{-1}$ using $HO_2$ measurements.

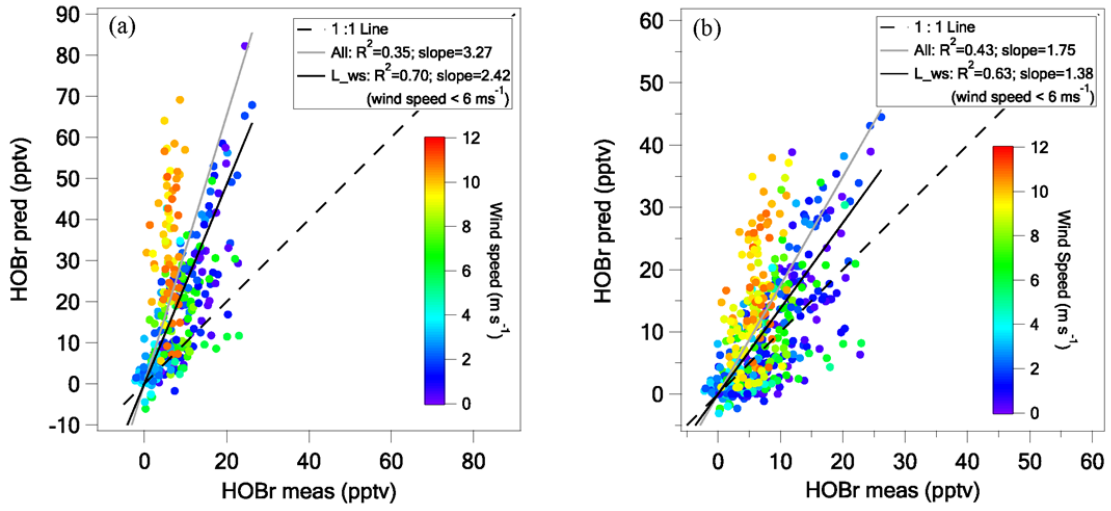


Figure 3.5 The concentrations of daytime (9am – 6pm) BrO (top panel) and HOBr (bottom panel) on a 1 minute average base are binned according to different wind speeds. One standard deviation (± 1σ) is denoted as the error bar. Each wind speed bin contained at least 400 1-minute measurements except the wind speed bin between 11–12 m $s^{-1}$ with 80 1-minute measurements.

Clearly, all three methods for predicting HOBr have a similar correlation with observations. The magnitude of the individual HOBr predictions shows larger differences. Both the base and halogen models give results 10% less than observations while those derived from $HO_2$ observations are approximately 50% higher. However, all three methods support the same conclusions. All of the methods over predict HOBr and are less well correlated to observations at high wind speeds. Because the HOBr predictions were highly constrained by BrO measurements, the over prediction of HOBr at high wind speeds are probably due to enhanced deposition of HOBr on blowing snow surfaces. It is likely that blowing snow at high wind speeds provided more surface area for HOBr loss which regenerates active bromine and eventually BrO. The correlation between HOBr predictions and measurements also indicates that HOBr can be predicted in the Arctic at

low wind speeds by relatively simple models that include the heterogeneous loss of HOBr on aerosol surfaces. However, it should be noted that the inclusion of chlorine in the halogen model significantly improves the magnitude of the HOBr predictions.

It is also worth noting that the role of organic peroxy radicals upon HOBr production is not well defined. For example, methyl peroxy ($CH_3O_2$) and other radicals are thought to react with BrO to produce HOBr [Aranda et al., 1997; Enami et al., 2007]. Including reaction R3.20 in the photochemical model increases predicted HOBr levels 5–10%.

$$CH_3O_2 + BrO \rightarrow HOBr + CH_2O_2 \qquad \text{R3.20}$$

Organic peroxy radicals other than $CH_3O_2$ may also react with BrO and plays a role in HOBr production. Lab experiments are needed to quantify the reaction rate constants of other organic peroxy radicals with BrO in order to better estimate the contribution of these reactions to HOBr budget. If the production of HOBr from organic peroxy radicals other than $CH_3O_2$ with BrO is significant, other loss mechanisms of HOBr would be needed to reconcile predictions with observations.

The impact of wind speeds on bromine recycling is further illustrated in Figure 3.6. The concentrations of BrO and HOBr in the daytime (9 am– 6 pm) are binned according to wind speed. The average values of BrO and HOBr in each bin are shown as the heights of the bins. The average BrO concentrations increases at higher wind speeds especially above 6 m $s^{-1}$; however, HOBr levels remained relatively constant as a function of wind speed. This is consistent with blowing snow at high wind speeds increasing the efficiency for regenerating active bromine (e.g. BrO) by providing more surfaces for heterogeneous loss of HOBr. Higher production rates of HOBr due to

enhanced BrO present at higher wind speeds seemed to be balanced by higher loss rates of HOBr on the blowing snow and resulted in a relatively constant HOBr concentration as a function of wind speed. It should also be noted that the sum of BrO and HOBr was also enhanced at higher wind speeds. These results provide direct evidence for the important role of high wind and blowing snow in activating bromine including potentially producing higher total inorganic gas phase bromine species. Jones et al. [2009] also found that enhanced BrO from satellite observations coincide with high wind speeds. Active bromine and BrO levels measured over the Arctic Ocean were highest when wind speeds were the greatest [Neuman et al., 2010]. Begoin et al. [2010] suggested that the activation of BrO was linked to a cyclone with very high surface wind speeds probably associated with blowing snow and that the transported aerosols and snow can also provide surfaces for BrO recycling within the BrO plume. The model of Yang et al. [2010] also showed that a bromine source from blowing snow is needed to explain the bromine "explosion" events. Moreover, Dibb et al. [2010] observed higher soluble bromide concentrations in the firn air than ambient air at Summit, Greenland, which indicates that snow pack may be a source of bromine.

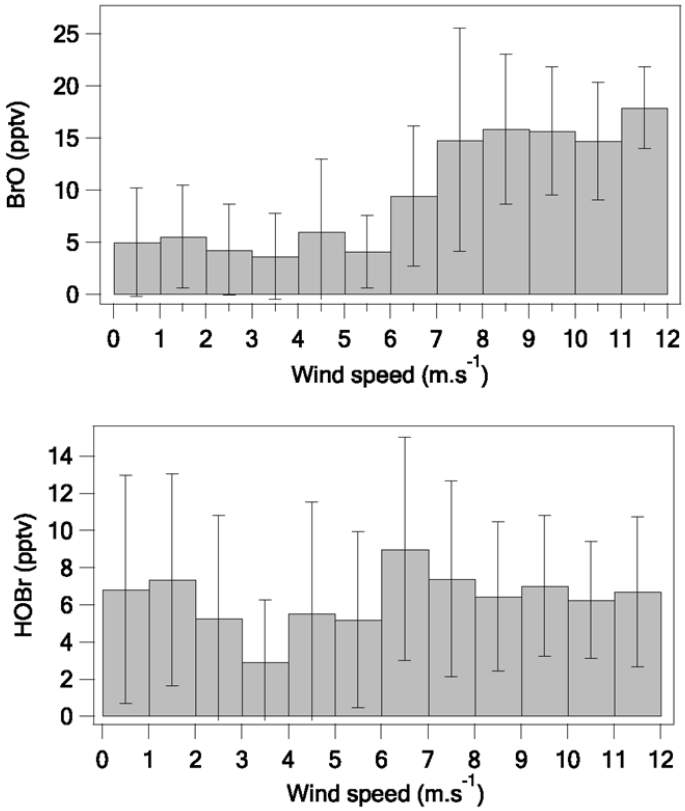


Figure 3.6 The concentrations of daytime (9am – 6pm) BrO (top panel) and HOBr (bottom panel) on a 1 minute average base are binned according to different wind speeds. One standard deviation (± 1σ) is denoted as the error bar. Each wind speed bin contained at least 400 1-minute measurements except the wind speed bin between 11–12 m $s^{-1}$ with 80 1-minute measurements.

3.3.1.3 $Br_2$ measurements

Diurnal variations of $Br_2$ were observed with maxima concentrations at night (Figure 3.3). On average about 15 pptv of $Br_2$ was observed at night (Figure 3.4). Observed $Br_2$ concentrations decreased rapidly as the sun rose. This is consistent with $Br_2$ accumulation at night followed by photolysis to produce bromine atoms at sunrise. Small but detectable levels of daytime $Br_2$ detected (see Figure 3.3) were due to the conversion of HOBr on the Teflon inlet wall [Neuman et al., 2010] and the uncertainty in

background signal measurements. The $Br_2$ measurements at night were without interference from HOBr as this species was not observed in the dark.

Nighttime $Br_2$ concentrations were clearly anti-correlated with $O_3$. The concentrations of nighttime $Br_2$ binned as a function of $O_3$ mixing ratios are shown in Figure 7. These observations are consistent with the transport of active bromine at night as $Br_2$ in ozone depleted air masses. The data also suggest that the magnitude of active bromine in the air mass is proportional to the loss of ozone.

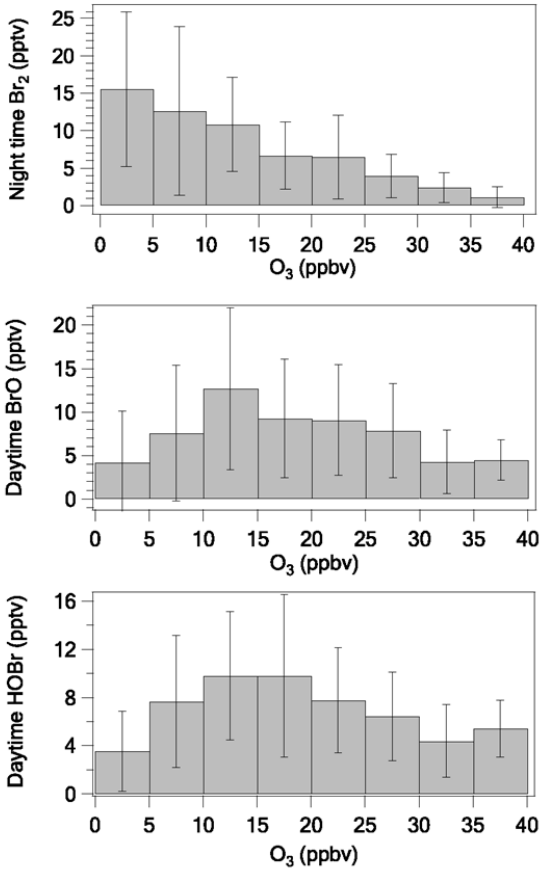


Figure 3.7 The nighttime (6pm – 9am) concentrations of $Br_2$ (top panel) and the daytime (9 am- 6 pm) concentrations of BrO (middle panel) and HOBr (bottom panel) on a 1 minute average base are binned according to different ozone levels. The error bar represents ± 1 standard deviation of $Br_2$ measurements at the binned ozone range. One standard deviation (± 1σ) is denoted as error bar and the number of measurements in each bin ranges from 100 to over 2500.

### 3.3.2 Predicted diurnal bromine speciation

A time dependent model is used to simulate the observed diurnal patterns of bromine species at Barrow shown in Figure 3.4. The time dependent model was run using four different bromine recycling mechanisms (see 3.2.3.2) and the results are shown in Figure 3.8.

In case A, which does not consider heterogeneous recycling, most of the gas phase bromine species are rapidly converted to HBr because HOBr and $BrONO_2$ are efficiently converted back to bromine radicals by photolysis. Predicted BrO and HOBr concentrations only have a morning peak and decrease to ~1 pptv around noon. These results are obviously inconsistent with observations. As expected, loss of bromine species to heterogeneous phase and recycling of heterogeneous bromine to gas phase bromine are needed to reproduce the observed gas phase bromine levels.

In case B, which simulates the maximum heterogeneous recycling rates, the model over predicted the bromine species by about a factor of 10 in the afternoon. This indicates that the production of $Br_2$ from a 100% conversion of heterogeneous loss of HOBr and $BrONO_2$ is too high and the availability of $Br^-$ may limit $Br_2$ production.

In case C, which assumes the heterogeneous loss rate of HOBr and production rate of $Br_2$ from HOBr are limited by the diffusion of gas phase HOBr to heterogeneous surfaces and the reaction rate of R3.7, the predicted HOBr diurnal profiles with high concentrations after sunset are inconsistent with the observations. These model results were found to be consistent over a wide range of pH. This suggests that the heterogeneous loss rate of HOBr estimated by the aqueous phase reaction rate of R3.7 is

too slow or the production rate of HOBr from hydrolysis of $BrONO_2$ is too high. The estimated heterogeneous loss rate of HOBr in case C highly depends on the concentrations of $Br^-$, which are dramatically depleted near sunset under the assumption that the heterogeneous loss of HBr is the dominant production of $Br^-$ [Simpson et al., 2007a]. Two slightly modified versions of case C were also investigated by assuming that (1) HOBr (aq) from hydrolysis of $BrONO_2$ is rapidly converted to $Br_2$ by reacting with $Br^-$ instead of emitting gas phase HOBr or (2) the $Br_2$ production rate from $BrONO_2$ is 50% of the diffusion rate of $BrONO_2$ to heterogeneous surfaces. The first modification showed similar results to figure 8(c) while the second modification predicted the profile of HOBr similar to case D. This indicates that low concentrations of predicted $Br^-$ in the late afternoon lead to the over prediction of HOBr in the model.

In case D, the model best reproduces the average diurnal patterns of gas phase HOBr, BrO and $Br_2$. The initial gas phase bromine (15 pptv) needs to be recycled very efficiently (~ 39 times in 24 hours) from heterogeneous phase to gas phase $Br_2$ to maintain the gas phase bromine concentrations. All of the gas phase bromine species HOBr, HBr, and $BrONO_2$ must be recycled to sustain the observed bromine concentrations. However, only aerosol surface area is used for bromine recycling in our study. Due to the uncertainty in mass accommodation coefficient measurements, this study cannot exclude the role of snowpack surfaces in bromine recycling. The sources of $Br^-$ other than heterogeneous loss of HBr may come from either the snowpack or aerosol surfaces.

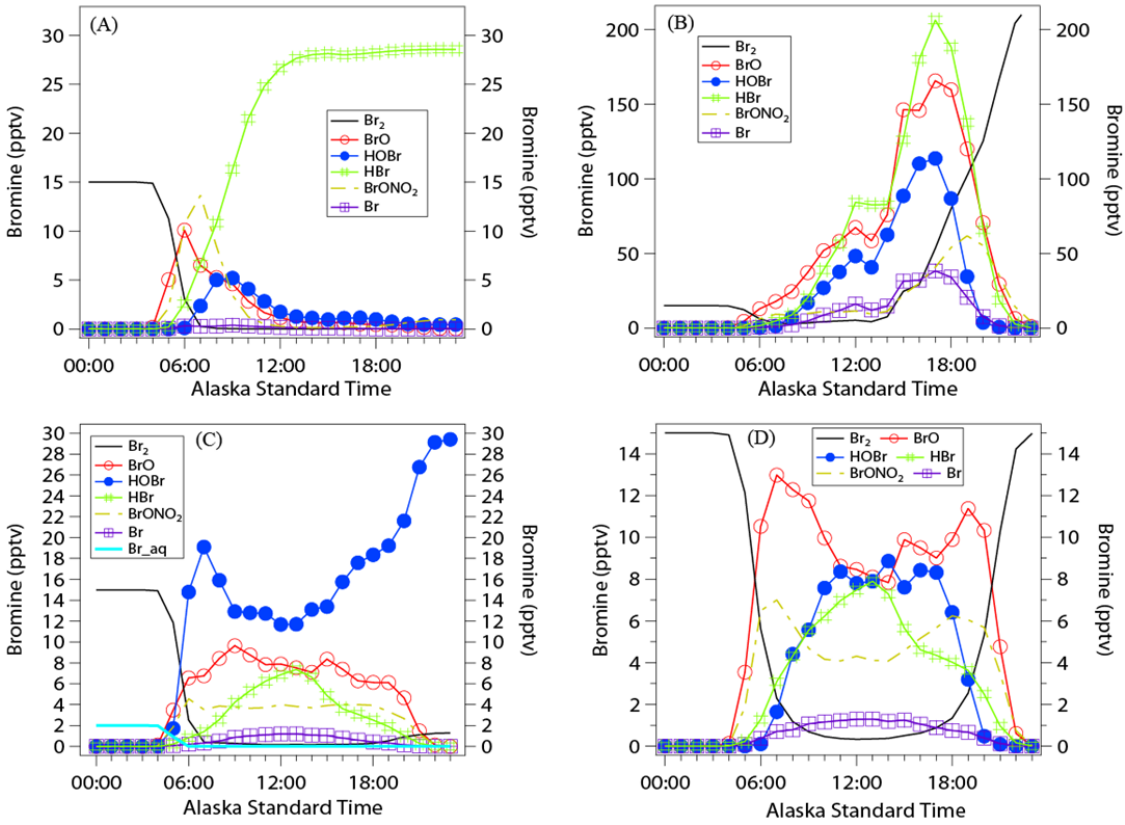


Figure 3.8 Prediction of hourly average diurnal profiles of bromine species (BrO, HOBr, $Br_2$, Br, $BrONO_2$ and HBr) from a time dependent model under four limiting cases. In (A) only gas phase reactions are considered. In (B), (C) and (D) loss of HOBr, $BrONO_2$ and HBr to the condensed phase and reproduction of $Br_2$ from condensed phase are also included. In (B) the maximum heterogeneous production rate of $Br_2$ from HOBr and $BrONO_2$ is assumed. In (C) the heterogeneous production rate of $Br_2$ from HOBr and $BrONO_2$ are assumed to be limited by the availability of $Br^-$ supplied from HBr. In (D) HOBr and $BrONO_2$ still react to form $Br_2$ to the gaseous phase with 50% efficiency when $Br^-$ from HBr is depleted.

The predicted $Br_2$ in case D, with an initial mixing ratio of 15 pptv at night, decreases to below 1 pptv at sunrise and builds back up to near original levels after sunset. The predicted average daytime (9 am – 6 pm) BrO and HOBr mixing ratios were 9.3 pptv and 7.7 pptv, which are comparable to the observations. The predicted HOBr concentrations also increased slightly later than BrO at sunrise and decreased slightly

earlier than BrO at sunset, similar to the observations. The model did not consider the dilution of chemical species due to evolution of boundary layer height, which may contribute to the differences between observed and predicted diurnal patterns.

No observations of HBr and $BrONO_2$ were available to compare to the model predictions. The ratio of predicted HBr to BrO and HOBr were within the range of previous predictions [Evans et al., 2003] in the Arctic, and the diurnal pattern of predicted HBr was similar to that predicted in Fan and Jacob [1992]. The predicted diurnal pattern of $BrONO_2$ had an early morning and a late afternoon peak with a local minimum at noon, which is likely due to the sharp peak in the $BrONO_2$ photolysis rate (~0.0015 $s^{-1}$) around noon. When $NO_x$ is abundant, its coupling with halogen chemistry is important to fully study the bromine catalyzed ozone depletions in the MBL. With average $NO_2$ concentrations of 7 pptv used in the model, the early morning and late afternoon peaks of $BrONO_2$ were then predicted to be ~7 pptv and noon time $BrONO_2$ was predicted to be 4 pptv. This indicates that the impact of $NO_x$ on bromine can be significant in the early morning and late afternoon in the MBL when significant $NO_2$ is present. This is consistent with observation of halogens along with NO and $NO_2$ in Antarctica [Bloss et al., 2010].

### 3.4 Conclusions

The simultaneous measurements of BrO, HOBr, and $Br_2$ at Barrow, AK by CIMS reveals gas phase bromine speciation in the Arctic MBL. The first direct observations of HOBr were achieved and were found to agree well ($R^2$ = 0.63; slope =1.38) at low wind speeds (< 6 m $s^{-1}$) with a simple photochemical model constrained to BrO observations. The concentrations of BrO were enhanced relative to HOBr at higher wind speeds. This

indicated that the high wind speeds, likely inducing blowing snow, favored bromine activation and provided more surfaces for HOBr heterogeneous loss. Nighttime levels of $Br_2$ were anti-correlated with $O_3$ at Barrow, which indicates that $O_3$ depleted air masses at Barrow were likely transported from regions rich in $Br_2$. The average diurnal patterns of observed HOBr, BrO and $Br_2$ can be explained by a time dependent model with efficient recycling of HBr, HOBr, and $BrONO_2$. Finally, sources of $Br^-$ other than HBr heterogeneous loss are needed to account for the bromine concentrations based on current bromine chemical mechanisms. Further observations of inorganic bromine species (e.g. HBr and $BrONO_2$) are needed to confirm the bromine catalyzed ozone depletion mechanisms.

# CHAPTER 4

# HIGH LEVELS OF MOLECULAR CHLORINE IN THE ARCTIC: IMPLICATION FOR METHANE OXIDATION AND OZONE DEPLETION

## 4.1 Introduction

Chlorine chemistry can significantly affect the fates of many tropospheric compounds and have a potential impact on climate change and human health. Chlorine atoms efficiently oxidize hydrocarbons including the important greenhouse gas methane ($CH_4$) [Platt et al., 2004]. Chlorine atoms may also intensify polar spring time surface ozone and mercury depletion events (ODEs and MDEs) [Tuckermann et al., 1997; Donohoue et al., 2005], where mercury is oxidized to more toxic forms and accumulated in the ecosystem. The reaction rate coefficient of Cl atoms with methane ($CH_4$) is ~20 times faster than for hydroxyl radicals (OH) at 250K [Sander et al., 2006]. Therefore, even relatively low concentrations of Cl atoms ($10^4$ – $10^5$ atom $cm^{-3}$) can significantly decrease the lifetime of $CH_4$ and have a potential impact on global energy balance. Cl can also oxidize gaseous elemental mercury to more soluble and toxic forms of mercury [Donohoue et al., 2005], but the rate coefficient for this reaction is not well defined. Cl atoms are also efficiently converted to chlorine oxide (ClO) in the atmosphere which can react with bromine oxide (BrO) to enhance ozone loss rates [Sander et al., 2006].

Direct measurements of Cl and ClO are difficult at lower altitudes and are limited [e.g. Tuckermann et al., 1997]. Consequently, significant effort has been made to detect chlorine radical precursors. Recently, high levels of nitryl chloride ($ClNO_2$), which rapidly photolyzes to form Cl atoms, have been observed coincident with $N_2O_5$ [Osthoff et al., 2008; Thornton et al., 2010] at night, demonstrating a mechanism to activate chloride ($Cl^-$) in high $NO_x$ regions. High levels of $Cl_2$ (up to 35 pptv at night) and HOCl (up to 173 pptv during the day) have been observed in the Atlantic marine boundary layer and cannot be explained by known chlorine chemical mechanisms [Lawler et al., 2011]. There are a few other observations of $Cl_2$ of up to ~30 pptv in the daytime and up to ~150 pptv at night in polluted coastal areas [Spicer et al., 1998; Finley and Saltzman, 2006; Finley and Saltzman, 2008; Lawler et al., 2009]. However, no observations of $Cl_2$ have been made in polar marine boundary layer.

BrCl is a potential chlorine radical precursor [Vogt et al., 1996]. Significant levels of bromine monochloride (BrCl) were detected during ozone depletion events (ODEs) in the Arctic polar sunrise [Foster et al., 2001]. However, BrCl was below detection limits of 0.5 pptv and 2 pptv when clearly elevated $Br_2$ was observed in recent campaigns in Pacific marine boundary and Arctic marine boundary [Finley and Saltzman, 2008; Neuman et al., 2010]. Lab experiments [Fickert et al., 1999; Adams et al., 2002] found that BrCl can be a significant product of uptake of HOBr on frozen salt surface when $[Br^-]/[Cl^-]$ ratio on the sea salt surfaces are smaller than ~$2.5 \times 10^{-4}$, which is much smaller than in sea water (0.0014). Moreover, lab experiment [Huff and Abbatt, 2000] found that BrCl besides $Br_2$ can be produced following uptake of $Cl_2$ or HOCl on chloride/bromide ice surfaces. More direct measurements of BrCl are helpful for investigating the

formation of BrCl and its importance as a halogen radical precursor in the Arctic environment.

Here we report high levels of molecular chlorine ($Cl_2$) and much less BrCl observed at Barrow, Alaska (71°19′ N, 156° 39′ W) in spring 2009 during the Ocean-Atmospheric-Sea Ice-Snowpack (OASIS) campaign. The *in situ* measurements of chlorine species were carried out by chemical ionization mass spectrometry (CIMS) [Liao et al., 2011a].

## 4.2 Methods

### 4.2.1 CIMS measurements

A chemical ionization mass spectrometer was used to measure speciated halogen compounds including $Cl_2$, HCl, BrCl, BrO, HOBr, and $Br_2$ at Barrow, AK in spring 2009 during the OASIS campaign. The details of measurement site and the CIMS instrument are described in Liao et al. [2011a]. The measurements of BrO, HOBr, and $Br_2$ are reported in Liao et al. [2011b]. The main reagent ion used after 18 March was hydrated $I^-$, and reagent ion $SF_6^-$, which allowed measurements of HCl, was used before 18 March. The CIMS was also set to detect BrCl from 19 March – 30 March, 2009.

$Cl_2$ was detected at mass 197 and 199 amu with $I^-$ and at mass 70 and 72 amu with $SF_6^-$. HCl was monitored only at mass 164 amu because $Br_2$ can be detected as $Cl_2^-$ with $SF_6^-$ at mass 162 amu. The ionized product and monitored masses of halogen species with $I^-$ are provided in Table 2.1 in chapter 2. The reactions of chlorine species with $SF_6^-$ and $I^-$ are shown below.

$$Cl_2 + SF_6^- \rightarrow Cl_2^- + SF_6 \quad \text{R4.1}$$

$$Cl_2 + I^- \rightarrow ICl_2^- \quad \text{R4.2}$$

$$HCl + SF_6^- \rightarrow SF_5Cl^- + HF \quad \text{R4.3}$$

$$BrCl + I^- \rightarrow IBrCl^- \quad \text{R4.4}$$

The signals at mass 197 were plotted versus 199 amu (Figure 4.1). The excellent correlation ($R^2 = 0.99$) between the signals at mass 197 and 199 amu and a slope of 0.65 indicates that chemical compound containing two chlorine atoms was detected at these masses. The concentrations of the detected species were determined by subtracting the background signals from the ambient signal and dividing the resulting net signals by sensitivity. The background of $Cl_2$ and HCl was well determined by frequently scrubbing by glass wool. The background of BrCl was less stable and the BrCl concentrations were often below the detection limits. $Cl_2$ and $Br_2$ permeation tubes were used to determine the sensitivity of $Cl_2$ and other halogen species.

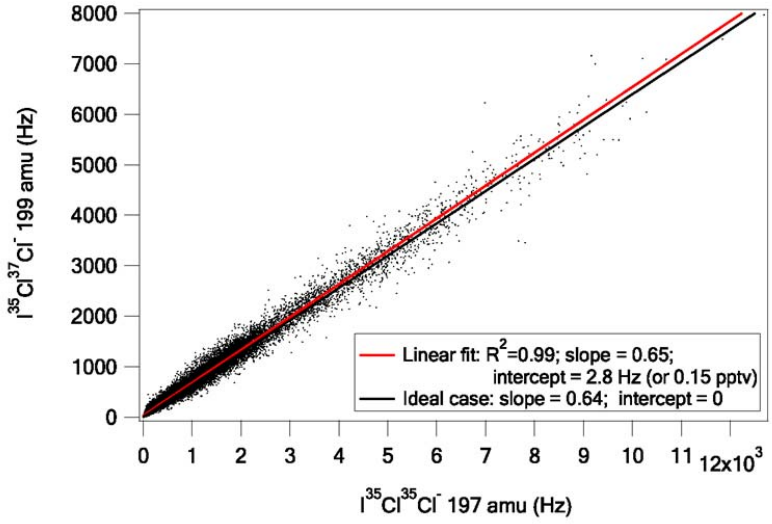


Figure 4.1 Correlation plot of chlorine isotopes at mass 199 amu and 197 amu of the ambient measurements. Black line represents the ideal regression of chlorine isotopes in

nature. Red line shows the equally weighted bivariate linear regression of the observed ambient chlorine isotopes at mass 199 amu and 197 amu.

### 4.2.2 Time dependent box model

A time dependent box model was employed to study the impact of observed $Cl_2$ on chlorine chemistry. Chlorine species (Cl, ClO, HOCl, and HCl) are simulated in the model. The model includes chemical reactions 1–21 (see Table 4.1) and is constrained to $Cl_2$ measurements. The model is also highly constrained to the measurements of $O_3$, nitrogen oxide (NO), nitric dioxide ($NO_2$), formaldehyde ($CH_2O$), hydrocarbons (RH), hydroxyl radical (OH) and hydroperoxy radicals ($HO_2$) every 10 minutes. The input data are average diurnal measurements. The typical concentrations of the input are shown in Table 4.2. Because high levels of NO and $NO_2$ were due to local pollution and the background NO and $NO_2$ concentrations were near the detection limits, NO concentrations are assumed to be 5 pptv in the daytime and 0 at night and $NO_2$ concentrations are assumed to be 2 pptv [Liao et al., 2011c].

Table 4.1 Reactions included in the time dependent model.

| | Gas phase reactions | Reaction rates (molec $cm^{-3}s^{-1}$) | Reaction rates (250K) |
|---|---|---|---|
| 1. | $Cl + O_3 \rightarrow ClO + O_2$ | $2.3\times10^{-11}exp(-200/T)$ | $1.03\times10^{-11}$ |
| 2. | $Cl + CH_4 \rightarrow HCl + CH_3$ | $7.3\times10^{-12}exp(-1280/T)$ | $4.36\times10^{-14}$ |
| 3. | $Cl + CH_2O \rightarrow HCl + CHO$ | $8.1\times10^{-11}exp(-30/T)$ | $7.18\times10^{-11}$ |
| 4. | $Cl + C_2H_6 \rightarrow HCl + C_2H_5$ | $7.2\times10^{-11}exp(-70/T)$ | $5.44\times10^{-11}$ |
| 5. | $Cl + C_3H_8 \rightarrow HCl + CH_3CHCH_3$ | $6.54\times10^{-11}$ | $6.54\times10^{-11}$ |
| | $\rightarrow HCl + CH_2CH_2CH_3$ | $7.85\times10^{-11}exp(-80/T)$ | $5.70\times10^{-11}$ |
| 6. | $Cl + n\text{-}C_4H_{10} \rightarrow HCl + 1\text{-}C_4H_9$ | $0.44exp(-120/T)\times2.04\times10^{-10}$ | $5.55\times10^{-11}$ |
| | $Cl + n\text{-}C_4H_{10} \rightarrow HCl + 2\text{-}C_4H_9$ | $0.59exp(55/T))\times2.04\times10^{-10}$ | $1.50\times10^{-10}$ |
| 7. | $Cl + CH_3CHO \rightarrow HCl + CH_3CO$ | $8.0\times10^{-11}$ | $8.0\times10^{-11}$ |
| | $\rightarrow HCl + CH_2OH$ | | |
| 8. | $Cl + CH_3OH \rightarrow HCl + CH_2OH$ | $5.5\times10^{-11}$ | $5.5\times10^{-11}$ |
| 9. | $Cl + CH_3C(O)CH_3 \rightarrow HCl + CH_3C(O)CH_2$ | $1.5\times10^{-11}exp(-590/T)$ | $1.4\times10^{-12}$ |
| 10. | $Cl + HO_2 \rightarrow HCl + O_2$ | $1.8\times10^{-11}exp(170/T)$ | $3.55\times10^{-11}$ |
| | $\rightarrow ClO + OH$ | $4.1\times10^{-11}exp(-450/T)$ | $6.78\times10^{-12}$ |

| | | | |
|---|---|---|---|
| 11. | $ClO + HO_2 \rightarrow HOCl + O_2$ | $2.7\times10^{-12}exp(220/T)$ | $6.51\times10^{-12}$ |
| 12. | $ClO + ClO \rightarrow Cl_2 + O_2$ | $1.0\times10^{-12}exp(-1590/T)$ | $1.73\times10^{-15}$ |
| | $\rightarrow ClOO + Cl$ | $3.0\times10^{-11}exp(-2450/T)$ | $1.66\times10^{-15}$ |
| | $\rightarrow OClO + Cl$ | $3.5\times10^{-13}exp(-1370/T)$ | $1.46\times10^{-15}$ |
| | $\rightarrow Cl_2O_2$ | $k_o= 1.6\times10^{-32}\times (T/300)^{-4.5}$<br>$k_\infty=2.0\times10^{-12} \times (T/300)^{-2.4}$ | $5.27\times10^{-13}$ |
| 13. | $ClO + NO \rightarrow Cl + NO_2$ | $6.4\times10^{-12}exp(220/T)$ | $1.54\times10^{-11}$ |
| 14. | $ClO + NO_2 \rightarrow ClONO_2$ | $k_o= 1.8\times10^{-31}\times (T/300)^{-3.4}$<br>$k_\infty=1.5\times10^{-11} \times (T/300)^{-1.9}$ | $4.29\times10^{-12}$ |
| 15. | $ClO + BrO \rightarrow Br + OClO$ | $9.5\times10^{-13}exp(550/T)$ | $8.57\times10^{-12}$ |
| | $\rightarrow Br + ClOO$ | $2.3\times10^{-12}exp(260/T)$ | $6.51\times10^{-12}$ |
| | $\rightarrow BrCl + O_2$ | $4.1\times10^{-13}exp(290/T)$ | $1.31\times10^{-12}$ |
| 16. | $Cl_2 + OH \rightarrow HOCl + Cl$ | $1.4\times10^{-12}exp(-900/T)$ | $3.83\times10^{-14}$ |
| 17. | $HOCl + OH \rightarrow ClO + H_2O$ | $3.0\times10^{-12}exp(-500/T)$ | $4.06\times10^{-13}$ |
| 18. | $HCl + OH \rightarrow Cl + H_2O$ | $2.6\times10^{-12}exp(-350/T)$ | $6.41\times10^{-13}$ |
| | Photolysis reactions | | |
| 19. | $Cl + h\nu \rightarrow 2Cl$ | $^*2.2\times10^{-3}$ | |
| 20. | $ClO + h\nu \rightarrow Cl + O$ | $^*3.8\times10^{-5}$ | |
| 21. | $HOCl + h\nu \rightarrow Cl + OH$ | $^*2.6\times10^{-4}$ | |
| 22. | $ClONO_2 + h\nu \rightarrow Cl + NO_3$ | $^*3.1\times10^{-5}$ | |
| | $\rightarrow ClO + NO_2$ | $^*4.0\times10^{-6}$ | |
| | $BrCl + h\nu \rightarrow Br + Cl$ | $^*0.012$ | |
| | Heterogeneous reactions | Lifetime due to heterogeneous loss | |
| 22. | $HOCl + Cl^- + H^+ \xrightarrow{het} Cl_2 + H_2O$ | 15.3 min | |
| 23. | $HCl \xrightarrow{het} Cl^- + H^+$ | 0.4 hr | |

*Midday 11: 00 – 16: 00 average

Table 4.2 The typical input concentrations in the box model.

| Input species | Concentration | Sources |
|---|---|---|
| $O_3$ | 17 ppbv | Chemiluminescence observations |
| $CH_2O$ | 270 pptv | Tunable Diode Laser Spectroscopy observations |
| NO | 5 pptv | Chemiluminescence observations (exclude polluted periods when NO > 20 pptv) |
| $NO_2$ | 7 pptv | Chemiluminescence observations (exclude polluted periods when NO > 20 pptv) |
| $HO_2$/OH | $2.0\times10^8$ molec.cm$^{-3}$ /$1.7\times10^6$ molec.cm$^{-3}$ (daytime) | CIMS observations |
| $CH_4$ | 1.83 ppm | Global average |
| $C_2H_6$ | 2.1 ppbv | canister observations |
| $C_3H_8$ | 811 pptv | canister observations |
| n-$C_4H_{10}$ | 486 pptv | canister observations |
| $CH_3CHO$ | 90 pptv | TOGA VOC analyzer |
| $CH_3OH$ | 667 pptv | TOGA VOC analyzer |
| $CH_3C(O)CH_3$ | 1.1 ppbv | TOGA VOC analyzer |
| Aerosol surfaces | 56 um$^2$ cm$^{-3}$ | SMPS observations |

Daytime = 09 : 00-18:00

Loss rates of HOCl, HCl, and $Cl_2$ to heterogeneous surfaces ($k_{HOCl}$, $k_{HCl}$, $k_{Cl2}$) are assumed to be the diffusion rates of the gas phase species to heterogeneous surfaces. The calculation method is described in Chapter 3. The heterogeneous surfaces likely include aerosol surface and snow surface. Because the surface area of snow is not well determined, aerosol surface is used and the heterogeneous loss rates may be underestimated. The mass accommodation coefficients of HOCl, HCl, and $Cl_2$ are 0.3 [Pratte and Rossi, 2006], 0.18 [Fluckiger and Rossi, 2003; Robinson et al., 1998], and 0.02 [Hu et al., 1995], respectively. The gas phase reaction rate constants are obtained from NASA Jet Propulsion Laboratory compilation [Sander et al., 2006] and IUPAC compilation [Atkinson et al., 2004]. The photolysis rates are derived from the Actinic flux measurements in the campaign.

### 4.2.3 HCl predictions

HCl is simulated with constraints from $Cl_2$ and other measurements. Cl atoms are calculated via Eqn. 4.2 with steady-state assumption. The concentrations of $Cl_2$, ClO, NO, $O_3$, OH, $HO_2$, RH, and aldehyde (RCHO) are from the measurements in the campaign. The ClO radicals were measured by the flowing chemical reaction method [Stephens et al., 2011].

$$[Cl]_{pred} = \frac{J_{Cl2}[Cl_2] + J_{ClO}[ClO] + k_1[ClO]^2 + k_2[ClO][NO] + k_3[ClO][OH] + k_4[Cl_2][OH]}{\sum k[RH] + \sum k'[RCHO] + k_5[O_3] + k_6[HO_2]} \quad \text{Eqn 4.2}$$

$$[HCl]_{pred} = \frac{(\sum k[RH] + \sum k'[RCHO])[Cl]_{pred}}{k_{HCl}} \quad \text{Eqn 4.3}$$

HCl is also assumed to be in steady-state, with an average lifetime of 0.4 hour due to loss on aerosol surfaces. $k_{HCl}$ is the diffusion rate of HCl to aerosol surfaces. The

accommodation coefficient of HCl is assumed to be 0.18 [Fluckiger and Rossi, 2003]. The reaction rate constants are also from Jet Propulsion Laboratory compilation [Sander et al., 2006].

### 4.2.4 ClO measurements and predictions

Sum of chlorine radicals ($ClO_x$ = ClO + Cl) were measured by flowing chemical reaction method, which quantitatively converts reactive chlorine radicals to a stable halogenated acetone product using a reactive alkene as halogen atom trap [Stephens et al., 2011] in the same campaign. Because Cl concentrations ($10^5$ atoms $cm^{-3}$) are much lower than ClO (pptv), the observed $ClO_x$ concentrations are assumed to be the concentrations of ClO. ClO concentrations can be calculated by eqn. 4.4 constrained to $Cl_2$ and other measurements.

$$k_1[Cl][O_3] = k_{12}[ClO]^2 + J_{ClO}[ClO] + k_{11}[ClO][HO_2] + k_{24}[BrO][ClO] + k_{13}[ClO][NO] + k_{25}[ClO][NO_2] \quad \text{Eqn 4.4}$$

### 4.2.5 Back trajectories footprint residence time

A FLEXPART Lagrangian particle dispersion model [Stohl et al., 2005] driven by windfields from the Weather Research and Forecasting (WRF) model [Fast and Easter, 2006] is used to simulate 2-day backward transport history of the air masses arriving at the measurement site (71° 17' 26" N, 156° 47' 19" W Barrow, Alaska). The WRF (V3.3) model was constrained by Climate Forecast System Reanalysis (CFSR) products from National Centers for Environmental Prediction (NCEP) (http://cfs.ncep.noaa.gov/cfsr/)

and the output windfield from the WRF (V3.3) model has a resolution of 36 km × 36 km in the horizontal and 46 layers from the surface to 10hpa in the vertical. The FLEXPART model shares the same horizontal and vertical resolution as WRF, and was run in the backward mode to calculate retroplumes every hour [Cooper et al., 2005, 2010; Stohl et al., 2003]. Each retroplume consisting of 5000 particles released from a 4 km × 4 km × 400 m volume box located at the measurement location. For each retroplume, a 3-D field of 24-hour integrated residence time in unit of second was output every day from FLEXPART and was further integrated over a 2-day period in each of the model grid. In order to identify the source regions of the $Cl_2$, a 2-D horizontal field of vertically integrated residence time from the surface to 400m, called footprint residence time (FRT) [Cooper et al., 2005; Stohl et al., 2003], for each retroplume is calculated. Non-zero FRT at a certain grid (location) indicates the overpassing of the air masses within the lowest 400 m in the vertical during the past 2 days [Cooper et al., 2005, 2010; Stohl et al., 2003].

QuikSCAT sea ice backscatter coefficient is used as a proxy of sea ice age [Kwok, 2004; Simpson et al., 2007b] (Figure 4.4a). QuikSCAT sea ice backscatter coefficient data were downloaded from http://www.ifremer.fr/. The data have a spatial resolution of 12.5 km × 12.5 km and temporal resolution of 1 day, and range from 0 to 250. Higher backscatter coefficient represents more multi-year sea ice fraction of the sea ice.

## 4.3 Results and discussion

### 4.3.1 $Cl_2$ measurements and predictions

High levels of $Cl_2$ were observed with maximum mixing ratios of ~400 pptv (Figure 4.2). The observed $Cl_2$ has maximum concentrations in the early morning or late afternoon, with no significant concentrations at night. Both the diurnal pattern and magnitude of the observed $Cl_2$ were surprising as $Cl_2$ rapidly photolyzes during the day [e.g. Vogt et al., 1996]. For this reason the $Cl_2$ observations were scrutinized for potential problems. Excellent isotope ratios of the detected masses (mass 197 and 199 amu) (see section 4.2.1) confirmed that the detected species contained two chlorine atoms. Measurements of hypobromous acid (HOBr), which is readily converted to $Br_2$ on the inlet surfaces [Neuman et al., 2010], by the same instrument during the campaign [Liao et al., 2011] demonstrated that the inlet of the CIMS was compatible with efficiently sampling reactive gases. Significant interferences in $Cl_2$ measurements due to conversion of HOCl on inlet are also unlikely as predicted levels of HOCl and ClO are much lower than the observed $Cl_2$ (Figure 4.3). The modeled HCl and ClO levels constrained by observed $Cl_2$ and other measurements were consistent with the detected HCl and ClO concentrations (see section 4.3.2). The calibration of the CIMS was also confirmed by comparison of BrO observations by the CIMS and long path differential optical absorption spectrometer (LPDOAS) during the Barrow campaign.

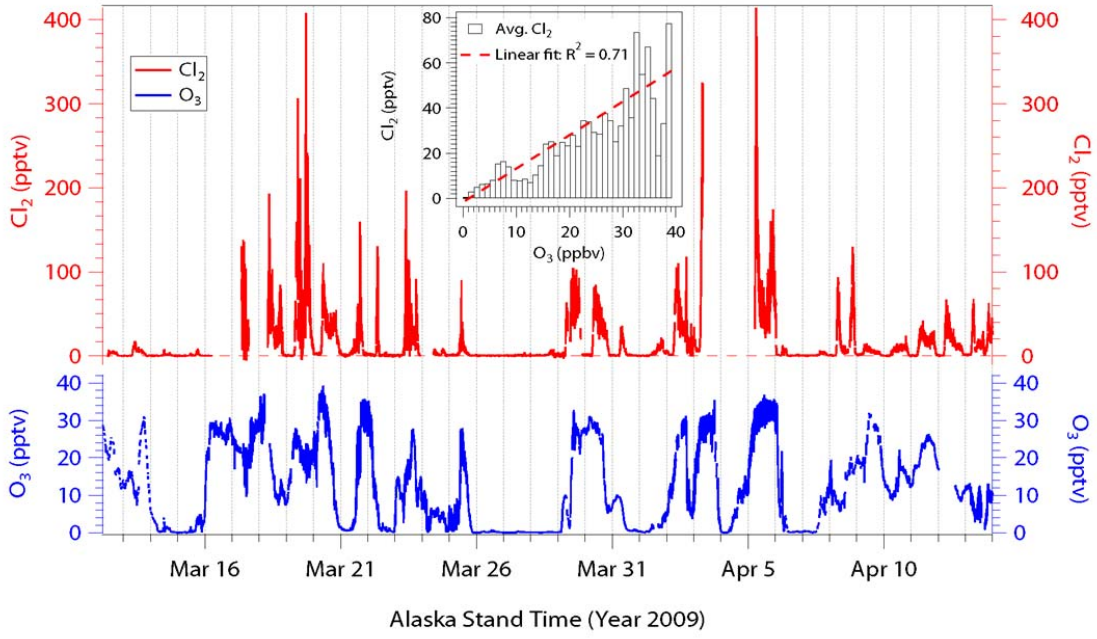


Figure 4.2 Time series of the observations of $Cl_2$ and $O_3$. Inset: The correlation between average $Cl_2$ and $O_3$ concentrations with a correlation coefficient $R^2 = 0.71$.

The sources and formation mechanisms of the observed $Cl_2$ are not determined, but $O_3$ and sunlight are likely required. The concentrations of $Cl_2$ are well correlated with $O_3$ (Figure 4.2). The average diurnal profile of $Cl_2$ accounted for the days when average daytime $Cl_2$ was higher than 10 pptv is shown in Figure 4.3 (red). The corresponding noontime production rate of the $Cl_2$ is estimated to be $2.0 \times 10^6$ molec $cm^{-3}$ $s^{-1}$ on average (orange), and had a diurnal profile similar to the photolysis rate of $Cl_2$ (Figure 4.3). This corresponds to a large $Cl_2$ flux of $8 \times 10^8$ molec $cm^{-2}$ $s^{-1}$ to the atmosphere around noon assuming a noontime boundary layer height of 400 m, which was estimated from the vertical temperature profiles from ozonesonde measurements. The average $Cl_2$ diurnal profile had a local minimum at noon, similar to nitrogen oxide (NO) from snow emission

at Summit, Greenland [Thomas et al., 2011]. This indicates that maximum boundary layer height around noon may contribute to $Cl_2$ noontime local minimum, similar to what it does to NO at Summit, Greenland based on 1D model prediction [Thomas et al., 2011]. The Lab experiments and model simulations [e.g. Oum et al., 1998; Knipping et *al.*, 2000] indicated that $Cl_2$ can be formed from photolysis of ozone and aqueous sea-salt particles. However, the UV radiation flux, ozone concentrations, and sea-salt particles surface areas in these experiments and simulations are much higher than in the Arctic environment [Oum et al., 1998; Knipping et al., 2000].

Average diurnal profiles of Cl, ClO, HOCl and HCl are simulated based on the known chlorine chemistry with constrained to $Cl_2$ observations (Figure 4.3). The modeled Cl, ClO, HOCl and HCl reached maximum concentrations near local noon. On average about $2.5 \times 10^5$ atom $cm^{-3}$ Cl atoms were predicted at local noon. The dominant chlorine species in the daytime is HCl. The concentrations of HOCl are similar to ClO but much less (4–5 times less) than $Cl_2$. This is consistent with the fact that Cl atoms not only react with $O_3$ but also efficiently react with methane and other VOCs, and that most Cl atoms are partitioned to HCl instead of ClO or HOCl. The ratios of predicted ClO to HOCl are similar to that of BrO to HOBr from either observations or predictions [Liao et al., 2011c].

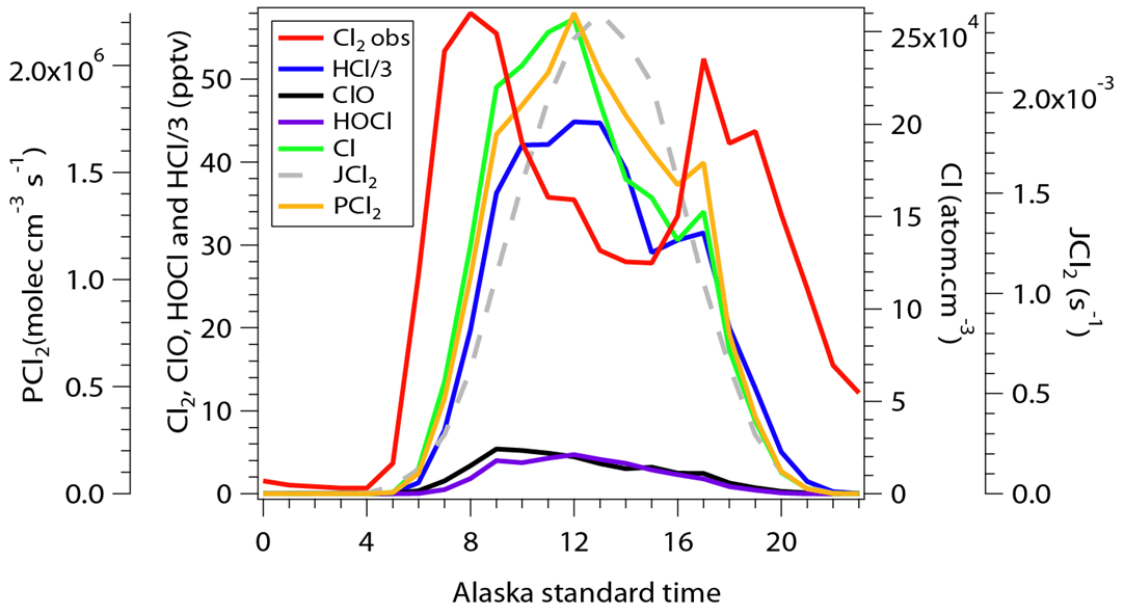


Figure 4.3 Observed average diurnal profiles of $Cl_2$ (red), $Cl_2$ photolysis rate (dashed grey), estimated average $Cl_2$ production rate ($J_{Cl2}$×$Cl_2$) (orange), and model-predicted average diurnal profiles of HCl (blue), ClO (black), HOCl (purple), and Cl atoms (green).

The average total gas phase chlorine is estimated to be 250 pptv from the observed $Cl_2$ and predicted HCl, HOCl, ClO, and Cl atoms. Assuming that the gas phase chlorine species were well mixed in the boundary layer of 400 m, 250 pptv total gas phase chlorine corresponds to 5 $\times 10^{-6}$ mol/m$^2$ chlorine. Surface snow chlorine ($Cl^-$) was measured to be 185 μM on average during the campaign. This corresponds to $1.85 \times 10^{-2}$ mol/m$^2$ $Cl^-$ the top 10 cm snow surface can provide. As no aerosol chemical mass loading was measured during the campaign, the particle phase $Cl^-$ is estimated to be 40 ng/m$^3$ based on several years' Arctic aerosol measurements in March and April [*Sturges and Barrie*, 1987]. This estimated aerosol $Cl^-$ loading equals to 4.5 $\times 10^{-7}$ mol/m$^2$ $Cl^-$ aerosols can provide within 400 m boundary layer. This comparison indicates that

particle phase $Cl^-$ is unlikely large enough to sustain the total gas phase chlorine and surface snow is likely to be the main source of the observed $Cl_2$.

Back trajectories from a Lagrangain particle dispersion model (Flexpart) [Stohl et al., 2005] driven by windfields from the Weather Research and Forecasting (WRF) are used to investigate the source of high levels of $Cl_2$. Detailed modeling information is provided in section 4.2.4. QuikSCAT sea ice backscatter coefficient is used as a proxy of sea ice age [Kwok, 2004; Simpson et al., 2007b] (Figure 4.4a). Footprint residence time of 2-day back trajectories for high daytime $Cl_2$ levels (91-100 percentiles) and low daytime $Cl_2$ levels (0-10 percentiles) are shown in Figure 4.4b and 4.4c, respectively. The air masses arriving at Barrow with high levels of $Cl_2$ observed had higher residence time (red) within the lowest 400 m near the surface around Barrow and to the northeast of Barrow, where the closest multiple year sea ice was present (Figure 4.4a). The air masses arriving at Barrow with low levels of $Cl_2$ observed likely spent more time above the boundary layer around Barrow and had more residence time further away to the north and northwest of Barrow in the boundary layer. This supports the idea that $Cl_2$ is likely produced or recycled on the snow suface. The lack of $Cl_2$ at night also indicates that $Cl_2$ likely reacts with the snow surface after deposition. The lag in the $Cl_2$ diurnal profile after sunset supports that $Cl_2$ has an extra loss like deposition besides photolysis.

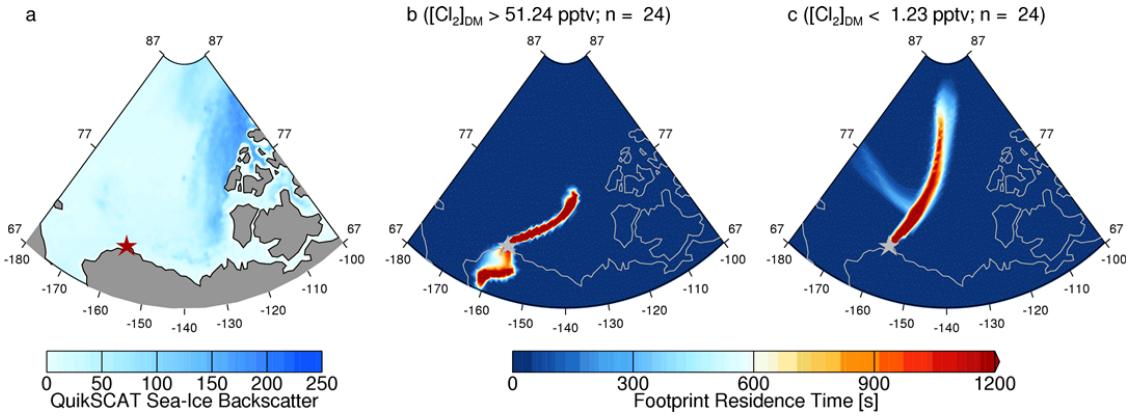


Figure 4.4 (a). QuikSCAT sea ice backscatter coefficient map. The sea ice consisting more multi-year fraction has higher sea ice backscatter coefficient (blue). (b). Average footprint residence time of two-day back trajectories for the days with high daytime $Cl_2$ cases (90-99 percentiles). Each day has 12 back trajectories. The number of back trajectories in the high $Cl_2$ cases is n=24. (c). Average footprint residence time of two-day back trajectories for the days with low daytime $Cl_2$ cases (0-10 percentiles). Each day has 12 back trajectories. The number of back trajectories in the low $Cl_2$ cases is n=24.

High levels of the chlorine atoms produced from photolysis of $Cl_2$ play a significant role in methane oxidation, $O_3$ loss, and mercury oxidation in Barrow (Figure 4.5). On average the oxidation rates of $CH_4$ by Cl atoms (60%) are higher than that by OH radicals (40%). Cl atom is the dominant oxidant (82%) of $CH_4$ during high $Cl_2$ periods (> 100 pptv). If high levels of $Cl_2$ are ubiquitous in the Arctic, they can play an important role in the $CH_4$ budget. On average ClO plays a smaller role (21%) than BrO (73%) in catalyzing ozone depletion in the Arctic. However, ClO can contribute to 41% of $O_3$ loss during high $Cl_2$ periods. Cl atoms have a smaller impact on mercury oxidation when the lowest published reaction rate constant of $Hg^0$ and Cl is used [Donohoue et al., 2005]. However, Cl atoms can still account for 13% of mercury oxidation during high $Cl_2$ periods. The estimated impact of Cl on mercury oxidation will be enhanced if larger reaction rate coefficients are used [Stephens et al., 2011].

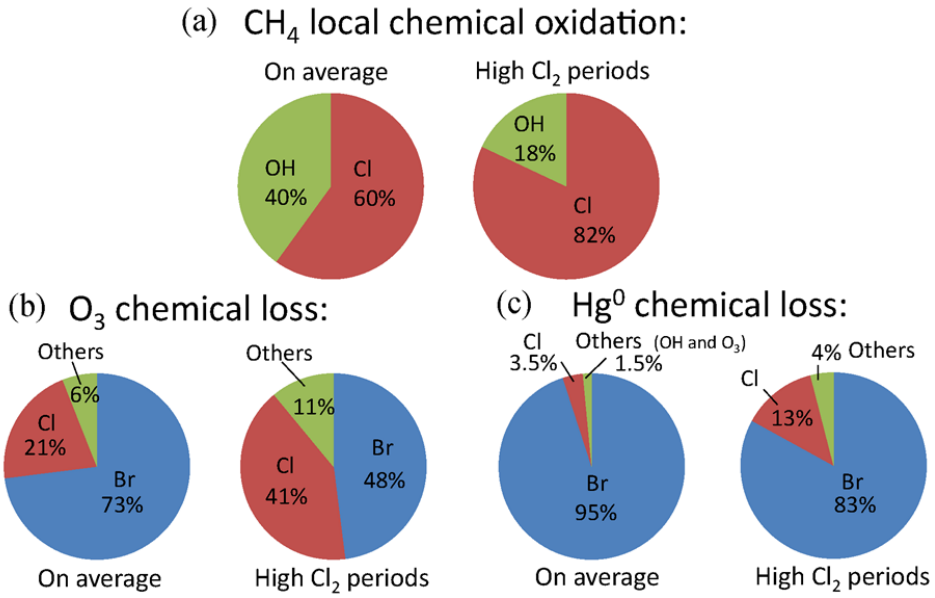


Figure 4.5 The impact of chlorine radicals compared to OH, bromine radicals, and other chemical species on methane oxidation (a), ozone loss (b), and mercury oxidation (c), on average (left) and during high $Cl_2$ periods ($Cl_2$ > 100 pptv) (right). The measurements of bromine species are provided in Liao et al. [2011c].

### 4.3.2 HCl measurements and predictions

The predicted HCl from steady-state calculation (section 4.2.3) reasonably agreed ($R^2$ = 0.69) with the observed HCl (Figure 4.6). The diffusion rate of HCl to aerosol surfaces is assumed to be the loss rate of HCl to hetereogeneous surfaces. In the remote marine boundary layer, significant HCl is not produced from acid displacement because the acidity is insufficient to titrate all sea salt alkanility [Erickson et al., 1999]. These indicate that the observed $Cl_2$ levels were generally consistent with the measured HCl concentrations.

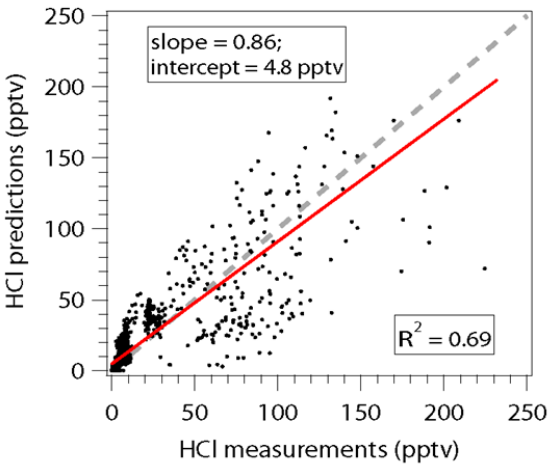


Figure 4.6 Predicted HCl plotted versus observed HCl. Gray dashed is the 1: 1 line. Red line represents the equally weighted bivariate regression. Correlation coefficient $R^2$ = 0.69.

### 4.3.3 ClO measurements and predictions

Up to ~10 pptv ClO was observed. ClO concentrations can be calculated by eqn. 4.4 constrained to $Cl_2$ and other measurements shown in section 4.2.4. The time series plot and the correlation plot between modeled and observed ClO when ($Cl_2$ > 1pptv) are shown in Fig. 4.7. The calculated ClO had a similar magnitude to the observed ClO although the ClO measurements are scattered.

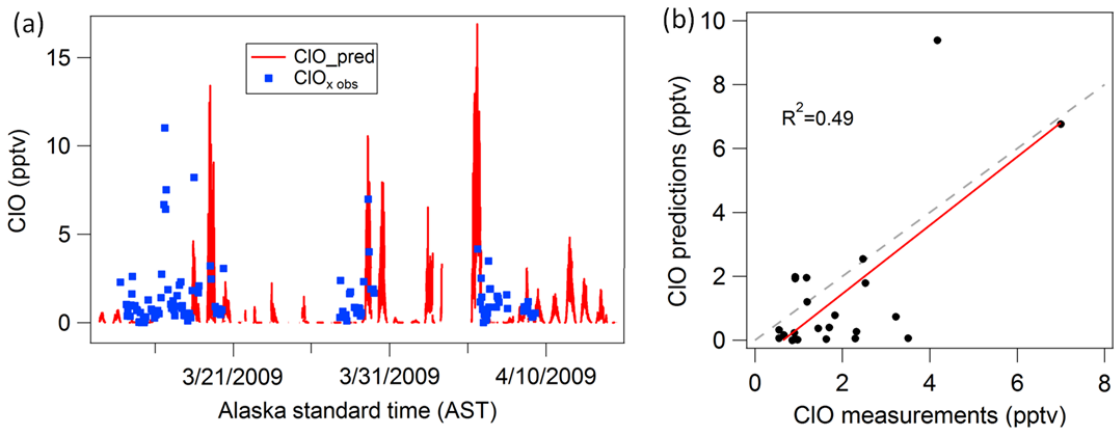


Figure 4.7 (a) Time series of predicted and observed ClO. (b) Predicted ClO plotted versus observed ClO when $Cl_2$ >1 pptv. Gray dashed is the 1: 1 line. Red line represents linear regression. Correlation coefficient $R^2$ = 0.49.

### 4.3.4 BrCl measurements

Much lower BrCl concentrations compared to $Cl_2$ were observed with concentrations above detection limit in the early morning or late afternoon. The BrCl concentrations have no clear correlation with other bromine species (BrO, HOBr, and $Br_2$). On the other hand, BrCl was detected only when $Cl_2$ was observed. The BrCl measurements are plotted against $Cl_2$ measurements divided by $J_{BrCl}$ when $J_{BrCl} > 1.5\times10^{-3}$ $s^{-1}$ (Figure 4.8). BrCl measurements were well correlated with $Cl_2/J_{BrCl}$ ($R^2$ =0.70) when BrCl was detected. The formation of BrCl from gas phase reaction of ClO with BrO was excluded due to the low reaction rate to synthesize BrCl. This indicates that BrCl is likely a product from heterogeneous reaction of chlorine compounds (e.g. $Cl_2$, HOCl, or HCl) and photolysis of BrCl is the dominant loss rate of BrCl in the daytime at Barrow. This implication is supported by the finding from Huff and Abbat [2000] that BrCl is formed from uptake of $Cl_2$ or HOCl on bromide-ice film. Bromide in aqueous phase then can be activated through the formation of BrCl.

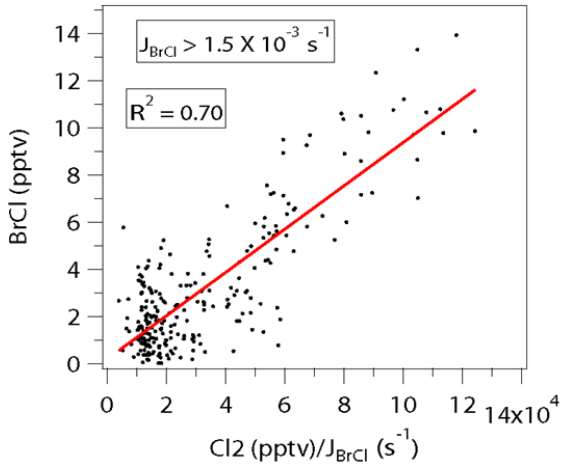


Figure 4.8 Observed BrCl plotted versus observed $Cl_2$ divided by $J_{BrCl}$ when $J_{BrCl}$ $>1.5\times10^{-3}$ $s^{-1}$. Red line represents the linear regression. Correlation coefficient $R^2 = 0.70$.

## 4.4 Conclusions

This study discovered unexpectedly high levels of $Cl_2$ at Barrow, AK. The average diurnal pattern of high levels of $Cl_2$ can be reasonably predicted by a time dependent model with inclusion of a $Cl_2$ source as a function of sun light. Back trajectories analysis indicates that surface covered by snow or sea ice especially multiple year sea ice is the source of $Cl_2$. The observed $Cl_2$ concentrations were generally consistent with the measured HCl levels. Much less BrCl was also detected and likely produced from heterogeneous reactions of chlorine compounds. More direct measurements of speciated chlorine especially $Cl_2$ and HOCl are needed to investigate if high levels of chlorine species are widespread in the Arctic. Lab experiments are also needed to explore the $Cl_2$ formation mechanisms and help evaluate the trend of the high levels of active chlorine species in the Arctic.

# CHAPTER 5

# OBSERVATIONS OF HYDROXYL AND PEROXYL RADICALS AND THE IMPACT OF BRO AT SUMMIT, GREENLAND IN 2007 AND 2008

## 5.1 Introduction

Summit, Greenland (72°34' N, 38°29' W, alt = 3.3 km) is located in the middle of the Greenland Ice Sheet and has been the site of a series of scientific studies beginning with ice coring in the 1980s [e.g. Hammer et al., 1980; Mayewski and Bender, 1995]. In more recent years, the interaction between photochemically active species in the snowpack and the overlying atmosphere has been studied in detail at Summit and other polar stations [e.g. Dibb and Jaffrezo, 1997; Grannas et al., 2007; Jones et al., 2008; Davis et al., 2001; Huey et al., 2004]. Elevated levels of species emitted from surface snow such as nitric oxide (NO), formaldehyde ($CH_2O$), and hydrogen peroxide ($H_2O_2$) have been observed over sunlit snow in a series of campaigns [Dibb et al., 2002 and 2004; Honrath et al., 1999 and 2002; Hutterli et al., 1999, 2001 and 2004; Davis et al., 2001; Slusher et al., 2002; Helmig et al., 2008]. Snowpack emissions of radical precursors (nitrous acid (HONO), $H_2O_2$, and $CH_2O$) and $NO_x$ (NO + $NO_2$) have the potential to significantly enhance $HO_x$ (hydroxyl (OH) + hydroperoxyl ($HO_2$) radicals) photochemistry in these locations [e.g. Yang et al., 2002; Chen et al., 2001].

The OH and peroxy radicals ($HO_2$+$RO_2$) have been measured in a few polar locations and the concentrations vary based on the radical sources as well as environmental conditions. The daytime mean value of OH observed at Palmer station (64°46' S, 64°3.0' W) in Antarctica was $3 \times 10^5$ molec.cm$^{-3}$ in austral summer [Jefferson et al., 1998]. The low OH levels were found to be consistent with the high solar zenith angle, extensive cloud coverage, no snow coverage, and low $NO_x$ levels (typically near detection limits of 2 – 4 pptv) [Jefferson et al., 1998]. OH concentrations observed at South Pole were unexpectedly high, with an average value of 2.0 (±0.9)$\times 10^6$ molecule cm$^{-3}$ in November and December from three field campaigns ISCAT 98, ISCAT 00 and ANTCI 03 [Mauldin et al., 2001, 2004 and 2010; Grannas et al., 2007]. The high OH levels at South Pole were due to low boundary layer height and snowpack emissions that gave high levels of $NO_x$ and to a lesser extent formaldehyde [Davis et al., 2001; Hutterli et al., 2004]. A photochemical model constrained to $CH_2O$ and $H_2O_2$ measurements predicted OH levels with a median modeled to observed (M/O) ratio of 1.27 [Chen et al., 2004]. However, the M/O ratio for OH was found to vary with NO levels at South Pole (Chen et al., 2001 and 2004). The model over predicted OH significantly at low NO (NO < 50 pptv; M/O > 1.5) and high NO (NO > 150 pptv; M/O = 1.5) levels but agreed better at moderate levels of NO [Chen et al., 2004]. Sjostedt et al. (2007) measured OH (mean $6.3 \times 10^6$ molec.cm$^{-3}$) and $HO_2$+$RO_2$ (mean $2.8 \times 10^8$ molec.cm$^{-3}$) levels at Summit, Greenland during summer 2003. The observed $HO_2$+$RO_2$ levels agreed well with the model predictions, although the measured OH levels were elevated compared to the predictions [Sjostedt et al., 2007; Chen et al., 2007]. Sjostedt et al. [2007] suggested that halogen may be present at Summit, perturbing the $HO_x$ cycling and enhancing OH levels.

In contrast, a later study at Halley Bay, Antarctica (75° 35' S, 26° 19' W) found average OH levels of $3.9 \times 10^5$ molec $cm^{-3}$ in February with typical maximum (local noontime) levels of $7.9 \times 10^5$ molec $cm^{-3}$ [Bloss et al., 2007; Bloss et al., 2010]. The OH levels at Halley Bay were slightly higher than measured at Palmer station in the same season of the year but significantly lower than observed at South Pole. The low levels of OH were surprising as mean diurnal NO levels of up to ~14 pptv and significant iodine monoxide (IO) and bromine oxide (BrO) levels of up to ~7 pptv and ~ 9 pptv were observed. A photochemical box model including halogen reactions significantly over predicted observed levels of OH and $HO_2$, although the model well predicted the mean levels and diurnal patterns of $NO_x$ (NO and $NO_2$) [Bloss et al. 2007 and 2010]. The mean daily maximum M/O ratio of OH was 3.8 and of $HO_2$ was 2.8. The mean observed $HO_2$ to OH ratio of 46 was in good agreement with the mean predicted value of 44 from the model considering bromine and iodine chemistry, and no elevated OH was observed.

Prior to the GSHOX campaign, there was only indirect evidence that BrO may exist at Summit, Greenland. Although the overall reservoir of bromine at Summit is much less than in the coastal Arctic where ozone depletion events (ODEs) are typically observed, vertical profiles of ozone obtained from balloon borne sensors have demonstrated that ozone in the boundary layer is consistently depleted relative to the air above [Helmig et al., 2002]. However, the reaction of NO (~20 pptv) and $RO_2$ (~$10^8$ molec.$cm^{-3}$) in the boundary layer at Summit should give a local ozone production of ~2 ppbv/day [Sjostedt et al, 2007]. This type of ozone production is evident in the $NO_x$ ($NO+NO_2$) rich South Pole boundary layer [Crawford et al, 2001] where boundary layer ozone is elevated relative to the air above [Helmig et al., 2002]. In addition, mercury

oxidation in snow has been observed at Summit, Greenland [Faïn et al., 2008, Brooks et al., 2011]. As Br + $Hg^0$ (GEM) → $Hg^{2+}$ (RGM) is the only well established reaction that can initiate such rapid conversion of gaseous element mercury (GEM) to reactive gaseous mercury (RGM) [Ariya et al., 2002; Donohoue et al., 2006], depleted GEM and elevated RGM may be a signature of active bromine chemistry as RGM is a relatively short lived species [Steffen et al., 2008].

High levels (up to 30–40 pptv) of BrO are typically found in the polar marine boundary layer near large sources of halides during ODEs [Tuckermann et al., 1997; Hausmann and Platt, 1994; Saiz-lopez et al., 2007; Liao et al, 2011a]. However, significant levels of BrO have been observed in a variety of other marine locations. For example, BrO was observed in the tropical marine boundary layer within the Cape Verde archipelago by Read et al. (2008) with an average daytime level of 2.5 pptv. Up to ~7 pptv of BrO was observed in the mid-latitude marine boundary layer at Roscoff, France (48.7˚N, 4.0˚W) [Mahajan et al., 2009] and at the Mace Head Atmospheric Research Station, Ireland (53.33˚N, 9.90˚W) [Saiz-lopez et al., 2006].

To investigate the hypothesis that BrO is present at Summit and that it impacts $HO_x$ photochemistry, a suite of instruments were used to measure OH, $HO_2$+$RO_2$, BrO and other species at Summit, Greenland in spring 2007 and summer 2008. The observations of OH and $HO_2$+$RO_2$, and their comparison to photochemical models are presented in this chapter. The BrO observations and the associated snowpack chemistry are discussed by Stutz et al. [2011] and Thomas et al. [2011], respectively.

## 5.2 Methods

A comprehensive collection of instruments were used at Summit, Greenland during May – June 2007 and June – July 2008 to measure trace gases and radicals, aerosols, actinic flux, and meteorological parameters. Table 5.1 provides a summary of the measurements during the campaign. The details of measurement techniques not specifically summarized are presented in the references in Table 5.1. Most of the measurements were located in a satellite camp ~1 km to the south of the main station. The layout of the experiment is shown in Figure 5.1.

Table 5.1 Summary of the measurements at Summit, Greenland 2007-2008.

| Species and parameters | Instrument | Uncertainty | Institution | Reference |
|---|---|---|---|---|
| $O_3$ | UV absorption ozone analyzer | <±5% | Ga. Tech | |
| NO | Chemiluminesent gas analyzer | ±10% | Ga. Tech | Ryerson et al. (2000) |
| CO | Canister/GC | <±5% | UCI | Swanson et al. (2002) |
| $CH_4$ | Canister/GC | <±5% | UCI | Swanson et al. (2002) |
| NMHC | Canister/GC | <±5% | UCI | Swanson et al. (2002) |
| OH | CIMS | ±30% | Ga. Tech | Sjostedt et al. (2007) |
| $HO_2 + RO_2$ | CIMS | ±35% | Ga. Tech | Sjostedt et al. (2007) |
| BrO | CIMS | ±30%-36% | Ga. Tech | Liao et al. (2011a) |
| BrO | DOAS | ±10% | UCLA | Stutz et al. (2011) |
| SMPS_N | SMPS/CPC | ±10% | UNH | Ziemba et al. (2010) |
| SMPS_S | SMPS/CPC | ±10% | UNH | Ziemba et al. (2010) |
| GEM | Tekran | ±2% | NOAA | Brooks et al. (2011) |
| RGM | Tekran | ±5% | NOAA | Brooks et al. (2011) |
| FPM | Tekran | ±5% | NOAA | Brooks et al. (2011) |
| $HNO_3$ | Mist Chamber | ±15%-20% | UNH | Dibb et al. (1998) |
| Soluble Bromine | Mist Chamber | ±15%-20% | UNH | Dibb et al. (1998) |
| HONO | Mist Chamber | ±15%-20% | UNH | Dibb et al. (1998) |
| Actinic Flux | SAFS | ±10% | U. Houston | Shetter and Muller (1999) |
| Temperature | F-Thermocouples | ±0.5°C | U. Houston | Haman et al. (2011) |
| WS/WD | AWS/Digital compass | | U. Houston | Haman et al. (2011) |

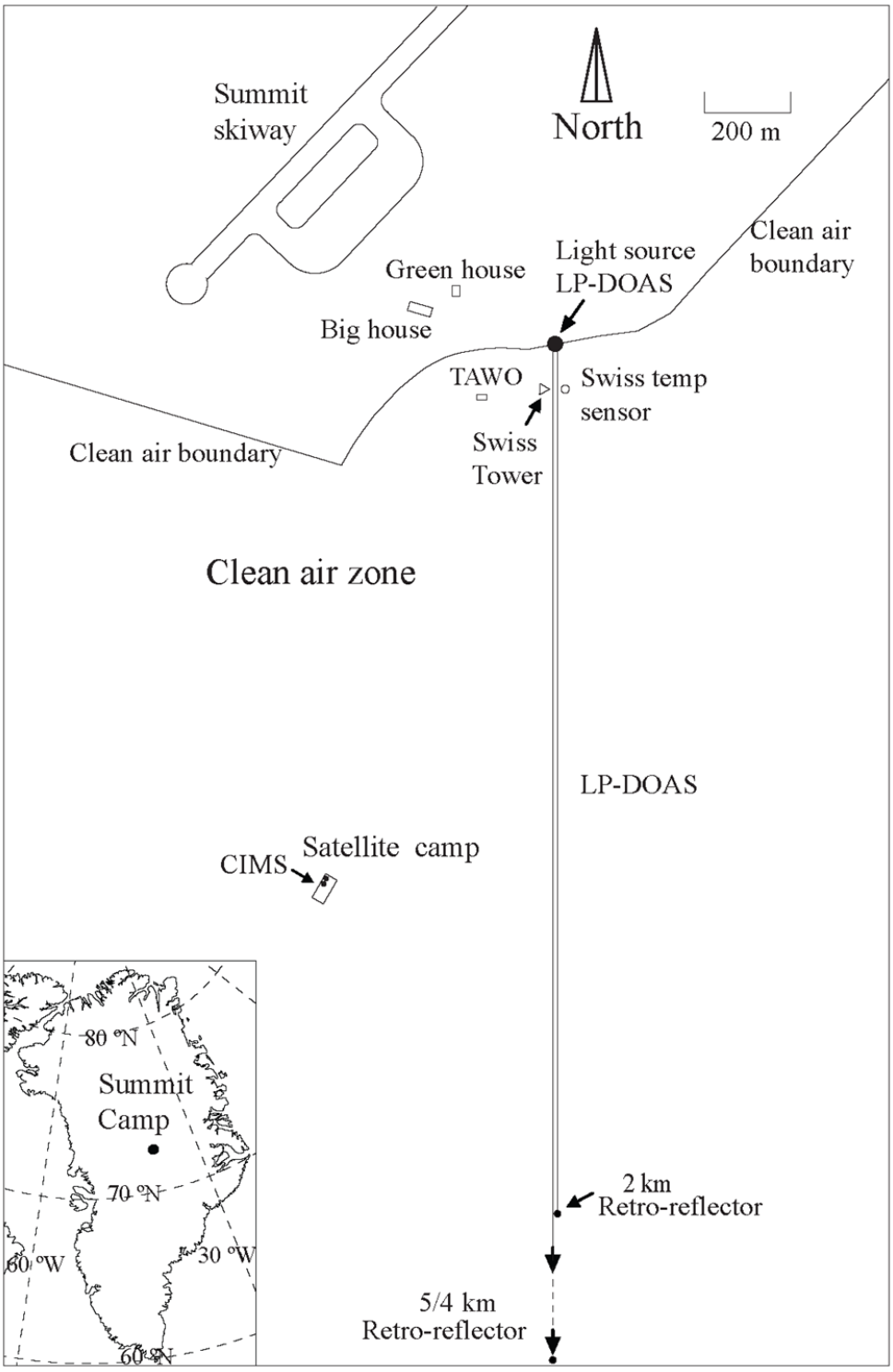


Figure 5.1 The layout of the CIMS and LP-DOAS instruments in the Summit campaign.

### 5.2.1 $HO_x$ measurements by CIMS

The chemical ionization mass spectrometry (CIMS) instrument to measure $HO_x$ (OH and sum of $HO_2$ + $RO_2$) is nearly identical to that used to measure $HO_x$ in 2003 [Sjostedt et al., 2007; Sjostedt, 2006]. The basic methods are based on the work of Tanner et al. [1997]. The CIMS was calibrated for OH and $HO_2$. Because many of the simple $RO_2$ species (e.g. $CH_3O_2$) are efficiently converted to $HO_2$ by this method [Edwards et al., 2003], we assumed that the sensitivities for $RO_2$ were the same as for $HO_2$. The CIMS was located in the satellite camp (Figure 5.1) and the inlet was about 1.5 m above the snow surface. The dominant uncertainty in the OH and $HO_2$+$RO_2$ measurements is the accuracy of the calibration source [Sjostedt et al., 2007]. The combined uncertainties are estimated to be ~30% for OH measurements and ~35% for $HO_2$+$RO_2$ measurements. The calibration standards for both OH and $HO_2$ measurements are produced from the photolysis of ambient water vapor, consequently, the uncertainty in the ratio of observed OH to $HO_2$+$RO_2$ is smaller than the absolute uncertainties.

### 5.2.2 BrO measurements by CIMS

The CIMS used to measure BrO levels at Summit is essentially identical to the low pressure CIMS systems used to measure halogens on the NASA DC-8 and NOAA P3 aircrafts during the ARCTAS and ARCPAC campaigns [Neuman et al., 2010], and at Barrow, Alaska during the OASIS 2009 campaign [Liao et al., 2011a]. The details of the instrument and air sampling inlet are described in [Liao et al., 2011a] and in chapter 2 and only significant differences are described here.

$SF_6^-$ was used as a reagent ion to ionize BrO and other species such as $SO_2$.

$$SO_2 + SF_6^- \rightarrow F_2SO_2^- + SF_4 \qquad \text{R5.1}$$

$$BrO + SF_6^- \rightarrow BrO^- + SF_6 \qquad \text{R5.2}$$

$$Br_2 + SF_6^- \rightarrow Br_2^- + SF_6 \qquad \text{R5.3}$$

The charge transfer reaction of $SF_6^-$ with BrO R5.2 was observed for the first time as part of this work. The rate constant for this reaction was determined relative to that of $SF_6^-$ with $Br_2$ R5.3 [Streit, 1982]. BrO was synthesized from the reaction of O ($^3$P) with $Br_2$ in excess ozone as described in Liao et al. [2011a]. The ratio of the rate constant for R5.3 to R5.2 was determined to be 1.0 ± 25% in the laboratory. The rate constant for R5.2 derived from this work is $(5 \pm 2) \times 10^{-10}$ cm$^3$ molec$^{-1}$ s$^{-1}$.

$SO_2$ was used as our primary calibration gas for determining the sensitivity of the CIMS system in the field [Kim et al., 2007; Slusher et al., 2001] and as a proxy to track the sensitivity of BrO. The ratio of the sensitivity of BrO to that of $SO_2$ was determined in the laboratory after the campaign as a function of dew point (dewpt). The average sensitivity of $SO_2$ was ~4 Hz/pptv in 2007 and ~60 Hz/pptv in 2008 summit campaign. The sensitivity ratio of $SO_2$ to BrO was determined as Eqn. 5.1

$$\frac{SO_2}{BrO} = \begin{cases} 0.76\text{-}0.096 \times \text{dewpt}\text{-}0.00154 \times \text{dewpt}^2 & (\text{dewpt} > -35^0\text{C}) \\ 2.2 & (\text{dewpt} < -35^0\text{C}) \end{cases}.$$

eqn. 5.1

The background signal level of BrO during the 2007 Summit campaign was determined by periodically scrubbing the sampled air with an active carbon filter, similar to that used before for removal of $SO_2$, $HO_2NO_2$, and $HNO_3$. In 2008 the background was determined by using glass wool because it was found to effectively remove halogen species [Neuman et al., 2010].

The detection limits of BrO measurements are estimated to be ~1.8 pptv in 2007 and ~0.7 pptv in 2008. Considering the uncertainty in $SO_2$ standard concentration (~10%), the uncertainties in the sensitivity ratios between BrO and $Br_2$ (~25%) and between $Br_2$ and $SO_2$ (~5%), the total uncertainty in BrO measurements is estimated to be ~36%. The concentrations of BrO at Summit in spring 2007 and summer 2008 were often near the detection limits of both instruments (detection limit of LP DOAS = 0.5–2 pptv; detection limit of CIMS = ~1–2 pptv). Moreover, the measurements of BrO at Summit were the earliest applications of CIMS to measure ambient BrO. $SF_6^-$ was used as the reagent ion to detect BrO at that time. After these campaigns the more selective reagent ion, $I^-$, was found to sensitively detect BrO [Neuman et al., 2010]. In addition, the capability of CIMS, using $I^-$, to accurately and sensitively measure BrO was demonstrated in Liao et al. [2011a]. Moving forward, CIMS observations of BrO with $I^-$ are preferred to $SF_6^-$ as the latter ion is more prone to interferences as it is more reactive [Huey et al., 1995]. Consequently, conclusions drawn from the CIMS BrO observations in this study must be considered in the context of potential interferences, although the specific candidates for the interference are not known at this time.

### 5.2.3 BrO measurements by DOAS

The primary BrO measurement during the Summit campaign was a long path differential absorption spectrometer (LP DOAS). The techniques of the LP DOAS instrument were based on the work of Stutz and Platt [1997]. The LP DOAS measured BrO over a path of either 2 km or 5 km (2007) /4 km (2008). The optical paths were 1.5–3 m above the snow. The LP DOAS telescope was located at the edge of the clean air

boundary in the south of the station and two reflectors were located 2 km and 5 km (2007)/4 km (2008) to the South of the light source (Figure 5.1). The details of BrO measurement by LP DOAS are provided by Stutz et al. [2011].

### 5.2.4 Mercury measurements

Tekran models 2537a/1130/1135 [Brooks et al., 2008] were used to measure gaseous elemental mercury (GEM), reactive gaseous mercury (RGM), also known as gaseous oxidized mercury (GOM), and fine particle mercury (FPM) via cold vapor atomic fluorescence. The details of the mercury measurements are described in the work of Brooks et al. [2011].

### 5.2.5 Actinic Flux measurements

Actinic Flux were measured by a Scanning Actinic Flux Spectrometer (SAFS) [Shetter and Muller, 1999] by University of Houston. The photolysis rate coefficients (J values) of atmospheric compounds were calculated based on the sum of downwelling and upwelling Actinic Flux.

### 5.2.6 Photochemical Models

A 0-Dimensional steady-state $HO_x - NO_x - CH_4$ model is used to evaluate the $HO_x$ chemistry at Summit. The model is identical to that described in Sjostedt et al. [2007] and is denoted as the base model (BM). The BM involves 46 chemical reactions which include 8 photolysis reactions and is constrained by the measurements of photolysis rate coefficients (J values) and the following gases: $H_2O$, $O_3$, CO, $CH_4$, and

NO. The model only considered $CH_4$ chemistry because previous studies by Chen et al. [2007] and Sjostedt et al [2007] found that including nonmethane hydrocarbons (NMHC) decreased OH number densities and increased $HO_2$+$RO_2$ number densities less than 10% and that most of the $RO_2$ is $CH_3O_2$ at Summit, Greenland. Typical levels of the dominant NMHC species ethane, propane, and butane are 1.0 ppbv, 0.07 ppbv, and 0.04 ppbv, respectively. The NMHC measured in 2007 and 2008 were generally consistent with the measurements in 2003. The average ethane, propane and butane levels were 1.1 ppbv, 0.14 ppbv, 0.03 ppbv, respectively in spring 2007 and 0.9 ppbv, 0.07 ppbv, 0.02 ppbv respectively in summer 2008. Because Summit Greenland is in the middle of Greenland Ice Sheet far away from biogenic and anthropogenic volatile organic carbons (VOCs) sources, we do not expect high levels of oxygenated VOCs reacting with OH at Summit, Greenland. Measurements of larger oxygenated VOCs at Summit, Greenland are needed to validate our assumption. The input data used to constrain the model were averaged to a 10 minute basis. A spin-up time of 1000 s was used for model calculations of relatively long-lived species (e.g. $H_2O_2$ and HCHO). The model predictions are compared to OH and $HO_2$+$RO_2$ measurements (assuming $RO_2$ is primarily $CH_3O_2$). The rate constants are taken from the JPL compilation (Sander et al., 2006), and the J values are derived from the measured actinic flux [Shetter and Muller, 1999]. Similar to the work of Sjostedt et al. [2007], the model can be run either constrained or unconstrained to HONO measurements. This allows evaluation of the impact of HONO on $HO_x$ levels and the radical budget. The model constrained to HONO observations is referred as BM_HONO.

To examine the impact of BrO on $HO_x$ levels, bromine reactions (see Table 5.2) were added to the BM. The model incorporating the bromine chemistry is referred as BM_BrO. Reaction 6 (in Table 5.2) acts as a source of $HO_x$. HOBr serves as a temporary reservoir of $HO_x$ and heterogeneous loss of HOBr is effectively a loss of $HO_x$. HOBr levels were assumed to be in steady-state and controlled by reactions 2, 8 and 9 (in Table 5.2). This assumption was valid because the photolysis lifetime of HOBr is relatively short (~5 minutes) at Summit Greenland in the daytime. The assumption was also found to reasonably predict the observed HOBr in Liao et al. [2011c]. The box model is constrained by BrO measurements from CIMS and LP DOAS to illustrate the effect of two BrO datasets on $HO_x$ levels. The mass accommodation coefficient of HOBr is assumed to be 0.6 [Wachsmuth et al., 2002]. This allowed predictions of OH and $HO_2$+$RO_2$ when BrO measurements were available. The model did not include the heterogeneous sinks of $BrONO_2$ because the model is constrained to BrO measurements and $BrONO_2$ does not directly impact the budget of OH and $HO_2$+$RO_2$. The impact of $BrONO_2$ on daytime $NO_2$ levels is also small due to the low BrO concentrations. Daytime $NO_2$ levels increased ~5% in 2007 and ~2% in 2008 when the model considered bromine reaction 4 and 5 in the table 5.2. As the photochemical lifetime (= ~2 minute) of $HO_2$ is much shorter than the lifetime due to heterogeneous loss (= ~150 minute) with a uptake coefficient of 0.1 [Mao et al., 2010], the model did not consider the heterogeneous loss of $HO_2$.

One significant difference from the work of Sjostedt et al. [2007] is that observations of $CH_2O$ and $H_2O_2$ were not available. For this reason, the BM was used to predict $CH_2O$ and $H_2O_2$ levels. In order to test the ability of the model to calculate these

species, predictions of $CH_2O$ and $H_2O_2$ using data from the 2004 Summit campaign were compared to observations. Both $CH_2O$ and $H_2O_2$ predictions are in reasonable agreement with the measurements ($CH_2O$: R=0.68, mean M/O = 1.3; $H_2O_2$: R=0.72, mean M/O = 2.4), which suggests that the steady state model is viable for estimation of $CH_2O$ and $H_2O_2$ within about a factor of two. The impact of this relatively high uncertainty in mixing ratios of $CH_2O$ and $H_2O_2$ on predictions of $HO_x$ and its partitioning are discussed in section 5.4.2.

Table 5.2 Bromine reactions included in the $HO_x$ model.

| Reaction number | Reactions | Reaction rate coefficient $k$ ($cm^3$ $molec^{-1}$ $s^{-1}$ or $s^{-1}$) | $k$ (T = 250 K) ($cm^3$ $molec^{-1}$ $s^{-1}$ or $s^{-1}$) |
|---|---|---|---|
| 1 | $Br + O_3 \rightarrow BrO + O_2$ | $1.7\times10^{-11}exp(-800/T)$ | $6.9\times10^{-13}$ |
| 2 | $BrO + HO_2 \rightarrow HOBr + O_2$ | $4.5\times10^{-12}exp(460/T)$ | $2.8\times10^{-11}$ |
| 3a | $BrO + BrO \rightarrow 2Br + O_2$ | $2.4\times10^{-12}exp(40/T)$ | $2.8\times10^{-12}$ |
| 3b | $\rightarrow Br_2 + O_2$ | $2.8\times10^{-14}exp(860/T)$ | $8.7\times10^{-13}$ |
| 4 | $BrO + NO \rightarrow Br + NO_2$ | $8.8\times10^{-12}exp(260/T)$ | $2.5\times10^{-11}$ |
| 5 | $BrO + NO_2 + M \rightarrow BrONO_2 + M$ | $k_0=5.2\times10^{-31}exp(T/300)^{-3.2}$ $k_\infty=6.9\times10^{-12}exp(T/300)^{-2.9}$ | $5.3\times10^{-12}$ |
| 6 | $Br + CH_2O \rightarrow HBr + HCO$ | $1.7\times10^{-11}$ exp(-800/T) | $6.9\times10^{-13}$ |
| 7 | $BrO + h\nu \rightarrow Br + O$ | 0.06–0.08 (at noon) | |
| 8 | $HOBr + h\nu \rightarrow Br + OH$ | $3\times10^{-3}$ –$4\times10^{-3}$ (at noon) | |
| 9 | Uptake of HOBr on heterogeneous surface | $\sim1\times10^{-4}$ | |

## 5.3 Results

### 5.3.1 OH and ($HO_2$+$RO_2$) observations

The time series of observations of OH, $HO_2$+$RO_2$, $J(O^1D)$, BrO, NO, $HNO_3$, HONO, $O_3$, RGM, temperature, wind speeds and wind directions on a 10 minutes time base in spring 2007 and summer 2008 are shown in Figure 5.2. The observations of OH and $HO_2$+$RO_2$ were filtered to exclude the periods when NO >50 pptv. High NO mixing

ratios at Summit are almost always due to pollution plumes from the station power generator. High NO dramatically brought down the $HO_2$+$RO_2$ concentrations and raised the OH concentrations (Figure 5.3). Similar phenomena were observed by previous works as well [e.g. Sjostedt et al., 2007; Bloss et al., 2007]. The $HO_x$ instrument was shut down to save reagent gases at night (22:00 – 06:00 Western Greenland Standard Time (WGST)) when the OH concentrations decreased to near detection limit ($10^5$ molec.cm$^{-3}$). The gaps in the data other than night time and high NO periods are due to instrument maintenance or malfunction.

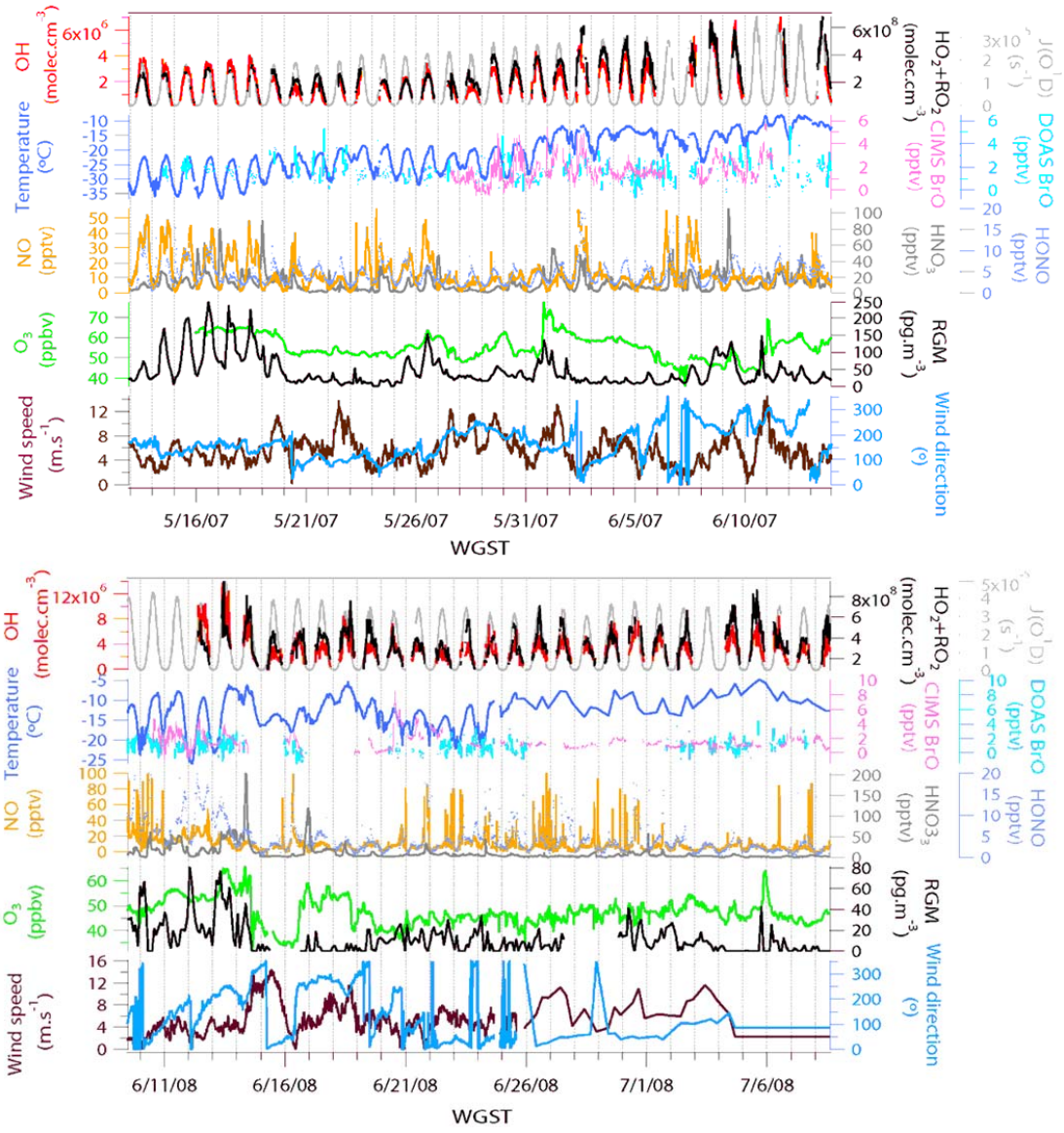


Figure 5.2 Time series of measurements of $HO_2$+$RO_2$, OH, J ($O^1D$), BrO, temperature, NO, $HNO_3$, HONO, $O_3$, RGM, wind speeds and directions on a 10 min time base in spring 2007 (top panel) and summer 2008 (bottom panel) Summit campaign.

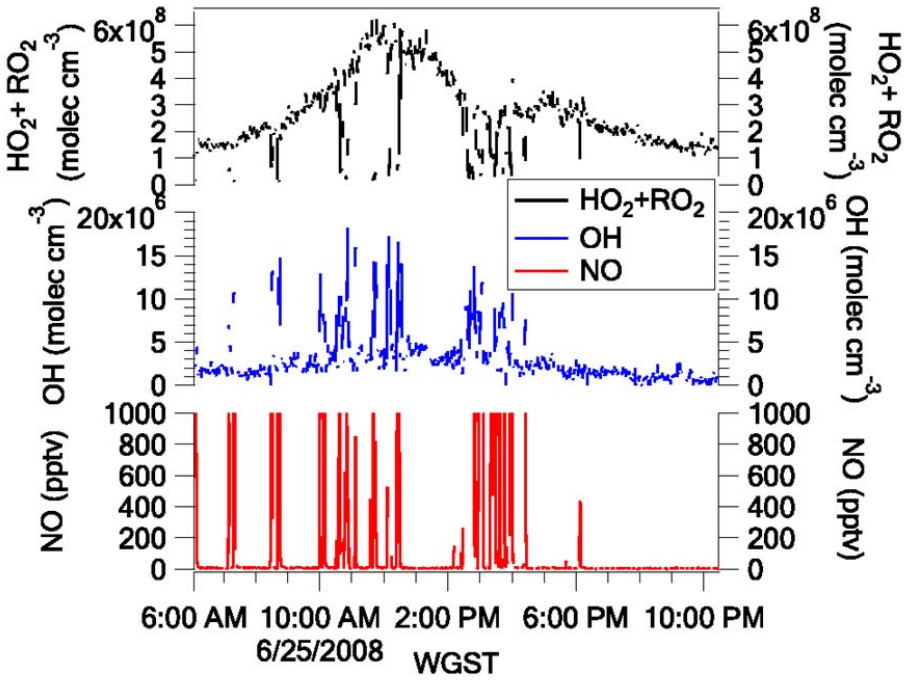


Figure 5.3 An example of elevated OH and depleted $HO_2$ + $RO_2$ at high NO conditions. The spikes in NO and the responses in OH and $HO_2$ + $RO_2$ are due to the measurement cite being impacted by the plume of the generator.

Diurnal profiles of OH and $HO_2$+$RO_2$ largely followed the patterns of $J(O^1D)$ with a maximum at local noon, consistent with the behaviors of short-lived photochemically active species. Although 24 hours of daylight are present in summer time at Summit, $J(O^1D)$ decreased by approximately a factor of 100 from noon to midnight. The maxima mid-day levels of OH and $HO_2$+$RO_2$ increased as temperature, $J(O^1D)$ and $O_3$ increased, which were consistent with the previous finding that $O^1D$ reacting with $H_2O$ and snow emissions of $H_2O_2$ were the dominant $HO_x$ sources at Summit [Chen et al., 2007] (Mid-day is defined as 10:00 – 15:00 WGST). Overall, the maximum mid-day OH and $HO_2$+$RO_2$ concentrations increased during the measurement

period in spring 2007 as the summer solstice was approached. There was no significant trend in the maximum mid-day OH and $HO_2$+$RO_2$ concentrations during summer 2008 (12 June 2008 – 08 July 2008) as the measurement period was centered about the solstice. The average mid-day OH and $HO_2$+$RO_2$ concentrations were higher in summer 2008 than that in spring 2007, likely a result of the higher radiative flux ($J_{O3}$_2007/$J_{O3}$_2008= 1 : 1.4) and dew points in summer time. The midday median ratio of $HO_2$+$RO_2$ to OH was 107 : 1 in spring 2007 and 102 : 1 in summer 2008 and the midday mean ratio of $HO_2$+$RO_2$ to OH was 109 : 1 with a standard deviation of 23 in spring 2007 and 108 : 1 with a standard deviation of 37 in summer 2008. The $HO_2$+$RO_2$ to OH ratios are comparable to other measurements performed in the lower troposphere in mid latitudes [Ren et al., 2008]. The mid-day median and mean values of OH and $HO_2$+$RO_2$ observations, as well as $J(O^1D)$, $J(NO_2)$, NO, $HNO_3$, HONO, $O_3$, BrO, RGM and temperature in spring 2007 and summer 2008 are summarized in Table 5.3.

Table 5.3 Photochemical species concentrations and parameters in the mid-day (10:00-15:00 WGST) at Summit, Greenland in 2007-2008. (Note: $HO_x$ predictions are from the base model).

| Species | Year 2007 (13 May – 13 June) | | Year 2008 (10 June – 08 July) | |
|---|---|---|---|---|
| | Median | Average | Median | Average |
| OH ($10^6$ molec.cm$^{-3}$) | 3.0 | 3.1 | 4.1 | 4.6 |
| $HO_2$+$RO_2$ ($10^8$ molec.cm$^{-3}$) | 2.7 | 3.3 | 4.2 | 4.4 |
| OH pred ($10^6$ molec.cm$^{-3}$) | 2.4 | 2.6 | 3.7 | 3.8 |
| $HO_2$+$RO_2$ pred ($10^8$ molec.cm$^{-3}$) | 3.0 | 3.2 | 4.6 | 4.6 |
| NO (pptv) | 12.8 | 17.2 | 8.6 | 11.4 |
| $O_3$ (ppbv) | 54.6 | 55.3 | 47.3 | 47.9 |
| $BrO_{LPDOAS}$ (pptv) | 1.5 | 1.6 | 1.0 | 0.9 |
| $BrO_{CIMS}$ (pptv) | 1.8 | 2.0 | 1.5 | 2.0 |
| RGM(pg/m$^{-3}$) | 41.8 | 64.8 | 7.2 | 9.6 |
| $HNO_3$ (pptv) | 12.9 | 15.9 | 5.5 | 11.5 |
| HONO (pptv) | 6.5 | 7.3 | 4.7 | 5.8 |
| $J(O^1D)$ ($10^{-5}$ s$^{-1}$) | 2.2 | 2.3 | 3.3 | 3.3 |
| $JNO_2$ ( s$^{-1}$) | 0.014 | 0.014 | 0.016 | 0.016 |
| Temperature(°C) | -19.5 | -18.2 | -10.7 | -10.6 |

### 5.3.2 NO, $HNO_3$ and HONO observations

Diurnal profiles of NO and HONO were also observed at Summit. The average mid-day concentrations of NO and HONO were ~12 pptv and ~6 pptv, respectively. HONO levels were obtained from measurements of soluble nitrite ($NO_2^-$) from the mist chamber [Dibb et al., 2002]. However, it should be noted that the derived HONO levels must be considered an upper limit to gas phase HONO as other species might also produce nitrite in solution. Following the simple $NO_x$ and HONO lifetime arguments in Chen et al. [2004]; NO levels of 12 ppt and HONO levels of 6 ppt would seem to indicate that the soluble nitrite measurement includes species other than HONO. Due to the increase of the boundary layer height through the day, the diurnal profiles of NO had a local minimum at noon [Thomas et al., 2011]. Elevated $HNO_3$ was observed by mist chamber during the days when photochemically enhanced NO was observed. Higher NO, $HNO_3$ and HONO concentrations were observed in spring 2007 than in summer 2008.

### 5.3.3 RGM and GEM observations

Up to ~250 $pg.m^{-3}$ RGM were observed in the spring 2007 campaign. Clear diurnal profiles of RGM were observed when RGM was greater than 100 $pg.m^{-3}$. Because bromine atoms are one of the few established species that efficiently converts GEM into RGM [Ariya et al., 2002; Donohoue et al., 2006], elevated RGM peaks indicated that significant levels of BrO may be present. Higher RGM levels were observed in spring 2007 than in summer 2008, which suggests that the concentrations of BrO at Summit might be higher in spring 2007 than in summer 2008. High RGM appeared to coincide

with photochemically enhanced NO and $HNO_3$ in most cases. This is consistent with snow photochemistry activating bromine chemistry as described in Thomas et al. [2011].

### 5.3.4 BrO observations

BrO mixing ratios detected by the LP DOAS ranged from below detection limit to 5.5 pptv with an average value of 1.6 pptv in 2007 at Summit. BrO was also measured by CIMS in the later period of the 2007 campaign with a mean value of 1.7 pptv, ranging from below detection limit to 6.4 pptv. Lower BrO mixing ratios were observed by both LP DOAS ($[BrO]_{mean}$ = 0.9 pptv for all data available) and CIMS ($[BrO]_{mean}$ = 1.5 pptv for all data available) in summer 2008. BrO mixing ratios in 2008 generally ranged from below detection limit to 4 pptv and 5 pptv detected by LP DOAS and CIMS respectively. To be noted, the BrO concentrations at Summit were often near detection limits of both instruments. Diurnal patterns of BrO were observed in spring 2007 and the early part (10 June to 13 June) of summer 2008 by the CIMS with maximum concentrations in the daytime, which is consistent with BrO as a photochemically active product. No significant diurnal patterns of BrO were observed by the CIMS in the later period of summer 2008 as the daytime BrO levels were near the detection limit.

## 5.4 Discussion

### 5.4.1 Model Comparison

5.4.1.1 Base Model (BM)

The predicted OH and $HO_2$+$RO_2$ from the BM are plotted against the observations in Figure 5.4. Note that, the discrepancy between $HO_x$ observations and

predictions increased at high wind speeds (WS > 8 m $s^{-1}$) and were excluded from the comparisons. On average 26% of the $HO_x$ data were excluded and the correlation coefficients were improved (R increase 0.03 on average for BM_model) when $HO_x$ data were filtered at high wind speed conditions. Higher wind speed conditions did not clearly correspond to low photolysis rate or lower $NO_x$ levels. The correlation coefficient (R) between photolysis rate and wind speeds were < 0.1 in 2007 and 2008. The correlation coefficient (R) between predicted $NO_2$ and wind speeds were –0.35 in 2007 and –0.29 in 2008. There is no clear systematic bias introduced when the $HO_x$ data were filtered at high wind speeds but this filter excluded the most scattered points. It is possible that the uncertainty in the CIMS calibration increases at high wind speeds (> 8 m $s^{-1}$) due to turbulent flow in the inlet as suggested in Sjostedt et al. (2007). Overall, the observed and predicted OH and $HO_2$+$RO_2$ from the BM were well correlated ($HO_2$+$RO_2$: R = 0.90, OH: R = 0.83 in 2007; $HO_2$+$RO_2$: R = 0.79, OH: R = 0.76 in 2008). The BM well predicted the magnitude of $HO_2$ + $RO_2$ and under predicted OH, especially in summer 2008 ($HO_2$+$RO_2$: slope = 0.87, OH: slope = 0.72 in 2007; $HO_2$+$RO_2$: slope = 0.96, OH: slope = 0.54 in 2008). The slopes were given by equally weighted bivariate regressions. The agreement between the predicted and observed $HO_2$+$RO_2$ (which is dominated by $HO_2$) indicates that we have a good understanding of the major sources and sinks of $HO_2$ which dominates the $HO_x$ family. However, our understanding of the OH sources and sinks is clearly lacking especially during periods of elevated RGM (see section 5.4.4). The model predicted an average midday $HO_2$+$RO_2$ to OH ratio of 121 : 1 in 2007 and 125 : 1 in 2008, consistent with the values predicted by Chen et al. [2007] using input data from the summit 2003 campaign. The observed average midday $HO_2$+$RO_2$ to OH

ratios were 109 : 1 in 2007 and 108 : 1 in 2008. The predicted and observed $HO_2$+$RO_2$ to OH ratios indicate that a mechanism rolling $HO_2$ back to OH may be missing, with halogen chemistry a likely prospect.

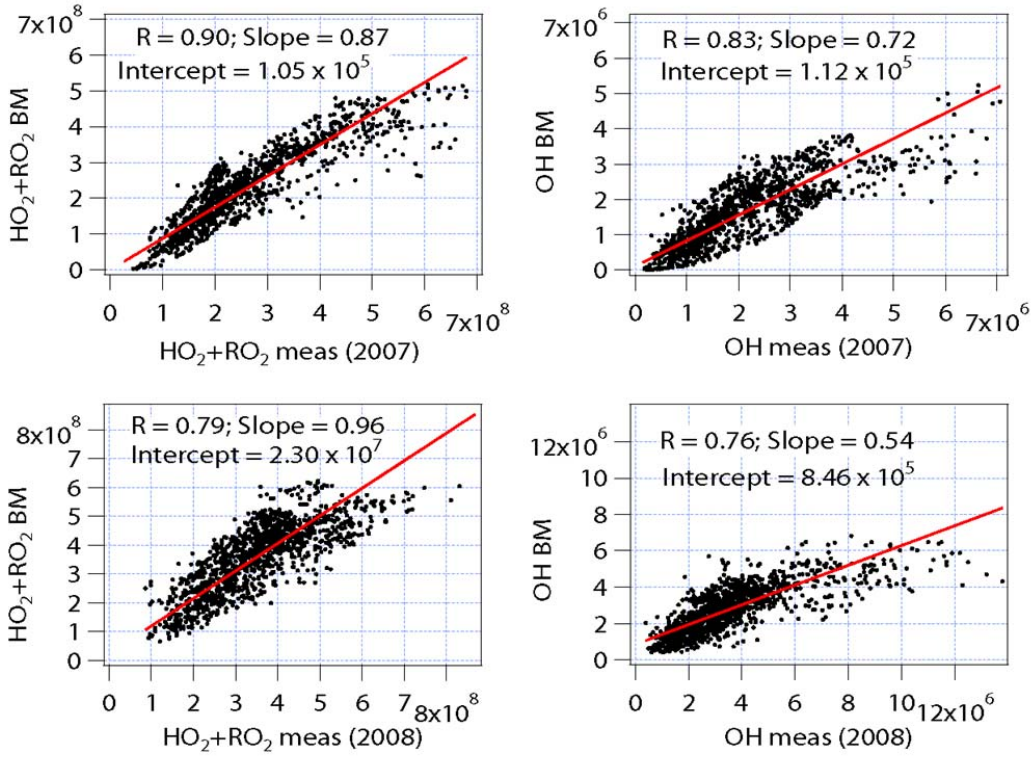


Figure 5.4 $HO_2$+$RO_2$ and OH predictions from the base mode (BM) plotted versus the observations in 2007 and 2008. The data are average on a 10 min time base. The correlation coefficient (R) and the slope and intercept from an equally weighted bivariate regression (red line) for each panel are also denoted in the figure. The units of OH and $HO_2$+$RO_2$ concentrations are molec $cm^{-3}$.

5.4.1.2 Base Model constrained to HONO measurements (BM_HONO)

The correlation coefficients and slopes between predictions from the BM_HONO and observations are shown in Figure 5.5 ($HO_2$+$RO_2$: R = 0.84, slope = 0.90 in 2007 and R = 0.79, slope = 1.09 in 2008; OH: R = 0.78, slope = 0.92 in 2007 and R = 0.78, slope =

0.72 in 2008). The slopes were given by equally weighted bivariate regressions. The correlation coefficient (R) between predicted and observed $HO_x$ did not improve when the model included HONO source. In 2007, the average modeled to observed (M/O) ratios of $HO_2$+$RO_2$ and OH were 0.87 and 0.84 from the BM, and were 1.18 and 1.25 from the BM_HONO. In 2008, the average M/O ratios of $HO_2$+$RO_2$ and OH were 1.06 and 0.87 from the BM, and were 1.22 and 1.05 from the BM_HONO. The predictions of both OH and $HO_2$+$RO_2$ from the BM_HONO were higher than that from the BM as this adds in a $HO_x$ source. However, the ratio of $HO_2$+$RO_2$ to OH changed by less than 10% on average. As the $HO_x$ predictions from the BM had more data points, the correlation between predicted and observed $HO_x$ did not improve when HONO was included in the model, and the observed HONO is likely to have interferences [Stutz et al., 2010; Sjostedt et al., 2007], the BM is preferred for comparison to $HO_x$ observations in this work.

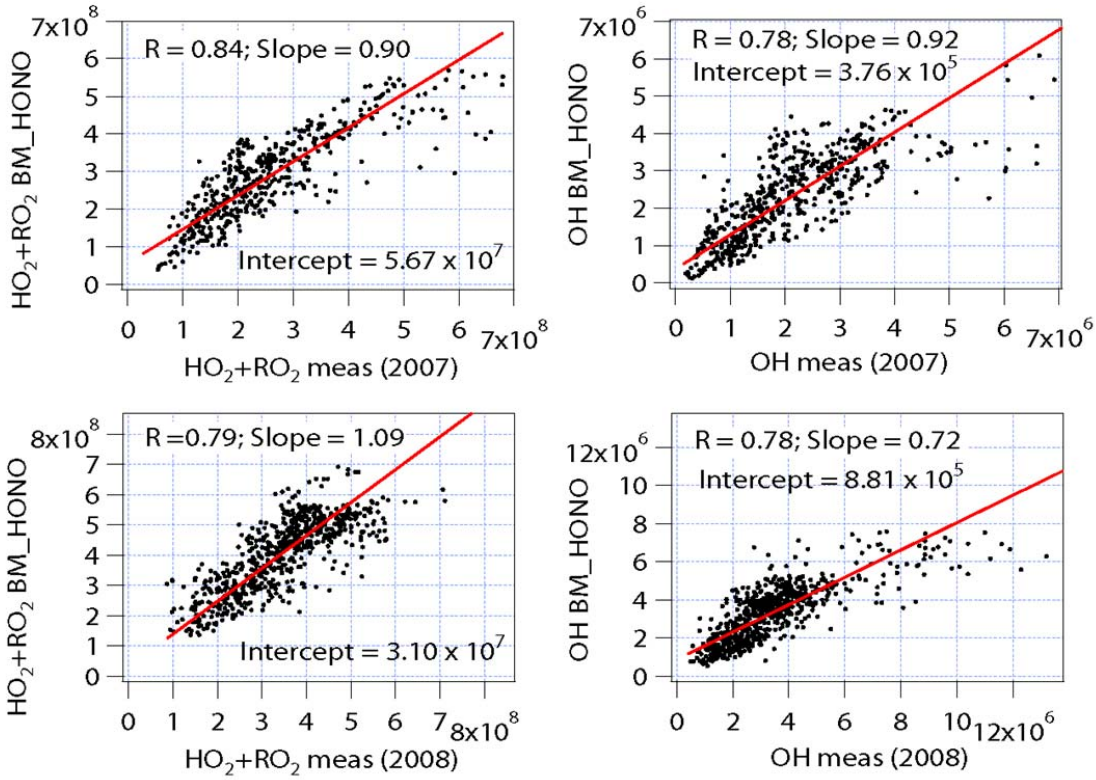


Figure 5.5 $HO_2$+$RO_2$ and OH predictions from the base model constrained to HONO measurements (BM_HONO) plotted versus the observations in 2007 and 2008. The data are average on a 10 min time base. The correlation coefficient (R) and the slope and intercept from an equally weighted bivariate regression (red line) for each panel are also denoted in the figure. The units of OH and $HO_2$+$RO_2$ concentrations are molec $cm^{-3}$.

5.4.1.3 Model incorporating halogen chemistry (BM_BrO)

To investigate the impact of BrO on $HO_x$, predicted OH and $HO_2$+$RO_2$ from the BM_BrO unconstrained by HONO measurements and constrained by BrO measurements from the CIMS ($BM\_BrO_{CIMS}$) and LP DOAS ($BM\_BrO_{LPDOAS}$) in 2007 and 2008 are also plotted against the observations (Figure 5.6). Overall, the correlation coefficients between the observed and predicted OH and $HO_2$+$RO_2$ were slightly improved (increased 0.03 except $HO_2$+$RO_2$ in 2007) by incorporation of bromine chemistry with the BrO constrained to the CIMS observations. When the model included bromine chemistry and

was constrained to CIMS BrO, the intercept increased from $1.12 \times 10^5$ molec $cm^{-3}$ to $1.65 \times 10^5$ molec $cm^{-3}$ and the slope increased from 0.72 to 0.78 in 2007 and the intercept increased from $8.64 \times 10^5$ molec $cm^{-3}$ to $9.23 \times 10^5$ molec $cm^{-3}$ and the slope increased from 0.54 to 0.56 in 2008 for OH. When the model included bromine chemistry and was constrained to LP DOAS BrO, the intercepts increased from $1.12 \times 10^5$ molec $cm^{-3}$ to $3.20 \times 10^5$ molec $cm^{-3}$ and the slope remained the same in 2007 and the intercept increased from $8.46 \times 10^5$ molec $cm^{-3}$ to $1.15 \times 10^6$ molec $cm^{-3}$ and the slope slightly decreased from 0.54 to 0.50 in 2008 for OH. To give a general idea of the difference between predicted OH and $HO_2$+$RO_2$ from the BM and BM_BrO, the average ratios of OH and $HO_2$+$RO_2$ from both models as well as the slopes and intercepts from linear equally weighted bivariate regression are also provided. Predicted OH increased 12% $([OH]_{pred\_BrO\_CIMS}/[OH]_{pred})_{avg}$ in 2007 and 10% in 2008, and predicted $HO_2$+$RO_2$ decreased 10% in 2007 and 8% in 2008 on average when the BM_BrO was constrained to CIMS BrO. Predicted OH increased 10% in 2007 and 4% in 2008, and predicted $HO_2$+$RO_2$ decreased 8% in 2007 and 3% in 2008 on average when the BM_BrO was constrained to LP DOAS BrO. These results indicate that BrO impacted the concentrations of OH and $HO_2$+$RO_2$ at Summit, although all of the enhancement in observed OH relative to model predictions cannot be explained by the influence of BrO.

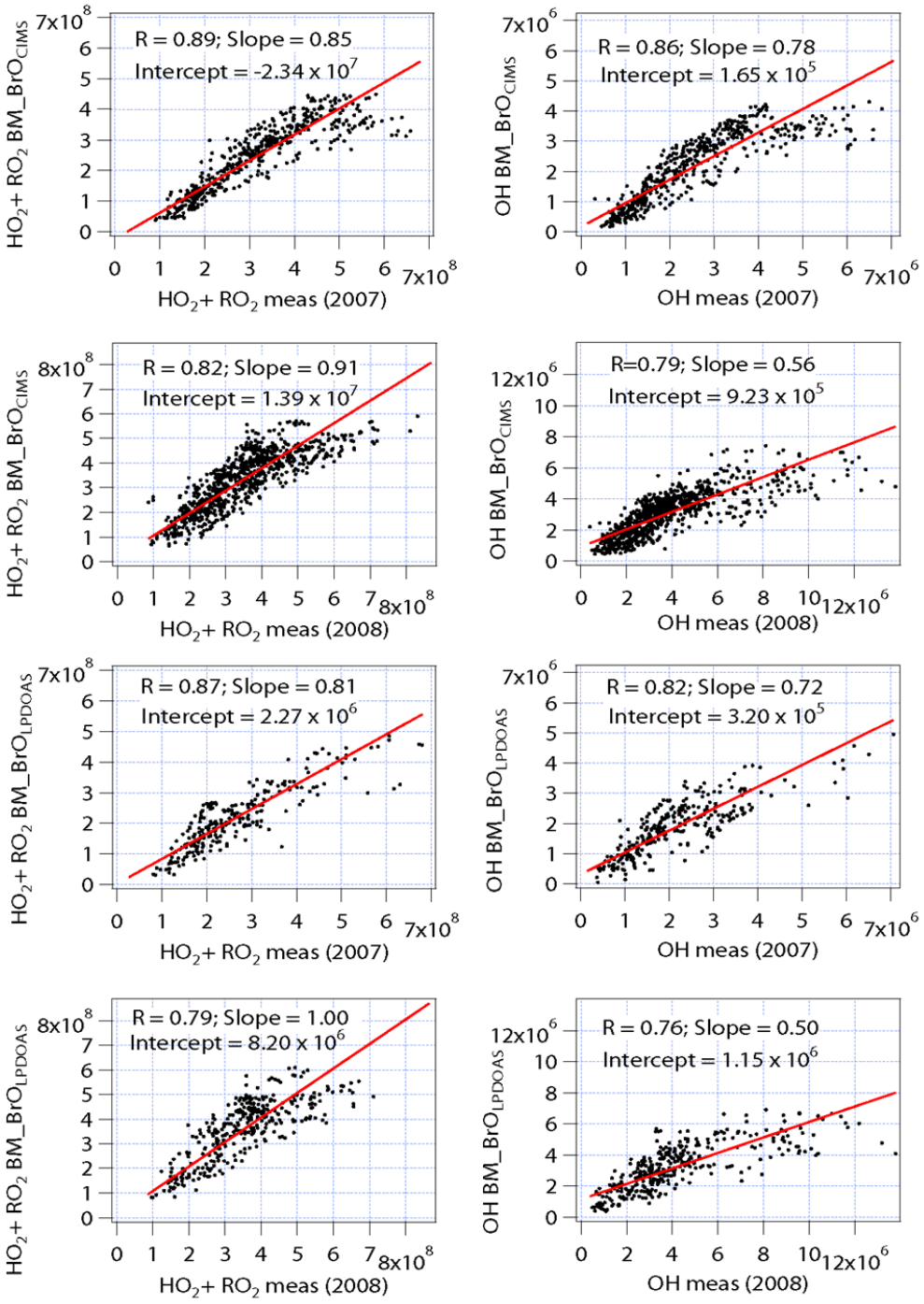


Figure 5.6 $HO_2$+$RO_2$ and OH predictions from the base model incorporating bromine chemistry constrained by BrO measurements by CIMS ($BM\_BrO_{CIMS}$) and LPDOAS ($BM\_BrO_{LPDOAS}$) plotted versus the observations in 2007 and 2008. The data are averaged on a 10 min time base. The correlation coefficient (R) and the slope and intercept from an equally weighted bivariate regression (red line) for each panel are also denoted in the figure. The units of OH and $HO_2$+$RO_2$ concentrations are molec $cm^{-3}$.

### 5.4.2 Impact of $H_2O_2$ and $CH_2O$

Because $CH_2O$ and $H_2O_2$ were not observed, they had to be predicted with the photochemical model which may lead to under estimation of them as they are emitted to the atmosphere from the snowpack [Hutterli et al., 1999 and 2001]. Under estimation of $CH_2O$ and $H_2O_2$ results in under prediction of OH and $HO_2$+$RO_2$, but does not significantly impact the ratios of OH/ $HO_2$+$RO_2$. For example, a 30% increase in the model production rate of $H_2O_2$ or $CH_2O$ would increase $HO_x$ levels by ~5% and ~10% but would impact the ratio of OH to $RO_2$ by less than 2%. According to the study of $HO_x$ at Summit in 2003 by Chen et al. [2007], $H_2O_2$ is the largest snow emitted $HO_x$ sources at Summit, contributing to 37% of the net $HO_x$ sources compared to only 3% from $CH_2O$. As snow emissions of $H_2O_2$ increase with temperature [Chen et al., 2007], the warmer temperature in summer 2008 may have contributed to the lower correlation between predicted and observed $HO_x$ in that year. For this reason, temperature dependent snow emissions of $H_2O_2$, based on net snow-air exchange rate shown as the following equation, were added to the BM.

$d[H_2O_2]/dt = A \times \exp(B/Temperature_{snow}) - C \times [H_2O_2]$ (molec.cm$^{-3}$.s$^{-1}$ or ppbv. hr$^{-1}$)

A, B and C are adjustable constants. Temperature is assumed to be ambient temperature instead of snow temperature. $[H_2O_2]$ represents ambient $H_2O_2$ concentration [Chen et al., 2007]. No significant improvement of the correlation was found between predicted and observed $HO_x$. However, as observations of $H_2O_2$ and $CH_2O$ were not carried out in 2007 or 2008, enhanced snow photochemistry producing these and potentially other radical precursors in 2008 cannot be ruled out.

### 5.4.3 Average Comparison

Figure 5.7 shows the average diurnal profiles of hourly OH and $HO_2$+$RO_2$ concentrations from observations and predictions from the BM and the BM_BrO constrained to CIMS measurements in 2007 and 2008. The error bars of the observations are the overall uncertainties including the measurement uncertainties and ambient fluctuations. The error bars of the predictions are the propagated uncertainties from the model inputs uncertainties and variations. The BM simulated the concentrations of OH and $HO_2$+$RO_2$ within the combined uncertainties, except for the OH concentrations in the late afternoons in summer 2008. This confirms that the BM captures the dominant $HO_x$ sources and sinks. The BM also under predicts the OH concentrations in both 2007 and 2008. The midday median modeled to observed (M/O) ratio of OH was 0.88 and 0.87 in 2007 and 2008, and the midday median M/O ratio of $HO_2$+$RO_2$ was 0.97 and 1.08 in 2007 and 2008. A low M/O ratio of OH was also reported in Sjostedt et al. [2007]. The average hourly $HO_2$+$RO_2$ and OH predictions from the BM_BrO constrained to CIMS BrO measurements in 2007 slightly over estimated their concentrations due to the absence of CIMS BrO measurements in the early period of the 2007 campaign and the increase in $HO_x$ levels in the late period of the 2007 campaign relative to the early period. The OH concentrations predicted from BM_BrO were higher compared to the results from the BM, and the average hourly predicted $HO_2$+$RO_2$ concentrations slightly decreased when BM incorporated bromine chemistry in 2008. The model including bromine chemistry brought the predictions both of OH and $HO_2$+$RO_2$ closer to the observations in 2008. The impact of bromine chemistry on $HO_2$+$RO_2$ concentrations was smaller than on OH concentrations. The box model consistently under predicts the OH

concentrations in the later afternoons, which indicates that box model underestimates the sources of OH as the radiation flux and boundary layer height decrease or there may be a change in the sinks or cycling. A similar behavior was observed by Sjostedt et al. [2007]. Snow emitted compounds with higher concentrations or steeper vertical gradients in the later afternoon not included in the photochemical box model may contribute to the under predictions of OH and impact the photochemistry at Summit in the later afternoon.

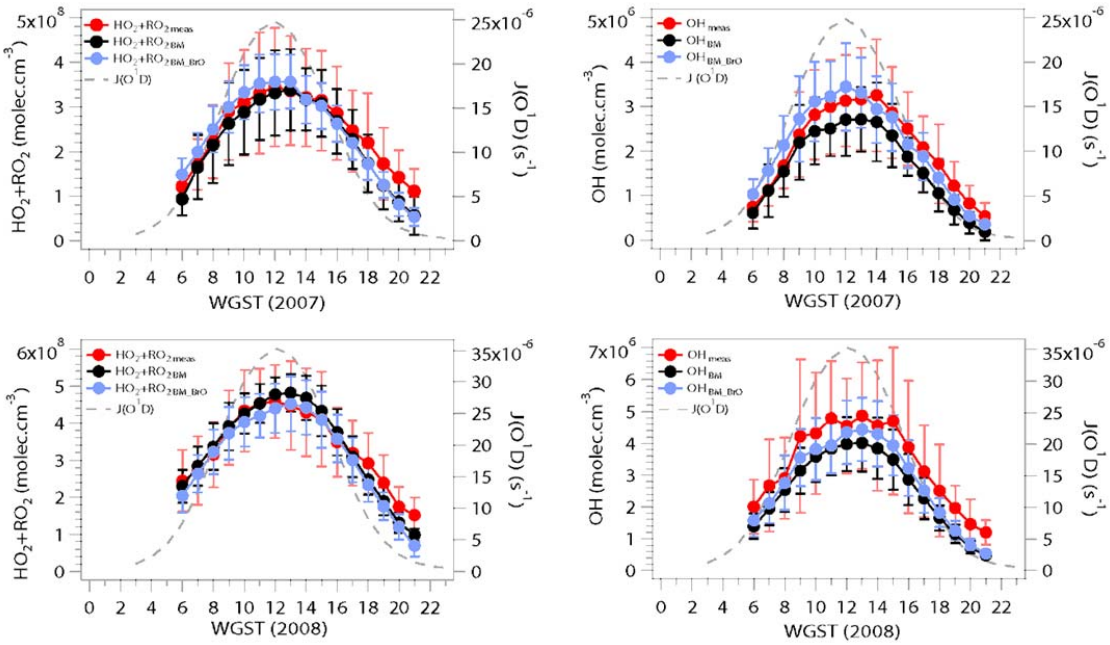


Figure 5.7 The average diurnal profiles of hourly OH and $HO_2$+$RO_2$ observations (red dots and line) and predictions from the BM (black dots and line) and BM_$BrO_{CIMS}$ (blue dots and line), and diurnal profile of $J(O^1D)$ (gray dash line) in spring 2007 and summer 2008. The error bars (red) of the observations are the overall uncertainties including the measurement uncertainties and ambient fluctuations. The error bars (gray and blue) of the predictions are the propagated uncertainties from the model input uncertainties and variations.

### 5.4.4 Enhanced OH and RGM

Due to the limitations of BrO measurements discussed earlier, observations of RGM were also investigated as a proxy for bromine and potentially other chemistry. The

correlations between the BM predictions and observations of $HO_x$ were examined for enhanced RGM levels (gray dots in Figure 5.8) and low RGM levels (black dots in Figure 5.8). RGM levels were considered to be enhanced when they were above average levels for each of the field seasons and season means were 45 and 11 pg $m^{-3}$ in 2007 and 2008, respectively.

When high RGM periods were excluded, the slope between the predicted and observed OH significantly increased: the slope of OH increased from 0.72 to 0.97 in 2007 and increased from 0.54 to 0.85 in 2008. The correlation between the predicted and observed OH and $HO_2$+$RO_2$ in 2007 also slightly improved: the correlation coefficient increased from 0.83 to 0.90 for OH and increased from 0.90 to 0.93 for $HO_2$+$RO_2$. For the 2008 data the correlation was essentially unchanged when high RGM periods were excluded. These results indicate that OH levels are enhanced above predictions when RGM is enhanced. This is consistent with other chemistry (e.g. other halogens) coincident with the Br chemistry that leads to elevated RGM impacting the production of OH from $HO_2$ and $RO_2$.

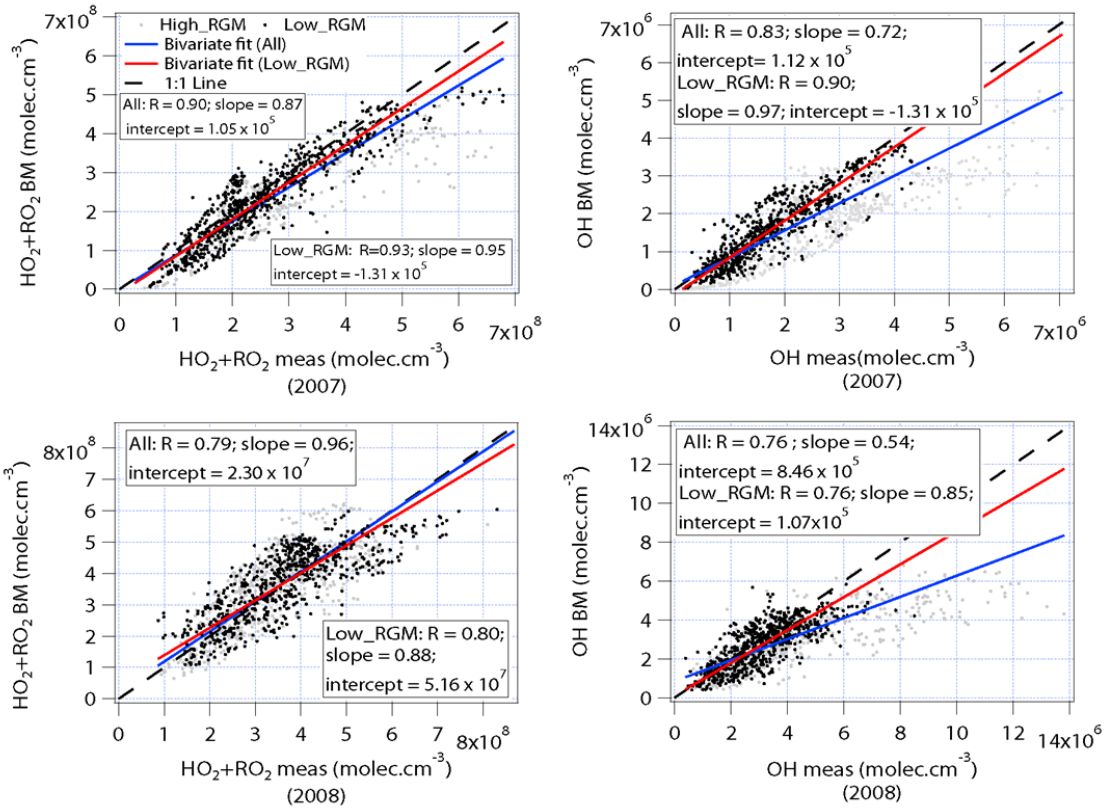


Figure 5.8 The correlation plots of observed and predicted OH and $HO_2$+$RO_2$ from the BM at low RGM conditions (black dots) and at high RGM conditions (gray dots) in 2007 and 2008. "All" represents the total data including low RGM and high RGM conditions. Equally weighted bivariate regressions are applied to all the data (blue line) and the data at low RGM conditions (red line), respectively. The relevant correlation coefficients, slopes, and intercepts are provided in the figure.

### 5.4.5 Case study with high RGM

The concentrations of OH, $O_3$, RGM, and BrO during two periods (16 May – 21 May 2007; 12 June – 17 June 2008) are shown in Figure 5.9. The BM clearly under predicted OH during 16 May – 18 May 2007 (Figure 5.9 (a)). Clear diurnal profiles of RGM were present during the same period, with a maximum concentration of near 250 $pg.m^{-3}$. The RGM peaks indicate that certain levels of Br and BrO may be present during

these periods. Small $O_3$ concentration drops also occurred with the RGM peaks, possibly a result of bromine catalyzed $O_3$ depletion. Up to 5 pptv of BrO were observed by LP DOAS and no CIMS BrO measurements were available during this time. OH predictions from BM_BrO constrained by LP DOAS BrO measurements cannot account for the enhanced OH observed.

Figure 5.9(b) shows the early period of 2008 campaign including three days (12 June – 14 June 2008) with obvious under prediction of OH. The RGM peaks during this period were the highest values in 2008 campaign with a maximum of ~80 $pg.m^{-3}$. During this period, up to 4–5 pptv of BrO were observed by CIMS, and up to ~3 pptv of BrO were observed by LP DOAS. The BrO levels were near the detection limits of the LP DOAS and CIMS instruments.The gaps of BrO and $HO_x$ measurements during 12 June – 14 June 2008 were due to the extremely high wind speeds (> 12 $m.s^{-1}$). The OH predictions from BM_BrO constrained by CIMS BrO measurements are also shown in Figure 5.9(b). These levels of BrO were not large enough to explain the under prediction of OH. The BrO concentrations during 12 June – 14 June 2008 only contribute ~10% to the OH production rate.

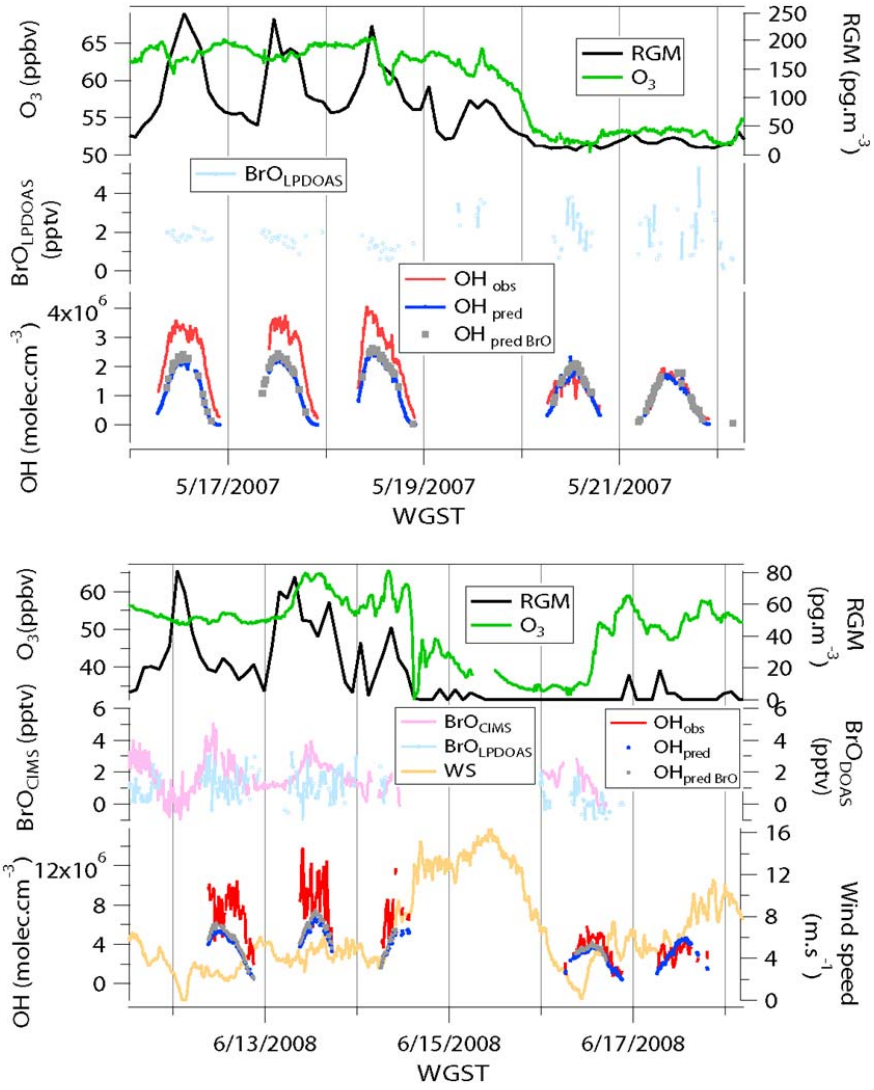


Figure 5.9(a): Observations of RGM, $O_3$, BrO by DOAS and OH, and predictions of OH from the BM and BM_BrO when enhanced RGM were observed in 2007 (16 May – 21 May 2007); Figure 5.9(b): The observations of RGM, $O_3$, OH, wind speeds, BrO by CIMS and DOAS, and the predictions of OH from the BM and BM_BrO when enhanced RGM were observed in 2008 (11 June –17 June 2008).

## 5.5 Conclusions

The median midday values of $HO_2$+$RO_2$ and OH concentrations observed by CIMS were $2.7 \times 10^8$ molec.cm$^{-3}$ and $3.0 \times 10^6$ molec.cm$^{-3}$ in spring 2007, and $4.2 \times 10^8$

molec.cm$^{-3}$ and 4.1× 10$^{6}$ molec.cm$^{-3}$ in summer 2008 at Summit. The BM was reasonably accurate for $HO_2$+$RO_2$ (R = 0.90, slope = 0.87 in 2007; R = 0.79, slope = 0.96 in 2008) but under predicted OH (R = 0.83, slope = 0.72 in 2007; R = 0.76, slope = 0.54 in 2008). This confirmed our understanding of the dominant $HO_x$ sources and sinks in this environment and that there may be mechanisms perturbing $HO_x$ cycling and enhancing OH above the snow pack. Inclusion of HONO source in the model did not impact the correlation between predictions and observations of $HO_x$ significantly and did not improve the ratio of OH to $HO_2$+$RO_2$. BrO levels detected by CIMS and LP DOAS generally ranged from below detection limits to ~6 pptv and ~5 pptv, respectively. The correlation between observed and predicted $HO_2$+$RO_2$ and OH from the BM_$BrO_{CIMS}$ slightly improved relative to the BM. The model incorporating bromine chemistry brought the average hourly OH and $HO_2$+$RO_2$ predictions closer to the observations in 2008. This indicates that BrO at Summit impacted the $HO_x$ levels, although most of the discrepancies between observations and models cannot be explained by the influence of detected BrO. High levels of RGM were found to be coincident with the significant under predictions of OH, and exclusion of high RGM periods significantly increased the agreement between predicted and observed OH. This is consistent with bromine chemistry and potentially other chemistry leading to elevated RGM and impacting the production OH from $HO_2$ and $RO_2$. Enhanced snow photochemistry producing $H_2O_2$, $CH_2O$ and potentially other radical precursors at higher temperature may have contributed to the larger discrepancy between predicted and observed $HO_x$ in summer 2008.

# CHAPTER 6

# CHARACTERIZATION OF SOLUBLE BROMIDE MEASUREMENTS AND A CASE STUDY OF BRO OBSERVATIONS DURING ARCTAS

## 6.1 Introduction

Tropospheric ozone depletion events (ODEs) have frequently been observed in or near the marine boundary layer in the Arctic [e.g. Oltmans, 1981; Bottenheim et al., 2009] and the Antarctic [e.g. Jones et al., 2009] during spring time. The ODEs can extend over horizontal scales of hundreds of kilometers [Ridley et al., 2003] and vertically from the surface to altitudes as high as several hundred meters to ~1 km [Bottenheim et al., 2002; Ridley et al., 2003]. In ODEs ozone mixing ratios drop from typical 30–40 ppbv to as low as 1 ppbv [e.g. Bottenheim et al., 2009 and 2002; Anlauf et al., 1994]. During ODEs, bromine compounds can oxidize gaseous elemental mercury (GEM) to more active and soluble mercury compounds [e.g. Lindberg et al., 2002], which can deposit to the surface and become involved in biogeochemical cycles. The oxidation of certain volatile organic compounds (VOCs) can also be enhanced during ODEs [e.g. Jobson et al., 1994].

Field measurements [e.g. Barrie et al., 1988; Hausmann and Platt, 1994] and modeling results [e.g. Fan and Jacob, 1992; McConnell et al., 1992] have demonstrated that bromine chemistry plays a large role in ODEs. The mechanisms of bromine

catalyzed ozone destruction are reviewed by Simpson et al. [2007a] and the key reactions are listed below.

$$Br_2 + h\nu \rightarrow 2Br \quad \text{R6.1}$$

$$Br + O_3 \rightarrow BrO + O_2 \quad \text{R6.2}$$

$$BrO + BrO \rightarrow 2Br + O_2 \quad \text{R6.3}$$

$$BrO + HO_2 \rightarrow HOBr + O_2 \quad \text{R6.4}$$

$$BrO + NO \rightarrow Br + NO_2 \quad \text{R6.5}$$

$$BrO + h\nu \rightarrow Br + O \quad \text{R6.6}$$

$$HOBr + h\nu \rightarrow Br + OH \quad \text{R6.7}$$

$$Br + CH_2O \rightarrow HBr + HCO \quad \text{R6.8}$$

$$Br + HO_2 \rightarrow HBr + O_2 \quad \text{R6.9}$$

$$HOBr\ (aq) + Br^- + H^+ \rightarrow Br_2\ (aq) + H_2O \quad \text{R6.10}$$

$$BrO + NO_2 + M \rightarrow BrONO_2 + M \quad \text{R6.11}$$

$$BrONO_2 + H_2O \rightarrow HOBr\ (aq) + HNO_3\ (aq) \quad \text{R6.12}$$

$Br_2$ photolyzes and produces Br atoms at sunrise (R6.1). Ozone is destroyed by a catalytic cycle initiated by the reaction of Br with $O_3$, followed by the self-reaction of BrO that regenerates Br atoms and destroys odd oxygen (R6.2 and R6.3). The efficiency of the cycle is suppressed by the conversion of bromine radicals to HBr, which is soluble and therefore can deposit to aerosols or the surface [Evans et al., 2003]. HOBr, which is produced by the reaction of BrO and $HO_2$ (R6.4) as well as $BrONO_2$ hydrolysis (R6.12), can photolyze to produce Br atoms (R6.7) or react with $Br^-$ on surfaces to regenerate $Br_2$ (R6.10) and sustain active bromine chemistry [Fan and Jacob, 1992]. The most abundant daytime gas-phase bromine species in the above mechanism, when ozone is above 1 ppbv

in a typical Arctic environment ($NO_2$ < 5 pptv), are BrO, HOBr and HBr [e.g. Evans et al., 2003; Liao et al., 2011c]. The most abundant night time species for these conditions is likely to be $Br_2$ [Liao et al., 2011c].

Models incorporating bromine chemistry have been developed to simulate global ozone and mercury concentrations [e.g. Zeng et al., 2003; Holmes et al., 2010]. However, the sources of active bromine in the atmosphere are not well quantified [e.g. Simpson et al., 2007a and references therein]. Consequently, the bromine source is often parameterized in models or obtained from satellite observations of BrO [e.g. Fan and Jacob, 1992; Zeng et al., 2003]. However, there are challenges deriving the tropospheric column BrO from satellite observations, which are obtained by subtracting the stratospheric contribution from a retrieval of total column BrO. Basic efforts at inferring tropospheric column BrO have assumed the stratospheric contribution is zonally symmetric. However, Theys et al. [2009] showed that the stratospheric burden of total bromine exhibits strong zonal asymmetries at high latitudes, particularly during boreal spring. In addition, Salawitch et al. [2010] demonstrated the sensitivity of tropospheric column BrO inferred from satellites to zonal asymmetries in the satellite burden. Another issue is the impact of clouds on the calculation of air mass factors (AMFs) and the retrieval processes for the altitudes below the clouds [Kühl et al., 2008; Theys et al., 2011; Choi et al., 2011]. The validation of tropospheric column BrO inferred from satellite retrievals using *in situ* measurements of BrO is an important research task, which we also address below.

The Arctic Research of the Composition of the Troposphere from Aircraft and Satellites (ARCTAS) [Jacob et al., 2010] mission and the Aerosol, Radiation, and Cloud

Processes affecting Arctic Climate (ARCPAC) study [Brock et al., 2011] in spring 2008 provided an excellent opportunity to validate satellite BrO observations with *in situ* measurements of bromine species. ARCTAS and ARCPAC both featured research flights in the Arctic using aircraft with large suites of instruments [Jacob et al., 2010; Brock et al., 2011]. Both the NASA DC-8 and NOAA WP-3D were equipped with chemical ionization mass spectrometers (CIMS) capable of measuring BrO and $Br_2$+HOBr [Neuman et al., 2010]. The NASA DC-8 was also equipped with a mist chamber (MC) measuring soluble bromide. The MC soluble bromide measurement is the sum of all gas phase species that dissolve in aqueous solution to form $Br^-$ [Ridley et al., 2003; Dibb et al., 2010]. This measurement has been used in several polar locations and has proved to be an excellent tracer for active bromine chemistry [Ridley et al., 2003]. Results from ARCTAS and ARCPAC indicated that tropospheric BrO levels were often much smaller than those derived from satellite data, particularly for an assumption of a zonally symmetric stratospheric burden. Salawitch et al. [2010] showed that low *in situ* BrO concentrations and background, non depleted levels of $O_3$ were often observed in the footprint of satellite BrO "hotspots", especially over Hudson Bay. They suggested this apparent discrepancy could be resolved if very short lived bromocarbons contribute large amounts of inorganic bromine to the lowermost stratosphere, leading to substantial BrO mixing ratios that could give elevated column BrO in regions of a low altitude (high pressure) tropopause. Neuman et al. [2010] analyzed a series of flights from ARCPAC and ARCTAS and showed that active bromine ($Br_2$ + HOBr) (up to ~16 pptv) was often detected in the marine boundary layer but found relatively low levels of BrO (up to ~4 pptv). The focus of this work is to investigate the ARCTAS DC-8 flight on 17 April 2008

when the highest BrO and soluble bromide levels were observed by CIMS and MC, respectively. The response of the MC to the most abundant bromine ($Br_2$, BrO, HOBr, and HBr) species is quantified to allow a thorough comparison of CIMS and MC data. Column abundances are derived from the *in situ* data and compared to satellite observations.

## 6.2 Methods

### 6.2.1 Mist chamber (MC) characterization

The response of the MC to the abundant bromine species ($Br_2$, BrO, HOBr, and HBr) was determined in a series of laboratory tests. A known amount of each species was quantitatively delivered to the MC inlet and the resulting concentration of bromide was measured. In this manner the MC response factor per atom of bromine was measured. A CIMS was used to quantify the $Br_2$, HOBr and BrO distribution delivered to the MC. This was critical as HOBr and BrO could not be delivered to the MC in a pure form.

#### 6.2.1.1 Chemical ionization mass spectrometer (CIMS)

The CIMS is very similar to that used to measure BrO, PANs, $HO_2NO_2$, and $SO_2$ [Liao et al., 2011a; Slusher et al., 2004; Kim et al., 2007; Huey, 2007]. The methods used to measure and calibrate the CIMS to BrO and $Br_2$ are described in Liao et al. [2011a]. Hydrated $I^-$ was utilized as a reagent ion to detect the bromine species and the corresponding reactions of the core ions are listed below;

$$Br_2 + I^- \rightarrow I\,Br_2^- \qquad \text{R6.13}$$

$$BrO + I^- \rightarrow IBrO^- \qquad \text{R6.14}$$

$$HOBr + I^- \rightarrow IHOBr^- \quad \text{R6.15}$$

$I^-$ was chosen as a reagent ion because it can selectively and accurately detect HOBr, BrO, and $Br_2$ [Liao et al., 2011a, c; Neuman et al., 2010]. $SF_6^-$ was not used as a reagent ion in this study as it is not capable of selectively detecting HOBr [Huey et al., 1995]. The accuracy of the $Br_2$, BrO and HOBr measurements in the laboratory were estimated to be 7%, 32%, and 32%, respectively.

6.2.1.2 Mist chamber (MC)

The mist chamber, similar to that used to measure $HNO_3$ and other soluble species [e.g. Dibb et al., 1998], can detect soluble bromide ($Br^-$) in gas phase and fine particles in the sampling flow. The gaseous species were concentrated into a small volume of ultrapure water and the stripping solutions were analyzed by ion chromatography as $Br^-$ in the solution [Dibb et al., 1994]. The $Br^-$ concentration in the sampling gases was determined from the concentration of $Br^-$ in the solution, the solution volume and the gas flow rate to the MC. The measurement uncertainty for soluble bromide was ~±15%. The uncertainty represents a combination of accuracy and precision at the one sigma level.

6.2.1.3 Experiment setup

The CIMS and MC were operated simultaneously in the same laboratory. Bromine compounds were delivered to both instruments through perfluoroalkoxy (PFA) Teflon tubing. In the initial experiments, setup A (Figure 6.1), a flow of $N_2$ at 3 standard liters per minute (slpm) containing bromine compounds was delivered to the inlets of the CIMS and the MC alternately with the same Teflon tubing. In later experiments, setup B,

a 3 slpm flow containing bromine compounds was symmetrically divided with a PFA tee between the CIMS and MC. The length of the Teflon tubing from the HOBr source to the MC was ~1.2 m longer than to the CIMS in setup B. As a consequence, any possible interactions of gas with the sampling line were the same in setup A for both instruments and were larger for the MC in setup B. Upon exiting the sample line, the gas flowed directly into the CIMS ion-molecule reaction tube (flow tube), where very little wall interaction and conversion of bromine species (e.g. HOBr to $Br_2$) occur [Neuman et al., 2010]. The potential interactions with other surfaces in the MC (e.g. the wetted glass walls of the mist chamber) may cause interconversion of bromine species. As setup B better represented the conversion of bromine compounds (e.g. HOBr) on the sampling inlet of the MC on the DC-8, the detection efficiencies of HOBr and $Br_2$ from setup B are used to predict soluble bromide concentrations.

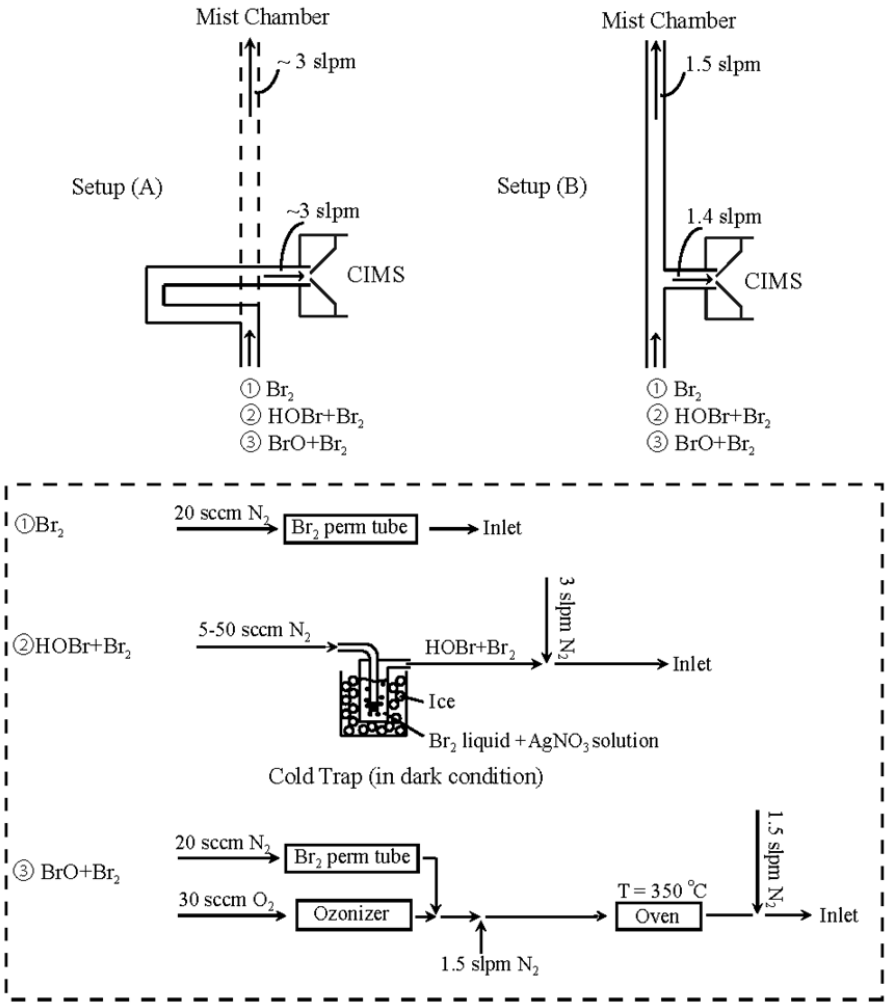


Figure 6.1 Inlet configurations and $Br_2$, HOBr and BrO sources for soluble bromide characterization. The solid inlet line presents the sampling inlet connecting to the CIMS and the dashed inlet line denotes the same inlet line connecting to the MC.

6.2.1.4 $Br_2$, BrO, HOBr and HBr preparation

Pure gas phase $Br_2$ was obtained from a permeation tube (Kin-tek Trace Source™ disposable permeation tube for bromine). 20 standard cubic centimeters per minute (sccm) of $N_2$ continuously flowed over the $Br_2$ permeation tube, which was held at a constant temperature (40˚C). The $Br_2$ permeation tube output was measured by

converting $I^-$ to $I_3^-$ in aqueous solution [Liao et al., 2011a] and was found to be 86 ± 6 ng/min ( ~4 ppbv in 3 slpm $N_2$ flow).

BrO was generated by the reaction of $Br_2$ with O ($^3P$) in excess $O_3$ [Liao et al., 2011a]. $O_3$ was produced by flowing 30 sccm of $O_2$ through a quartz tube illuminated by a UV lamp. The $O_3/Br_2$ mixture was diluted in ~1.5 slpm $N_2$ and flowed through an oven. When the oven was heated to ~350 ˚C, BrO was produced by the following series of reactions.

$$O_3 + M \rightarrow O_2 + O(^3P) + M \qquad \text{R6.16}$$

$$Br_2 + O(^3P) \rightarrow BrO + Br \qquad \text{R6.17}$$

$$Br + O_3 \rightarrow BrO + O_2 \qquad \text{R6.18}$$

The CIMS sensitivity ratio of BrO to $Br_2$ was estimated to be 0.47 ± 25%, based on the amount of BrO synthesized and the amount of $Br_2$ decomposed [Liao et al., 2011a].

Gas phase HOBr was prepared by adding 5–7 drops of liquid $Br_2$ to $AgNO_3$ aqueous solution (2.2g $AgNO_3$ in 100mL de-ionized $H_2O$) in a glass trap that was kept at 0˚C in the dark [Jin et al., 2007]. The $AgNO_3$ is used to precipitate out $Br^-$ as AgBr. This drives the equilibrium towards HOBr and reduces the degassing of HBr from the solution.

$$Br_2 + H_2O \Leftrightarrow HOBr + H^+ + Br^- \qquad \text{R6.19}$$

$$Ag^+ + Br^- \rightarrow AgBr\downarrow \qquad \text{R6.20}$$

Gas phase HOBr and $Br_2$ were removed from the trap in a flow of $N_2$ (5-50 sccm). The resulting gas phase mixture of HOBr and $Br_2$ was diluted into a $N_2$ flow of ~3 slpm and used as a source of HOBr. In general, the ratio of HOBr to $Br_2$ in the source flow was

3–4 depending on $N_2$ flow rates. The amount of HOBr in the flow was determined by conversion of the HOBr to $Br_2$ via reactions on humidified NaBr crystals.

$$HOBr + NaBr \rightarrow Br_2 + Na^+ + OH^- \qquad R6.21$$

Assuming a 1:1 yield for this reaction, the relative CIMS sensitivity of HOBr to $Br_2$ was determined to be 0.5 ± 25%.

HBr was obtained from a commercial source tube (Kin-tek Trace Source$^{TM}$ 57Series Hydrogen bromide), which is a small stainless steel cylinder (15 cm l. × 4.5 cm OD) with a Teflon membrane that allows permeation of the HBr. The source was kept at a constant temperature of 30˚C and 20 sccm of $N_2$ was continuously passed over the source. The output of the HBr from the source was determined to be 23 ng $min^{-1}$ by passing the flow through aqueous solution followed by ion chromatographic measurements.

### 6.2.2 BrO and soluble bromide measurements from the DC-8

The CIMS instrument aboard the NASA DC-8 aircraft that measured halogens was mechanically nearly identical to the one in the laboratory experiments here but used different ion chemistry. The CIMS utilized $SF_6^-$ as a reagent to detect halogen and other species (e.g. BrO, $SO_2$) as negative product ions (e.g. $BrO^-$, $F_2SO_2^-$). The configuration and performance of the CIMS instrument are described in Neuman et al. [2010]. The CIMS and the MC sampling inlets on the DC-8 were ~1 m and heated to 40°C. The detection limits of BrO from the DC-8 ranged from 2-5 pptv for a 30s sampling period and the measurement uncertainty was ± 40%. The DC-8 MC measurements were performed using an instrument described in detail by Scheuer et al. [2003, 2010]. The

soluble bromide detection limit was 1 pptv for a 1.5 min sampling period in the boundary layer and increased with flight altitude to ~6 pptv at 12 km. The soluble bromide measurement uncertainty was ± (15% + 0.5 pptv).

### 6.2.3 HBr, HOBr and soluble bromide prediction during ARCTAS

A simple photochemical model was used to predict HBr and HOBr levels from CIMS measurements of BrO. The mechanism used in the model includes reactions R6.2 – R6.9 as well as the heterogeneous loss of HBr and HOBr. HBr and HOBr were assumed to be in steady state due to their relatively short lifetimes of ~1 hour and ~8 minutes, respectively. The lifetime of HBr is mainly determined by heterogeneous loss on aerosol surfaces [Fan and Jacob et al., 1992; Liao et al., 2011b]. Because $NO_2$ concentrations (< 5 pptv) were near or below detection limits when significant BrO was detected (BrO > 3 pptv), $BrONO_2$ formation was neglected. The photochemical model was constrained by observations of BrO, $CH_2O$, NO, $O_3$, $HO_2$, J values, temperature, pressure, aerosol surface area and aerosol number density on DC-8. $CH_2O$ was measured by a difference frequency generation absorption spectrometer [Weibring et al., 2006]. NO and $O_3$ were measured from a 4-channel chemiluminescence instrument [Weinheimer et al., 1998]. J values were obtained from NCAR actinic flux spectroradiometers [Shetter and Muller, 1999]. Aerosol surface area and number density were measured by an ultra-high sensitivity aerosol spectrometer (UHSAS) [Cai et al., 2008]. Constrained HBr and HOBr calculations combined with the measured response factors of the MC to these species allowed soluble bromide to be predicted from CIMS observations of BrO.

### 6.2.4 Satellite-derived tropospheric BrO vertical column density

The tropospheric BrO vertical column density (VCD) is derived using the residual method [Theys et al., 2011; Choi et al., 2011]. The analysis uses: the slant column density (SCD) of BrO as provided in the publicly released Ozone Monitoring Instrument (OMI) BrO v3.0 data product [Kurosu and Chance, 2011]; air mass factors (ratio of slant to vertical columns) found using a radiative transfer model [Choi et al., 2011]; as well as stratospheric column BrO obtained from a model simulation for boreal spring 2008 [Salawitch et al., 2010]. A detailed explanation and discussion of the sensitivity of satellite-derived tropospheric column BrO is given in Choi et al. (2011). Here we provide a brief overview.

OMI is a nadir-viewing ultraviolet and visible (UV/Vis) sensor on the NASA Aura satellite, which is in a sun-synchronous polar orbit with a local overpass time near 13:30. BrO SCD is retrieved by direct fitting of backscattered UV radiances to absorption cross-sections of BrO (the target gas), $NO_2$, HCHO, $SO_2$ and inelastic rotational-Raman scattering (also known as the Ring effect) using a non-linear least-squares approach [Chance, 1998] with a spectral fitting window between 319 and 347.5 nm.

An estimate of stratospheric BrO VCD is calculated from a model simulation [Salawitch et al., 2010]. Distributions of all species other than bromine bearing compounds originate from a run of the Whole Atmosphere Community Climate Model (WACCM) [Garcia et al., 2007] conducted using analyzed winds for April 2008. Vertical distributions of $Br_y$ (the sum of inorganic bromine species) are specified, using the relation between $Br_y$ and CFC-12, as well as profiles of CFC-12 from the NASA Global Modeling and Assimilation Office (GMAO) Goddard Earth Observing System Data

Assimilation System Version 5 (GEOS-5) [Rienecker et al., 2007]. The contribution of very short lived (VSL) bromocarbons is represented by adding 7 pptv to the baseline $Br_y$ versus CFC-12 relation, which represents gas injection of bromine from very short lived sources. The baseline $Br_y$ relation represents source of gas injection of the organic bromocarbons that cross the tropopause: $CH_3Br$, halons, and $CH_2Br_2$. Mixing ratios of BrO at the time of satellite overpass are determined using a photochemical steady state model constrained by radical precursors (e.g., $O_3$, $H_2O$, $CH_4$, $Cl_y$, $NO_y$, $Br_y$, etc) from WACCM [Choi et al., 2011]. The stratospheric BrO VCD is obtained by integrating the BrO mixing ratio from the tropopause (WMO definition of thermal tropopause) to 0.01 hPa.

AMFs, a ratio of SCD to VCD by definition, are used to convert SCD to VCD (VCD = SCD / AMF). The stratospheric AMF is provided as an OMI total column product. The tropospheric AMF is calculated using the Linearized Discrete Ordinate Radiative Transfer (LIDORT) model [Spurr et al., 2001], which considers the effects of the tropospheric BrO profile, surface albedo, and viewing geometry [Choi et al., 2011].

The tropospheric BrO VCD is calculated from a tropospheric residual column obtained by subtracting the stratospheric SCD (product of stratospheric VCD and stratospheric AMF) from the total SCD. The tropospheric BrO VCD is then obtained by dividing the residual tropospheric slant column by the tropospheric AMF. Further details are given in Choi et al. [2011]. Our approach is similar to that of Theys et al. [2011], except our

stratospheric VCD is larger than that used by Theys et al. [2011] and we use an independent radiative transfer model.

## 6.3 Results and Discussion

### 6.3.1 Response of the MC to $Br_2$, HOBr, BrO and HBr

BrO, HOBr, HBr are likely the most abundant daytime bromine species when $O_3$ is not completely depleted in the typical Arctic environment (NO < 5 pptv) [Evans et al., 2003]. $Br_2$ is the likely dominant nighttime bromine species under this condition. As a result, the detection efficiencies of BrO, HOBr, HBr and $Br_2$ by the MC were characterized and reported in this study.

Table 6.1 The response of MC to different levels of $Br_2$ and HOBr sources from setup A and B.

| Setup A | Soluble bromide $Br^-$ (ppbv) | $Br_2$ source (ppbv) | HOBr source (ppbv) | Ratio= $Br^-$ /($Br_2$×2+HOBr) |
|---|---|---|---|---|
| HOBr +$Br_2$ mixture ($N_2$ flow = 25 sccm) | 5.6 | 1.7 | 9.8 | 0.42 |
| $Br_2$ permeation tube | 2.5 | 3.3 | 0.0 | 0.38 |
| HOBr + $Br_2$ mixture ($N_2$ flow = 25 sccm) | 5.1 | 2.2 | 7.9 | 0.42 |
| HOBr + $Br_2$ mixture ($N_2$ flow = 10 sccm) | 1.8 | 0.9 | 3.3 | 0.36 |
| $Br_2$ permeation tube | 2.7 | 3.3 | 0.0 | 0.41 |
| HOBr + $Br_2$ mixture ($N_2$ flow = 10sccm) | 1.9 | 0.8 | 2.8 | 0.44 |
| **Setup B** | **Soluble bromide $Br^-$ (ppbv)** | **$Br_2$ source (ppbv)** | **HOBr source (ppbv)** | **Ratio= $Br^-$ /($Br_2$×2+HOBr×2)** |
| $Br_2$ permeation tube | 3.4 | 3.8 | 0 | 0.45 |
| HOBr + $Br_2$ mixture ($N_2$ flow = 30 sccm) | 10.5 | 2.4 | 8.8 | 0.47 |
| HOBr + $Br_2$ mixture ($N_2$ flow = 30 sccm) | 12.4 | 2.7 | 9.1 | 0.53 |
| HOBr + $Br_2$ mixture ($N_2$ flow = 20 sccm) | 9.6 | 1.7 | 6.4 | 0.59 |

Table 6.2 The ratio of detected $Br^-$ to $Br_2$, HOBr and BrO. The errors are estimated from the uncertainties in $Br_2$, HOBr, BrO and $Br^-$ measurements and the variance (one standard deviation) of the individual ratio measurements.

| | $Br^-/(Br_2 \times 2)$ | $Br^-/HOBr$ | $Br^-/BrO$ |
|---|---|---|---|
| Setup A | 0.40 ± 0.10 | 0.41 ± 0.15 | --------- |
| Setup B | 0.45 ± 0.10 | 1.06 ± 0.30 | 0.4 ± 0.1 |

6.3.1.1 $Br_2$

The MC responded to the presence of $Br_2$ in the gas phase as $Br^-$ (Table 6.1). The ratio of detected $Br^-$ to $Br_2$ was found to be 0.40 ± 0.10 per Br atom for setup A and 0.45 ± 0.10 per Br atom for setup B (Table 6.2). The error bars are estimated from a combination of the estimated potential systematic error in $Br_2$ and $Br^-$ measurements and variance of the individual $Br^-$ to $Br_2$ ratio measurements. To confirm the nearly complete dissolution of $Br_2$, the $Br_2$ permeation tube output was passed through a trap containing deionized water. The output of the trap was monitored by the CIMS and effectively all $Br_2$ was found to be scrubbed by the solution, consistent with efficient detection of $Br_2$ by the MC. $Br_2$ is hydrolyzed to form $Br^-$ and HOBr in aqueous solution, with a hydrolysis rate constant, $k_{6.19,}$ of 110 $s^{-1}$ (at 20°C) [Eigen and Kustin,1962]. This suggests that each $Br_2$ molecule produces one bromide ion which is detected with near 100% efficiency by the MC. The HOBr produced in aqueous solution in the MC does not appear to convert to bromide on the time scale of the measurement (5 minutes). Thus an efficiency of ~0.5 (on a per molecule basis) for detecting the bromine atoms in $Br_2$ as bromide is consistent with its known solution chemistry.

6.3.1.2 HOBr

The MC was found to consistently respond to the presence of HOBr as bromide (Table 6.1). This is likely due to conversion of HOBr on the sampling surfaces to $Br_2$, which is detected by the MC as $Br^-$. The ratio of HOBr to $Br^-$ detected is 0.41 ± 0.15 for setup A and is 1.06 ± 0.30 for setup B (Table 6.2). The error bars are calculated from a combination of the estimated potential systematic error in HOBr and $Br^-$ measurements and the variance of the individual $Br^-$ to HOBr ratio measurements. The results for $Br_2$ indicate that HOBr in aqueous solution in the MC is not detected as bromide. However, Neuman et al. [2010] have demonstrated that gas phase HOBr is readily converted to $Br_2$ on even nominally clean surfaces. The greater detection efficiency for HOBr in the MC for the longer inlet setup B is also consistent with conversion of HOBr to $Br_2$, with some of the bromine coming from the inlet surface. The resulting $Br_2$ will hydrolyze and be detected in the MC as described above. Consequently, HOBr will be detected efficiently as bromide by the MC via conversion on the inlet and other surfaces to $Br_2$.

$$HOBr \rightarrow Br_2 \xrightarrow{k6.19} Br^- \qquad \text{R6.22}$$

6.3.1.3 BrO

BrO was also detected as soluble bromide by the MC. The ratio of BrO to $Br^-$ was found to be 0.4 ± 0.1 (Table 6.2). As this result was somewhat surprising, it was confirmed by repeatedly turning on and off the BrO from the $Br_2/O_3$ source by modulating the ozone levels. In addition, tests with the CIMS confirmed that BrO in a gas stream is removed by deionized water. At this time the mechanism for the conversion of ~40% of BrO to $Br^-_{(aq)}$ is not determined.

6.3.1.4 HBr

The sensitivity ratio of HBr to $Br_2$ measured by CIMS using reagent ion $I^-$ was less than 1 : 100, which implies that the CIMS instrument using reagent ion $I^-$ has a very low sensitivity for detecting HBr. The CIMS then was not used to quantify HBr and the HBr permeation tube output was determined to be 23 ng/min by ion chromatography. The MC detected HBr with 0.95 ± 0.1 efficiency. This is consistent with detection of effectively 100% of HBr as soluble bromide by the MC.

6.3.1.5 Implications for soluble bromide measurements

The results above indicate that the MC measurements of soluble bromide during ARCTAS (and other missions such as Tropospheric Ozone Production around the Spring Equinox (TOPSE)) [Ridley et al., 2003] are due to a multitude of compounds. As conversion of HOBr to $Br_2$ on the walls of the MC or sampling line was very likely, soluble bromide ($[Br^-]$) can be estimated by the following equation.

$$[Br^-] = 0.9\,[Br_2] + 1.06\,[HOBr] + 0.4\,[BrO] + 0.95\,[HBr]. \qquad \text{Eqn 6.1}$$

This indicates that a MC can be used to examine the areas of active bromine chemistry where BrO and HOBr are enhanced.

### 6.3.2 Case study of BrO and soluble bromide measurements

On research flight 17 April 2008 of ARCTAS the highest bromine levels for the mission were observed. During this flight the NASA DC-8 frequently sampled ozone depleted air masses, with significant levels of bromine in the Arctic boundary layer. The aircraft track for this flight from Fairbanks, AK to the North Pole is displayed in the top

panel of Figure 6.2. The flight track is color coded by altitude. The aircraft sampled the boundary layer air five times during this flight. $O_3$ depletions were clearly observed when the boundary layer was sampled (middle panel of Figure 6.2). Further description of this flight is given by Choi et al. [2011].

The observations of BrO, $Br_2$+HOBr, soluble bromide, $O_3$, and altitude on one flight leg in the boundary layer, where maximum bromine was detected, are shown in the bottom panel of Figure 6.2. The corresponding region on the map is denoted with the red circle in the top panel of Figure 6.2. Ozone depletion and elevated bromine (soluble bromide, $Br_2$+HOBr and BrO) were clearly measured when the aircraft flew down to the boundary layer (altitude < 200 m). The maximum soluble bromide detected during this flight was ~31 pptv, when ozone was depleted to ~10 ppbv, and up to ~7 pptv BrO and HOBr + $Br_2$ were detected. Due to the conversion of HOBr on the Teflon inlet [Neuman et al., 2010], the CIMS $Br_2$ signal represents the lower limit to the sum $Br_2$ + HOBr. As the mixing ratio of rapidly photolyzed $Br_2$ in the daytime is likely to be very low (<= ~ 1 pptv) [Fan and Jacob, 1992, Liao et al., 2011b], the $Br_2$ signal is highly likely to correspond to HOBr.

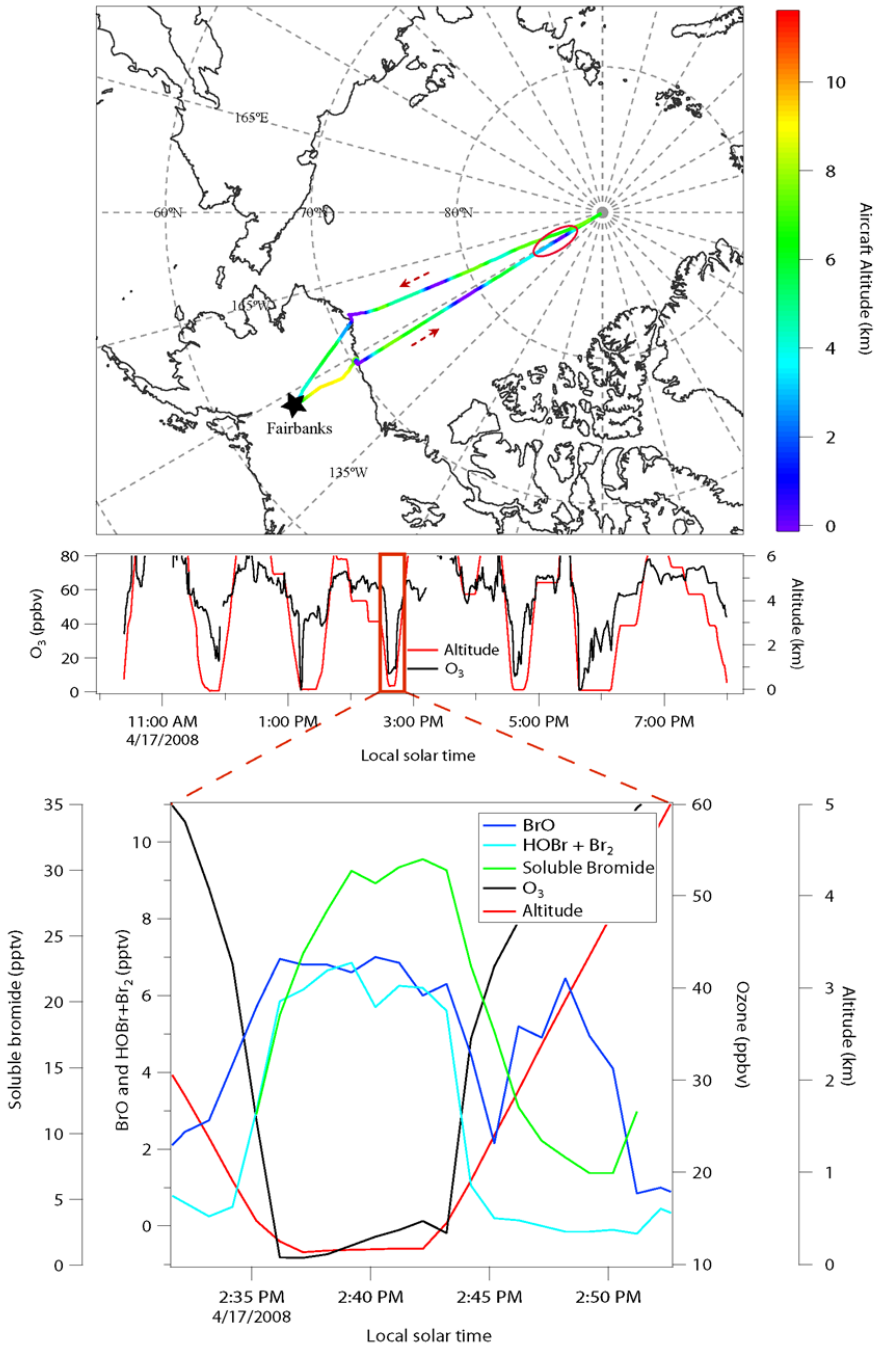


Figure 6.2 Top panel: The flight track of ARCTAS on 17 April 2008 color-coded with aircraft altitudes. The black star denotes the beginning of the flight and the dashed arrows represents the direction of the flight. The red circle shows the location on the flight track that corresponds to the bottom panel. Middle panel: Time series of observations of ozone and altitude. Bottom panel: Observations of soluble bromide, BrO, lower limit of $Br_2$+HOBr, $O_3$ and altitude for the flight leg with the highest levels of bromine.

To assess whether the concentrations of BrO reported by the CIMS instrument are consistent with the soluble bromide observations from the MC, we first calculated the abundances of HBr and HOBr using a photochemical model (described in section 6.2.3) constrained by the measurements of BrO and other species. Soluble bromide was then calculated based on the measured detection efficiency for BrO, HOBr, and HBr. An example of observed BrO and soluble bromide and modeled HOBr, HBr and soluble bromide on two flight legs, both with BrO above detection limit (> 2 pptv), is shown in Figure 6.3. The correlation plot of modeled and observed soluble bromide during 17 April 2008 flight when BrO was above detection limit (> 2 pptv) under unpolluted conditions (NO < 100 pptv) is shown in the left panel of Figure 6.4. Considering the measurement uncertainties in BrO (~40%), soluble bromide, J values, reaction rates, mass accommodation coefficients, and aerosol surface areas, the agreement ($R^2$ = 0.76; slope = 0.98; intercept = –3.5 pptv) between measured and modeled soluble bromide indicates that reported soluble bromide concentrations by the MC are consistent with the BrO measurements from the CIMS instrument as well as our current understanding of inorganic bromine photochemistry. It is also interesting to note that the modeled HOBr was well correlated with the measured HOBr + $Br_2$ ($R^2$ = 0.86, slope = 1.42, intercept = 1.71 pptv) (figure 6.4 right panel), consistent with the assumption of efficient conversion of HOBr on the inlet walls.

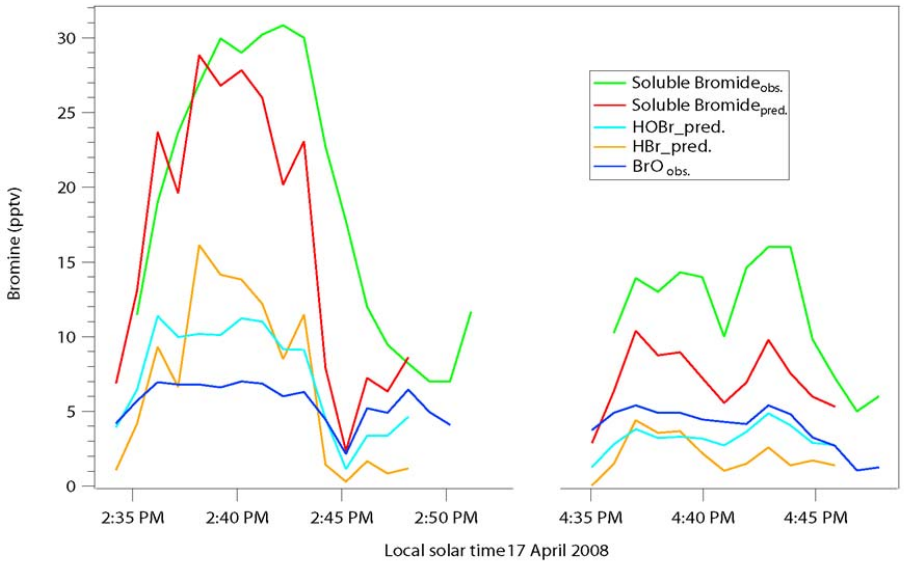


Figure 6.3 Example of observed BrO and soluble bromide, and predicted HOBr, HBr and soluble bromide for two marine boundary layer flight legs when the highest levels of BrO and soluble bromide were observed.

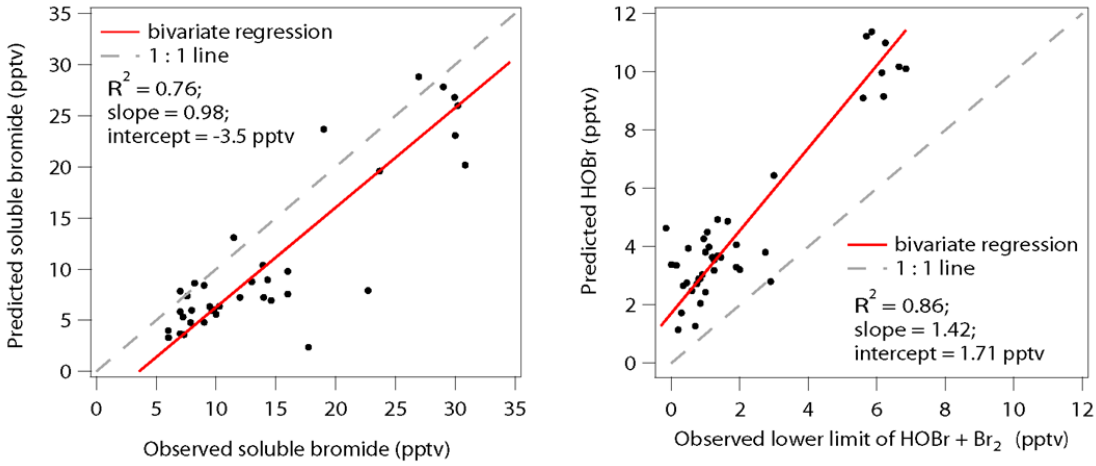


Figure 6.4 Left panel: correlation plot of predicted and observed soluble bromide in the boundary layer when BrO was above the detection limit (> 2 pptv) under unpolluted conditions (NO < 100 pptv). The correlation coefficient for this plot is 0.76. An equally weighted bivariate regression yields a slope of 0.98 and an intercept of –3.5 pptv. Right panel: correlation plot of predicted HOBr and observed lower limit of HOBr + $Br_2$ when BrO were above detection limit (> 2 pptv) under unpolluted condition (NO < 100 pptv). The correlation coefficient ($R^2$) for this plot is 0.86. An equally weighted bivariate regression yields a slope of 1.42 and an intercept of 1.71 pptv.

### 6.3.3 Comparison of BrO Satellite observations with *in situ* BrO measurements

The region of the Artic sampled by the DC-8 17 April 2008 provides ideal conditions for comparison of satellite and aircraft determinations of tropospheric BrO. The sky was clear, the surface was bright, and the viewing geometry was amenable for high sensitivity to tropospheric BrO by satellite sensors [Choi et al., 2011]. Here, the comparisons are made in terms of tropospheric BrO vertical column density ($BrO_{TROP}^{VCD}$). The OMI retrieval team reports total vertical column density of BrO. These data are post-processed using a radiative transfer model and an estimate of the stratospheric burden to yield $BrO_{TROP}^{VCD}$ [Theys et al., 2011; Choi et al., 2011].

Estimated $BrO_{TROP}^{VCD}$ from DC-8 *in situ* measurements of BrO on the 17 April 2008 flight are compared to $BrO_{TROP}^{VCD}$ retrieved from OMI pixels closest in space and time to the DC-8 flight track [Choi et al., 2011] in Figure 6.5. $BrO_{TROP}^{VCD}$ from airborne *in situ* BrO was calculated by integrating the profile of BrO from the surface to 7.5 km altitude. The lowest altitude sampled by the aircraft during individual profiles ranged from 100 to 500 m. When finding $BrO_{TROP}^{VCD}$, we assumed the BrO mixing ratio between the surface and the lowest sampled altitude was the median of values between 500 m and the lowest sampled altitude. The median DC-8 profile of BrO, for all of ARCTAS, was used for altitudes between the highest sampled by the DC-8 for a particular profile and 7.5 km. Since BrO was below the detection limit of CIMS above 7.5 km altitude, we assumed BrO was zero between 7.5 km and the tropopause. The error bars in Figure 6.5 represent

the uncertainties in satellite $BrO_{TROP}^{VCD}$ (horizontal) and *in situ* $BrO_{TROP}^{VCD}$ (vertical), respectively. These uncertainties are described in detail by Choi et al. [2011].

An orthogonal least square regression was used analyze the agreement between satellite and *in situ* $BrO_{TROP}^{VCD}$. Reduced chi-square is calculated by the minimum of the sum of the squared orthogonal distance between the measurements and the 1: 1 Line.

$$\chi^2 = \frac{1}{n-2}\sum_i \frac{(X_i - x_i)^2}{\sigma_{xi}^2} + \frac{(Y_i - y_i)^2}{\sigma_{yi}^2}$$

A value for reduced chi-square of 0.88 means the determinations of $BrO_{TROP}^{VCD}$ from *in situ* sampling and satellite retrieval agree, to within the measurement uncertainty. The satellite retrievals of tropospheric BrO using updated methods [Choi et al., 2011] captures the levels of BrO found by our CIMS instrument. This result, combined with the consistency between CIMS BrO and MC soluble bromide, represents an important advance in our quantitative understanding of tropospheric bromine chemistry.

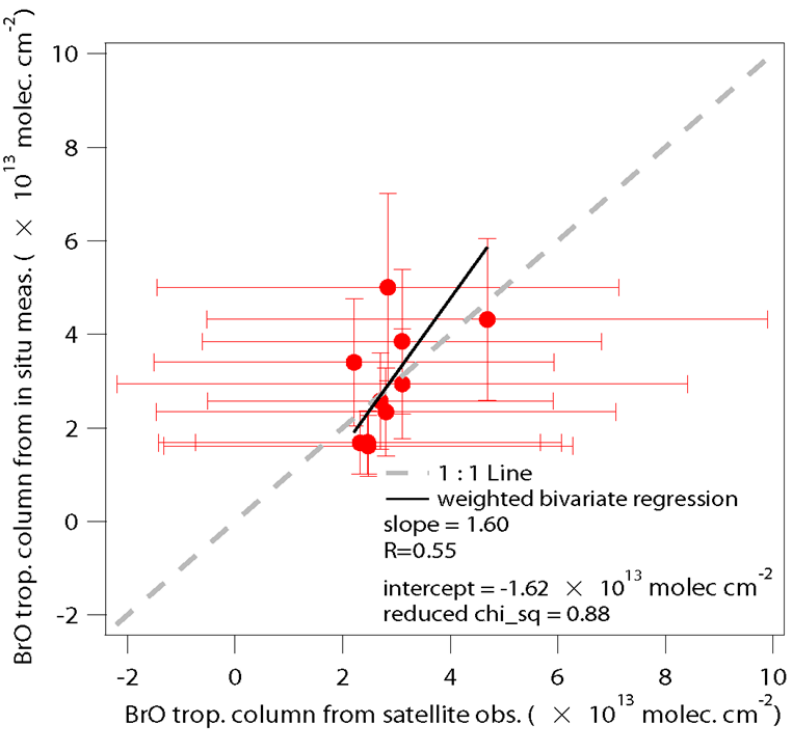


Figure 6.5 Scatter plot of calculated $BRO_{TROP}^{VCD}$ from *in situ* measurements along the flight track of flight on April 17 versus $BRO_{TROP}^{VCD}$ from OMI satellite observations. The satellite columns are for pixels closest in space and time to the aircraft profiles that resulted in the tropospheric columns (see text). Slope and intercept from weighted bivariate regression and the reduced chi-square are given.

## 6.4 Summary

Characterization of the MC response to gas phase bromine species enables better use of soluble bromide data from previous and future field missions focusing on polar halogen chemistry. In this study, the response of the MC to $Br_2$, HOBr, BrO and HBr as soluble bromide ($Br^-$) was measured. The MC was found to detect bromine in the following compounds $Br_2$, HOBr, BrO, and HBr as soluble bromide with an efficiency per molecule of 0.9 ± 0.1, 1.06 ± 0.30, 0.4 ± 0.1, and 0.95 ± 0.1, respectively. These

measured response factors (except that of $Br_2$) were used to model soluble bromide from CIMS measurements of BrO obtained on the 17 April 2008 flight of ARCTAS. The agreement ($R^2$ = 0.76; slope = 0.98; intercept = –3.5 pptv) between measured and observed soluble bromide, when BrO was above the detection limit (> 2 pptv) under unpolluted conditions (NO < 100 pptv), indicates *in situ* BrO measurements by CIMS were consistent with the observed soluble bromide. BrO column densities calculated from CIMS measurements were also consistent with the tropospheric BrO columns derived from OMI satellite data, using a stratospheric burden that includes a significant contribution from VSL bromocarbons.

# CHAPTER 7

# CONCLUSIONS

In this thesis the detailed bromine and chlorine chemistry in the Arctic is investigated by chemical ionization mass spectrometry. This work advances our understanding of the concentrations of speciated bromine and chlorine compounds and their impact, and the conditions likely favoring bromine and chlorine activation in the Arctic boundary layer. It also demonstrates the advantages of the application of CIMS, with low detection limits, fast time response and the capability to measure a series of compounds simultaneously, to investigate bromine and chlorine chemistry.

The excellent agreement ($R^2 = 0.85$) of BrO measurements between CIMS and long path-differential optical absorption spectroscopy (LP-DOAS) demonstrates the capability of chemical ionization mass spectrometry (CIMS) to accurately and sensitively measure BrO, an important bromine radical critical to estimate the bromine induced ozone loss rate. The first measurements of speciated HOBr were also achieved by CIMS in this work. The HOBr measurements can be reasonably well predicted by a photochemical model except at high wind speeds. High wind speeds associated with blowing snow are found to enhance active bromine concentrations likely by providing more surface area for heterogeneous recycling. Comparison of the observed BrO, HOBr and $Br_2$ diurnal speciation to a time dependent model simulation provided insight into the bromine recycling efficiency.

This thesis reports unexpected high levels of molecular chlorine ($Cl_2$) of up to

~400 pptv at Barrow, AK. Surfaces covered by snow and sea ice (especially multiple year sea ice) are probably the utlitmate source of the $Cl_2$. High levels $Cl_2$ have a large impact on methane oxidation and also significantly contribute to ODEs and MDEs.

Moreover, this thesis investigates the impact of BrO on $HO_x$ cycling above the Greenland ice sheet. Inclusion of bromine chemistry in the $HO_x$ box model brought the average OH and $HO_2$ + $RO_2$ predictions closer to the observations; however, the discrepancy between predicted and observed OH cannot be explained by the observed BrO levels. It is also interesting to find that the model under predicted OH when high levels of RGM were observed.

Finally, the thesis examines the detection efficiency of the mist chamber method to $Br_2$, HOBr, BrO and HBr as soluble bromide. The measured detection efficiencies were used to calculate the concentrations of soluble bromide during the ARCTAS campaign based on the CIMS BrO measurements and known bromine photochemistry. The good agreement between observed and calculated soluble bromide indicated that the BrO measurements were consistent with the soluble bromide measurements. This contributes to better use of soluble bromide measurements from both previous and future campaigns.

The discovery of unexpectedly high levels of $Cl_2$ at Barrow, AK in spring 2009 in the thesis encourages more measurements of chlorine species (e.g. $Cl_2$, HOCl, and ClO) in the Arctic to investigate if high levels of $Cl_2$ are ubiquitious in Arctic regions. Lab studies relevant to the Arctic environment are also urged to explore the source and formation mechanisms of $Cl_2$. Although the diurnal BrO, HOBr and $Br_2$ speciation according to the known bromine chemical mechanisms is confirmed by the *in situ*

measurements in the thesis, measurements of $BrONO_2$ and HBr are also needed to fully examine the bromine speciation especially in marine boundary layer.

# APPENDIX A

## IGOR CODE OF A STEADY-STATE $HO_X$ BOX MODEL WITH INCLUSION OF BROMINE CHEMISTRY

```
Macro PredictOH()

KillWaves/A/Z


//Concentrations

//Determinedewpt1()

DetermineKelvin()

DetermineDDPerNitric()

DetermineH2Ovapor()

DetermineNumDen()

DetermineNumDenH2O()

DetermineNumDenN2()

DetermineNumDenO2()

DetermineNumDenO3()

DetermineNumDenNO()


NumDenCH4()

NumDenCO()

NumDenBrO()
```

```
//rates
 RateConstantkk1()
 RateConstantkk2()
 RateConstantkk3()
 RateConstantkk4()
 RateConstantkk5()
 RateConstantkk6()
 RateConstantkk7()
 RateConstantkk8()
 RateConstantkk9()
 RateConstantkk10()
 RateConstantkk11()
 RateConstantkk12()
 RateConstantkk13()
 RateConstantkk14()
 RateConstantkk15()
 RateConstantkk16()
 RateConstantkk17()
 RateConstantkkt18()
 RateConstantkk19()
 RateConstantkk20()
 RateConstantkk21()
```

RateConstantkk22()

RateConstantkk23()

RateConstantkk24()

RateConstantkk25()

RateConstantkk26()

RateConstantkk27()

RateConstantkk28()

RateConstantkk29()

RateConstantkk30()

RateConstantkk31()

RateConstantkk32()

RateConstantkk33()

RateConstantkk34()

DetermineFractionO_H2O()

PredictHOx()

endMacro

```
//Determine Temp in Kelvin
Function DetermineKelvin()
	wave temp1
	Duplicate/o temp1 temp
	temp +=273.15
end

//Determine Dry Depostion Rate for (Per)Nitric
Function DetermineDDPerNitric()
	wave temp1
	Duplicate/o temp1 DDPN
	DDPN = 9.26e-5
end

//Determine the amount of water vapor as a function of Dew Point
Function DetermineH2Ovapor()
	wave Dewpt1
duplicate/o Dewpt1 vap
	 if (DewPt1 >= 0)
		vap = 6.11*10^(7.567*DewPt1/(239.7+DewPt1))

	else
		vap= 6.11*10^(9.716*DewPt1/(271.5+DewPt1))
```

```
	endif
end

//Determine Number Density as a function of Pressure
Function DetermineNumDen()
	wave temp, pressure
	Duplicate/o temp1 M
	M = ((Pressure/1013)*6.02e23)/(0.08206*Temp*1000)
end

//Determine Number Density of H2O
Function DetermineNumDenH2O()
	wave vap, M, Pressure
	duplicate/o vap H2Oc
	H2Oc = (vap/Pressure)*M
end

//Determine Number Density of Nitrogen
Function DetermineNumDenN2()
	wave M
	duplicate/o M N2c
	N2c = 0.78*M
```

```
end

//Determine Number Density of Oxygen
Function DetermineNumDenO2()
	wave  M
	duplicate/o M O2c
	O2c = 0.21*M
end

//Determine Number Density of Ozone
Function DetermineNumDenO3()
	wave O3, M
	duplicate/o O3 O3c
	O3c = (O3*1e-9)*M
end

	//Determine Number Density of NO
Function DetermineNumDenNO()
	wave NO, M
	duplicate/o NO NOc
	NOc = (NO*1e-12)*M
end
```

```
	//Determine Number Density of Methane
Function NumDenCH4()
	wave CH4, M
	duplicate/o CH4 CH4c
	CH4c = (CH4*1e-6)*M
end

	//Determine Number Density of CO
Function NumDenCO()
	wave CO, M
	duplicate/o CO COc
	COc = (CO*1e-9)*M
end
Function NumDenBrO()
	wave BrO, M
	duplicate/o BrO BrOc
	BrOc = (BrO*1e-12)*M
end

	//Determine rate constant O(D) + O2
Function RateConstantkk1()
```

```
	wave temp
	duplicate/o temp kk1
	kk1 = 3.3e-11*exp(55/Temp)
end

	//Determine rate constant O(D) + N2
Function RateConstantkk2()
	wave temp
	duplicate/o temp kk2
	kk2 = 2.15e-11*exp(110/Temp)
end

	//Determine rate constant O(D) + H2O
Function RateConstantkk3()
	wave Temp
	duplicate/o temp kk3
	kk3 = 1.63e-10*exp(60/Temp)
end

	//Determine rate constant OH + CO
Function RateConstantkk4()
	wave temp, M
	Duplicate/o  temp kHOCOhigh kHOCOlow kHCO2high kHCO2low kk4
```

```
	kHOCOlow = 5.9e-33*(temp/300)^(-1.4)
	kHOCOhigh  = 1.1e-12*(temp/300)^1.3
	kHCO2low = 1.5e-13*(temp/300)^0.6
	kHCO2high  = 2.1e9*(temp/300)^6.1
	kk4
=((kHOCOlow*M/(1+kHOCOlow*M/kHOCOhigh))*0.6^(1+(log(kHOCOlow*M/kHO
COhigh))^2)^-
1)+((kHCO2low/(1+kHCO2low/(kHCO2high/M)))*0.6^(1+(log(kHCO2low/(kHCO2hig
h/M)))^2)^-1)
end

	//Determine rate constant OH + CH4
Function RateConstantkk5()
	wave temp
	duplicate/o temp kk5
	kk5 = 2.45e-12*exp(-1775/Temp)
end

	//Determine rate constant CH3O2 + NO
Function RateConstantkk6()
	wave temp
	duplicate/o temp kk6
```

```
	kk6 = 2.8e-12*exp(300/Temp)
end



	//Determine rate constant CH3O2 + HO2
Function RateConstantkk7()
	wave temp
	duplicate/o temp kk7
	kk7 = 4.1e-13*exp(750/Temp)
end



	//Determine rate constant HO2 + NO
Function RateConstantkk8()
	wave temp
	duplicate/o temp kk8
	kk8 = 3.5e-12*exp(250/Temp)
end

	//Determine rate constant OH + HO2
Function RateConstantkk9()
	wave temp
	duplicate/o temp kk9
```

```
	kk9 = 4.8e-11*exp(250/Temp)
end

	//Determine rate constant HO2 + HO2
Function RateConstantkk10()
	wave temp, M,H2Oc
	duplicate/o temp kk10 fw
	fw = (1+1.4e-21*H2Oc*exp(2200/Temp))
	kk10 =((3.5e-13*exp(430/Temp))+(1.7e-33*M*exp(1000/Temp)))*fw
end

	//Determine rate constant NO + O3
Function RateConstantkk11()
	wave temp
	duplicate/o temp kk11
	kk11 = 3.0e-12*exp(-1500/Temp)
end
	// Determine rate constant OH + NO
Function RateConstantkk12()
	wave temp, M
	Duplicate/o  temp khonohigh khonolow kk12

	khonolow = 7.0e-31*(temp/300)^-2.6
```

```
	khonohigh  = 3.6e-11*(temp/300)^-0.1
	kk12 =
(khonolow*M/(1+khonolow*M/khonohigh))*0.6^((1+(log(khonolow*M/khonohigh))^2)
^-1)
end

	//Determine rate constant HO2 + O3
Function RateConstantkk13()
	wave temp
	duplicate/o temp kk13
	kk13 = 1.0e-14*exp(-490/Temp)
end

	//Determine rate constant OH + O3
Function RateConstantkk14()
	wave temp
	duplicate/o temp kk14
	kk14 = 1.7e-12*exp(-940/Temp)
end

	//Determine rate constant OH + HONO
Function RateConstantkk15()
	wave temp
```

```
        duplicate/o temp kk15
        kk15 = 1.8e-11*exp(-390/Temp)
end

        //Determine rate constant OH + NO2
Function RateConstantkk16()
        wave temp, M
        Duplicate/o  temp khno3high khno3low kk16

        khno3low = 9.1e-32*(temp/300)^-3.9
        khno3high  = 4.2e-11*(temp/300)^-0.5
        kk16 =
(khno3low*M/(1+khno3low*M/khno3high))*0.6^((1+(log(khno3low*M/khno3high))^2)
^-1)
end

        //Determine rate constant OH +HNO3
Function RateConstantkk17()
        wave temp, M
        Duplicate/o  temp1 kNO30 kNO32 kNO33 kk17

        kNO30 = 2.4e-14*exp(460/temp)
        kNO32  = 2.7e-17*exp(2199/temp)
```

```
	kNO33 = 6.5e-34*exp(1335/temp)
	kk17 = kNO30+(kNO33*M/(1+(kNO33*M/kNO32)))
end

	//Determine rate constant OH + OH
Function RateConstantkkt18()
	wave temp, M
	Duplicate/o  temp kh2o2high kh2o2low kk18
	kh2o2low = 6.9e-31*(temp/300)^-1.0
	kh2o2high  = 2.6e-11*(temp/300)^-0
	kk18
=((kh2o2low*M/(1+kh2o2low*M/kh2o2high))*0.6^((1+(log(kh2o2low*M/kh2o2high))^
2)^-1))+1.8e-12*exp(-0/temp)
end

	//Determine rate constant OH + H2O2
Function RateConstantkk19()
	wave temp
	duplicate/o temp kk19
	kk19 = 1.8e-12*exp(0/Temp)
end

	//Determine rate constant OH + CH2O
```

```
Function RateConstantkk20()
        wave temp
        duplicate/o temp kk20
        kk20 = 5.5e-12*exp(125/Temp)
end

        //Determine Rate constant HO2 + NO2
Function RateConstantkk21()
        wave temp, M
        Duplicate/o  temp khno4high khno4low kk21
        khno4low = 2.0e-31*(temp/300)^-3.4
        khno4high  = 2.9e-12*(temp/300)^-1.1
        kk21 =
(khno4low*M/(1+khno4low*M/khno4high))*0.6^((1+(log(khno4low*M/khno4high))^2)
^-1)
end

        //Thermal Decomposition of HNO4
Function RateConstantkk22()
        wave temp, kk21
        Duplicate/o  temp  kHNO4eq kk22
        kHNO4eq = temp*1.363e-22*exp((24/(1.987e-3*temp))-20.634)
        kk22 = kk21/KHNO4eq
```

```
end

        //Determine rate constant OH + HNO4
Function RateConstantkk23()
        wave temp
        duplicate/o temp kk23
        kk23 = 1.3e-12*exp(380/Temp)
end

        //Determine rate constant CH3O2 + CH3O2 => CH3OH+CH2O+O2
Function RateConstantkk24()
        wave temp
        duplicate/o temp  fr1 kk24
        fr1 = 26.2*exp(-1100/Temp)
        kk24 = 9.5e-14*exp(390/Temp)/(1+fr1)
end

//Determine rate constant CH3O2 + CH3O2 =>  2CH2O+2HO2+O2
Function RateConstantkk25()
        wave temp, kk24
        duplicate/o temp kk25 fr1
        fr1 = 26.2*exp(-1100/Temp)
        kk25 = fr1*kk24
```

```
end

        //Determine rate constant OH+CH3OOH =>  CH3O2+H2O
Function RateConstantkk26()
        wave temp
        duplicate/o temp kk26
        kk26 =0.7* 3.8e-12*exp(200/Temp)
end

        //Determine rate constant OH+CH3OOH =>  CH2O+OH+H2O
Function RateConstantkk27()
        wave temp
        duplicate/o temp kk27
        kk27 =0.3* 3.8e-12*exp(200/Temp)
end

        //Determine Rate constant CH3O2+ NO2
Function RateConstantkk28()
        wave temp, M
        Duplicate/o  temp kch3no4high kch3no4low kk28
        kch3no4low = 1.0e-30*(temp/300)^-4.8
        kch3no4high  = 7.2e-12*(temp/300)^-2.1
        kk28 =
```

```
(kch3no4low*M/(1+kch3no4low*M/kch3no4high))*0.6^((1+(log(kch3no4low*M/kch3n
o4high))^2)^-1)
end

        //Thermal Decomposition of CH3OONO2
Function RateConstantkk29()
        wave temp, kk28
        Duplicate/o  temp  kCH3NO4eq kk29
        kCH3NO4eq = 9.5e-29*exp(11234/temp)
        kk29 = kk28/KCH3NO4eq
end

        //Determine rate constant OH+CH3OH
Function RateConstantkk30()
        wave temp
        duplicate/o temp kk30
        kk30 = 2.9e-12*exp(-345/Temp)
end
        //Determine rate constant HO2+BrO
Function RateConstantkk31()
        wave temp
        duplicate/o temp kk31
        kk31 =4.5e-12*exp(460/Temp)
```

```
end
        //Determine rate constant BrO+BrO
Function RateConstantkk32()
        wave temp
        duplicate/o temp kk32
        kk32 =1.5e-12 *exp(230/Temp)
end
        //Determine rate constant BrO+NO
Function RateConstantkk33()
        wave temp
        duplicate/o temp kk33
        kk33 =8.8e-12*exp(260/Temp)
end
//Determine rate constant Br+O3
Function RateConstantkk34()
        wave temp
        duplicate/o temp kk34
        kk34 =1.7e-11*exp(-800/Temp)
end
        // Fraction of O(D) reacting with H2O
Function DetermineFractionO_H2O()
        wave vap,kk1,kk2,kk3,H2Oc,N2c,O2c
        duplicate/o vap Fract
```

```
        Fract = (kk3*H2Oc)/(kk1*O2c+kk2*N2c+kk3*H2Oc)
end

Function Determinedepositionvelocity()
wave ws
duplicate/o ws Dvelocity tRGM
Dvelocity=nan
variable i,u, z1,z
i=0
z=1e-3

do
        if (ws[i]>1e-5)
        do
                u=0.4*ws[i]/(ln(10/z))
              z1=z
                z=0.016*u^2/9.8
                //print z
        while ((z1-z)/z>0.0001)
        Dvelocity[i]=0.4*u/(ln(10/z))
      else
      Dvelocity[i]=nan
        endif
```

```
i+=1


while (i<numpnts(ws))
tRGM=(200/Dvelocity)/3600



end



Function PredictHOx()
	wave
DDPN,kk1,kk2,kk3,kk4,kk5,kk6,kk7,kk8,kk9,kk10,kk11,kk12,kk13,kk14,kk15,kk16,kk1
7,kk18,kk19,kk20,kk21,kk22,kk23,kk24,kk25,kk26,kk27,kk28,kk29,kk30,kk31, kk32,
kk33,kk34,Fract,NOc,O3c,CH4c,COc, J_O3 ,J_NO2 , J_HNO2, J_H2O2, J_CH2O,
J_HNO3,J_HO2NO2_HO2_NO2, J_HO2NO2_OH_NO3,J_CH3OOH,M,
JCH2O_H_HCO,JCH2O_H2_CO, J_HOBr, J_BrO, BrOc, OH, HO2, CH2o_meas,
H2O2_meas
	wave temp1
	variable i,j
	i = 0


	Make/N=1000/D/O/R OHsource OHsink HO2source HO2sink NO2source
```

NO2sink OHint HO2int CH3O2int NO2int HNO4int CH3OOHint CH3OONO2int CH3OHint HONOint HNO3int H2O2int CH2Oint OHsource_BrO HO2sink_BrO HOBrint OHint_BrO HO2int_BrO Brint OHsink_CH2O HO2source_CH2O OHint_CH2O HO2int_CH2O OHint_H2O2 HO2int_H2O2 OHsource_H2O2 OHsink_H2O2 HO2source_H2O2

OHint=Nan

HO2int=Nan

CH3O2int=Nan

NO2int=Nan

HNO4int=Nan

CH3OONO2int=Nan

CH3OHint=Nan

HONOint=Nan

HNO3int=Nan

H2O2int=Nan

CH2Oint=Nan

HOBrint=Nan

duplicate/o kk1 OHpred O2pred CH3O2pred NO2pred HNO4pred CH3OOHpred CH3OONO2pred CH3OHpred HONOpred HNO3pred H2O2pred CH2Opred HOBrpred Brpred

duplicate/o kk1 Total_Source_OH jO3_Source NO_source_OH jHONO_Source O3_source_OH jH2O2_source jHNO3_source J_CH3OOH_source

CH3OOH_source_OH jHOBr_source

duplicate/o kk1 Total_loss_OH CO_loss_OH CH4_loss_OH HO2_loss_OH O3_loss_OH H2O2_loss_OH CH2O_loss_OH NO_loss_OH HONO_loss_OH NO2_loss_OH HNO3_loss_OH OH_loss_OH HNO4_loss_OH CH3OOH_loss_OH CH3OH_loss_OH

duplicate/o kk1 Total_Source_HO2 CO_source_HO2 JCH2O_source CH3O2_Source_HO2 O3_source_HO2 CH2O_source_HO2 H2O2_source_HO2 HNO4_source_HO2 JHNO4_source CH3O2_sq_source CH3OH_source_HO2

duplicate/o kk1 Total_loss_HO2 CH3O2_loss_HO2 NO_loss_HO2 OH_loss_HO2 HO2_loss_HO2 O3_loss_HO2 NO2_loss_HO2 BrO_loss_HO2

duplicate/o kk1 Total_source_CH3O2 CH4_source_CH3O2 CH3OOH_source_CH3O2 CH3OONO2_source_CH3O2 Total_loss_CH3O2 NO_loss_CH3O2 HO2_loss_CH3O2 CH3O2_loss_CH3O2 NO2_loss_CH3O2

duplicate/o kk1 Total_source_NO2 CH3O2_source_NO2 HO2_source_NO2 O3_source_NO2 HONO_source_NO2 JHNO3_source_NO2 HNO3_source_NO2 HNO4_source_NO2 JHNO4_source_NO2 OH_source_NO2 CH3OONO2_source_NO2

duplicate/o kk1 Total_loss_NO2 JNO2_loss OH_loss_NO2 CH3OONO2_loss_NO2 NO_O3_prod

duplicate/o kk1 Total_source_CH3OOH Snow_source_CH3OOH OH_loss_CH3OOH J_CH3OOH_loss Total_loss_CH3OOH

duplicate/o kk1 Total_source_CH3OONO2 Total_loss_CH3OONO2 Total_source_CH3OH Total_loss_CH3OH

duplicate/o kk1 Total_source_HONO Total_loss_HONO JHONO_loss

OH_loss_HONO

duplicate/o kk1 Total_Source_HOx HONO_source_HOx H2O2_source_HOx HNO3_source_HOx CH2O_source_HOx HNO4_source_HOx

duplicate/o kk1 Total_loss_HOx HO2_OH_loss_HOx HO2_HO2_loss_HOx OH_OH_loss_HOx CH4_loss_HOx CH3O2_source_HOx CH3O2_loss_HOx CH3OOH_source_HOx CH3OOH_loss_HOx Total_CH4_loss_HOx HNO4_loss_HOx Net_Source_Sink_HOx HNO3_loss_HOx

duplicate/o kk1 Rad_Rad_loss_HOx H2O2_loss_HOx HONO_loss_HOx

duplicate/o kk1 Total_Source_HNO4 HNO4_loss_NO2 Total_loss_HNO4 Decomp_HNO4 JHNO4_loss Dry_Dep_HNO4 OH_loss_HNO4 O3_diff

duplicate/o kk1 Total_Source_HNO3 OH_NO2_Source Total_loss_HNO3 JHNO3_loss OH_loss_HNO3

duplicate/o kk1 Total_Source_H2O2 HO2_HO2_Source OH_OH_source Total_loss_H2O2 OH_loss_H2O2 jH2O2_loss

duplicate/o kk1 Total_Source_CH2O CH3O2_NO_Source CH3O2_1_Source CH3O2_2_Source OH_CH3OH_Source OH_CH3OOH_Source jCH3OOH_Source

duplicate/o kk1 Total_loss_CH2O NO_loss_CH2O OH_loss_CH2O jCH2O_loss

do

```
j=0
        do
        OHint[0] = 1e6
        HO2int[0] = 1e8
        CH3O2int[0] = 1e7
        NO2int[0] = 1e8
        HNO4int[0] = 1e8
        CH3OOHint[0] = 1e9
        CH3OONO2int[0] = 1e6
        CH3OHint[0]= 1e7
        HONOint[0] = 1e6
        HNO3int[0]=1e8
        H2O2int[0]=1e9
        CH2Oint[0]=1e8
        HOBrint[0]=1e8
        Brint[0]=1e8

            OHsource[j]=
(2*J_O3[i]*O3c[i]*Fract[i]+kk8[i]*HO2int[j]*NOc[i]+J_HNO2[i]*HONOint[j]+2*J_H2
O2[i]*H2O2int[j]+J_HNO3[i]*HNO3int[j]+
kk13[i]*O3c[i]*HO2int[j]+J_CH3OOH[i]*CH3OOHint[j]+J_HOBr[i]*HOBrint[j])
            OHsink[j] =
(kk4[i]*COc[i]+kk5[i]*CH4c[i]+kk9[i]*HO2int[j]+kk12[i]*NOc[i]+kk14[i]*O3c[i]+kk1
```

5[i]*HONOint[j]+kk16[i]*NO2int[j]+kk17[i]*HNO3int[j]+2*kk18[i]*OHint[j]+kk19[i]*H2O2int[j]+kk20[i]*CH2Oint[j]+kk23[i]*HNO4int[j]+kk26[i]*CH3OOHint[j]+kk30[i]*CH3OHint[j])

OHint[j+1]=OHsource_BrO[j]/OHsink[j]

HO2source[j] =

(kk4[i]*OHint[j]*COc[i]+kk6[i]*CH3O2int[j]*NOc[i]+kk14[i]*OHint[j]*O3c[i]+2*JCH2O_H_HCO[i]*CH2Oint[j]+

kk19[i]*H2O2int[j]*OHint[j]+kk20[i]*CH2Oint[j]*OHint[j]+kk22[i]*HNO4int[j]+J_HO2NO2_HO2_NO2[i]*HNO4int[j]+2*kk25[i]*CH3O2int[j]*CH3O2int[j]+J_CH3OOH[i]*CH3OOHint[j]+kk30[i]*CH3OHint[j]*OHint[j])

HO2sink[j]=(kk7[i]*CH3O2int[j]+kk8[i]*NOc[i]+kk9[i]*OHint[j]+2*kk10[i]*HO2int[j]+kk13[i]*O3c[i]+kk21[i]*NO2int[j]+kk31[i]*BrOc[i])

HO2int[j+1]=HO2source[j]/HO2sink_BrO[j]

CH3O2int[j+1] =

(kk5[i]*OHint[j]*CH4c[i]+kk26[i]*CH3OOHint[j]*OHint[j]+kk29[i]*CH3OONO2int[j])/(kk6[i]*NOc[i]+kk7[i]*HO2int[j]+2*kk24[i]*CH3O2int[j]+2*kk25[i]*CH3O2int[j]+kk28[i]*NO2int[j])

CH3OONO2int[j+1] = (kk28[i]*CH3O2int[j]*NO2int[j])/(kk29[i])

CH3OOHint[j+1] =

(kk7[i]*CH3O2int[j]*HO2int[j])/(kk26[i]*OHint[j]+kk27[i]*OHint[j]+J_CH3OOH[i])

CH3OHint[j+1] =

(kk24[i]*CH3O2int[j]*CH3O2int[j])/(kk30[i]*OHint[j])

NO2source[j] =

(kk6[i]*CH3O2int[j]*NOc[i]+kk8[i]*HO2int[j]*NOc[i]+kk11[i]*NOc[i]*O3c[i]+kk15[i]*OHint[j]*HONOint[j]+J_HNO3[i]*HNO3int[j]+kk22[i]*HNO4int[j]+kk23[i]*HNO4int[j]*OHint[j]+J_HO2NO2_HO2_NO2[i]*HNO4int[j]+kk29[i]*CH3OONO2int[j])

NO2sink[j] =

(J_NO2[i]+kk16[i]*OHint[j]+kk21[i]*HO2int[j]+kk28[i]*CH3O2int[j])

NO2int[j+1] = NO2source[j]/NO2sink[j]

HNO4int[j+1] =

(kk21[i]*HO2int[j]*NO2int[j])/(kk22[i]+J_HO2NO2_HO2_NO2[i]+J_HO2NO2_OH_NO3+DDPN[i]+kk23[i]*OHint[j])

HONOint[j+1] =

(kk12[i]*OHint[j]*NOc[i])/(J_HNO2[i]+kk15[i]*OHint[j])

HNO3int[j+1]=(kk16[i]*OHint[j]*NO2int[j])/(kk17[i]*OHint[j]+J_HNO3[i])

H2O2int[j+1]=(kk10[i]*HO2int[j]*HO2int[j]+kk18[i]*OHint[j]*OHint[j])/(kk19[i]*OHint[j]+J_H2O2[i])

CH2Oint[j+1]=(kk6[i]*CH3O2int[j]*NOc[i]+kk24[i]*CH3O2int[j]*CH3O2int[j]+2*kk25[i]*CH3O2int[j]*CH3O2int[j]+kk27[i]*OHint[j]*CH3OOHint[j]+kk30[i]*OHint[j]*CH3OHint[j]+J_CH3OOH[i]*CH3OOHint[j])/(kk20[i]*OHint[j]+J_CH2O[i])

HOBrint[j+1]=kk31[i]*HO2int[j]*BrOc[i]/(J_HOBr[i]+2.9e-4)

```
Brint[i+1]=(2*kk32[i]*BrOc[i]*BrOc[i]+kk31[i]*BrOc[i]*HO2int[j]+kk33[i]*N
Oc[i]*BrOc[i]+J_BrO[i]*BrOc[i])/(kk34[i]*O3c[i])
                    j+=1

                    while (j<=numpnts(OHint)-1)                    // as long as
expression is true
                OHpred[i]=OHint[j]
                HO2pred[i]=HO2int[j]+CH3O2int[j]
                CH3O2pred[i]=CH3O2int[j]
                NO2pred[i]=NO2int[j]
                HNO4pred[i]=HNO4int[j]
                CH3OOHpred[i] = CH3OOHint[j]
                CH3OONO2pred[i] = CH3OONO2int[j]
                CH3OHpred[i] = CH3OHint[j]
                HONOpred[i] = HONOint[j]
                HNO3pred[i]=HNO3int[j]
                H2O2pred[i]=H2O2int[j]
                CH2Opred[i]=CH2Oint[j]
                HOBrpred[i]=HOBrint[j]
                Brpred[i]=Brint[j]

                    //OH source
                JO3_source[i] = 2*J_O3[i]*O3c[i]*Fract[i]
```

NO_source_OH[i] = kk8[i]*HO2pred[i]*NOc[i]

jHONO_source[i] = J_HNO2[i]*HONOpred[i]

jH2O2_source[i] = 2*J_H2O2[i]*H2O2pred[i]

jHNO3_source[i] = J_HNO3[i]*HNO3pred[i]

O3_source_OH[i] = kk13[i]*O3c[i]*HO2pred[i]

J_CH3OOH_source[i] = J_CH3OOH[i]*CH3OOHpred[i]

jHOBr_source[i]=J_HOBr[i]*HOBrpred[i]

Total_Source_OH[i]=JO3_source[i]+NO_source_OH[i]+jHONO_source[i]+jH2O2_source[i]+jHNO3_source[i]+O3_source_OH[i]+J_CH3OOH_source[i]+jHOBr_source[i]

//OH sink

CO_loss_OH[i]= kk4[i]*COc[i]*OHpred[i]

CH4_loss_OH[i]=kk5[i]*CH4c[i]*OHpred[i]

HO2_loss_OH[i]=kk9[i]*HO2pred[i]*OHpred[i]

NO_loss_OH[i]=kk12[i]*NOc[i]*OHpred[i]

O3_loss_OH[i] = kk14[i]*O3c[i]*OHpred[i]

HONO_loss_OH[i] = kk15[i]*HONOpred[i]*OHpred[i]

NO2_loss_OH[i] = kk16[i]*NO2pred[i]*OHpred[i]

HNO3_loss_OH[i] = kk17[i]*HNO3pred[i]*OHpred[i]

OH_loss_OH[i] = 2*kk18[i]*OHpred[i]*OHpred[i]

H2O2_loss_OH[i] = kk19[i]*H2O2pred[i]*OHpred[i]

CH2O_loss_OH[i] = kk20[i]*CH2Opred[i]*OHpred[i]

```
HNO4_loss_OH[i] = kk23[i]*HNO4pred[i]*OHpred[i]

CH3OOH_loss_OH[i] = kk26[i]*CH3OOHpred[i]*OHpred[i]

CH3OH_loss_OH[i] = kk30[i]*CH3OHpred[i]*OHpred[i]
```

```
Total_loss_OH[i]=CO_loss_OH[i]+CH4_loss_OH[i]+HO2_loss_OH[i]+NO_loss
_OH[i]+O3_loss_OH[i]+HONO_loss_OH[i]+NO2_loss_OH[i]+HNO3_loss_OH[i]+OH
_loss_OH[i]+H2O2_loss_OH[i]+CH2O_loss_OH[i]+HNO4_loss_OH[i]+CH3OOH_loss
_OH[i]+CH3OH_loss_OH[i]
```

```
//HO2 source

CO_source_HO2[i] = kk4[i]*OHpred[i]*COc[i]

CH3O2_Source_HO2[i] = kk6[i]*CH3O2pred[i]*NOc[i]

O3_source_HO2[i] = kk14[i]*OHpred[i]*O3c[i]

JCH2O_source[i] = 2*JCH2O_H_HCO[i]*CH2Opred[i]

CH2O_source_HO2[i] = kk20[i]*CH2Opred[i]*OHpred[i]

H2O2_source_HO2[i] = kk19[i]*H2O2pred[i]*OHpred[i]

HNO4_source_HO2[i] = kk22[i]*HNO4pred[i]

JHNO4_source[i] =
(J_HO2NO2_HO2_NO2[i]*J_HO2NO2_OH_NO3[i])*HNO4pred[i]

CH3O2_sq_source[i]= 2*kk25[i]*CH3O2pred[i]*CH3O2pred[i]

J_CH3OOH_source[i] = J_CH3OOH[i]*CH3OOHpred[i]

CH3OH_source_HO2[i] = kk30[i]*CH3OHpred[i]*OHpred[i]

Total_Source_HO2[i] =
```

CO_source_HO2[i]+CH3O2_Source_HO2[i]+O3_source_HO2[i]+JCH2O_source[i]+C
H2O_source_HO2[i]+H2O2_source_HO2[i]+HNO4_source_HO2[i]+JHNO4_source[i]+
CH3O2_sq_source[i]+J_CH3OOH_source[i]+CH3OH_source_HO2[i]

//HO2 sink

CH3O2_loss_HO2[i] = kk7[i]*CH3O2pred[i]*HO2pred[i]

NO_loss_HO2[i] = kk8[i]*NOc[i]*HO2pred[i]

OH_loss_HO2[i] = kk9[i]*OHpred[i]*HO2pred[i]

HO2_loss_HO2[i] =2*kk10[i]*HO2pred[i]*HO2pred[i]

O3_loss_HO2[i] = kk13[i]*O3c[i]*HO2pred[i]

NO2_loss_HO2[i] = kk21[i]*NO2pred[i]*HO2pred[i]

BrO_loss_HO2[i]=kk31[i]*BrOc[i]*HO2pred[i]

Total_loss_HO2[i] =
CH3O2_loss_HO2[i]+NO_loss_HO2[i]+OH_loss_HO2[i]+HO2_loss_HO2[i]+O3_loss_
HO2[i]+NO2_loss_HO2[i]+BrO_loss_HO2[i]

//CH3O2 source

CH4_source_CH3O2[i] = kk5[i]*OHpred[i]*CH4c[i]

CH3OOH_source_CH3O2[i] = kk26[i]*CH3OOHpred[i]*OHpred[i]

CH3OONO2_source_CH3O2[i] = kk29[i]*CH3OONO2pred[i]

Total_source_CH3O2[i]=CH4_source_CH3O2[i]+CH3OOH_source_CH3O2[i]+
CH3OONO2_source_CH3O2[i]

//CH3O2 sink

NO_loss_CH3O2[i]=kk6[i]*NOc[i]*CH3O2pred[i]

HO2_loss_CH3O2[i]=kk7[i]*HO2pred[i]*CH3O2pred[i]

CH3O2_loss_CH3O2[i]

=2*kk24[i]*CH3O2pred[i]*CH3O2pred[i]+2*kk25[i]*CH3O2pred[i]*CH3O2pred[i]

NO2_loss_CH3O2[i] = kk28[i]*CH3O2pred[i]*NO2pred[i]

Total_loss_CH3O2[i]=NO_loss_CH3O2[i]+HO2_loss_CH3O2[i]+CH3O2_loss_CH3O2[i]+NO2_loss_CH3O2[i]

//NO2 source

CH3O2_source_NO2[i]=kk6[i]*CH3O2pred[i]*NOc[i]

HO2_source_NO2[i]=kk8[i]*HO2pred[i]*NOc[i]

O3_source_NO2[i]=kk11[i]*NOc[i]*O3c[i]

HONO_source_NO2[i] = kk15[i]*OHpred[i]*HONOpred[i]

JHNO3_source_NO2[i] = J_HNO3[i]*HNO3pred[i]

HNO3_source_NO2[i] = kk17[i]*OHpred[i]*HNO3pred[i]

HNO4_source_NO2[i] = kk22[i]*HNO4pred[i]

JHNO4_source_NO2[i] =

(J_HO2NO2_HO2_NO2[i]*J_HO2NO2_OH_NO3[i])*HNO4pred[i]

OH_source_NO2[i] = kk23[i]*HNO4pred[i]*OHpred[i]

CH3OONO2_source_NO2[i] = kk29[i]*CH3OONO2pred[i]

Total_source_NO2[i]=CH3O2_source_NO2[i]+HO2_source_NO2[i]+O3_source

_NO2[i]+HONO_source_NO2[i]+JHNO3_source_NO2[i]+HNO3_source_NO2[i]+HNO4_source_NO2[i]+JHNO4_source_NO2[i]+OH_source_NO2[i]+CH3OONO2_source_NO2[i]

//NO2 sink

JNO2_loss[i]=J_NO2[i]*NO2pred[i]

OH_loss_NO2[i]=kk16[i]*OHpred[i]*NO2pred[i]

HNO4_loss_NO2[i] = kk21[i]*HO2pred[i]*NO2pred[i]

CH3OONO2_loss_NO2[i] = kk28[i]*CH3O2pred[i]*NO2pred[i]

Total_loss_NO2[i]=JNO2_loss[i]+OH_loss_NO2[i]+HNO4_loss_NO2[i]+CH3OONO2_loss_NO2[i]

//HNO4 source & sink

Total_Source_HNO4[i] = kk21[i]*HO2pred[i]*NO2pred[i]

Decomp_HNO4[i] = kk22[i]*HNO4pred[i]

JHNO4_loss[i] = (J_HO2NO2_HO2_NO2[i]*J_HO2NO2_OH_NO3[i])*HNO4pred[i]

Dry_Dep_HNO4[i] = DDPN[i]*HNO4pred[i]

OH_loss_HNO4[i] = kk23[i]*HNO4pred[i]*OHpred[i]

Total_loss_HNO4[i] = Decomp_HNO4[i]+JHNO4_loss[i]+Dry_Dep_HNO4[i]+OH_loss_HNO4[i]

//HONO source & sink

```
Total_Source_HONO[i] = kk12[i]*OHpred[i]*NOc[i]

Total_loss_HONO[i] =
J_HNO2[i]*HONOpred[i]+kk15[i]*OHpred[i]*HONOpred[i]

JHONO_loss[i] = J_HNO2[i]*HONOpred[i]

OH_loss_HONO[i] = kk15[i]*OHpred[i]*HONOpred[i]


//CH3OOH source & sink

Total_source_CH3OOH[i] = kk7[i]*CH3O2pred[i]*HO2pred[i]

OH_loss_CH3OOH[i] =
kk26[i]*CH3OOHpred[i]*OHpred[i]+kk27[i]*CH3OOHpred[i]*OHpred[i]

J_CH3OOH_loss[i] = J_CH3OOH[i]*CH3OOHpred[i]

Total_loss_CH3OOH[i] = OH_loss_CH3OOH[i]+J_CH3OOH_loss[i]


//CH3OONO2 source & sink

Total_source_CH3OONO2[i] = kk28[i]*CH3O2pred[i]*NO2pred[i]

Total_loss_CH3OONO2[i] = kk29[i]*CH3OONO2pred[i]


//CH3OH source & sink

Total_source_CH3OH[i] = kk24*CH3O2pred[i]*CH3O2pred[i]

Total_loss_CH3OH[i] = kk30[i]*CH3OHpred[i]*OHpred[i]


//HOx Production

H2O2_source_HOx[i] = jH2O2_source[i]
```

```
CH2O_source_HOx[i] = JCH2O_source[i]

HNO3_source_HOx[i] = jHNO3_source[i]

Total_Source_HOx[i] =
JO3_source[i]+H2O2_source_HOx[i]+CH2O_source_HOx[i]+HNO3_source_HOx[i]


//HOx Loss

HO2_OH_loss_HOx[i] = 2*kk9[i]*HO2pred[i]*OHpred[i]

HO2_HO2_loss_HOx[i] = 2*kk10[i]*HO2pred[i]*HO2pred[i]

OH_OH_loss_HOx[i] = 2*kk18[i]*OHpred[i]*OHpred[i]

Rad_Rad_loss_HOx[i] = HO2_OH_loss_HOx[i]

H2O2_loss_HOx[i] = HO2_HO2_loss_HOx[i]+OH_OH_loss_HOx[i]

//Methane

CH4_loss_HOx[i] = kk5[i]*CH4c[i]*OHpred[i]

CH3O2_source_HOx[i] =
kk6*CH3O2pred[i]*NOc[i]+2*kk25[i]*CH3O2pred[i]*CH3O2pred[i]

CH3O2_loss_HOx[i] = kk7[i]*HO2pred[i]*CH3O2pred[i]

CH3OOH_source_HOx[i] = 2*J_CH3OOH[i]*CH3OOHpred[i]

CH3OOH_loss_HOx[i] = kk26[i]*CH3OOHpred[i]*OHpred[i]

Total_CH4_loss_HOx[i] = CH4_loss_HOx[i]-
CH3O2_source_HOx[i]+CH3O2_loss_HOx[i]-
CH3OOH_source_HOx[i]+CH3OOH_loss_HOx[i]


HNO3_loss_HOx[i] =
```

kk16[i]*OHpred[i]*NO2pred[i]+kk17[i]*OHpred[i]*HNO3pred[i]

HNO4_loss_HOx[i] = kk21[i]*HO2pred[i]*NO2pred[i]-
(kk22[i]*HNO4pred[i]+
(J_HO2NO2_HO2_NO2[i]*J_HO2NO2_OH_NO3[i])*HNO4pred[i])+kk23[i]*HNO4pr
ed[i]*OHpred[i]+DDPN[i]*HNO4pred[i]

HONO_loss_HOx[i] =
kk15[i]*HONOpred[i]*OHpred[i]+kk12[i]*OHpred[i]*NOc[i]-jHONO_source[i]

Total_loss_HOx[i] =
Rad_Rad_loss_HOx[i]+H2O2_loss_HOx[i]+HNO4_loss_HOx[i]+Total_CH4_loss_HOx
[i]+HNO3_loss_HOx[i]+HONO_loss_HOx[i]

Net_Source_Sink_HOx[i] = Total_Source_HOx[i]-Total_loss_HOx[i]

O3_diff[i] =
((J_NO2[i]*NO2pred[i])/(J_O3[i]*Fract[i]+kk11[i]*NOc[i]+kk13[i]*HO2pred[i]+kk14[i
]*OHpred[i])*(1e9/M[i]))-(O3c[i]*1e9/M[i])

// HNO3 Source&Sink

OH_NO2_Source[i]=kk16[i]*OHpred[i]*NO2pred[i]

Total_Source_HNO3[i]=OH_NO2_Source

JHNO3_loss[i]=J_HNO3[i]*HNO3pred[i]

OH_loss_HNO3[i]=kk17[i]*OHpred[i]*HNO3pred[i]

```
Total_loss_HNO3[i]=JHNO3_loss+OH_loss_HNO3

//H2O2 Source&Sink
HO2_HO2_Source[i]=kk10[i]*HO2pred[i]*HO2pred[i]
OH_OH_Source[i]=kk18[i]*OHpred[i]*OHpred[i]
Total_Source_H2O2[i]=HO2_HO2_Source[i]+OH_OH_Source[i]
OH_loss_H2O2[i]=kk19[i]*OHpred[i]*H2O2pred[i]
jH2O2_loss[i]=J_H2O2[i]*H2O2pred[i]
Total_loss_H2O2[i]=OH_loss_H2O2[i]+jH2O2_loss[i]

// CH2O Source&Sink
CH3O2_NO_Source[i] =kk6[i]*CH3O2pred[i]*NOc[i]
CH3O2_1_Source[i]=kk24[i]*CH3O2pred[i]*CH3O2pred[i]
CH3O2_2_Source[i]=2*kk25[i]*CH3O2pred[i]*CH3O2pred[i]
OH_CH3OOH_Source[i] =kk27[i]*OHpred[i]*CH3OHpred[i]
OH_CH3OH_Source[i]=kk30*OHpred[i]*CH3OHpred[i]
jCH3OOH_Source[i]=J_CH3OOH[i]*CH3OOHpred[i]
Total_Source_CH2O[i] = CH3O2_NO_Source+ CH3O2_1_Source
+CH3O2_2_Source +
OH_CH3OOH_Source+OH_CH3OH_Source[i]+jCH3OOH_Source[i]
OH_loss_CH2O[i]=kk20[i]*OHpred[i]*CH2Opred[i]
jCH2O_loss[i]=J_CH2O[i]*CH2Opred[i]
```

```
Total_loss_CH2O[i]=OH_loss_CH2O+ jCH2O_loss




        i+=1
                                                                    // execute the loop
body
        while (i<=numpnts(kk2)-1)                          // as long as expression is true

                                        end
```

# APPENDIX B

# IGOR CODE OF A TIME DEPENDENT MODEL TO SIMULATE BROMINE SPECIATION

```
Function reaction_rates()
//**********************Reaction_rates*********************************
wave temp, pressure
duplicate/o temp M temp1 kk1 kk2 kk3 kk4 kk5 kk6 kk7 kk8 kk9 kk10 kk6low kk6high
kk10low kk10high
temp1=273.15+temp
M=((Pressure /1013)*6.02e23)/(0.08206*Temp1*1000)
// ************Br+O3--->BrO+O2
kk1=1.7e-11*exp(-800/Temp1)
//************BrO+BrO--->2Br+O2
kk2=1.60*exp(-190/temp1) *1.5e-12 *exp(230/Temp1)
//************BrO+BrO--->Br2+O2
kk3=(1-1.60*exp(-190/temp1) )*1.5e-12 *exp(230/Temp1)
//************BrO+HO2--->HOBr+O2
kk4=4.5e-12*exp(460/Temp1)
//************BrO+NO---->Br+NO2
kk5=8.8e-12*exp(260/Temp1)
//************BrO+NO2-->BrONO2
kk6low=5.2e-31*(temp1/300)^-3.2
kk6high=6.9e-12*(temp1/300)^-2.9
kk6=(kk6low*M/(1+kk6low*M/kk6high))*0.6^((1+(log(kk6low*M/kk6high))^2)^-1)
```

```
//************Br+HCHO--->HBr+CHO
kk7=1.7*1e-11*exp(-800/temp1)
//************Br+HO2--->HBr+O2
kk8=4.8e-12*exp(-310/temp1)
// ***********OH+HBr---> H2O+Br
kk9=5.5e-12*exp(200/temp1)
//***********Br+NO2--->BrNO2
kk10low=4.2e-31*(temp1/300)^-2.4
kk10high=2.7e-11*(temp1/300)^-0
kk10=(kk10low*M/(1+kk10low*M/kk10high))*0.6^((1+(log(kk10low*M/kk10high))^2)
^-1)
//*******************Loss of HOBr, HBr and BrONO2 on aerosols***********
wave Aerosol_S, Aerosol_N, Aerosol_V
duplicate/o temp radius velocity_HOBr velocity_HBr velocity_BrONO2 Kn_HOBr
Kn_HBr kn_BrONO2 F_HOBr F_HBr F_BrONO2 k_HOBr k_HBr k_BrONO2
mass_HOBr mass_HBr mass_BrONO2 stk_HOBr stk_HBr stk_BrONO2 Dg
mass_HOBr=97
mass_HBr=81
mass_BrONO2=142
mass_Br2=160
Dg=0.1
stk_HOBr=0.6
stk_HBr=0.3
stk_BrONO2=0.8 //0.2//0.063-0.80[Hanson](from JPL )
stk_Br2=0.01
radius=(aerosol_S/aerosol_N/4/3.14)^0.5*1e-4
velocity_HOBr=(8*8.314*temp1*1000/4.13/mass_HOBr)^0.5*100
```

```
velocity_HBr=(8*8.314*temp1*1000/4.13/mass_HBr)^0.5*100
velocity_BrONO2=(8*8.314*temp1*1000/4.13/mass_BrONO2)^0.5*100
velocity_Br2=(8*8.314*temp1*1000/4.13/mass_Br2)^0.5*100
kn_HOBr=3*Dg/velocity_HOBr/radius
kn_HBr=3*Dg/velocity_HBr/radius
kn_BrONO2=3*Dg/velocity_BrONO2/radius
kn_Br2=3*Dg/velocity_Br2/radius

F_HOBr=0.75*stk_HOBr*(1+kn_HOBr)/(kn_HOBr^2+kn_HOBr+0.283*kn_HOBr*stk
_HOBr+0.75*stk_HOBr)
F_HBr=0.75*stk_HBr*(1+kn_HBr)/(kn_HBr^2+kn_HBr+0.283*kn_HBr*stk_HBr+0.75
*stk_HBr)
F_BrONO2=0.75*stk_BrONO2*(1+kn_BrONO2)/(kn_BrONO2^2+kn_BrONO2+0.283
*kn_BrONO2*stk_BrONO2+0.75*stk_BrONO2)
F_Br2=0.75*stk_Br2*(1+kn_Br2)/(kn_Br2^2+kn_Br2+0.283*kn_Br2*stk_Br2+0.75*stk
_Br2)

k_HOBr =4*3.14*radius*aerosol_N*Dg*F_HOBr
k_HBr =4*3.14*radius*aerosol_N*Dg*F_HBr
k_BrONO2 =4*3.14*radius*aerosol_N*Dg*F_BrONO2
k_Br2 =4*3.14*radius*aerosol_N*Dg*F_Br2

//k_HOBr=1e-3
//k_HBr=5e-4
//k_BrONO2=1e-4
end
//**********************************************************************
```

```
Function bromine_speciation()
variable deltat, c
deltat=0.1
c=86400/deltat

wave J_Br2, J_BrO, J_HOBr, J_BrONO2_Br_NO3, J_BrONO2_BrO_NO2, k_HOBr,
k_HBr, k_BrONO2, kk1, kk2, kk3, kk4, kk5, kk6, kk7, kk8, kk9,O3c, NOc,  NO2c,
HO2pred, OHpred, CH2Oc

make/O/N=(c)/D Br2pred Brpred HOBrpred HBrpred BrOpred time_series BrONO2pred
min_pro_HOBr min_pro_BrONO2 pro_HBr min_pro_HBr left_pro //2000000


Br2pred= Nan
Brpred= Nan
HOBrpred= Nan
HBrpred= Nan
BrOpred= Nan
BrClpred= Nan
time_series=Nan

time_series[0]=0
Brpred[0]=0
BrOpred[0]=0
HOBrpred[0]=0
HBrpred[0]=0
BrONO2pred[0]=0
```

```
Br2pred[0]=15*3e7
i=0
j=0
        do
                min_pro_HOBr[i]=k_HOBr[j]*HOBrpred[i]
                min_pro_BrONO2[i]=K_BrONO2[j]*BrONO2pred[i]
                pro_HBr[i]=K_HBr[j]*HBrpred[i]
                min_pro_HBr[i]=(pro_HBr[i]<min_pro_BrONO2[i]+min_pro_HOBr[i]) ?
pro_HBr[i] : min_pro_BrONO2[i]+min_pro_HOBr[i]
                left_pro[i]=(pro_HBr[i]<min_pro_HOBr[i]+min_pro_BrONO2[i]) ?
min_pro_HOBr[i]+min_pro_BrONO2[i]- pro_HBr[i] : 0
                Br2pred[i+1]=Br2pred[i]+(-
J_Br2[j]*Br2pred[i]*deltat+kk3[j]*BrOpred[i]^2*deltat+0.5*left_pro[i]*deltat+min_pro
_HBr [i]*deltat)
                Brpred[i+1]=Brpred[i]+(2*J_Br2[j]*Br2pred[i]*deltat-
kk1[j]*Brpred[i]*O3c[j]*deltat+J_BrO[j]*BrOpred[i]*deltat+J_HOBr[j]*HOBrpred[i]*d
eltat+2*kk2[j]*BrOpred[i]^2*deltat-kk7[j]*CH2Oc[j]*Brpred[i]*deltat-
kk8[j]*HO2pred[j]*Brpred[i]*deltat+kk5[j]*BrOpred[i]*NOc[j]*deltat+kk9[j]*OHpred[j
]*HBrpred[i]*deltat+BrONO2pred[i]*J_BrONO2_Br_NO3[j]*deltat)
                BrOpred[i+1]=BrOpred[i]+(kk1[j]*Brpred[i]*O3c[j]*deltat-
J_BrO[j]*BrOpred[i]*deltat-2*kk2[j]*BrOpred[i]^2*deltat-
2*kk3[j]*BrOpred[i]^2*deltat-kk4[j]*BrOpred[i]*HO2pred[j]*deltat-
kk5[j]*BrOpred[i]*NOc[j]*deltat-
kk6[j]*BrOpred[i]*NO2c[j]*deltat+BrONO2pred[i]*J_BrONO2_BrO_NO2[j]*deltat)
                HOBrpred[i+1]=HOBrpred[i]+(kk4[j]*BrOpred[i]*HO2pred[j]*deltat-
J_HOBr[j]*HOBrpred[i]*deltat-min_pro_HOBr[i]*deltat)
```

```
        HBrpred[i+1]=HBrpred[i]+(kk7[j]*CH2Oc[j]*Brpred[i]*deltat+kk8[j]*HO2pred[
j]*Brpred[i]*deltat-kk9[j]*OHpred[j]*HBrpred[i]*deltat- pro_HBr[i]*deltat)
                BrONO2pred[i+1]=BrONO2pred[i]+(kk6[j]*BrOpred[i]*NO2c[j]*deltat-
BrONO2pred[i]*J_BrONO2_Br_NO3[j]*deltat-
BrONO2pred[i]*J_BrONO2_BrO_NO2[j]*deltat-min_pro_BrONO2[i]*deltat)
                time_series[i+1]=(i+1)*deltat

         i+=1
         j=floor(i*deltat/600) //1871    //+1876

        while (i<c-1)

end
```

# APPENDIX C

# IGOR CODE OF A TIME DEPENDENT MODEL TO SIMULATE CHLORINE SPECIES

```
#pragma rtGlobals=1  // Use modern global access method.
#include <AxisSlider>

Function reaction_rate ()
wave temp, pressure_NOAA
duplicate/o temp M temp_int pressure_int kk1 kk2 kk3 kk4 kk5 kk6 kk7 kk8 kk9 kk10
kk11 kk12 kk13 kk14 kk15 kk16 kk17 kk18 kk19 kk20 kk21 kk22 kk23 kk24 kk13low
kk13high kk14low kk14high kk20low kk20high kk21low kk21high kk25 kk26 kk27
interpolatewave(temp_int,temp)
interpolatewave(pressure_int, pressure_NOAA)
//temp_int=-25
//pressure_int=1013
M=((Pressure_int/1013)*6.02e23)/(0.08206*Temp_int*1000)
//Cl+O3-->ClO + O2
kk1=2.3e-11*exp(-200/temp_int)
//ClO+ HO2--> HOCl + O2
kk2=2.7e-12*exp(220/temp_int)
//ClO+NO-->Cl +NO2
kk3=6.4e-12*exp(290/temp_int)
//Cl + CH4--> HCl + CH3
kk4=7.3e-12*exp(-1280/temp_int)
```

```
//Cl + H2CO--> HCl + HCO
kk5=8.1e-11*exp(-30/temp_int)
//HO2+ Cl --> HCl+O2
kk6=1.8e-11*exp(170/temp_int)
//HO2+ Cl--> OH + ClO
kk7=4.1e-11*exp(-450/temp_int)
//OH+ Cl2--> HOCl + Cl
kk8=1.4e-12*exp(-900/temp_int)
//OH+HOCl-->H2O+ ClO
kk9=3.0e-12*exp(-500/temp_int)
//ClO+ClO--> Cl2 + O2
kk10=1.0e-12*exp(-1590/temp_int)
//ClO+ClO-->ClOO + Cl
kk11=3.0e-11*exp(-2450/temp_int)
//ClO + ClO--OClO + Cl
kk12=3.5e-13*exp(-1370/temp_int)
//ClO + ClO-->Cl2O2
kk13low=1.6e-32*(temp_int/300)^(-4.5)
kk13high=2.0e-12*(temp_int/300)^(-2.4)
kk13=(kk13low*M/(1+kk13low*M/kk13high))*0.6^((1+(log(kk13low*M/kk13high))^2)
^-1)
//ClO + NO2--> ClONO2
kk14low=1.8e-31*(temp_int/300)^(-3.4)
kk14high=1.5e-11*(temp_int/300)^(-1.9)
kk14=(kk14low*M/(1+kk14low*M/kk14high))*0.6^((1+(log(kk14low*M/kk14high))^2)
^-1)
//BrO+ClO-->Br+ OClO
```

```
kk15=9.5e-13*exp(550/temp_int)
//BrO+ClO--> Br + ClOO
kk16=2.3e-12*exp(260/temp_int)
//BrO+ClO-->BrCl + O2
kk17=4.1e-13*exp(290/temp_int)
//Cl +C2H6-->HCl + C2H5 (ethane)
kk18=7.2e-11*exp(-70/temp_int)
//Cl + C3H8-->HCl + C3H7 (propane)
kk19= 6.54e-11*exp(0/temp_int)+7.85e-11*exp(-80/temp_int)
//Cl+C2H2 (ethyne)-->ClC2H2
kk20low=5.2e-30*(temp_int/300)^(-2.4)
kk20high=2.2e-10*(temp_int/300)^(-0.7)
kk20=(kk20low*M/(1+kk20Low*M/kk20high))*0.6^((1+(log(kk20low*M/kk20high))^2
)^-1)
//Cl +C2H4 --> ClC2H4
kk21low=1.6e-29*(temp_int/300)^(-3.3)
kk21high=3.1e-10*(temp_int/300)^(-1.0)
kk21=(kk21low*M/(1+kk21low*M/kk21high))*0.6^((1+(log(kk21low*M/kk21high))^2)
^-1)
//Cl + n C4H10( n-butane)--> C4H9 +HCl ///IUPAC
kk22=0.44*exp(-120/temp_int)*2.05e-10+0.59*exp(55/temp_int)*2.05e-10
//Cl + C3H6--> IUPAC
kk23=2.7e-10
//OH+ HCl-->H2O+ Cl
kk24=2.6e-12*exp(-350/temp_int)
//Cl + CH3CHO-->HCl+CH3CO
//->HCl+ CH2CHO-
```

```
kk25=8.0e-11 // IUPAC
//Cl + CH3OH (Methanol)->HCl +CH2OH
kk26=5.5e-11
//Cl+CH3C(O)CH3 (acetone)->HCl + CH3C(O)CH2 // from IUPAC correct
kk27=1.5e-11*exp(-590/temp)
end

Function loss_on_aerosol()
wave Aerosol_S, Aerosol_N, Aerosol_V,temp_int
duplicate/o temp radius velocity_HOCl Kn_HOCl F_HOCl k_HOCl mass_HOCl Dg
stk_HOCl k_HOCl_ori
duplicate/o temp mass_HCl stk_HCl velocity_HCl Kn_HCl F_HCl k_HCl k_HCl_ori
duplicate/o temp mass_Cl2 stk_Cl2 velocity_Cl2 Kn_Cl2 F_Cl2 k_Cl2 k_Cl2_ori
mass_HCl=36.5
mass_HOCl=52.5
mass_Cl2=70.9
Dg=0.1
stk_HOCl=0.3 // 0.3 //Pratte, PCCP, 2006
stk_HCl=0.18 // Fluckiger 2003// 0.8 Robinson 1998
stk_Cl2=0.02//0.02// Hu et al JPC 1995
radius=(aerosol_S/aerosol_N/4/3.14)^0.5*1e-4
velocity_HOCl=(8*8.314*temp_int*1000/4.13/mass_HOCl)^0.5*100
velocity_HCl=(8*8.314*temp_int*1000/4.13/mass_HCl)^0.5*100
velocity_Cl2=(8*8.314*temp_int*1000/4.13/mass_Cl2)^0.5*100
kn_HOCl=3*Dg/velocity_HOCl/radius
kn_HCl=3*Dg/velocity_HCl/radius
kn_Cl2=3*Dg/velocity_Cl2/radius
```

```
F_HOCl=0.75*stk_HOCl*(1+kn_HOCl)/(kn_HOCl^2+kn_HOCl+0.283*kn_HOCl*stk_
HOCl+0.75*stk_HOCl)
F_HCl=0.75*stk_HCl*(1+kn_HCl)/(kn_HCl^2+kn_HCl+0.283*kn_HCl*stk_HCl+0.75*
stk_HCl)
F_Cl2=0.75*stk_Cl2*(1+kn_Cl2)/(kn_Cl2^2+kn_Cl2+0.283*kn_Cl2*stk_Cl2+0.75*stk_
Cl2)
//F_N2O5=0.03 // uptake coefficient [George JPC, 1994]
k_HOCl=4*3.14*radius*aerosol_N*Dg*F_HOCl
k_HCl=4*3.14*radius*aerosol_N*Dg*F_HCl
k_Cl2=4*3.14*radius*aerosol_N*Dg*F_Cl2
end

function model_chlorine()
wave Cl2c, O3c, HO2c, OHc, NOc, NO2c, CH2Oc, BrOc, ethanec,ethenec, propanec,
propenec, n_butanec, ethynec, M_avg, temp_avg, pressure_avg, CH4c, BrClc,
J_BrCl_avg, k_Cl2_avg, CH3CHOc, methanolc, acetonec, temp_avg, boundaryH2,
Cl2_prod_time_mean
wave kk1, kk2, kk3, kk4, kk5, kk6, kk7,  kk8, kk9, kk10, kk11, kk12, kk13, kk14, kk15,
kk16, kk17, kk18, kk19, kk20, kk21, kk22, kk23, kk24, kk25, kk26, kk27, k_HCl_avg,
k_HOCl_avg, J_Cl2_avg, J_HOCl_avg, J_ClO_avg, J_O3_avg, J_NO2_avg, J_Br2_avg,
J_ClONO2_Cl_avg, J_ClONO2_ClO_avg
variable deltat, c, i, j, k, alpha
deltat=0.01//0.01
c=86400/deltat
//alpha=100//100//2.5e-9 //1e-12*2e3 //7.5e-4/20/3e7//1.5e-12
//duplicate/o temp_avg boundaryH
//boundaryH=(temp_avg-247)*50
```

```
//duplicate/o Cl2c P_Cl2
//P_Cl2=Cl2c*(J_Cl2_avg)

make/o/n=(c)/D ClOpred HOClpred Clpred HClpred time_series Clpred_source
Clpred_loss ClOpred_source ClOpred_loss Cl2pred total_Clpred Cl_ionpred
Cl2_extrasource BrClpred ClONO2pred
ClOpred[0]=0
HOClpred[0]=0
Clpred[0]=0
HClpred[0]=0
Cl2pred[0]=3*3e7
Cl_ionpred[0]=200*3e7
BrClpred[0]=0
ClONO2pred[0]=0
i=0
j=0

        do
//Cl2_extrasource[i]=0.5*J_O3_avg[j]*O3c[j]*Cl_ionpred[i]*alpha
//Cl2pred[i+1]=Cl2pred[i]+(J_O3_avg[j]*O3c[j]*alpha/boundaryH2[j]+k_HOCl_avg[j]*
HOClpred[i]+kk10[j]*ClOpred[i]^2-Cl2pred[i]*J_Cl2_avg[j]-kk8[j]*OHc[j]*Cl2pred[i]-
k_Cl2_avg[j]*Cl2pred[i])*deltat
                //Cl2pred[i+1]=Cl2pred[i]+(P_Cl2[j]-J_Cl2_avg[j]*Cl2pred[i]-
k_Cl2_avg[j]*Cl2pred[i])*deltat

        Clpred_source[i]=(J_Cl2_avg[j]*Cl2c[j]*2+J_ClO_avg[j]*ClOpred[i]+J_HOCl_a
vg[j]*HOClpred[i]+kk3[j]*NOc[j]*ClOpred[i]+(kk11[j]+kk12[j])*ClOpred[i]^2*2+kk24
```

[j]*OHc[j]*HClpred[i]+ClONO2pred[i]*J_ClONO2_CL_avg[j]+J_BrCl_avg[j]*BrClpred[i])*deltat //

Clpred_loss[i]=(kk1[j]*O3c[j]+kk4[j]*CH4c[j]+kk5[j]*CH2Oc[j]+kk18[j]*ethanec[j]+kk19[j]*propanec[j]+kk22[j]*n_butanec[j]+kk6[j]*HO2c[j]+kk7[j]*HO2c[j]+kk25[j]*CH3CHOc[j]+kk26[j]*2.0e10+kk27[j]*3.3e10)*Clpred[i]*deltat
//+kk20[j]*ethynec[j]+kk21[j]*ethenec[j]+kk23[j]*propenec[j]
//+kk26[j]*Methanolc[j]+kk27[j]*Acetonec[j]

Clpred[i+1]=Clpred[i]+(Clpred_source[i]-Clpred_loss[i])

ClOpred_source[i]=(kk1[j]*O3c[j]*Clpred[i]+kk7[j]*HO2c[j]*Clpred[i]+kk9[j]*OHc[j]*HOClpred[i]+ClONO2pred[i]*J_ClONO2_ClO_avg[j])*deltat //

ClOpred_loss[i]=(J_ClO_avg[j]*ClOpred[i]+kk2[j]*HO2c[j]*ClOpred[i]+kk3[j]*ClOpred[i]*NOc[j]+2*kk10[j]*ClOpred[i]^2+2*kk11[j]*ClOpred[i]^2+2*kk12[j]*ClOpred[i]^2+kk14[j]*ClOpred[i]*NO2c[j]+kk13[j]*ClOpred[i]^2+kk15[j]*BrOc[j]*ClOpred[i]+kk16[j]*BrOc[j]*ClOpred[i]+kk17[j]*BrOc[j]*ClOpred[i])*deltat //

ClOpred[i+1]=ClOpred[i]+(ClOpred_source[i]-ClOpred_loss[i])

HOClpred[i+1]=HOClpred[i]+((kk2[j]*HO2c[j]*ClOpred[i]+kk8[j]*OHc[j]*Cl2c[j])*deltat-
(kk9[j]*OHc[j]*HOClpred[i]+J_HOCl_avg[j]*HOClpred[i]+k_HOCl_avg[j]*HOClpred[i])*deltat)

HClpred[i+1]=HClpred[i]+((kk4[j]*CH4c[j]*Clpred[i]+kk5[j]*CH2Oc[j]*Clpred[i]+kk6[j]*HO2c[j]*Clpred[i]+kk18[j]*ethanec[j]*Clpred[i]+kk19[j]*propanec[j]*Clpred[i]+kk22[j]*n_butanec[j]*Clpred[i]+kk25[j]*CH3CHOc[j]*Clpred[i]+kk26[j]*2.0e10*Cl

```
pred[i]+kk27[j]*3.3e10*Clpred[i])*deltat-
(kk24[j]*OHc[j]*HClpred[i]+k_HCl_avg[j]*HClpred[i])*deltat)
                //Cl_ionpred[i+1]=Cl_ionpred[i]+(k_HCl_avg[j]*HClpred[i]-
J_O3_avg[j]*O3c[j]*Cl_ionpred[i]*alpha+k_Cl2_avg[j]*Cl2pred[i]-
k_HOCl_avg[j]*HOClpred[i])*deltat
                ClONO2pred[i+1]=ClONO2pred[i]+(kk14[j]*ClOpred[i]*NO2c[j]-
ClONO2pred[i]*J_ClONO2_ClO_avg[j]-
ClONO2pred[i]*J_ClONO2_ClO_avg[j])*deltat //-
ClONO2pred[i]*J_ClONO2_ClO_avg[j]
                BrClpred[i+1]=BrClpred[i]+(kk17[j]*BrOc[j]*ClOpred[i]-
J_BrCl_avg[j]*BrClpred[i])*deltat
                time_series[i+1]=(i+1)*deltat
        i+=1
        j=floor(i*deltat/600)
        while (i<c-1)
                                        end
```

# REFERENCES


Adams, J.W., Holmes, N.S., and Crowley, J.N., 2002: Uptake and reaction of HOBr on frozen and dry NaCl/NaBr surfaces between 253 and 233 K. Atmospheric Chemistry and Physics, 2, 79-91.

Anderson, J.G., Toohey, D.W., and Brune, W.H., 1991: Free-radicals within the Antarctic vortex – The role of CFCS in Antarctic ozone loss. Science, 251, 39-46.

Anlauf, K.G., Mickle, R.E., and Trivett, N.B.A., 1994: Measurement of ozone during polar sunrise experiment 1992. Journal of Geophysical Research-Atmospheres, 99, 25345-25353.

Aranda, A., Lebras, G., Laverdet, G., and Poulet, G., 1997: The $BrO+CH_3O_2$ reaction: Kinetics and role in the atmospheric ozone budget. Geophysical Research Letters, 24, 2745-2748.

Ariya, P.A., Khalizov, A., and Gidas, A., 2002: Reactions of gaseous mercury with atomic and molecular halogens: Kinetics, product studies, and atmospheric implications. Journal of Physical Chemistry A, 106, 7310-7320.

Atkinson, R., Baulch, D.L., Cox, R.A., Crowley, J.N., Hampson, R.F., Hynes, R.G., Jenkin, M.E., Rossi, M.J., and Troe, J., 2004: Evaluated kinetic and photochemical data for atmospheric chemistry: Volume I - gas phase reactions of O(x), HO(x), NO(x) and SO(x) species. Atmospheric Chemistry and Physics, 4, 1461-1738.

Avallone, L.M., Toohey, D.W., Fortin, T.J., Mckinney, K.A., and Fuentes, J.D., 2003: In situ measurements of bromine oxide at two high-latitude boundary layer sites: Implications of variability. Journal of Geophysical Research-Atmospheres, 108, NO. D3, 4089.

Avallone, L.M., Toohey, D.W., Schauffler, S.M., Pollock, W.H., Heidt, L.E., Atlas, E.L., and Chan, K.R., 1995: In-situ measurements of BrO during AASE-II. Geophysical Research Letters, 22, 831-834.

Ball, S.M., Langridge, J.M., and Jones, R.L., 2004: Broadband cavity enhanced absorption spectroscopy using light emitting diodes. Chemical Physics Letters, 398, 68-74.

Barrie, L.A., Bottenheim, J.W., Schnell, R.C., Crutzen, P.J., and Rasmussen, R.A., 1988: Ozone destruction and photochemical-reactions at polar sunrise in the lower Arctic atmosphere. Nature, 334, 138-141.

Begoin, M., Richter, A., Weber, M., Kaleschke, L., Tian-Kunze, X., Stohl, A., Theys, N., and Burrows, J.P., 2010: Satellite observations of long range transport of a large BrO plume in the Arctic. Atmospheric Chemistry and Physics, 10, 6515-6526.

Berg, T., Sommar, J., Wangberg, I., Gardfeldt, K., Munthe, J., and Schroeder, B., 2003: Arctic mercury depletion events at two elevations as observed at the Zeppelin Station and Dirigibile Italia, Ny-Alesund, spring 2002. Journal De Physique Iv, 107, 151-154.

Bloss, W.J., Camredon, M., Lee, J.D., Heard, D.E., Plane, J.M.C., Saiz-Lopez, A., Bauguitte, S.J.B., Salmon, R.A., and Jones, A.E., 2010: Coupling of HO(x), NO(x) and halogen chemistry in the antarctic boundary layer. Atmospheric Chemistry and Physics, 10, 10187-10209.

Bloss, W.J., Lee, J.D., Heard, D.E., Salmon, R.A., Bauguitte, S.J.B., Roscoe, H.K., and Jones, A.E., 2007: Observations of OH and $HO_2$ radicals in coastal Antarctica. Atmospheric Chemistry and Physics, 7, 4171-4185.

Bogumil, K., Orphal, J., Homann, T., Voigt, S., Spietz, P., Fleischmann, O.C., Vogel, A., Hartmann, M., Kromminga, H., Bovensmann, H., Frerick, J., and Burrows, J.P., 2003: Measurements of molecular absorption spectra with the SCIAMACHY pre-flight model: instrument characterization and reference data for atmospheric remote-sensing in the 230-2380 nm region. Journal of Photochemistry and Photobiology a-Chemistry, 157, 167-184.

Bottenheim, J.W., Gallant, A.G., and Brice, K.A., 1986: Measurements of $NO_y$ species and $O_3$ at 82-degree-N latitude. Geophysical Research Letters, 13, 113-116.

Bottenheim, J.W., Fuentes, J.D., Tarasick, D.W., and Anlauf, K.G., 2002: Ozone in the Arctic lower troposphere during winter and spring 2000 (ALERT2000). Atmospheric Environment, 36, 2535-2544.

Bottenheim, J.W., Netcheva, S., Morin, S., and Nghiem, S.V., 2009: Ozone in the boundary layer air over the Arctic Ocean: measurements during the TARA transpolar drift 2006-2008. Atmospheric Chemistry and Physics, 9, 4545-4557.

Boudries, H., and Bottenheim, J.W., 2000: Cl and Br atom concentrations during a surface boundary layer ozone depletion event in the Canadian high Arctic. Geophysical Research Letters, 27, 517-520.

Brock, C.A., Cozic, J., Bahreini, R., Froyd, K.D., Middlebrook, A.M., Mccomiskey, A., Brioude, J., Cooper, O.R., Stohl, A., Aikin, K.C., De Gouw, J.A., Fahey, D.W., Ferrare, R.A., Gao, R.S., Gore, W., Holloway, J.S., Huebler, G., Jefferson, A., Lack, D.A., Lance, S., Moore, R.H., Murphy, D.M., Nenes, A., Novelli, P.C., Nowak, J.B., Ogren, J.A., Peischl, J., Pierce, R.B., Pilewskie, P., Quinn, P.K., Ryerson, T.B., Schmidt, K.S., Schwarz, J.P., Sodemann, H., Spackman, J.R., Stark, H., Thomson, D.S., Thornberry, T., Veres, P., Watts, L.A., Warneke, C., and Wollny, A.G., 2011: Characteristics, sources, and transport of aerosols measured in spring 2008 during the aerosol, radiation, and cloud processes affecting Arctic Climate (ARCPAC) Project. Atmospheric Chemistry and Physics, 11, 2423-2453.

Brooks, S., Arimoto, R., Lindberg, S., and Southworth, G., 2008: Antarctic polar plateau snow surface conversion of deposited oxidized mercury to gaseous elemental mercury with fractional long-term burial. Atmospheric Environment, 42, 2877-2884.

Brooks, S., Moore, C., Lew, D., Lefer, B., Huey, G., and Tanner, D., 2011: Temperature and sunlight controls of mercury oxidation and deposition atop the Greenland ice sheet. Atmospheric Chemistry and Physics, 11, 8295-8306.

Brune, W.H., Anderson, J.G., and Chan, K.R., 1989: Insitu observations of BrO over Antarctica –ER-2 aircraft results from 54-degree-S to 72-degree-S latitude. Journal of Geophysical Research-Atmospheres, 94, 16639-16647.

Burrows, J.P., Dehn, A., Deters, B., Himmelmann, S., Richter, A., Voigt, S., and Orphal, J., 1998: Atmospheric remote-sensing reference data from GOME: Part I. Temperature-dependent absorption cross-sections of $NO_2$ in the 231-794 nm range. Journal of Quantitative Spectroscopy & Radiative Transfer, 60, 1025-1031.

Burrows, J.P., Richter, A., Dehn, A., Deters, B., Himmelmann, S., and Orphal, J., 1999: Atmospheric remote-sensing reference data from GOME - 2. Temperature-dependent absorption cross sections of O-3 in the 231-794 nm range. Journal of Quantitative Spectroscopy & Radiative Transfer, 61, 509-517.

Cai, Y., Montague, D.C., Mooiweer-Bryan, W., and Deshler, T., 2008: Performance characteristics of the ultra high sensitivity aerosol spectrometer for particles

between 55 and 800 nm: Laboratory and field studies. Journal of Aerosol Science, 39, 759-769.

Cantrell, C.A., Edwards, G.D., Stephens, S., Mauldin, R.L., Zondlo, M.A., Kosciuch, E., Eisele, F.L., Shetter, R.E., Lefer, B.L., Hall, S., Flocke, F., Weinheimer, A., Fried, A., Apel, E., Kondo, Y., Blake, D.R., Blake, N.J., Simpson, I.J., Bandy, A.R., Thornton, D.C., Heikes, B.G., Singh, H.B., Brune, W.H., Harder, H., Martinez, M., Jacob, D.J., Avery, M.A., Barrick, J.D., Sachse, G.W., Olson, J.R., Crawford, J.H., and Clarke, A.D., 2003: Peroxy radical behavior during the Transport and Chemical Evolution over the Pacific (TRACE-P) campaign as measured aboard the NASA P-3B aircraft. Journal of Geophysical Research-Atmospheres, 108.

Chance, K., 1998: Analysis of BrO measurements from the Global Ozone Monitoring Experiment. Geophysical Research Letters, 25, 3335-3338.

Chen, G., Davis, D., Crawford, J., Nowak, J.B., Eisele, F., Mauldin, R.L., Tanner, D., Buhr, M., Shetter, R., Lefer, B., Arimoto, R., Hogan, A., and Blake, D., 2001: An investigation of South Pole HOx chemistry: Comparison of model results with ISCAT observations. Geophysical Research Letters, 28, 3633-3636.

Chen, G., Davis, D., Crawford, J., Hutterli, L.M., Huey, L.G., Slusher, D., Mauldin, L., Eisele, F., Tanner, D., Dibb, J., Buhr, M., Mcconnell, J., Lefer, B., Shetter, R., Blake, D., Song, C.H., Lombardi, K., and Arnoldy, J., 2004: A reassessment of HOx South Pole chemistry based on observations recorded during ISCAT 2000. Atmospheric Environment, 38, 5451-5461.

Chen, G., Huey, L.G., Crawford, J.H., Olson, J.R., Hutterli, M.A., Sjostedt, S., Tanner, D., Dibb, J., Lefer, B., Blake, N., Davis, D., and Stohl, A., 2007: An assessment of the polar HOx photochemical budget based on 2003 Summit Greenland field observations. Atmospheric Environment, 41, 7806-7820.

Chesnavich, W.J., Su, T., and Bowers, M.T., 1980: Collisions in a non-central field-variational and trajectory investigation of ion-dipole capture. Journal of Chemical Physics, 72, 2641-2655.

Crawford, J.H., Davis, D.D., Chen, G., Buhr, M., Oltmans, S., Weller, R., Mauldin, L., Eisele, F., Shetter, R., Lefer, B., Arimoto, R., and Hogan, A., 2001: Evidence for photochemical production of ozone at the South Pole surface. Geophysical Research Letters, 28, 3641-3644.

Crutzen, P.J., and Arnold, F., 1986: Nitric-acid cloud formation in the cold Antarctic

stratosphere- A major cause for the springtime ozone hole. Nature, 324, 651-655.

Davis, D., Nowak, J.B., Chen, G., Buhr, M., Arimoto, R., Hogan, A., Eisele, F., Mauldin, L., Tanner, D., Shetter, R., Lefer, B., and Mcmurry, P., 2001: Unexpected high levels of NO observed at South Pole. Geophysical Research Letters, 28, 3625-3628.

Deiber, G., George, C., Le Calve, S., Schweitzer, F., and Mirabel, P., 2004: Uptake study of $ClONO_2$ and $BrONO_2$ by Halide containing droplets. Atmospheric Chemistry and Physics, 4, 1291-1299.

Dibb, J.E., Talbot, R.W., and Bergin, M.H., 1994: Soluble acidic species in air and snow at Summit, Greenland. Geophysical Research Letters, 21, 1627-1630.

Dibb, J.E., and Jaffrezo, J.L., 1997: Air-snow exchange investigations at Summit, Greenland: An overview. Journal of Geophysical Research-Oceans, 102, 26795-26807.

Dibb, J.E., Arsenault, M., Peterson, M.C., and Honrath, R.E., 2002: Fast nitrogen oxide photochemistry in Summit, Greenland snow. Atmospheric Environment, 36, 2501-2511.

Dibb, J.E., Huey, L.G., Slusher, D.L., and Tanner, D.J., 2004: Soluble reactive nitrogen oxides at South Pole during ISCAT 2000. Atmospheric Environment, 38, 5399-5409.

Dibb, J.E., Ziemba, L.D., Luxford, J., and Beckman, P., 2010: Bromide and other ions in the snow, firn air, and atmospheric boundary layer at Summit during GSHOX. Atmospheric Chemistry and Physics, 10, 9931-9942.

Donohoue, D.L., Bauer, D., and Hynes, A.J., 2005: Temperature and pressure dependent rate coefficients for the reaction of Hg with Cl and the reaction of Cl with Cl: A pulsed laser photolysis-pulsed laser induced fluorescence study. Journal of Physical Chemistry A, 109, 7732-7741.

Donohoue, D.L., Bauer, D., Cossairt, B., and Hynes, A.J., 2006: Temperature and pressure dependent rate coefficients for the reaction of Hg with Br and the reaction of Br with Br: A pulsed laser photolysis-pulsed laser induced fluorescence study. Journal of Physical Chemistry A, 110, 6623-6632.

Dorf, M., 2005, Investigation of Inorganic Stratospheric Bromine using Balloon-Borne DOAS Measurements and Model Simulations, Ph.D. thesis, University of Heidelberg, Heidelberg, Germany.

Edwards, G.D., Cantrell, C.A., Stephens, S., Hill, B., Goyea, O., Shetter, R.E., Mauldin, R.L., Kosciuch, E., Tanner, D.J., and Eisele, F.L., 2003: Chemical ionization mass spectrometer instrument for the measurement of tropospheric $HO_2$ and $RO_2$. Analytical Chemistry, 75, 5317-5327.

Eigen, M., and Kustin, K., 1962: Kinetics of halogen hydrolysis. Journal of the American Chemical Society, 84, 1355-&.

Eisele, F.L., Mauldin, R.L., Tanner, D.J., Fox, J.R., Mouch, T., and Scully, T., 1997: An inlet/sampling duct for airborne OR and sulfuric acid measurements. Journal of Geophysical Research-Atmospheres, 102, 27993-28001.

Enami, S., Yamanaka, T., Nakayama, T., Hashimoto, S., Kawasaki, M., Shallcross, D.E., Nakano, Y., and Ishiwata, T., 2007: A gas-phase kinetic study of the reaction between bromine monoxide and methylperoxy radicals at atmospheric temperatures. Journal of Physical Chemistry A, 111, 3342-3348.

Erickson, D.J., Seuzaret, C., Keene, W.C., and Gong, S.L., 1999: A general circulation model based calculation of HCl and $ClNO_2$ production from sea salt dechlorination: Reactive Chlorine Emissions Inventory. Journal of Geophysical Research-Atmospheres, 104, 8347-8372.

Evans, M.J., Jacob, D.J., Atlas, E., Cantrell, C.A., Eisele, F., Flocke, F., Fried, A., Mauldin, R.L., Ridley, B.A., Wert, B., Talbot, R., Blake, D., Heikes, B., Snow, J., Walega, J., Weinheimer, A.J., and Dibb, J., 2003: Coupled evolution of BrO(x)-ClO(x)-HO(x)-NO(x) chemistry during bromine-catalyzed ozone depletion events in the arctic boundary layer. Journal of Geophysical Research-Atmospheres, 108.

Fain, X., Ferrari, C.P., Dommergue, A., Albert, M., Battle, M., Arnaud, L., Barnola, J.M., Cairns, W., Barbante, C., and Boutron, C., 2008: Mercury in the snow and firn at Summit Station, Central Greenland, and implications for the study of past atmospheric mercury levels. Atmospheric Chemistry and Physics, 8, 3441-3457.

Fan, S.M., and Jacob, D.J., 1992: Surface ozone depletion in Arctic spring sustained by bromine reactions on aerosols. Nature, 359, 522-524.

Fickert, S., Adams, J.W., and Crowley, J.N., 1999: Activation of Br-2 and BrCl via uptake of HOBr onto aqueous salt solutions. Journal of Geophysical Research-Atmospheres, 104, 23719-23727.

Finley, B.D., and Saltzman, E.S., 2006: Measurement of Cl-2 in coastal urban air. Geophysical Research Letters, 33.

Finley, B.D., and Saltzman, E.S., 2008: Observations of Cl(2), Br(2), and I(2) in coastal marine air. Journal of Geophysical Research-Atmospheres, 113.

Fitzenberger, R., Bosch, H., Camy-Peyret, C., Chipperfield, M.P., Harder, H., Platt, U., Sinnhuber, B.M., Wagner, T., and Pfeilsticker, K., 2000: First profile measurements of tropospheric BrO. Geophysical Research Letters, 27, 2921-2924.

Fleischmann, O.C., Hartmann, M., Burrows, J.P., and Orphal, J., 2004: New ultraviolet absorption cross-sections of BrO at atmospheric temperatures measured by time-windowing Fourier transform spectroscopy. Journal of Photochemistry and Photobiology a-Chemistry, 168, 117-132.

Fluckiger, B., and Rossi, M.J., 2003: Common precursor mechanism for the heterogeneous reaction of D2O, HCl, HBr, and HOBr with water ice in the range 170-230 K: Mass accommodation coefficients on ice. Journal of Physical Chemistry A, 107, 4103-4115.

Foster, K.L., Plastridge, R.A., Bottenheim, J.W., Shepson, P.B., Finlayson-Pitts, B.J., and Spicer, C.W., 2001: The role of Br-2 and BrCl in surface ozone destruction at polar sunrise. Science, 291, 471-474.

Fried, A., Crawford, J., Olson, J., Walega, J., Potter, W., Wert, B., Jordan, C., Anderson, B., Shetter, R., Lefer, B., Blake, D., Blake, N., Meinardi, S., Heikes, B., O'sullivan, D., Snow, J., Fuelberg, H., Kiley, C.M., Sandholm, S., Tan, D., Sachse, G., Singh, H., Faloona, I., Harward, C.N., and Carmichael, G.R., 2003: Airborne tunable diode laser measurements of formaldehyde during TRACE-P: Distributions and box model comparisons. Journal of Geophysical Research-Atmospheres, 108.

Friedl, R.R., and Sander, S.P., 1989: Kinetics and product studies of the reaction ClO + BrO using discharge-flow mass-spectrometry. Journal of Physical Chemistry, 93, 4756-4764.

Friess, U., Chipperfield, M.P., Harder, H., Otten, C., Platt, U., Pyle, J., Wagner, T., and Pfeilsticker, K., 1999: Intercomparison of measured and modelled BrO slant column amounts for the Arctic winter and spring 1994/95. Geophysical Research Letters, 26, 1861-1864.

Garcia, R.R., Marsh, D.R., Kinnison, D.E., Boville, B.A., and Sassi, F., 2007: Simulation of secular trends in the middle atmosphere, 1950-2003. Journal of Geophysical Research-Atmospheres, 112.

Grannas, A.M., Jones, A.E., Dibb, J., Ammann, M., Anastasio, C., Beine, H.J., Bergin, M., Bottenheim, J., Boxe, C.S., Carver, G., Chen, G., Crawford, J.H., Domine, F., Frey, M.M., Guzman, M.I., Heard, D.E., Helmig, D., Hoffmann, M.R., Honrath, R.E., Huey, L.G., Hutterli, M., Jacobi, H.W., Klan, P., Lefer, B., Mcconnell, J., Plane, J., Sander, R., Savarino, J., Shepson, P.B., Simpson, W.R., Sodeau, J.R., Von Glasow, R., Weller, R., Wolff, E.W., and Zhu, T., 2007: An overview of snow photochemistry: evidence, mechanisms and impacts. Atmospheric Chemistry and Physics, 7, 4329-4373.

Greenblatt, G.D., Orlando, J.J., Burkholder, J.B., and Ravishankara, A.R., 1990: Absorption-measurements of oxygen between 330 nm and 1140 nm. Journal of Geophysical Research-Atmospheres, 95, 18577-18582.

Hall, B., 1995: The gas-phase oxidation of elemental mercury by ozone. Water Air and Soil Pollution, 80, 301-315.

Haman, C., Lefer, B., Dibb, J. E., and Clements, C.: Evidence for a mid- to upper-tropospheric source of bromide reaching Summit, Atmos. Chem. Phys. Discuss., in preparation, 2011.

Hammer, C.U., Clausen, H.B., and Dansgaard, W., 1980: Greenland ice-sheet evidence of post-glacial volcanism and its climatic impact. Nature, 288, 230-235.

Hanson, D.R., Ravishankara, A.R., and Lovejoy, E.R., 1996: Reaction of $BrONO_2$ with $H_2O$ on submicron sulfuric acid aerosol and the implications for the lower stratosphere. Journal of Geophysical Research-Atmospheres, 101, 9063-9069.

Hausmann, M., and Platt, U., 1994: Spectroscopic measurement of bromine oxide and ozone in the high Arctic during polar sunrise experiment 1992. Journal of Geophysical Research-Atmospheres, 99, 25399-25413.

Hebestreit, K., Stutz, J., Rosen, D., Matveiv, V., Peleg, M., Luria, M., and Platt, U., 1999: DOAS measurements of tropospheric bromine oxide in mid-latitudes. Science, 283, 55-57.

Helmig, D., Boulter, J., David, D., Birks, J.W., Cullen, N.J., Steffen, K., Johnson, B.J., and Oltmans, S.J., 2002: Ozone and meteorological Summit, Greenland, boundary-layer conditions at during 3-21 June 2000. Atmospheric Environment, 36, 2595-2608.

Helmig, D., Johnson, B.J., Warshawsky, M., Morse, T., Neff, W.D., Eisele, F., and Davis, D.D., 2008: Nitric oxide in the boundary-layer at South Pole during the Antarctic Tropospheric Chemistry Investigation (ANTCI). Atmospheric Environment, 42, 2817-2830.

Hendrick, F., Van Roozendael, M., Chipperfield, M.P., Dorf, M., Goutail, F., Yang, X., Fayt, C., Hermans, C., Pfeilsticker, K., Pommereau, J.P., Pyle, J.A., Theys, N., and De Maziere, M., 2007: Retrieval of stratospheric and tropospheric BrO profiles and columns using ground-based zenith-sky DOAS observations at Harestua, 60 degrees N. Atmospheric Chemistry and Physics, 7, 4869-4885.

Holmes, C.D., Jacob, D.J., Corbitt, E.S., Mao, J., Yang, X., Talbot, R., and Slemr, F., 2010: Global atmospheric model for mercury including oxidation by bromine atoms. Atmospheric Chemistry and Physics, 10, 12037-12057.

Honninger, G., and Platt, U., 2002: Observations of BrO and its vertical distribution during surface ozone depletion at Alert. Atmospheric Environment, 36, 2481-2489.

Honrath, R.E., Lu, Y., Peterson, M.C., Dibb, J.E., Arsenault, M.A., Cullen, N.J., and Steffen, K., 2002: Vertical fluxes of $NO_x$, HONO, and $HNO_3$ above the snowpack at Summit, Greenland. Atmospheric Environment, 36, 2629-2640.

Honrath, R.E., Peterson, M.C., Guo, S., Dibb, J.E., Shepson, P.B., and Campbell, B., 1999: Evidence of $NO_x$ production within or upon ice particles in the Greenland snowpack. Geophysical Research Letters, 26, 695-698.

Hu, J.H., Shi, Q., Davidovits, P., Worsnop, D.R., Zahniser, M.S., and Kolb, C.E., 1995: Reactive uptake of $Cl_{2(g)}$ and $Br_{2(g)}$ by aqueous surfaces as a function of $Br^-$ and $I^-$ ion concentration-The effect of chemical-reaction at the interface. Journal of Physical Chemistry, 99, 8768-8776.

Huey, L.G., Hanson, D.R., and Howard, C.J., 1995: Reactions of $SF_6^-$ AND $I^-$ with atmospheric trace gases. Journal of Physical Chemistry, 99, 5001-5008.

Huey, L.G., Tanner, D.J., Slusher, D.L., Dibb, J.E., Arimoto, R., Chen, G., Davis, D., Buhr, M.P., Nowak, J.B., Mauldin, R.L., Eisele, F.L., and Kosciuch, E., 2004: CIMS measurements of $HNO_3$ and $SO_2$ at the South Pole during ISCAT 2000. Atmospheric Environment, 38, 5411-5421.

Huey, L.G., 2007: Measurement of trace atmospheric species by chemical ionization mass spectrometry: Speciation of reactive nitrogen and future directions. Mass Spectrometry Reviews, 26, 166-184.

Huff, A.K., and Abbatt, J.P.D., 2000: Gas-phase Br-2 production in heterogeneous reactions of Cl-2, HOCl, and BrCl with halide-ice surfaces. Journal of Physical Chemistry A, 104, 7284-7293.

Hutterli, M.A., Rothlisberger, R., and Bales, R.C., 1999: Atmosphere-to-snow-to-firn transfer studies of HCHO at Summit, Greenland. Geophysical Research Letters, 26, 1691-1694.

Hutterli, M.A., Mcconnell, J.R., Stewart, R.W., Jacobi, H.W., and Bales, R.C., 2001: Impact of temperature-driven cycling of hydrogen peroxide (H2O2) between air and snow on the planetary boundary layer. Journal of Geophysical Research-Atmospheres, 106, 15395-15404.

Hutterli, M.A., Mcconnell, J.R., Chen, G., Bales, R.C., Davis, D.D., and Lenschow, D.H., 2004: Formaldehyde and hydrogen peroxide in air, snow and interstitial air at South Pole. Atmospheric Environment, 38, 5439-5450.

Impey, G.A., Mihele, C.M., Anlauf, K.G., Barrie, L.A., Hastie, D.R., andShepson, P.B., 1999: Measurements of photolyzable halogen compounds and bromine radicals during the Polar Sunrise Experiment 1997. Journal of Atmospheric Chemistry, 34, 21-37.

Jacob, D.J., Crawford, J.H., Maring, H., Clarke, A.D., Dibb, J.E., Emmons, L.K., Ferrare, R.A., Hostetler, C.A., Russell, P.B., Singh, H.B., Thompson, A.M., Shaw, G.E., Mccauley, E., Pederson, J.R., and Fisher, J.A., 2010: The Arctic Research of the Composition of the Troposphere from Aircraft and Satellites (ARCTAS) mission: design, execution, and first results. Atmospheric Chemistry and Physics, 10, 5191-5212.

Jefferson, A., Tanner, D.J., Eisele, F.L., Davis, D.D., Chen, G., Crawford, J., Huey, J.W., Torres, A.L., and Berresheim, H., 1998: OH photochemistry and methane sulfonic acid formation in the coastal Antarctic boundary layer. Journal of Geophysical Research-Atmospheres, 103, 1647-1656.

Jin, R., and Chu, L.T., 2007: Uptake of $NH_3$ and $NH_3$+HOBr reaction on ice surfaces at 190 k. Journal of Physical Chemistry A, 111, 7833-7840.

Jobson, B.T., Niki, H., Yokouchi, Y., Bottenheim, J., Hopper, F., and Leaitch, R., 1994: Measurements of $C_2$-$C_6$ hydrocarbons during the polar sunrise 1992 experiment – Evidence for Cl atom and Br atom chemistry. Journal of Geophysical Research-Atmospheres, 99, 25355-25368.

Johnson, R. D., 2010: NIST Computational Chemistry Comparison and Benchmark Database, NIST Standard Reference Data Number 101, release 15a, National Institute of Standards and Technology, Gaithersburg, MD.

Jones, A.E., Anderson, P.S., Wolff, E.W., Turner, J., Rankin, A.M., and Colwell, S.R., 2006: A role for newly forming sea ice in springtime polar tropospheric ozone loss? Observational evidence from Halley station, Antarctica. Journal of Geophysical Research-Atmospheres, 111.

Jones, A.E., Wolff, E.W., Salmon, R.A., Bauguitte, S.J.B., Roscoe, H.K., Anderson, P.S., Ames, D., Clemitshaw, K.C., Fleming, Z.L., Bloss, W.J., Heard, D.E., Lee, J.D., Read, K.A., Hamer, P., Shallcross, D.E., Jackson, A.V., Walker, S.L., Lewis, A.C., Mills, G.P., Plane, J.M.C., Saiz-Lopez, A., Sturges, W.T., and Worton, D.R., 2008: Chemistry of the Antarctic Boundary Layer and the Interface with Snow: an overview of the CHABLIS campaign. Atmospheric Chemistry and Physics, 8, 3789-3803.

Jones, A.E., Anderson, P.S., Begoin, M., Brough, N., Hutterli, M.A., Marshall, G.J., Richter, A., Roscoe, H.K., and Wolff, E.W., 2009: BrO, blizzards, and drivers of polar tropospheric ozone depletion events. Atmospheric Chemistry and Physics, 9, 4639-4652.

Jones, A.E., Anderson, P.S., Wolff, E.W., Roscoe, H.K., Marshall, G.J., Richter, A., Brough, N., and Colwell, S.R., 2010: Vertical structure of Antarctic tropospheric ozone depletion events: characteristics and broader implications. Atmospheric Chemistry and Physics, 10, 7775-7794.

Kazantseva, N.N., Ernepesova, A., Khodjamamedov, A., Geldyev, O.A., and Krumgalz,

B.S., 2002: Spectrophotometric analysis of iodide oxidation by chlorine in highly mineralized solutions. Analytica Chimica Acta, 456, 105-119.

Kercher, J.P., Riedel, T.P., and Thornton, J.A., 2009: Chlorine activation by N(2)O(5): simultaneous, in situ detection of ClNO(2) and N(2)O(5) by chemical ionization mass spectrometry. Atmospheric Measurement Techniques, 2, 193-204.

Kim, S., Huey, L.G., Stickel, R.E., Tanner, D.J., Crawford, J.H., Olson, J.R., Chen, G., Brune, W.H., Ren, X., Lesher, R., Wooldridge, P.J., Bertram, T.H., Perring, A., Cohen, R.C., Lefer, B.L., Shetter, R.E., Avery, M., Diskin, G., and Sokolik, I., 2007: Measurement of HO(2)NO(2) in the free troposphere during the intercontinental chemical transport experiment - North America 2004. Journal of Geophysical Research-Atmospheres, 112.

Knipping, E.M., Lakin, M.J., Foster, K.L., Jungwirth, P., Tobias, D.J., Gerber, R.B., Dabdub, D., and Finlayson-Pitts, B.J., 2000: Experiments and simulations of ion-enhanced interfacial chemistry on aqueous NaCl aerosols. Science, 288, 301-306.

Kraus, S.,2004: DOASIS: DOAS Intelligent System, Software, copyright 2004 Stefan Kraus, Institute of Environmental Physics, University of Heidelberg, Heidelberg, In cooperation with Hoffmann Messtechnik GmbH.

Kuehl, S., Pukite, J., Deutschmann, T., Platt, U., and Wagner, T., 2008: SCIAMACHY limb measurements of NO(2), BrO and OClO. Retrieval of vertical profiles: Algorithm, first results, sensitivity and comparison studies. Advances in Space Research, 42, 1747-1764.

Kwok, R., 2004: Annual cycles of multiyear sea ice coverage of the Arctic Ocean: 1999-2003. Journal of Geophysical Research-Oceans, 109.

Langridge, J.M., Ball, S.M., and Jones, R.L., 2006: A compact broadband cavity enhanced absorption spectrometer for detection of atmospheric NO2 using light emitting diodes. Analyst, 131, 916-922.

Lawler, M.J., Finley, B.D., Keene, W.C., Pszenny, A.A.P., Read, K.A., Von Glasow, R., and Saltzman, E.S., 2009: Pollution-enhanced reactive chlorine chemistry in the eastern tropical Atlantic boundary layer. Geophysical Research Letters, 36.

Lawler, M.J., Sander, R., Carpenter, L.J., Lee, J.D., Von Glasow, R., Sommariva, R., and Saltzman, E.S., 2011: HOCl and Cl(2) observations in marine air. Atmospheric

Chemistry and Physics, 11, 7617-7628.

Liao, J., Sihler, H., Huey, L.G., Neuman, J.A., Tanner, D.J., Friess, U., Platt, U., Flocke, F.M., Orlando, J.J., Shepson, P.B., Beine, H.J., Weinheimer, A.J., Sjostedt, S.J., Nowak, J.B., Knapp, D.J., Staebler, R.M., Zheng, W., Sander, R., Hall, S.R., and Ullmann, K., 2011a: A comparison of Arctic BrO measurements by chemical ionization mass spectrometry and long path-differential optical absorption spectroscopy. Journal of Geophysical Research-Atmospheres, 116.

Liao, J., Huey, L.G., Tanner, D.J., Brough, N., Brooks, S., Dibb, J.E., Stutz, J., Thomas, J.L., Lefer, B., Haman, C., and Gorham, K., 2011b: Observations of hydroxyl and peroxy radicals and the impact of BrO at Summit, Greenland in 2007 and 2008. Atmospheric Chemistry and Physics, 11, 8577-8591.

Liao, J., Huey, L.G., Tanner, D. J., Flocke, F. M., Orlando, J. J., Neuman, J.A., Nowak, J. B., Weinheimer A. J., Hall, S. R., Smith, J. N., Fried, A., Staebler, R. M., Wang, Y., Koo, J.-H., Cantrell, C. A., Weibring, P., Walega, J., Knapp, D. J., Shepson, P. B., and Stephens, C. R., 2011c: Observed and modeled inorganic bromine (HOBr, BrO, and $Br_2$) speciation at Barrow, AK in spring 2009, Journal of Geophysical Research-Atmospheres, in review.

Liao, J., Huey, L. G., Scheuer, E., Dibb, J. E., Stickel, R. E., Tanner, D. J., Neuman, J. A., Nowak, J. B., Choi, S., Wang, Y., Salawitch, R. J., Canty, T., Chance, K., Kurosu, T., Suleiman, R., Weinheimer, A. J., Shetter, R. E., Fried, A., Brune, W., Anderson, B., Zhang, X., Chen, G., Crawford, J., Hecobian, A., and Ingall, E. D., 2011d: Characterization of soluble bromide measurements and a case study of BrO observations during ARCTAS, Atmospheric Chemistry and Physics Discussion, 11, 26999-27030, doi:10.5194/acpd-11-26999-2011.

Liao, J., Huey, L. G., Z. Liu, D. J. Tanner, P. B. Shepson, A. J. Weinheimer, S. R. Hall, Y. Wang, E. D. Ingall, and C. R. Stephens, 2011d: High levels of molecular chlorine in the Arctic impact methane oxidation and ozone depletion, to be submitted to Nature.

Lindberg, S.E., Brooks, S., Lin, C.J., Scott, K.J., Landis, M.S., Stevens, R.K., Goodsite, M., and Richter, A., 2002: Dynamic oxidation of gaseous mercury in the Arctic troposphere at polar sunrise. Environmental Science & Technology, 36, 1245-1256.

Lorenzen-Schmidt, H., Wessel, S., Unold, W., Solberg, S., Gernandt, H., Stordal, F., and Platt, U., 1998: Ozone measurements in the European Arctic during the ARCTOC

1995 campaign. Tellus Series B-Chemical and Physical Meteorology, 50, 416-429.

Mahajan, A.S., Oetjen, H., Lee, J.D., Saiz-Lopez, A., Mcfiggans, G.B., and Plane, J.M.C., 2009: High bromine oxide concentrations in the semi-polluted boundary layer. Atmospheric Environment, 43, 3811-3818.

Mao, J., Jacob, D.J., Evans, M.J., Olson, J.R., Ren, X., Brune, W.H., St Clair, J.M., Crounse, J.D., Spencer, K.M., Beaver, M.R., Wennberg, P.O., Cubison, M.J., Jimenez, J.L., Fried, A., Weibring, P., Walega, J.G., Hall, S.R., Weinheimer, A.J., Cohen, R.C., Chen, G., Crawford, J.H., Mcnaughton, C., Clarke, A.D., Jaegle, L., Fisher, J.A., Yantosca, R.M., Le Sager, P., and Carouge, C., 2010: Chemistry of hydrogen oxide radicals (HO(x)) in the Arctic troposphere in spring. Atmospheric Chemistry and Physics, 10, 5823-5838.

Mauldin, R.L., Eisele, F.L., Tanner, D.J., Kosciuch, E., Shetter, R., Lefer, B., Hall, S.R., Nowak, J.B., Buhr, M., Chen, G., Wang, P., and Davis, D., 2001: Measurements of OH, H2SO4, and MSA at the South Pole during ISCAT. Geophysical Research Letters, 28, 3629-3632.

Mauldin, R.L., Kosciuch, E., Henry, B., Eisele, F.L., Shetter, R., Lefer, B., Chen, G., Davis, D., Huey, G., and Tanner, D., 2004: Measurements of OH, HO2+RO2, H2SO4, and MSA at the south pole during ISCAT 2000. Atmospheric Environment, 38, 5423-5437.

Mauldin, R., Kosciuch, E., Eisele, F., Huey, G., Tanner, D., Sjostedt, S., Blake, D., Chen, G., Crawford, J., and Davis, D., 2010: South Pole Antarctica observations and modeling results: New insights on HO(x) radical and sulfur chemistry. Atmospheric Environment, 44, 572-581.

Mayewski, P.A., and Bender, M., 1995: The GISP2 ice core record – Paleoclimate highlights. Reviews of Geophysics, 33, 1287-1296.

Mcconnell, J.C., Henderson, G.S., Barrie, L., Bottenheim, J., Niki, H., Langford, C.H., and Templeton, E.M.J., 1992: Photochemical bromine production implication in boundary - layer ozone depletion. Nature, 355, 150-152.

Meller, R., and Moortgat, G.K., 2000: Temperature dependence of the absorption cross sections of formaldehyde between 223 and 323 K in the wavelength range 225-375 nm. Journal of Geophysical Research-Atmospheres, 105, 7089-7101.

Neuman, J.A., Nowak, J.B., Huey, L.G., Burkholder, J.B., Dibb, J.E., Holloway, J.S., Liao, J., Peischl, J., Roberts, J.M., Ryerson, T.B., Scheuer, E., Stark, H., Stickel, R.E., Tanner, D.J., and Weinheimer, A., 2010: Bromine measurements in ozone depleted air over the Arctic Ocean. Atmospheric Chemistry and Physics, 10, 6503-6514.

Nowak, J.B., Huey, L.G., Russell, A.G., Tian, D., Neuman, J.A., Orsini, D., Sjostedt, S.J., Sullivan, A.P., Tanner, D.J., Weber, R.J., Nenes, A., Edgerton, E., and Fehsenfeld, F.C., 2006: Analysis of urban gas phase ammonia measurements from the 2002 Atlanta Aerosol Nucleation and Real-Time Characterization Experiment (ANARChE). Journal of Geophysical Research-Atmospheres, 111.

Oltmans, S.J., 1981: Surface ozone measurements in clean-air. Journal of Geophysical Research-Oceans and Atmospheres, 86, 1174-1180.

Oltmans, S.J., and Komhyr, W.D., 1986: Surface ozone distributions and variations from 1973-1984 measurements at the NOAA geophysical monitoring for climatic – change base-line observatories. Journal of Geophysical Research-Atmospheres, 91, 5229-5236.

Oltmans, S.J., and Levy, H., 1994: Surface ozone measurements from a global network. Atmospheric Environment, 28, 9-24.

Orlando, J.J., Burkholder, J.B., Bopegedera, A., and Howard, C.J., 1991: Infrared measurements of BrO (X2-PI-3/2). Journal of Molecular Spectroscopy, 145, 278-289.

Osthoff, H.D., Roberts, J.M., Ravishankara, A.R., Williams, E.J., Lerner, B.M., Sommariva, R., Bates, T.S., Coffman, D., Quinn, P.K., Dibb, J.E., Stark, H., Burkholder, J.B., Talukdar, R.K., Meagher, J., Fehsenfeld, F.C., and Brown, S.S., 2008: High levels of nitryl chloride in the polluted subtropical marine boundary layer. Nature Geoscience, 1, 324-328.

Oum, K.W., Lakin, M.J., Dehaan, D.O., Brauers, T., and Finlayson-Pitts, B.J., 1998: Formation of molecular chlorine from the photolysis of ozone and aqueous sea-salt particles. Science, 279, 74-77.

Platt, U., 1994: Differential Optical Absorption Spectroscopy (DOAS), in Air Monitoring by Spectroscopic Techniques, edited by M. W. Sigrist, pp. 27-84, John Wiley, New York.

Platt, U., Allan, W., and Lowe, D., 2004: Hemispheric average Cl atom concentration from C-13/C-12 ratios in atmospheric methane. Atmospheric Chemistry and Physics, 4, 2393-2399.

Platt, U., and J. Stutz, 2008: Differential Optical Absorption Spectroscopy: Principles and Applications, Springer, Heidelberg.

Pohler, D., Vogel, L., Friess, U., and Platt, U., 2010: Observation of halogen species in the Amundsen Gulf, Arctic, by active long-path differential optical absorption spectroscopy. Proceedings of the National Academy of Sciences of the United States of America, 107, 6582-6587.

Pratte, P., and Rossi, M.J., 2006: The heterogeneous kinetics of HOBr and HOCl on acidified sea salt and model aerosol at 40-90% relative humidity and ambient temperature. Physical Chemistry Chemical Physics, 8, 3988-4001.

Pukite, J., Kuehl, S., Deutschmann, T., Platt, U., and Wagner, T., 2010: Extending differential optical absorption spectroscopy for limb measurements in the UV. Atmospheric Measurement Techniques, 3, 631-653.

Read, K.A., Mahajan, A.S., Carpenter, L.J., Evans, M.J., Faria, B.V.E., Heard, D.E., Hopkins, J.R., Lee, J.D., Moller, S.J., Lewis, A.C., Mendes, L., Mcquaid, J.B., Oetjen, H., Saiz-Lopez, A., Pilling, M.J., and Plane, J.M.C., 2008: Extensive halogen-mediated ozone destruction over the tropical Atlantic Ocean. Nature, 453, 1232-1235.

Ren, X., Olson, J.R., Crawford, J.H., Brune, W.H., Mao, J., Long, R.B., Chen, Z., Chen, G., Avery, M.A., Sachse, G.W., Barrick, J.D., Diskin, G.S., Huey, L.G., Fried, A., Cohen, R.C., Heikes, B., Wennberg, P.O., Singh, H.B., Blake, D.R., and Shetter, R.E., 2008: HO(x) chemistry during INTEX-A 2004: Observation, model calculation, and comparison with previous studies. Journal of Geophysical Research-Atmospheres, 113.

Richter, A., Wittrock, F., Eisinger, M., and Burrows, J.P., 1998: GOME observations of tropospheric BrO in northern hemispheric spring and summer 1997. Geophysical Research Letters, 25, 2683-2686.

Richter, A., F. Wittrock, A. Ladstatter-Weissenmayer, and J. P. Burrows, 2002: GOME measurements of stratospheric and tropospheric BrO, in Remote Sensing of Trace Constituents in the Lower Stratosphere, Troposphere and the Earth's Surface: Global Observations, Air Pollution and the Atmospheric Correction, edited by J.

P. Burrows and N. Takeucki, pp. 1667-1672, Pergamon-Elsevier Science Ltd, Oxford.

Ridley, B.A., Atlas, E.L., Montzka, D.D., Browell, E.V., Cantrell, C.A., Blake, D.R., Blake, N.J., Cinquini, L., Coffey, M.T., Emmons, L.K., Cohen, R.C., Deyoung, R.J., Dibb, J.E., Eisele, F.L., Flocke, F.M., Fried, A., Grahek, F.E., Grant, W.B., Hair, J.W., Hannigan, J.W., Heikes, B.J., Lefer, B.L., Mauldin, R.L., Moody, J.L., Shetter, R.E., Snow, J.A., Talbot, R.W., Thornton, J.A., Walega, J.G., Weinheimer, A.J., Wert, B.P., and Wimmers, A.J., 2003: Ozone depletion events observed in the high latitude surface layer during the TOPSE aircraft program. Journal of Geophysical Research-Atmospheres, 108.

Robinson, G.N., Worsnop, D.R., Jayne, J.T., Kolb, C.E., Swartz, E., and Davidovits, P., 1998: Heterogeneous uptake of HCl by sulfuric acid solutions. Journal of Geophysical Research-Atmospheres, 103, 25371-25381.

Ryerson, T.B., Williams, E.J., and Fehsenfeld, F.C., 2000: An efficient photolysis system for fast-response $NO_2$ measurements. Journal of Geophysical Research-Atmospheres, 105, 26447-26461.

Saiz-Lopez, A., Shillito, J.A., Coe, H., and Plane, J.M.C., 2006: Measurements and modelling of $I_2$, IO, OIO, BrO and $NO_3$ in the mid-latitude marine boundary layer. Atmospheric Chemistry and Physics, 6, 1513-1528.

Saiz-Lopez, A., Mahajan, A.S., Salmon, R.A., Bauguitte, S.J.B., Jones, A.E., Roscoe, H.K., and Plane, J.M.C., 2007: Boundary layer halogens in coastal Antarctica. Science, 317, 348-351.

Salawitch, R.J., Canty, T., Kurosu, T., Chance, K., Liang, Q., Da Silva, A., Pawson, S., Nielsen, J.E., Rodriguez, J.M., Bhartia, P.K., Liu, X., Huey, L.G., Liao, J., Stickel, R.E., Tanner, D.J., Dibb, J.E., Simpson, W.R., Donohoue, D., Weinheimer, A., Flocke, F., Knapp, D., Montzka, D., Neuman, J.A., Nowak, J.B., Ryerson, T.B., Oltmans, S., Blake, D.R., Atlas, E.L., Kinnison, D.E., Tilmes, S., Pan, L.L., Hendrick, F., Van Roozendael, M., Kreher, K., Johnston, P.V., Gao, R.S., Johnson, B., Bui, T.P., Chen, G., Pierce, R.B., Crawford, J.H., and Jacob, D.J., 2010: A new interpretation of total column BrO during Arctic spring. Geophysical Research Letters, 37.

Sander, S. P, Friedl, R. R., Golden, D. M., Kurylo, M. J., Moortgat, Keller-Rudek, H., G. K., Wine, P. H., Ravishankara, A. R., Kolb, C. E., Molina, M. J., Finlayson-Pitts, B., Huie, R. E., and Orkin, V. L, 2006: Chemical Kinetics and Photochemical

Data for Use in Atmospheric Studies Evaluation Number 15, JPL Publ. 06-2, NASA Jet Propulsion Laboratory, California Institute of Technology, Pasadena, CA.

Scheuer, E., Talbot, R.W., Dibb, J.E., Seid, G.K., Debell, L., and Lefer, B., 2003: Seasonal distributions of fine aerosol sulfate in the North American Arctic basin during TOPSE. Journal of Geophysical Research-Atmospheres, 108.

Scheuer, E., Dibb, J.E., Twohy, C., Rogers, D.C., Heymsfield, A.J., and Bansemer, A., 2010: Evidence of nitric acid uptake in warm cirrus anvil clouds during the NASA TC4 campaign. Journal of Geophysical Research-Atmospheres, 115.

Schroeder, W.H., Anlauf, K.G., Barrie, L.A., Lu, J.Y., Steffen, A., Schneeberger, D.R., and Berg, T., 1998: Arctic springtime depletion of mercury. Nature, 394, 331-332.

Schroeder, W.H., and Munthe, J., 1998: Atmospheric mercury - An overview. Atmospheric Environment, 32, 809-822.

Schofield, R., Kreher, K., Connor, B.J., Johnston, P.V., Thomas, A., Shooter, D., Chipperfield, M.P., Rodgers, C.D., and Mount, G.H., 2004: Retrieved tropospheric and stratospheric BrO columns over Lauder, New Zealand. Journal of Geophysical Research-Atmospheres, 109.

Shetter, R.E., and Muller, M., 1999: Photolysis frequency measurements using actinic flux spectroradiometry during the PEM-Tropics mission: Instrumentation description and some results. Journal of Geophysical Research-Atmospheres, 104, 5647-5661.

Simpson, W.R., Von Glasow, R., Riedel, K., Anderson, P., Ariya, P., Bottenheim, J., Burrows, J., Carpenter, L.J., Friess, U., Goodsite, M.E., Heard, D., Hutterli, M., Jacobi, H.W., Kaleschke, L., Neff, B., Plane, J., Platt, U., Richter, A., Roscoe, H., Sander, R., Shepson, P., Sodeau, J., Steffen, A., Wagner, T., and Wolff, E., 2007a: Halogens and their role in polar boundary-layer ozone depletion. Atmospheric Chemistry and Physics, 7, 4375-4418.

Simpson, W.R., Carlson, D., Honninger, G., Douglas, T.A., Sturm, M., Perovich, D., and Platt, U., 2007b: First-year sea-ice contact predicts bromine monoxide (BrO) levels at Barrow, Alaska better than potential frost flower contact. Atmospheric Chemistry and Physics, 7, 621-627.

Sinnhuber, B.M., Rozanov, A., Sheode, N., Afe, O.T., Richter, A., Sinnhuber, M., Wittrock, F., Burrows, J.P., Stiller, G.P., Von Clarmann, T., and Linden, A., 2005: Global observations of stratospheric bromine monoxide from SCIAMACHY. Geophysical Research Letters, 32.

Sjostedt, S. J., 2006: Investigation of photochemistry at high latitudes: comparison of model predictions to measurements of short lived species, Ph.D thesis, Georgia Institute of Technology, Atlanta.

Sjostedt, S.J., Huey, L.G., Tanner, D.J., Peischl, J., Chen, G., Dibb, J.E., Lefer, B., Hutterli, M.A., Beyersdorf, A.J., Blake, N.J., Blake, D.R., Sueper, D., Ryerson, T., Burkhart, J., and Stohl, A., 2007: Observations of hydroxyl and the sum of peroxy radicals at Summit, Greenland during summer 2003. Atmospheric Environment, 41, 5122-5137.

Slusher, D.L., Pitteri, S.J., Haman, B.J., Tanner, D.J., and Huey, L.G., 2001: A chemical ionization technique for measurement of pernitric acid in the upper troposphere and the polar boundary layer. Geophysical Research Letters, 28, 3875-3878.

Slusher, D.L., Huey, L.G., Tanner, D.J., Flocke, F.M., and Roberts, J.M., 2004: A thermal dissociation-chemical ionization mass spectrometry (TD-CIMS) technique for the simultaneous measurement of peroxyacyl nitrates and dinitrogen pentoxide. Journal of Geophysical Research-Atmospheres, 109.

Solomon, S., 1999: Stratospheric ozone depletion: A review of concepts and history. Reviews of Geophysics, 37, 275-316.

Sommar, J., Gardfeldt, K., Stromberg, D., and Feng, X.B., 2001: A kinetic study of the gas-phase reaction between the hydroxyl radical and atomic mercury. Atmospheric Environment, 35, 3049-3054.

Spicer, C.W., Chapman, E.G., Finlayson-Pitts, B.J., Plastridge, R.A., Hubbe, J.M., Fast, J.D., and Berkowitz, C.M., 1998: Unexpectedly high concentrations of molecular chlorine in coastal air. Nature, 394, 353-356.

Spurr, R.J.D., Kurosu, T.P., and Chance, K.V., 2001: A linearized discrete ordinate radiative transfer model for atmospheric remote-sensing retrieval. Journal of Quantitative Spectroscopy & Radiative Transfer, 68, 689-735.

Steffen, A., Douglas, T., Amyot, M., Ariya, P., Aspmo, K., Berg, T., Bottenheim, J.,

Brooks, S., Cobbett, F., Dastoor, A., Dommergue, A., Ebinghaus, R., Ferrari, C., Gardfeldt, K., Goodsite, M.E., Lean, D., Poulain, A.J., Scherz, C., Skov, H., Sommar, J., and Temme, C., 2008: A synthesis of atmospheric mercury depletion event chemistry in the atmosphere and snow. Atmospheric Chemistry and Physics, 8, 1445-1482.

Stephens, C. R., P. B. Shepson, A. Steffen, J. W. Bottenheim, J. Liao, L. G. Huey, E. Apel, A. Weinheimer, S. R. Hall, C. Cantrell, B. C. Sive, D. J. Knapp, and D. D. Montzka, 2011: The relative importance of chlorine and bromine radicals in the oxidation of atmospheric mercury at Barrow, AK, Journal of Geophysical Research-Atmospheres, in review.

Stohl, A., Forster, C., Frank, A., Seibert, P., and Wotawa, G., 2005: Technical note: The Lagrangian particle dispersion model FLEXPART version 6.2. Atmospheric Chemistry and Physics, 5, 2461-2474.

Streit, G.E., 1982: Negative-ion chemistry and the electron- affinity of $SF_6$. Journal of Chemical Physics, 77, 826-833.

Sturges, W.T., and Barrie, L.A., 1988: Chlorine, bromine and iodine in Arctic aerosols. Atmospheric Environment, 22, 1179-1194.

Stutz, J., and Platt, U., 1996: Numerical analysis and estimation of the statistical error of differential optical absorption spectroscopy measurements with least-squares methods. Applied Optics, 35, 6041-6053.

Stutz, J., and Platt, U., 1997: Improving long-path differential optical absorption spectroscopy with a quartz-fiber mode mixer. Applied Optics, 36, 1105-1115.

Stutz, J., Kim, E.S., Platt, U., Bruno, P., Perrino, C., and Febo, A., 2000: UV-visible absorption cross sections of nitrous acid. Journal of Geophysical Research-Atmospheres, 105, 14585-14592.

Stutz, J., Ackermann, R., Fast, J.D., and Barrie, L., 2002: Atmospheric reactive chlorine and bromine at the Great Salt Lake, Utah. Geophysical Research Letters, 29.

Stutz, J., Oh, H.-J., Whitlow, S.I., Anderson, C., Dibbb, J.E., Flynn, J.H., Rappenglueck, B., and Lefer, B., 2010: Simultaneous DOAS and mist-chamber IC measurements of HONO in Houston, TX. Atmospheric Environment, 44, 4090-4098.

Su, T., and Chesnavich, W.J., 1982: Parameteriztion of the ion-polar molecule collision rate-constant by trajectory calculations. Journal of Chemical Physics, 76, 5183-5185.

Swanson, A.L., Blake, N.J., Dibb, J.E., Albert, M.R., Blake, D.R., and Rowland, F.S., 2002: Photochemically induced production of $CH_3Br$, $CH_3I$, $C_2H_5I$, ethene, and propene within surface snow at Summit, Greenland. Atmospheric Environment, 36, 2671-2682.

Tanner, D.J., Jefferson, A., and Eisele, F.L., 1997: Selected ion chemical ionization mass spectrometric measurement of OH. Journal of Geophysical Research-Atmospheres, 102, 6415-6425.

Theys, N., Van Roozendael, M., Errera, Q., Hendrick, F., Daerden, F., Chabrillat, S., Dorf, M., Pfeilsticker, K., Rozanov, A., Lotz, W., Burrows, J.P., Lambert, J.C., Goutail, F., Roscoe, H.K., and De Maziere, M., 2009: A global stratospheric bromine monoxide climatology based on the BASCOE chemical transport model. Atmospheric Chemistry and Physics, 9, 831-848.

Theys, N., Van Roozendael, M., Hendrick, F., Yang, X., De Smedt, I., Richter, A., Begoin, M., Errera, Q., Johnston, P.V., Kreher, K., and De Maziere, M., 2011: Global observations of tropospheric BrO columns using GOME-2 satellite data. Atmospheric Chemistry and Physics, 11, 1791-1811.

Thomas, J.L., Stutz, J., Lefer, B., Huey, L.G., Toyota, K., Dibb, J.E., and Von Glasow, R., 2011: Modeling chemistry in and above snow at Summit, Greenland - Part 1: Model description and results. Atmospheric Chemistry and Physics, 11, 4899-4914.

Thornton, J.A., Kercher, J.P., Riedel, T.P., Wagner, N.L., Cozic, J., Holloway, J.S., Dube, W.P., Wolfe, G.M., Quinn, P.K., Middlebrook, A.M., Alexander, B., and Brown, S.S., 2010: A large atomic chlorine source inferred from mid-continental reactive nitrogen chemistry. Nature, 464, 271-274.

Toohey, D.W., Anderson, J.G., Brune, W.H., and Chan, K.R., 1990: Insitu measurements of BrO in the Arctic stratosphere. Geophysical Research Letters, 17, 513-516.

Tuckermann, M., Ackermann, R., Golz, C., Lorenzenschmidt, H., Senne, T., Stutz, J., Trost, B., Unold, W., and Platt, U., 1997: DOAS-observation of halogen radical-catalysed arctic boundary layer ozone destruction during the ARCTOC-campaigns 1995 and 1996 in Ny-Alesund, Spitsbergen. Tellus Series B-Chemical

and Physical Meteorology, 49, 533-555.

Turnipseed, A.A., Birks, J.W., and Calvert, J.G., 1991: Kinetics and temperature-dependence of the BrO + ClO reaction. Journal of Physical Chemistry, 95, 4356-4364.

Vogt, R., Crutzen, P.J., and Sander, R., 1996: A mechanism for halogen release from sea-salt aerosol in the remote marine boundary layer. Nature, 383, 327-330.

Wachsmuth, M., Gaggeler, H.W., Von Glasow, R., and Ammann, M., 2002: Accommodation coefficient of HOBr on deliquescent sodium bromide aerosol particles. Atmospheric Chemistry and Physics, 2, 121-131.

Wagner, T., and Platt, U., 1998: Satellite mapping of enhanced BrO concentrations in the troposphere. Nature, 395, 486-490.

Wagner, T., and Platt, U., 1998: Satellite mapping of enhanced BrO concentrations in the troposphere. Nature, 395, 486-490.

Waschewsky, G.C.G., and Abbatt, J.P.D., 1999: HOBr in sulfuric acid solutions: Solubility and reaction with HCl as a function of temperature and concentration. Journal of Physical Chemistry A, 103, 5312-5320.

Weibring, P., Richter, D., Fried, A., Walega, J.G., and Dyroff, C., 2006: Ultra-high-precision mid-IR spectrometer II: system description and spectroscopic performance. Applied Physics B-Lasers and Optics, 85, 207-218.

Weinheimer, A.J., Montzka, D.D., Campos, T.L., Walega, J.G., Ridley, B.A., Donnelly, S.G., Keim, E.R., Del Negro, L.A., Proffitt, M.H., Margitan, J.J., Boering, K.A., Andrews, A.E., Daube, B.C., Wofsy, S.C., Anderson, B.E., Collins, J.E., Sachse, G.W., Vay, S.A., Elkins, J.W., Wamsley, P.R., Atlas, E.L., Flocke, F., Schauffler, S., Webster, C.R., May, R.D., Loewenstein, M., Podolske, J.R., Bui, T.P., Chan, K.R., Bowen, S.W., Schoeberl, M.R., Lait, L.R., and Newman, P.A., 1998: Comparison between DC-8 and ER-2 species measurements in the tropical middle troposphere: NO, $NO_y$, $O_3$, $CO_2$, $CH_4$, and $N_2O$. Journal of Geophysical Research-Atmospheres, 103, 22087-22096.

Wilmouth, D.M., Hanisco, T.F., Donahue, N.M., and Anderson, J.G., 1999: Fourier transform ultraviolet spectroscopy of the A (2)Pi(3/2) <- X (II3/2)-I-2 transition of BrO. Journal of Physical Chemistry A, 103, 8935-8945.

Woo, K.S., Chen, D.R., Pui, D.Y.H., and Mcmurry, P.H., 2001: Measurement of Atlanta aerosol size distributions: Observations of ultrafine particle events. Aerosol Science and Technology, 34, 75-87.

Wu, C., Birky, M.M., and Hepler, L.G., 1963: Thermochemistry of some bromine and iodine species in aqueous solution. Journal of Physical Chemistry, 67, 1202-&.

Yang, J., Honrath, R.E., Peterson, M.C., Dibb, J.E., Sumner, A.L., Shepson, P.B., Frey, M., Jacobi, H.W., Swanson, A., and Blake, N., 2002: Impacts of snowpack emissions on deduced levels of OH and peroxy radicals at Summit, Greenland. Atmospheric Environment, 36, 2523-2534.

Yang, X., Pyle, J.A., Cox, R.A., Theys, N., and Van Roozendael, M., 2010: Snow-sourced bromine and its implications for polar tropospheric ozone. Atmospheric Chemistry and Physics, 10, 7763-7773.

Zeng, T., Wang, Y.H., Chance, K., Browell, E.V., Ridley, B.A., and Atlas, E.L., 2003: Widespread persistent near-surface ozone depletion at northern high latitudes in spring. Geophysical Research Letters, 30.

Zeng, T., 2005: Three-Dimensional Model Analysis of Tropospheric Photochemical Processes in the Arctic and Northern Mid-latitudes, Ph.D. thesis, Georgia Institute of Technology, Atlanta.

Ziemba, L.D., Dibb, J.E., Griffin, R.J., Huey, L.G., and Beckman, P., 2010: Observations of particle growth at a remote, Arctic site. At*mospheric Environment,* 44, 1649-1657.

# VITA

Jin Liao was born in Shantou, China on July 28, 1983 to Shizao Liao and Daina Chen. She went to Guangzhou, China to attend Sun Yat-Sen University in September 2002 and received a B. S. in Environmental Science in 2006. She then moved to Atlanta, GA, USA in August 2006 to pursue graduate studies and join Prof. Greg Huey's group at Georgia Tech. In 2011, Jin was invited to participate in the Atmospheric Chemistry Colloquium for Emerging Senior Scientists (ACCESS). She defended her PhD in Atmospheric Chemistry in October 2011.